Industrial Wastewater Treatment with Cavitation based Hybrid Advanced Oxidation Processes

A

Thesis

Submitted in

Partial Fulfillment of the

Requirements for the degree of

DOCTOR OF PHILOSOPHY

By

Komal Verma

Department of Chemical Engineering

Indian Institute of Technology Guwahati

Guwahati- 781039, Assam, India

June 2025

Dedicated

to

My Parents

And

My Mentor

INDIAN INSTITUTE OF TECHNOLOGY GUWAHATI

Department of Chemical Engineering

STATEMENT

I do hereby declare that the content embodied in this thesis entitled "**Industrial Wastewater Treatment with Cavitation based Hybrid Advanced Oxidation Processes**" is the result of investigations carried out by me in the Department of Chemical Engineering, Indian Institute of Technology Guwahati, Guwahati, India, under the guidance of Prof. Vijayanand S. Moholkar. In keeping with the general practice of reporting scientific observations, due acknowledgments have been made wherever the work described is based on the findings of other investigators.

Komal Verma

June 2025

Komal Verma

(Roll No: 206107015)

INDIAN INSTITUTE OF TECHNOLOGY GUWAHATI

Department of Chemical Engineering

CERTIFICATE

This is to certify that the work described in this thesis entitled "**Industrial Wastewater Treatment with Cavitation based Hybrid Advanced Oxidation Processes,**" which is being submitted by **Mrs. Komal Verma (Roll No.: 206107015)** to the Indian Institute of Technology Guwahati, India, for the award of Doctor of Philosophy, is a record of bonafide research work carried out by her under my supervision. The work embodied in this thesis has not been submitted elsewhere for a degree.

June 2025

Prof. Vijayanand S. Moholkar

Department of Chemical Engineering

Indian Institute of Technology Guwahati

Guwahati- 781039, Assam, India

ACKNOWLEDGEMENTS

This thesis marks the end of my cherished memories as a research scholar at IITG. It gives me immense pleasure to express my deepest gratitude to each and every one of you who made this thesis possible and constantly encouraged me during my research work.

My first and foremost appreciation goes to my supervisor, Prof. Vijayanand S. Moholkar, for encouragement and relentless support throughout my research. I want to thank him for sharing his technical thoughts, which have always motivated me to progress towards new aspects. I am fortunate that he took me under his wing and considered me to work under his esteemed guidance. I have thoroughly enjoyed working with him, and I firmly believe he has brought out the best in me in every aspect. His profound knowledge has helped me to understand the mechanistic features of cavitation-based hybrid advanced oxidation processes.

I want to acknowledge my sincere gratitude to my doctoral committee members, **Prof. Mihir Kumar Purkait**, **Prof. Animes Golder**, and **Prof. Pranab Kumar Ghosh** (Department of Civil Engineering), for their insightful advice and suggestions throughout the research that led to the successful completion of the thesis.

My sincere thanks go to the Chemical Engineering Department faculty members for their continuous inspiration and valuable suggestions. The kind and constant help of the Department of Chemical Engineering staff members is also acknowledged. The advanced analytical facilities from the Central Instruments Facility (CIF) of the Indian Institute of Technology Guwahati are duly acknowledged.

I am immensely thankful to my seniors, Dr. Kuldeep Roy, Dr. Kajal Igntipi, Dr Bhaskarjyoti, Dr. Karan Kumar, and research group members Aradhana, Pushpita, Rishiraj, Avinash, Harshendra, Umesh, Arjita, Rahul, Annaya, Divyansh, and Gurleen. I am highly thankful to my friends, Debraj, Soumaya, Rubeka, Namrata, and Sapna, for their love and support.

I want to thank my husband (**Mr. Anurag**) and my parents (**Maa and Papa**), my brother (**Kapil Verma**), and my in-law's family for showering their endless love, care, and support throughout my life. I owe my gratitude to all of them.

Last, I express my deepest gratitude to **Almighty GOD** for blessing me and giving me the strength to complete this research work.

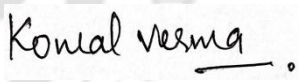

June 2025, Komal Verma

ABSTRACT

This thesis investigates the advanced treatment and mineralization of industrial wastewater using innovative hybrid advanced oxidation processes (AOPs). Industrial wastewater, characterized by high chemical oxygen demand (COD) and total organic carbon (TOC), was treated through various ternary hybrid AOPs, combining adsorption, Fenton reactions, and sonication or hydrodynamic cavitation (HC).

The development and efficacy of advanced oxidation processes (AOPs) employing Fe_3O_4-based nanocomposites for industrial wastewater (WW) treatment. A ternary hybrid AOP combining sonication, Fenton reactions, and adsorption was employed using Fe_3O_4@AC nanocomposites, achieving 94.75% COD and 89% TOC removal within 60 min. LC-MS analysis identified the effective degradation of over 25 organic pollutants, including herbicides and pesticides, with a 60% reduction in wastewater toxicity. Synergistic interactions between activated charcoal adsorption, Fenton reactions, and sonication-induced microconvection were responsible for the enhanced mineralization. Next, work extended to sonoenzymatic treatments using laccase immobilized on Fe_3O_4 nanoparticles (Fe_3O_4@Laccase), demonstrating 90.3% COD removal with sonication-assisted enzymatic activity. Structural analysis via FTIR revealed enzyme conformational changes contributing to improved kinetics and substrate affinity. Toxicity analysis indicated a 70% reduction, the biocatalyst retained activity over six cycles. Additionally, Fe_3O_4@AC nanocomposites were incorporated into chitosan-based hydrogel beads (Fe_3O_4@AC@CH) to develop a floatable hybrid AOP system. Under optimized conditions, COD and TOC removal reached 96.12% and 78.14%, respectively, with significant degradation of major pollutants. Sonication enhanced mass transfer, while the hydrogel's porous structure facilitated adsorption and surface Fenton reactions, resulting in synergistic pollutant degradation. The beads maintained catalytic performance for six reuse cycles. Lastly,

a novel combination of hydrodynamic cavitation (HC), Fe_3O_4@AC nanocomposites, and Fenton reactions was investigated. Optimized conditions yielded 99.37% COD and 88.80% TOC removal. The HC-based process exhibited superior cavitational yields and significantly enhanced reaction kinetics. The Fe_3O_4@AC nanocomposites demonstrated high stability and reusability. The findings illustrate the potential of these hybrid AOPs for scalable and efficient industrial wastewater treatment, contributing to sustainable environmental management.

CONTENTS

LIST OF TABLES

CHAPTER 1

CHAPTER 2

CHAPTER 3

CHAPTER 4

CHAPTER 5

LIST OF FIGURES

CHAPTER 1

CHAPTER 2

CHAPTER 3

CHAPTER 5

LIST OF NOMENCLATURE

ACRONYMS

AC	Activated charcoal
AF-MNPs	Amino-functionalized magnetic nanoparticles
ANOVA	Analysis of variance
AOP	Advanced oxidation processes
BBD	Box-Behnken design
BET	Brunauer-Emmett-Teller
BOD	Biological oxygen demand
CCD	Central composite design
CH	Chitosan
COD	Chemical oxygen demand
EDX	Energy-dispersive X-ray spectroscopy
FE-SEM	Field emission scanning electron microscopy
FE-TEM	Field emission transmission electron microscopy
FTIR	Fourier transform infrared spectroscopy
HC	Hydrodynamic cavitation
LC-MS	Liquid chromatography-mass –spectroscopy
NPs	Nanoparticles
RSM	Response surface methodology
TOC	Total organic carbon
US	Ultrasound

VFD	Variable frequency drive
VSM	Vibrating sample magnetometer
WW	Wastewater
XRD	X-ray diffraction

SYMBOLS

C_v	Cavitation number
f	Density of water
k	Kinetic rate constant
b	Langmuir constant
q_m	Maximum adsorption capacity
k_m	Michaelis constant
V_{max}	Reaction velocity
P_2	Recovered downstream pressure
M_s	Saturated magnetization
R_L	Separation factor
P_v	Vapor pressure of the liquid
v_o	Velocity at the throat of the cavitation device
Q	Volumetric flow rate

CHAPTER 1

GENERAL INTRODUCTION AND LITERATURE REVIEW

1.1 Introduction

As the global population continues to grow with fast urbanization, industrial development is expanding to satisfy human demands. The industrial activities lead to the generation of significant quantities of wastewater and solid waste, which contribute to severe environmental pollution. Water pollution has emerged as one of the most critical environmental challenges globally, with industrial wastewater serving as a significant contributor. The complex nature, low biodegradability, and high toxicity of industrial wastewater can severely affect ecosystems (Kamali and Khodaparast 2015; Ganiyu et al. 2020; Mehrkhah et al. 2024). The effluents discharged from these industries typically consist of a diverse array of persistent organic compounds of varying toxicity alongside various inorganic molecules and heavy metals. These contaminants may potentially lead to carcinogenic and mutagenic effects in humans and aquatic organisms (Madhavan et al. 2019; Gałązka and Jankiewicz 2022). Researchers worldwide have been striving to tackle the daunting issue of wastewater pollution by developing various treatment processes to remove contaminants effectively. These processes range from single or one-step treatment to sequential combinations of treatments. Once widely regarded as a practical solution, chlorination has fallen out of favor due to concerns over the harmful by-products it produces and the increasingly strict drinking water standards (Kurian

2021). A diverse array of physical, chemical, and biological wastewater treatments has been investigated as more efficient and economical alternatives. However, despite their advantages, many of these techniques are inadequate for large-scale applications and fall short of fully breaking down the organic pollutants present in industrial wastewater (Wang et al. 2014; Alfaia et al. 2019). This limitation underscores the urgent need for new and innovative technologies to address the persistent challenges posed by refractory industrial pollutants.

In this regard, advanced oxidation processes (AOPs) are regarded as an effective technique for the elimination of organic pollutants. These processes can successfully eliminate a wide range of contaminants, including micro-pollutants and organic molecules (Ahmed et al. 2017; Mandal et al. 2017; Mehrkhah et al. 2024). Figure 1.1 represents the schematic representation of different AOPs practiced for the degradation of the pollutants. The breakdown of organic pollutants through various methods shows significant potential. Notably, advanced oxidation processes that utilize reactive radical species allow for effective oxidation and even complete mineralization of organic compounds. Advanced Oxidation Processes (AOPs) involve the generation and utilization of highly reactive transient species, primarily hydroxyl ($^{\bullet}OH$) radicals (Rodríguez-Narváez et al. 2021; Mehrkhah et al. 2024). These radicals can be produced from water using various energy sources such as solar, electrical, or sound energy, or through the use of chemicals like hydrogen peroxide (H_2O_2) or ozone, with or without the aid of a catalyst. The key difference lies in the method of hydroxyl radical generation. Other reactive oxygen species, such as the superoxide ion radical $O_2^{\bullet -}$ and its conjugate acid form, the hydroperoxyl radical $HO_2^{\bullet}$, are also formed in many AOPs but are much less reactive than hydroxyl radicals. Table 1.1 represents the characteristics of oxidative radicals generated during the cavitation process.

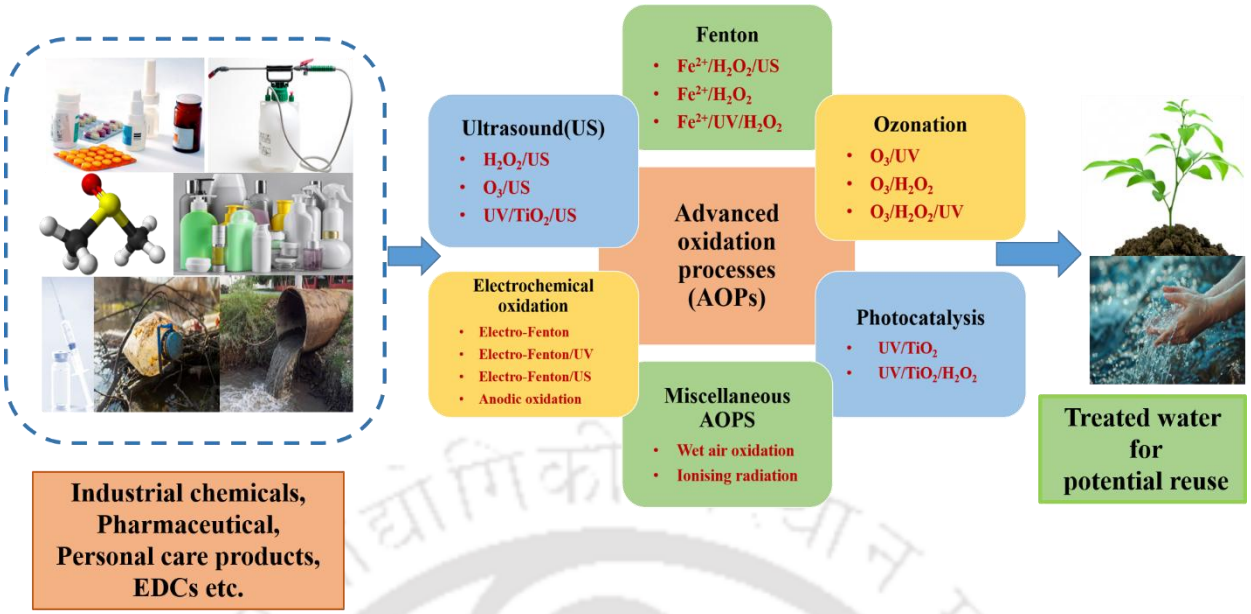

Figure 1.1. Schematic representation of different advanced oxidation processes for pollutant degradation

Table 1.1. Characteristics of oxidative radicals involved in the cavitation-based treatment process

Oxidant	**Average lifetime in groundwater**	**Oxidation potential (eV)**
H_2O_2	hours to day	1.8
O_3	< 1 h	2.1
PDS ($S_2O_8^{2-}$)	> 5 months	2.1
PMS (HSO_5^-)	hours to day	1.82
$^{\bullet}OH$	10^{-3} µs (half-life)	2.8
$SO_4^{\bullet-}$	30-40 µs (half-life)	2.5-3.1

The hydroxyl radical $^{\bullet}OH$, with an oxidation potential of 2.8 eV, is a highly potent and non-selective oxidizing agent that reacts rapidly with most organic compounds. As a result, it is

often the preferred oxidant for the chemical oxidation processes (Gogate and Pandit 2004; Madhavan et al. 2010; Kurian and Nair 2015). Figure 1.2 depicts the schematic representation of the properties of hydroxyl radicals. The final products of complete oxidation typically include water, carbon dioxide, oxygen, and mineral acids, depending on the target pollutant.

Figure 1.2. Schematic representation of properties of hydroxyl radicals

Among the relatively new AOPs, cavitation is highly effective in the degradation of pollutants, particularly in an aqueous medium. Cavitation is especially advantageous for wastewater treatment due to its ability to degrade complex and refractory organic compounds. Moreover, it can be used in combination with other AOPs, such as ozonation or hydrogen peroxide addition, to enhance efficiency (Gogate 2002; Bagal and Gogate 2014a; Agarkoti et al. 2022; Bagal et al. 2023). Cavitation is a technique that can be effectively utilized for the breakdown of complex organic compounds and bio-refractory substances. It is generally defined as the process of microbubble or cavity formation, growth, and subsequent collapse, all occurring

within extremely short time intervals-on the scale of few nanoseconds-resulting in the release of substantial energy in very localized areas. This phenomenon takes place at millions of sites within the reactor simultaneously. The intensity of the resulting pressures (~ 1000 bar) and temperatures (~ 5000 K) is highly dependent on the reactor's operating conditions and geometric design (Shirgaonkar and Pandit 1997; BlakePerutz et al. 1999). The violent collapse of these cavities generates reactive species such as hydrogen atoms and hydroxyl radicals through thermal dissociation of the gas and vapor molecules present in the bubble. The mechanism of the radical formation during the transient collapse of the cavitation bubble can be described briefly as follows:

During the rarefaction half cycle of the ultrasound wave, the cavitation bubble undergoes expansion. This expansion is accompanied by evaporation of the liquid (usually water) molecules at the gas-liquid interface. These molecules diffuse towards the core of the bubble during the expansion of the bubble. During the ensuing compression cycle, the bubble wall (or the gas-liquid interface) recedes as the bubble undergoes size reduction due to compression. The vapor molecules present in the bubble now start diffusing towards the bubble wall (or gas-liquid interface) and condense there. However, the compression phase is driven by both pressure and inertial forces. As the bubble is compressed, it creates a void in the medium. The liquid elements surrounding the bubble gush into this void space, which results in further compression of the bubble due to kinetic energy imparted to it (or the work done) by the liquid elements. The bubble wall undergoes a fast acceleration, and the velocity at which the gas-liquid interface recedes reaches very high (~ 500 – 1000 m/s). At these conditions, the vapor molecules at the core of the bubble do not have sufficient time to diffuse to the bubble wall and undergo condensation. The molecules that are in the vicinity of the bubble wall also do not undergo a phase change, as they cannot “stick” to the fast-moving gas-liquid interface. This phenomena essentially results in “trapping” of the vapor molecules inside the bubble.

Moreover, the bubble compression is adiabatic, and hence, the temperature and pressure inside the bubble reach extreme (5000 K and ~ 1000 bar). The molecules trapped inside the bubble are subjected to these extreme conditions, at which they undergo thermal dissociation into numerous radical and molecular species. The compressed cavitation bubble (at the minimum size) is extremely energetic due to the high temperature and pressure conditions that reach inside it. At these conditions, this bubble may undergo fragmentation with the release of the radical and other species inside the bulk medium. The radical species released into the medium are highly reactive and can react with the pollutant molecules present in the immediate vicinity. In case the radicals are not able to "find" a pollutant molecule, they may simply react with each other (or recombine) to produce molecular species. For example, two $^{*}OH$ radicals can recombine to form H_2O_2, hydrogen peroxide. Figure 1.3 depicts the schematic representation of the mechanism of cavitation. Cavitation is generally categorized into four types based on how it is generated: acoustic cavitation, hydrodynamic cavitation, optical cavitation, and particle cavitation. Among these, acoustic and hydrodynamic cavitation have attracted significant academic and industrial interest due to their operational simplicity and the ease with which they generate the necessary cavitational intensities.

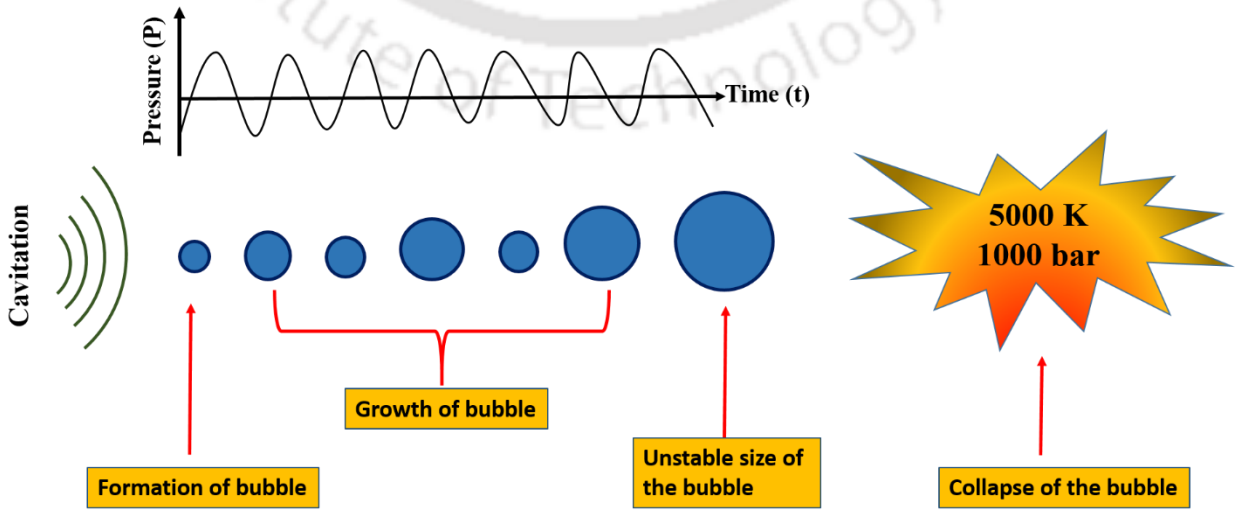

Figure 1.3. Schematic representation of the cavitation phenomenon

The chemical processes which can be intensified using acoustic cavitation, popularly known as sonochemical processes, have been extensively researched over the past several decades. Numerous comprehensive reviews are available in the literature, detailing the scope and applications of ultrasound-based processes (Hoffmann et al. 1996; BlakePerutz et al. 1999; Gogate and Pandit 2000; Lu and Weavers 2002; Appaw and Adewuyi 2002; Moholkar and Warmoeskerken 2003; Chatel et al. 2017). Ultrasound refers to sound waves with frequencies above 20 kHz, and can be categorized into three main frequency ranges: low (20–100 kHz), medium (300–1000 kHz), and high (2–10 MHz) (de Andrade et al. 2021). It is recognized as an eco-friendly, efficient method for breaking down organic pollutants through sonochemical reactions, offering several advantages such as simple equipment, rapid processing, high efficiency, and minimal space requirements. Acoustic cavitation is triggered by sound waves produced by an ultrasound generator. This process involves microbubbles' nucleation, growth, and eventual collapse. Figure 1.4 represents the ultrasound cavitation phenomenon. Variations in bulk system pressure caused by the propagation of ultrasound waves can grow numerous cavitation bubbles in the liquid from the nuclei already present in the liquid. These bubbles undergo volume oscillations (growth and rapid collapse), releasing substantial energy in an extremely small space, which leads to the generation of extremely high temperatures and pressures inside the bubble. At these extreme temperatures and pressures, the molecules trapped inside the bubble undergo thermal dissociation to generate reactive radicals, including hydrogen, hydroperoxy, and hydroxyl radicals (Eqs. 1.1–1.5) (Prakash et al. 2021). These radicals, with their strong oxidative power, effectively degrade organic pollutants. Additionally, the ultrahigh temperatures can cause the thermal decomposition of organic compounds.

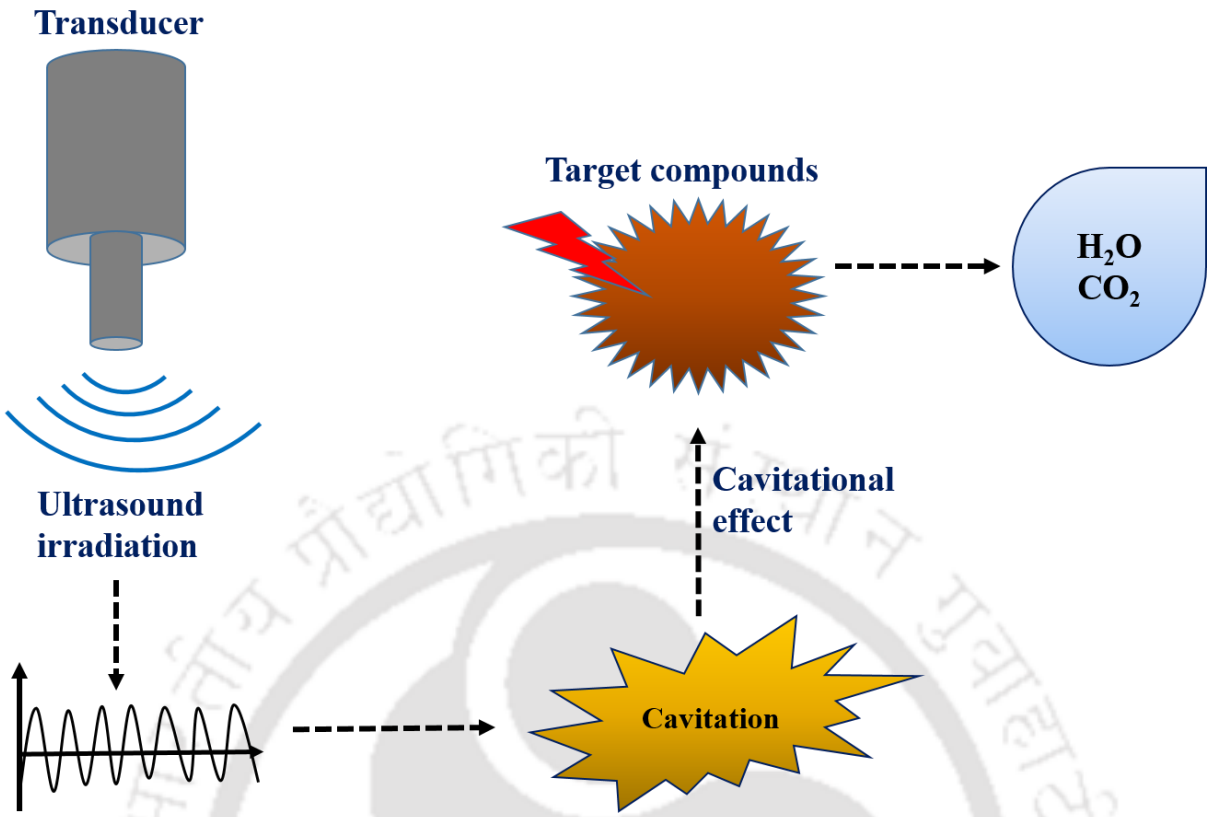

Figure 1.4. Schematic representation of ultrasound cavitation process

Recently, ultrasound has gained growing attention for pollutant treatment, particularly in areas such as sludge processing, drinking water disinfection, degradation of micropollutants, and the treatment of industrial effluents with high organic pollutant loads. Ultrasound application in AOPs for degrading organic pollutants is regarded as both technically and economically viable. Its primary benefits include high selectivity and improved reactivity. Typical sonochemical reactions in aqueous medium are as follows:

$$H_2O +))) \longrightarrow {}^{\bullet}OH + {}^{\bullet}H \quad (1.1)$$

$${}^{\bullet}OH + 2{}^{\bullet}H \longrightarrow H_2O_2 \quad (1.2)$$

$$O_2 + {}^{\bullet}H \longrightarrow {}^{\bullet}HO_2 \quad (1.3)$$

$$2^{\cdot}HO_2 \longrightarrow H_2O_2 + O_2 \quad (1.4)$$

$$H_2O + {}^{\cdot}OH \longrightarrow H_2O_2 + {}^{\cdot}H \quad (1.5)$$

Sonochemical reactions typically occur in three distinct zones: the center of the cavitation bubble (cavity interior), the bubble–fluid interface (gas-liquid interface), and the bulk solution (Adewuyi 2001).

Cavity interior (gaseous region): In this zone, volatile and hydrophobic molecules are degraded due to extremely high temperatures. Cavitation bubbles generate free radicals, such as HO• and H•, through the pyrolysis of water molecules.

Gas-liquid interface: Primary radicals formed within the cavitation bubbles interact with solutes at the gas-liquid interface, initiating the degradation process.

Bulk solution: Free radicals migrate from the gas-liquid interface into the bulk solution, where secondary sonochemical reactions occur. The degradation pathways of molecules depend on the pollutant's properties, such as solubility, volatility, and surface interactions.

Despite the distinct advantages of ultrasonic cavitation as an advanced oxidation treatment, it has been revealed in many studies that this technique alone is insufficient to achieve the required wastewater post-treatment standards - such as the extent of COD reduction or toxicity removal. Therefore, cavitation-based processes are coupled with other advanced oxidation processes. Hybrid advanced oxidation processes (AOPs) in wastewater treatment combine different AOPs either sequentially or simultaneously, aiming to enhance the degradation and mineralization of stubborn pollutants compared to individual methods. These configurations leverage synergistic interactions among their distinct mechanisms, leading to improved kinetics and final COD/toxicity removal through in-situ chemical oxidation. The efficiency of the

cavitation-based wastewater treatment technique is limited due to the net utility of the oxidizing radicals produced in the system. These radicals are extremely reactive and do not diffuse into the medium from their point of generation. Therefore, the probability of interaction between the pollutants and the radicals is a critical factor governing the oxidative degradation of the pollutants. The synergy in the hybrid AOP is based on enhancing the interactions among the radicals and achieving higher degradation. For example, a combination of adsorption and advanced oxidation processes (radical generation either through Fenton reactions or photochemical reactions) can yield much higher degradation of pollutants than individual processes. The synergy is also based on complementary interactions between the physical and chemical effects of the AOPs. For example, sonication creates intense micro-convection and micro-mixing in the system. This can have beneficial effects on the solid catalyst in the system. Microconvection can assist in the deagglomeration of catalyst particles, which helps expose the surface area. The micromixing can also cause washing of the catalyst surface, leading to desorption of the product species from the surface. This effect can also prevent the deactivation of the catalyst surface due to the adsorption of poisoning species. These kinds of synergistic interactions enhance the rates of reaction to pollutant desorption. Despite various combinations reported in the literature, the precise mechanisms underlying these hybrid AOPs and their synergies remain incompletely understood. Establishing these mechanisms is crucial for effectively designing large-scale commercial processes employing hybrid AOPs, providing essential guidelines for their efficient application. Babu et al. (2016) explored various combined AOPs, including sonolysis, sono-ozone processes, sonophotocatalysis, sono-Fenton systems, and sonophoto-Fenton methods, for pollutant degradation. Studies also demonstrate that combining ultrasound (US) with other AOPs generally offers better performance compared to using individual processes, likely due to the synergistic effects of these hybrid systems.

Ultrasound has been widely utilized not only in the synthesis of active catalysts but also in numerous wastewater treatment applications (Ince 2018; Yurtseven et al. 2023).

1.2. Ultrasound-assisted Hybrid Advanced Oxidation Processes (AOPs)

Ultrasound has both chemical and physical effects. The chemical effect is the generation of highly reactive radicals, as discussed in the preceding section. The physical effect is the generation of intense micro-convection and micro-mixing in the system. The physical and chemical effects of ultrasonic cavitation have several beneficial effects on the physical or chemical process, such as mass transfer enhancement with improved contact between contaminants and added oxidants, fine dispersion, and emulsification in solid/liquid, and liquid/liquid heterogeneous systems, fast mineralization of the pollutants with no formation of secondary intermediates, cost-effectiveness with ease of implementation. In the last two decades, vast literature (more than 1000 journal papers) has been published on the degradation of all kinds of pollutants (aromatic compounds, dyes, pharmaceuticals, and drug molecules, poly-aromatic hydrocarbons, halo-aromatic hydrocarbons, herbicides, pesticides, etc.) using cavitation-aided processes. Several reviews have also been published, which provide a critical analysis of this literature. Lu et al. (2021) discussed the use of sonochemical advanced oxidation processes (AOPs) for pollutant degradation, with a particular focus on how external oxidants and inorganic anions can enhance the efficiency of these processes. Similarly, de Andrade et al. (2021) provided an overview of ultrasonic wastewater treatment, covering both the fundamental mechanisms of ultrasound and its combination with AOPs for effective organic pollutant removal. Wang et al. (2019) summarized the key principles and process parameters, emphasizing how ultrasound can be combined with biocatalysts, adsorption, and chemical oxidation to improve pollutant degradation. Compared to other methods, ultrasound

techniques present fewer safety concerns and higher remediation rates. Additionally, they are unaffected by the toxicity or biodegradability of pollutants and can be easily integrated with chemical, physical, and biological processes. However, the effectiveness of sonolysis is limited by its energy requirements. To enhance efficiency and reduce energy consumption, ultrasound-based hybrid AOPs have gained significant attention in recent years. These include hybrid Fenton (US + Fe^{2+}/H_2O_2), Fenton-like (Fe^{3+}/H_2O_2), hybrid photo-Fenton (US + Fe^{2+}/H_2O_2/UV), hybrid hydrogen peroxide (US + H_2O_2), and hybrid catalytic (photo/electro) techniques. Ultrasound-assisted AOPs have been widely investigated for contaminant degradation due to several benefits, such as the absence of a need for additional chemical catalysts and their ability to operate at ambient conditions. Similar to techniques like photolysis (UV or UV/H_2O_2), ultrasound generates reactive oxygen species (ROS), resulting in efficient pollutant removal.

1.3 Ultrasound-assisted Hybrid Advanced Oxidation Processes (AOPs) in the presence of nanocatalyst

The standalone ultrasound (US) processes have certain limitations, such as the high cost of equipment and significant energy requirements, making it insufficient for fully degrading or mineralizing pollutants on its own. Compared to other advanced oxidation processes (AOPs), Fenton and Fenton-like reactions are widely used for generating free radicals. These processes have garnered significant interest in the removal of persistent organic pollutants due to their low energy requirements and strong oxidation potential. While traditional homogeneous catalysts show excellent catalytic performance because of their well-defined active sites, they face challenges such as the need for strict pH control and difficulty in recovering the involved ions. In the field of heterogeneous catalysis, a key goal in the long-term removal of organic

pollutants is the development of highly active and stable catalysts (Roy and Moholkar 2020). A novel synergistic approach has been developed to address the limitations of standalone processes by combining Fenton/Fenton-like reactions with ultrasound (US). This integration leads to enhanced free radical generation, lower energy consumption, reduced usage of Fenton reagents, and increased cost-effectiveness, all while improving pollutant degradation efficiency (Rabiee et al. 2024). The potential of the US-Fenton/Fenton-like system in environmental remediation has gained significant attention in recent years. Although conventional US-Fenton systems effectively degrade organic pollutants, the recycling of Fe^{2+} presents a major challenge. Soluble iron salts dissolve easily and are difficult to recover, leading to waste of metal ions and environmental contamination. To tackle these issues, the US-Fenton-like process was developed, utilizing a solid catalyst instead of soluble iron salts. This offers the benefits of a reusable catalyst and the flexibility to treat wastewater originating from different sources (Huang et al. 2012a). This approach not only lowers costs but also reduces the environmental impact. The US-Fenton-like process has demonstrated excellent adaptability across different types of wastewater, with the solid catalyst exhibiting high stability and activity across a wide range of pH conditions, making the technology more practical. Additionally, the ultrasonication enhances the contact frequency and surface interaction between the substrate and catalyst, further boosting the reaction efficiency. Overall, the US-Fenton-like system is both economical and environmentally sustainable due to its use of recyclable solid catalysts, which have shown high effectiveness in various wastewater treatments. Figure 1.5 represents the US-Fenton-like system. The rapid advancements in nanotechnology have garnered considerable attention for environmental applications. Nanomaterials, available in various shapes, morphologies, and forms, are crucial in improving water and air quality treatment in natural environments. By combining nanocatalysts with ultrasonication, heterogeneous sonocatalytic processes are devised, with significantly higher efficiency of organic pollutant

degradation (Sajjadi et al. 2017; Mehrizad et al. 2019). Sonocatalysts provide better mass transfer due to their larger surface area and serve as nucleation sites for the formation of more cavitation bubbles. Compared to other transition metal oxides, magnetically separable Fe_3O_4 nanoparticles (NPs) provide several advantages, including a larger specific surface area, lower cost, non-toxicity, and ease of recycling (Wei et al. 2015; Jaafarzadeh et al. 2018; Prakash et al. 2021). These characteristics make Fe_3O_4 an appealing catalyst for the remediation of organic pollutants in US-Fenton-like systems.

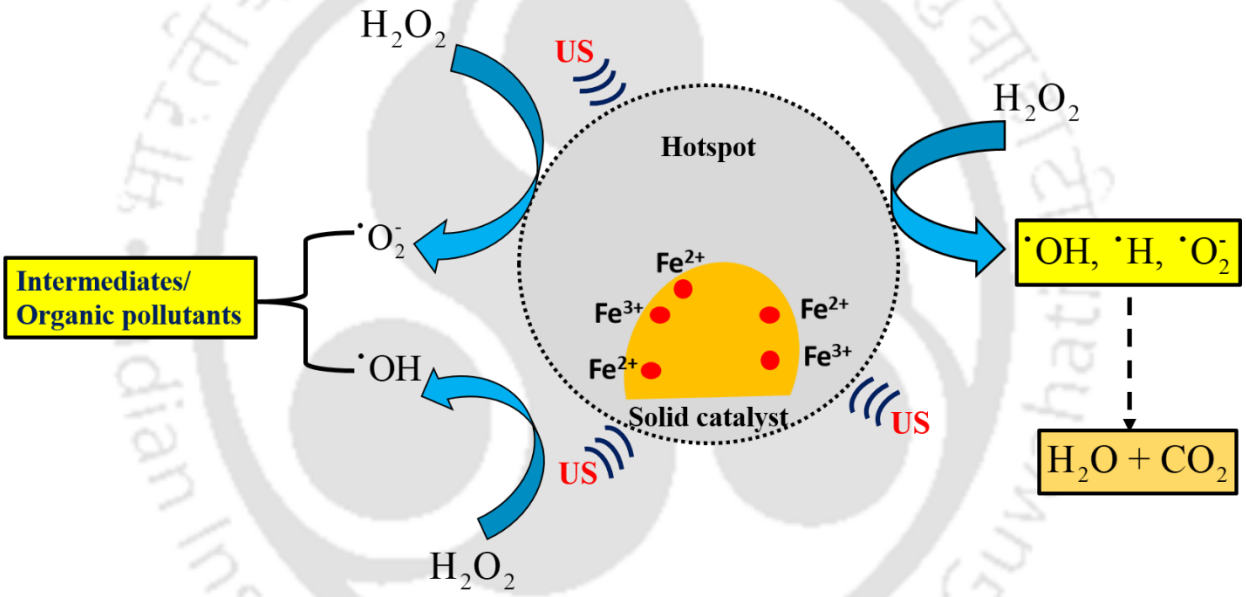

Figure 1.5. Schematic representation of US/Fenton-like system

1.4 Hydrodynamic cavitation-assisted hybrid advanced oxidation processes

Over the past decade, ultrasonic cavitation has been widely studied due to its similar oxidation potential to other advanced oxidation processes (AOPs). However, its complexity and challenges in scaling to industrial levels have limited its practical application. Hydrodynamic cavitation (HC), on the other hand, has demonstrated effectiveness in oxidizing organic

pollutants, including volatile compounds. Though HC offers less flexibility and can be more challenging to optimize, it has distinct advantages over ultrasonic cavitation. For instance, HC systems typically include components such as pumps, tanks, fluid constriction devices, and pipes, which are significantly less costly than ultrasonic systems of similar scale. Operational costs for HC are also relatively low due to efficient energy utilization, and HC has shown efficacy across both small- and large-scale applications, unlike ultrasonic cavitation, which has largely been effective only at the laboratory scale. HC has proven particularly effective in degrading complex contaminants, with its efficiency influenced by factors such as wastewater physicochemical properties, reactor geometry, operating pressure, and cavitation number (C_v) (Gogate and Pandit 2000; Chakinala et al. 2008; Gogate and Bhosale 2013). Research has shown that combining HC with other AOPs amplifies •OH radical production, which accelerates pollutant breakdown more effectively than individual treatments. By controlling parameters such as operating pressure, cavitation range, and the fluid's physicochemical properties, HC performance can be further optimized. Integrating HC with other treatment operations in a continuous process presents a promising solution for treating emerging contaminants. This combination approach not only offers a greener and more cost-effective treatment but also enhances compatibility with conventional wastewater treatment methods, effectively breaking down more complex pollutants (Askarniya et al. 2020; Agarkoti et al. 2022; Azizollahi et al. 2023).

As an introduction to the thesis, the following section provides summaries of the existing literature organized into three tables: (1) Table 1.2 gives a summary of representative literature in US-assisted hybrid AOPs (homogeneous system), (2) Table 1.3 presents a summary of representative literature in US-assisted hybrid AOPs using catalyst (heterogeneous systems), and (3) Table 1.4 presents a summary of literature in hydrodynamic cavitation (HC) assisted

hybrid advanced oxidation processes. Due to the rather vast amount of literature published in these areas, we have reviewed different studies published in the past 10 years only.

Table 1.2. Literature survey of US-assisted hybrid AOPs

Pollutant	US-assisted hybrid AOPs	Experimental details	Results/ Important findings	Reference
Tetracycline	US/ PMS & Heat/ PMS	[PMS] = 0.3mM, [TC] = 20 mg/L, pH = 6.4, Power = 550 W and T = 20 ℃	80% removal of TC was achieved	Deng et al. (2024b)
Ciprofloxacin	US/ H_2O_2/ KPS/ O_3	[CIP] = 15 mg/L, [H_2O_2] = 100 mg/L, pH = 7 and T = 30 ℃	US + H_2O_2 = 44.30%; US + KPS = 35.41%; US + O_3 = 100% degradation was achieved in 90 min	Lakshmi et al. (2024)
Procion Brilliant purple H-3R	US/ Fenton/ H_2O_2/ KPS	f = 22 kHz, P = 250 W, [H_2O_2] = 0.5 g/L, [KPS] = 0.75 g/ L, H_2O_2/Fe^{2+} = 50:1 and pH = 12	US alone = 70.25%; US + H_2O_2 = 95.99%; US + H_2O_2/Fe^{2+} = 99.79%; US + KPS = 99.05% degradation was achieved respectively.	Momin and Gogate (2024)
Coke oven plant effluent	US/ H_2O_2/ Ozone/ Fenton/ Peroxone/ Catalyst	[Catalyst] = 1 g/L, [H_2O_2] = 40 mL/L, [O_3] = 1 LPM and Fe^{2+}/H_2O_2 = 1:1	US + Peroxone = 90.48%; US + Fenton = 85.29%; US + H_2O_2 = 81.96; US + Ozone = 81.75%; US + Catalyst = 65.15% COD removal was achieved	Dey and Gogate (2024)
Malathion pesticide	US/ UV/ Fe^{2+}/ H_2O_2	[Malathion] = 20 ppm, [H_2O_2] = 700 ppm, [Fe^{2+}] = 20 ppm and pH = 3	degradation follows: 98.79% sono-Photo-Fenton > 70.92% photo-Fenton > 55.94% Fenton	Vasseghian et al. (2022)

Pollutant	US-assisted hybrid AOPs	Experimental details	Results/ Important findings	Reference
Acid violet 7	US + Fe^{2+} + H_2O_2	f = 40 kHz (100W), $[H_2O_2]$ = 50 ppm, pH = 3 and t = 2 min	99.9% removal was achieved.	Kodavatiganti et al. (2021)
Dermacid red, Dermacid black and Dermacid brown	US + Fe^{2+} + UV + H_2O_2	f = 860 kHz (250 W), pH = 3, $[H_2O_2]$ = 0.12 mM and t = 120 min	77.31 %, 88.1%, and 86.09% removal of Dermacid red, Dermacid black, and Dermacid brown achieved.	Maroudas et al. (2021)
Reactive black-5	US + Fe^{2+} + UV + H_2O_2	UV = 254 nm, US frequency = 40 kHz (100W), pH = 3, $[H_2O_2]$ = 200 ppm and t = 30 min	100% removal was achieved	Yosofi and Mousavi (2020)
Reactive black-5	US + H_2O_2	US frequency = 40 kHz (100W), pH = 3, $[H_2O_2]$ = 200 ppm and t = 30 min	more than 90% removal was achieved.	Yosofi and Mousavi (2020)
Abattoir wastewater	US + O_3	US frequency = 300 kHz, $[O_3]$ = 71 ppm and t = 60 min	The US achieved 18% COD & 50% BOD removal, O3 achieved 33% COD & 74% BOD removal, and US + O_3 achieved 44% COD & 78% BOD removal, respectively.	Alfonso-Muniozguren et al. (2020)

Pollutant	US-assisted hybrid AOPs	Experimental details	Results/ Important findings	Reference
Rhodamine B	US bath + stirrer	[RB] = 10 ppm, US frequency = 40 kHz and stirring speed = 700 rpm	98 % degradation of RB achieved.	Zhang et al. (2019)
Amoxicillin (AMX)	US + UV + Fenton	[AMX] = 10 ppm, $[H_2O_2]$ = 375 ppm, $[Fe^{2+}]$ = 30 ppm and pH = 3	100 % degradation of AMX achieved by Photo–Fenton in 3.5 min of reaction time.	Verma and Haritash (2019)
Acid orange 7	US + O_3 + UV	[AO7] = 57 µM, $[O_3]$ = 0.25 L/min, T = 25 ℃, US frequency = 520 kHz and t = 60 min	The mineralization was obtained by each process: alone US = 0%, O_3 = 24%, US + UV = 10%, O_3 + UV = 34% and US + O_3 + UV = 41%	Ince (2018)
Ibuprofen	US + Fenton	[IBP] = 20 ppm, pH = 2.6, T = 25 ℃, $[H_2O_2]$ = 6.4 mM, $[Fe^{2+}]$ = 0.134 mM and t = 180 min	50 % TOC removal was obtained by the sono-Fenton process.	Adityosulindro et al. (2017)
Direct Red 81 (DR81)	US + Fenton	$[Fe^{2+}]$ = 0.2 g/L, [DR81] = 50 ppm, pH = 3 and $[H_2O_2]$ = 5.1 mM	Alone US degrades only 20% while 99% degradation was obtained by the US + Fenton	Harichandran and Prasad (2016)

Pollutant	US-assisted hybrid AOPs	Experimental details	Results/ Important findings	Reference
Polycyclic aromatic hydrocarbons	US + Fenton	$[Fe^{2+}]$ = 140 mmol/L, pH = 3, US frequency = 20kHz and t = 60 min	Alone US = 41.4 % degradation achieved, Alone Fenton = 70.3% degradation achieved and, US + Fenton = 73 % degradation was achieved.	Lin et al. (2016)
Methylene Blue (MB)	US + UV + Fenton	[MB] = 0.063mM, $[Fe^{2+}]$ = 0.2mM, $[H_2O_2]$ = 5 mM, pH = 3 and T = 298 K	6.84 % degradation was achieved by alone US, 99.65 % degradation was achieved by US + Fenton and 96.39 % degradation was achieved by US + Fenton + UV	Chakma et al. (2015a)
Acid Red B (ARB)	US + UV + Fenton	[ARB] = 0.04mM, $[Fe^{2+}]$ = 0.2mM, $[H_2O_2]$ = 5 mM, pH = 3 and T = 298 K	14.76 % degradation was achieved by alone US, 68.94 % degradation was achieved by US + Fenton and 85.87 % degradation was achieved by US + Fenton + UV	Chakma et al. (2015a)

Table 1.3. Literature survey of US-assisted hybrid AOPs using the catalyst

Pollutant	US-assisted hybrid AOPs	Catalysts	Experimental details	Results/ Important findings	Reference
Favipiravir	US + Fenton + Peroxydisulfate	$FeMnO_x$	pH = 10, [catalyst] = 500 mg/L and t = 180 min	70.1% removal was achieved	Bagheri et al. (2024)
Acetaminophen (ACE)	US + adsorption + PMS	Biochar	f = 40 kHz, [ACE] = 40 µM, [PMS] = 0.1 mM and [BC] = 50 mg/L	95% removal of ACE in 10 min and 20% toxicity reduced after treatment	Estrada-Flórez et al. (2024)
2,4 Dinitrophenol (DNP)	US + Photo-Fenton	$Fe_3O_4@TiO_2$	P = 26.58 W/L, [DNP] = 5.96 mg/L, [$Fe_3O_4@TiO_2$] = 0.16 g/L, pH = 4.47 and t = 30 min	91.45% removal of DNP & 73% and 64.2% COD & TOC removal was achieved	Rabiee et al. (2024)
Industrial wastewater	US + Fenton + stirring	Fe_3O_4@Laccase	f = 35 kHz, stirring = 300 rpm, pH=4.5, T =66.5°C, [Fe_3O_4@Laccase] = 1.46 g/L and t = 60 min	90.3 % COD removal and 70% toxicity reduction were achieved	Verma and Moholkar (2024)
Methylene blue	US + Fenton	SnO_2-Fe_3O_4@MWCNT	f = 60 kHz, [catalyst] = 16 mg/L, [MB] = 45 mg/L, pH = 8, [H_2O_2] = 15 mM and t = 60 min	85% degradation was achieved	Yurtseven et al. (2023)

Pollutant	US-assisted hybrid AOPs	Catalysts	Experimental details	Results/ Important findings	Reference
Penicillin	US + Fenton	γ-Fe_2O_3	[Penicillin] = 10 mg/L, f = 35 kHz, pH = 3, [catalyst] = 0.3 g/L and t = 90 min	95.26% COD removal was achieved	Abdipour and Hemati (2023)
Industrial wastewater	US + Fenton + adsorption	Fe_3O_4@AC	pH = 4.2, [H_2O_2] = 0.71 M, [catalyst] =0.34 g/L and t = 60 min	94.75% COD and 89% TOC removal were achieved.	Verma and Moholkar (2023)
Ciprofloxacin	US + UV	TiO_2 / biochar/ chitosan hydrogel beads (TBCB)	[TBCB] = 0.03g, [CIP] = 30 mg/L, lamp power = 150 W and pH = 6	85.23% degradation was achieved	Afzal et al. (2022)
Toluidine blue (TB)	US + UV + Fenton + Magnetic field	PVP/Fe_3O_4@SiO_2	[H_2O_2] = 0.5 M, pH = 4 and t = 60 min	76.55% removal in 60 min in absence of MF; 95.3% removal in 10 min in presence of MF	Ghobashy et al. (2021)
Acid blue 15	US + Fe^{3+} + H_2O_2	Fe_3O_4 nanoparticles	[AB15] = 100 ppm, [Fe_3O_4] = 1 g/L, [H_2O_2] = 10 mM. pH = 3 and t = 20 min	99.3% removal of AB15 and 40.4% TOC reduction were achieved.	Prakash et al. (2021)
Methyl violet 10B	US + UV + Fe^{2+} + H_2O_2	Fe_2O_3-Al_2O_3-Ga_2O_3	Mercury lamp = 254 nm, pH = 3, [MV10B] = 10 ppm, [catalyst] = 50 ppm, [H_2O_2] = 25 ppm and t = 30 min	96.5% removal was achieved.	Bekakria et al. (2021)

Pollutant	US-assisted hybrid AOPs	Catalysts	Experimental details	Results/ Important findings	Reference
Methylene blue (MB) and Methyl orange (MO)	US + Fe^{3+} + H_2O_2	γ-Fe_2O_3/ biochar	f = 37 kHz (35.3 W/L), [H_2O_2] = 200 mM, pH = 7 and t = 60 min	99.5% and 68.69% removal of MB & MO was achieved.	Chu et al. (2020)
Acid red 73	US + PS + Fenton	Fe_3O_4@AC	[AR73] = 50 mg/L, [PS] = 7.5 mmol/L, [catalyst] = 2 g/L, f = 80 kHz and T = 50 ℃	100% decolorization was achieved in 10 min	Liu et al. (2020)
4-acetamidophenol	US + UV	TiO_2	f = 20 kHz, P = 300 W, [catalyst] = 2 g/L, pH = 6.8 and t = 180 min	87% degradation was achieved	Rajoriya et al. (2019)
Sunset yellow and tartrazine	US + adsorption	Ni-Ag NPs/rGO	[catalyst] = 0.045g, [sunset yellow] = 10 mg/L, [tartrazine] = 8.5 mg/L and t = 15 min	maximum adsorbent capacity for sunset yellow was 28.57 mg/g and tartrazine was 26.31 mg/g	Mirzajani and Karimi (2019)
Brilliant green (BG)	US + UV	NiO_2@CeO_2	f = 25 kHz, power = 100 W, [catalyst] = 0.2 g/L, [BG] = 10 mg/L, T = 30 ℃	82% degradation was achieved.	Sancheti et al. (2018)
Reactive orange 107	US + Fe^{3+} + H_2O_2	Fe_3O_4 nanoparticles	intensity = 300 W/L, pH = 5, [Fe_3O_4] = 0.89 g/L, [H_2O_2] = 10 mM and t = 25 min	91.8% removal was achieved	Jaafarzadeh et al. (2018)

Pollutant	US-assisted hybrid AOPs	Catalysts	Experimental details	Results/ Important findings	Reference
Acid blue 185	US + Fe^{2+} + H_2O_2	Fe_3O_4 nanoparticles	f = 40 kHz, [H_2O_2] = 15 mM, [Fe_3O_4] = 1.5 g/L, pH = 3 and t = 80 min	88% removal was achieved.	Acisli et al. (2017)
Tetracycline	US + Fenton + H_2O_2	Fe_3O_4	P = 80 W, pH = 3.7, [catalyst] = 1 g/L, [H_2O_2] = 150 mM, [Tetracycline] = 100 mg/L, T = 22 ℃ and t = 60 min	93.6% and 31.8% degradation and TOC removal were achieved	Hou et al. (2016)
Crystal violet	US + adsorption	Zno-NRs-AC	pH = 7, [catalyst] = 0.025 g, [crystal violet] = 24 mg/L and t = 5 min	99.82% removal was achieved	Dil et al. (2016)
Basic blue 3	US + catalyst	TiO_2/MMT	f = 40 kHz, power = 300 W, [catalyst] = 1 g/L, [BB3] = 10 mg/L and pH = 7	80% decolorization was achieved.	Khataee et al. (2015)

Table 1.4. Hydrodynamic-assisted hybrid advanced oxidation processes

Pollutant/wastewater	HC-assisted hybrid AOPs	Experimental details	Results/ Important findings	Reference
Congo Red	HC (venturi) + UV + PS	Pressure = 4.5 bar, [PS] = 30 mg/L, UV power = 16 W and volume = 4 L	92.01% decolorization and 63.45% CR degradation were achieved	Dehghani et al. (2024)
Coking wastewater	HC (venture) + Fenton	Pressure = 0.1 MPa, pH = 3, $[H_2O_2]$ = 12 mmol/L, $[Fe^{2+}]$ = 3 mmol/L, t = 15 min and volume = 3.5 L	33.2% COD removal was achieved.	Deng et al. (2024a)
Dairy wastewater	HC (orifice) + Fenton	Pressure = 5 bar, pH = 3, Fe^{2+}:H_2O_2 = 1:10, $[H_2O_2]$ = 85 mmol/L, t = 60 min and volume = 12 L	HC/Fenton = 89.3% & HC/H_2O_2 = 73.4% degradation was achieved in 60 min	Gawande et al. (2024)
Orange II	HC (orifice)	Pressure = 3 bar, pH = 2, T = 34 ℃,	90% decolorization was achieved	Kakama et al. (2024)
Cellulosic fiber (CF) industry	HC (venturi) + Fenton	Pressure = 3 bar, Fe^{2+}:H_2O_2 = 1:3, t = 60 min and volume = 500 L	90% COD removal was achieved	Kanthale et al. (2023)
Textile dye wastewater	HC (venturi) + UV + PPMS	Pressure = 8 kgf/cm^2, UV power = 30 W, pH = 7, [PPMS] = 2.5 g/L, t = 360 min and volume = 10 L	87.7% COD reduction and 1.92 synergistic index were achieved	Kore et al. (2023)

Pollutant/wastewater	HC-assisted hybrid AOPs	Experimental details	Results/ Important findings	Reference
Tannery wastewater	HC (orifice) + PAA + Fenton	Pressure = 7.5 bar, pH = 2, [PAA] = 17.5 g/L, t = 97.5 min and volume = 20 L	72.36% COD, 94.54% TDS and 98.89% turbidity were achieved	Korpe et al. (2023)
Lake water	HC (orifice) + H_2O_2	Pressure = 5 bar, pH = 3, [H_2O_2] = 3 g/L, t = 60 min and volume = 5 L	64% COD and BOD were achieved	Patil et al. (2023)
Methylene Blue (MB)	HC (orifice) / O_3 / PS	Pressure = 3 bar, pH = 2, [MB] = 10 mg/L, O_3 rate = 0.12 g/h, t = 120 min and volume = 2 L	HC + O_3 > HC + PS	Wang et al. (2022)
Common effluent plant	HC (venturi) + Fenton	Pressure = 4 bar, T = 30℃, t = 60 min and volume = 4 L	97.28% COD reduction was achieved	Agarkoti et al. (2021)
Sulfadiazine (SDZ)	HC (orifice) + Fenton + PS	Pressure = 10 atm, [SDZ] = 20 ppm, pH = 4, [PS] = 348.5 mg/L, [H_2O_2] = 0.95 mL/L, [α-Fe_2O_3] = 181.8 mg/L, t = 90 min and volume = 5 L	81% degradation was achieved	Roy and Moholkar (2020)
Industrial wastewater	HC (orifice) +Fenton	Pressure = 6 bar, [H_2O_2] = 15 g/L, Fe^{2+}:H_2O_2 = 1:20, t = 180 min and volume = 70 L	63% COD removal was achieved	Joshi and Gogate (2019)
Textile dyeing wastewater	HC (venturi) / Fenton /O_3 / O_2	Pressure = 5 bar, pH = 6.8, Fe^{2+}:H_2O_2 = 1:5, [O_2] = 2 L/min, [O_3] = 3 g/h, t = 120 min and volume = 6 L	TOC and COD removal follows: HC + Fenton > HC + O_2 > HC + O_3	Rajoriya et al. (2018)

Industrial wastewater with hazardous contents, such as high levels of COD, sulfides, phenols, amines, hydroxides, and disulfides, poses a serious environmental threat. As a result, selecting an appropriate treatment technology based on the type of wastewater is crucial. While conventional wastewater treatment infrastructures are often too costly to implement in developing countries, some integrated hybrid technologies have been developed for treating industrial wastewater with high COD and TOC levels. Therefore, innovative hybrid approaches are necessary to reliably treat industrial wastewater and minimize the health risks of organic contaminants. This thesis focuses on developing advanced oxidation-based hybrid technologies that reduce sludge generation and energy consumption in industrial wastewater treatment. The study aims to assess the removal rates of numerous organic pollutants in industrial wastewater, including high concentrations of COD and TOC, using a sequential combination of treatment technologies and optimizing the performance of these hybrid systems.

Over the past two decades, extensive research worldwide has focused on the degradation and mineralization of bio-recalcitrant pollutants using ultrasound-based (or cavitation-based) advanced oxidation processes (AOPs). However, most of these studies have reported degradation of a single pollutant. The main emphasis of these studies is on deducing the chemical mechanism of the degradation of the pollutant. Important parameters such as COD reduction or TOC mineralization are not reported in these studies. The actual wastewater originating from industry contains large numbers of pollutants. Therefore, a practical industrial application of cavitation-based technology would necessitate the study of the treatment of actual wastewater, which will involve the simultaneous degradation of numerous pollutants with strong mutual interaction. Moreover, the reduction in the COD and BOD values of the wastewater and complete mineralization of the organic matter present in the wastewater also need to be studied.

More recently, several studies have explored the combination of novel nanocatalysts with AOPs to enhance the degradation and mineralization of specific pollutants only. However, despite these efforts, the application of ultrasound hybrid AOPs for treating real industrial wastewater remains largely underexplored. The primary goal of this thesis is to address this gap by investigating ternary hybrid AOPs and the synergistic effects between them for the treatment of real wastewater.

1.5 Aim, Approach, and Scope of the Present Thesis

In the previous sections, an introduction was provided on advanced oxidation processes (AOPs), with a focus on ultrasound-assisted hybrid AOPs. A comprehensive literature review of cavitation-based ultrasound hybrid AOP systems, which combine various AOPs, was presented. A key takeaway from the review is that hybrid AOPs consistently achieve faster and more efficient degradation and mineralization of organic pollutants compared to conventional single AOPs. This outcome holds true regardless of the type of pollutant or its physical and chemical characteristics. Such promising results pave the way for the potential design and application of these systems on a larger scale. However, the majority of prior studies have been limited to the degradation of individual pollutants.

Effective scaling of this technology demands a deep understanding of the fundamental mechanisms governing the basic physics, chemistry, and biology of the process, which helps in translational research for application in real systems. In the context of hybrid AOPs, a thorough understanding of the synergistic interactions, both positive and negative, between the individual AOPs is crucial for achieving enhanced and accelerated pollutant degradation. This thesis aims to address this knowledge gap by focusing on the degradation and mineralization of real industrial wastewater using ultrasound-assisted hybrid AOPs. Both ultrasonic and

hydrodynamic cavitation have been combined with other AOPs such as persulfate, heterogeneous Fenton, and photolysis. Additionally, novel catalysts have been synthesized for the heterogeneous Fenton system. An outline of the thesis is as follows:

Chapter 1 (the present chapter) begins with an introduction to the thesis topic. It starts with an overview of cavitation-based ultrasound-assisted AOPs and other conventional methods. This is followed by a literature review of ultrasound-assisted hybrid AOPs for the degradation of recalcitrant pollutants in wastewater. Based on this review, the objectives and approach of the thesis are presented.

Chapter 2 describes the mineralization of industrial wastewater by a hybrid technique of adsorption (Fe_3O_4@AC nanocomposite) + heterogeneous Fenton + sonication and discernment of synergistic effects. Fe_3O_4@AC nanocomposites were synthesized using the co-precipitation method, and the characterization of the Fe_3O_4@AC nanocomposite by using standard techniques of FTIR, FE-SEM, EDX, TEM, BET surface area analysis, XRD and magnetic property determination using VSM. Statistical optimization was done using COD removal as the response variable to deduce the effect of process parameters on mineralization. The compositional assessment of treated water was identified using LC-MS analysis. The assessment of adsorption characteristics and kinetics of the Fe_3O_4@AC nanocomposite under ultrasonication was proposed. Finally, the toxicity reduction achieved by the optimized treatment was evaluated.

Chapter 3 presents the investigations in sonoenzymatic treatment of industrial wastewater using Fe_3O_4@Laccase nanocomposite. Fe_3O_4@Laccase nanocomposite was synthesized by immobilization of laccase on magnetic Fe_3O_4 nanoparticles. The statistical technique of CCD (central composite design) was used to optimize the physical parameters in the sonoenzymatic treatment. The kinetic model was proposed to quantify the enhancement effect of ultrasound

in the sonoenzymatic treatment. The synergy between enzymatic oxidation and sonication was deduced using changes in the secondary structure of enzyme proteins. The removal of the major contaminants from the wastewater post-treatment was assessed using LC-MS analysis. The toxicity reduction of wastewater after treatment was analyzed. The separation and reusability of Fe_3O_4@Laccase nanocomposite was assessed in six consecutive treatment cycles.

Chapter 4 presents the COD and toxicity reduction of wastewater using a hybrid advanced oxidation process of sonication with chitosan-based hydrogel beads. The floatable Fe_3O_4@AC@CH hydrogel beads have been synthesized. The operating parameters like hydrogel bead dosage, pH, and H_2O_2 loading were optimized for maximum COD removal. LC-MS analysis was done to identify major contaminants in both original and treated wastewater. The adsorption properties and kinetics of the Fe_3O_4@AC@CH hydrogel beads in ultrasound-based hybrid AOPs were evaluated. The toxicity reduction of wastewater after treatment was assessed by using a seed germination test.

Chapter 5 presents the intensification of the treatment of industrial wastewater using hydrodynamic cavitation-based hybrid ternary advanced oxidation processes. Despite its benefits, ultrasound technology faces challenges such as costly equipment and high energy requirements, which significantly restrict its use in large-scale water treatment applications. To address this, a pilot-scale study was conducted utilizing 10 liters of wastewater, employing a hydrodynamic cavitation-assisted hybrid advanced oxidation process. The key innovation in this chapter is the treatment of high-COD effluent in a 10 L capacity setup using a ternary hybrid advanced oxidation process (hydrodynamic cavitation + Fenton reaction + adsorption), a combination not previously reported to the best of our knowledge. This investigation examines the impact of process parameters such as inlet pressure, nanocomposite dosage, pH, and H_2O_2 concentration on COD and TOC removal from industrial wastewater. LC-MS analysis was conducted to identify major compounds present in wastewater post-treatment.

Kinetic and adsorption isotherm analyses were performed to evaluate the adsorption characteristics of the Fe_3O_4@AC nanocomposite within the ternary hybrid advanced oxidation process. Additionally, cavitational yields for both binary and ternary hybrid AOPs were calculated to assess their efficiency.

Chapter 6 gives the overall summary of the thesis using ultrasound-assisted hybrid advanced oxidation processes. A pilot scale study using hydrodynamic cavitation-assisted hybrid AOPs has also been discussed briefly. Some suggestions for furthering research in the area of wastewater treatment using hybrid AOP are also given.

References

Abdipour H, Hemati H (2023) Sonocatalytic process of penicillin removal using Fe_2O_3 / effect of different parameters/degradation mechanism/ kinetic study/optimisation with response surface model. International Journal of Environmental Analytical Chemistry 104: 1–22. https://doi.org/10.1080/03067319.2023.2207465

Acisli O, Khataee A, Karaca S, et al (2017) Combination of ultrasonic and Fenton processes in the presence of magnetite nanostructures prepared by high-energy planetary ball mill. Ultrasonics Sonochemistry 34: 754–762. https://doi.org/10.1016/j.ultsonch.2016.07.011

Adewuyi YG (2001) Sonochemistry: Environmental Science and Engineering Applications. Ind Eng Chem Res 40: 4681–4715. https://doi.org/10.1021/ie010096l

Adityosulindro S, Barthe L, González-Labrada K, et al (2017) Sonolysis and sono-Fenton oxidation for removal of ibuprofen in (waste)water. Ultrason Sonochem 39: 889–896. https://doi.org/10.1016/j.ultsonch.2017.06.008

Afzal MZ, Sun X-F, Liu J, et al (2018) Enhancement of ciprofloxacin sorption on chitosan/biochar hydrogel beads. Science of The Total Environment 639: 560–569. https://doi.org/10.1016/j.scitotenv.2018.05.129

Afzal MZ, Zu P, Zhang C-M, et al (2022) Sonocatalytic degradation of ciprofloxacin using hydrogel beads of TiO_2 incorporated biochar and chitosan. Journal of Hazardous Materials 434:128879. https://doi.org/10.1016/j.jhazmat.2022.128879

Agani I, K. Fatombi J, A. Osseni S, et al (2020) Removal of atrazine from aqueous solutions onto a magnetite/chitosan/activated carbon composite in a fixed-bed column system: optimization using response surface methodology. RSC Advances 10:41588–41599. https://doi.org/10.1039/D0RA07873E

Agarkoti C, Gogate PR, Pandit AB (2022) Coupling of acoustic/hydrodynamic cavitation with ozone (O_3), hydrogen peroxide (H_2O_2), magnesium oxide (MgO) and manganese dioxide (MnO_2) for the effective treatment of CETP effluent. Separation and Purification Technology 284:120281. https://doi.org/10.1016/j.seppur.2021.120281

Agarkoti C, Gogate PR, Pandit AB (2021) Comparison of acoustic and hydrodynamic cavitation based hybrid AOPs for COD reduction of commercial effluent from CETP. Journal of Environmental Management 281:111792. https://doi.org/10.1016/j.jenvman.2020.111792

Agarry SE, Audu TOK, Solomon BO (2009) Substrate inhibition kinetics of phenol degradation by Pseudomonas fluorescence from steady state and wash-out data. Int J Environ Sci Technol 6:443–450. https://doi.org/10.1007/BF03326083

Ahmed MB, Zhou JL, Ngo HH, et al (2017) Progress in the biological and chemical treatment technologies for emerging contaminant removal from wastewater: A critical review. Journal of Hazardous Materials 323:274–298. https://doi.org/10.1016/j.jhazmat.2016.04.045

Aleboyeh A, Olya ME, Aleboyeh H (2008) Electrical energy determination for an azo dye decolorization and mineralization by UV/H_2O_2 advanced oxidation process. Chemical Engineering Journal 137:518–524. https://doi.org/10.1016/j.cej.2007.05.016

Alfaia RGSM, Nascimento MMP, Bila DM, Campos JC (2019) Coagulation/flocculation as a pretreatment of landfill leachate for minimizing fouling in membrane processes. Desalination and Water Treatment 159:53–59. https://doi.org/10.5004/dwt.2019.24280

Alfonso-Muniozguren P, Hazzwan Bohari M, Sicilia A, et al (2020) Tertiary treatment of real abattoir wastewater using combined acoustic cavitation and ozonation. Ultrason Sonochem 64:104986. https://doi.org/10.1016/j.ultsonch.2020.104986

Alsaiari NS, Amari A, Katubi KM, et al (2021) The Biocatalytic Degradation of Organic Dyes Using Laccase Immobilized Magnetic Nanoparticles. Applied Sciences 11:8216. https://doi.org/10.3390/app11178216

Anastas PT, Kirchhoff MM (2002) Origins, Current Status, and Future Challenges of Green Chemistry. Acc Chem Res 35:686–694. https://doi.org/10.1021/ar010065m

Anfar Z, Amedlous A, Majdoub M, et al (2020) New amino group functionalized porous carbon for strong chelation ability towards toxic heavy metals. RSC Advances 10:31087–31100. https://doi.org/10.1039/D0RA05220E

Ansari F, Ghaedi M, Taghdiri M, Asfaram A (2016) Application of ZnO nanorods loaded on activated carbon for ultrasonic assisted dyes removal: Experimental design and derivative spectrophotometry method. Ultrasonics Sonochemistry 33:197–209. https://doi.org/10.1016/j.ultsonch.2016.05.004

Anulekshmi PS, Nithya K, Kumar PS, et al (2024) Design of biocompatible gelatin hydrogels reinforced with magnetite nanoparticles: Effective removal of chromium from water environment. Environmental Research 260:119768. https://doi.org/10.1016/j.envres.2024.119768

Appaw C, Adewuyi YG (2002) Destruction of carbon disulfide in aqueous solutions by sonochemical oxidation. Journal of Hazardous Materials 90:237–249. https://doi.org/10.1016/S0304-3894(01)00350-8

Askarniya Z, Baradaran S, Sonawane SH, Boczkaj G (2022) A comparative study on the decolorization of Tartrazine, Ponceau 4R, and Coomassie Brilliant Blue using persulfate and hydrogen peroxide based Advanced Oxidation Processes combined with Hydrodynamic Cavitation. Chemical Engineering and Processing - Process Intensification 181:109160. https://doi.org/10.1016/j.cep.2022.109160

Askarniya Z, Sadeghi M-T, Baradaran S (2020) Decolorization of Congo red via hydrodynamic cavitation in combination with Fenton's reagent. Chemical Engineering and Processing - Process Intensification 150:107874. https://doi.org/10.1016/j.cep.2020.107874

American Public Health Association. (1926). *Standard methods for the examination of water and wastewater* (Vol. 6). American Public Health Association.

Azizollahi N, Taheri E, Mehdi Amin M, et al (2023) Hydrodynamic cavitation coupled with zero-valent iron produces radical sulfate radicals by sulfite activation to degrade direct red 83. Ultrasonics Sonochemistry 95:106350. https://doi.org/10.1016/j.ultsonch.2023.106350

Babaei AA, Kakavandi B, Rafiee M, et al (2017) Comparative treatment of textile wastewater by adsorption, Fenton, UV-Fenton and US-Fenton using magnetic nanoparticles-functionalized carbon (MNPs@C). Journal of Industrial and Engineering Chemistry 56:163–174. https://doi.org/10.1016/j.jiec.2017.07.009

Babu SG, Ashokkumar M, Neppolian B (2016) The Role of Ultrasound on Advanced Oxidation Processes. Top Curr Chem (Z) 374:75. https://doi.org/10.1007/s41061-016-0072-9

Bagal M, Ramos B, Mahajan S, et al (2023) Parametric optimization of a hybrid cavitation-based fenton process for the degradation of methyl violet 2B in a packed bed reactor. Chemical Engineering Research and Design 189:440–451. https://doi.org/10.1016/j.cherd.2022.11.034

Bagal MV, Gogate PR (2014a) Wastewater treatment using hybrid treatment schemes based on cavitation and Fenton chemistry: A review. Ultrasonics Sonochemistry 21:1–14. https://doi.org/10.1016/j.ultsonch.2013.07.009

Bagal MV, Gogate PR (2014b) Wastewater treatment using hybrid treatment schemes based on cavitation and Fenton chemistry: A review. Ultrasonics Sonochemistry 21:1–14. https://doi.org/10.1016/j.ultsonch.2013.07.009

Bagheri A, Fallah A, Karczewski J, et al (2024) Investigating COVID-19 active pharmaceutical ingredients (APIs) degradation using Peroxydisulfate/FeMnOx binary metal oxide/Ultrasound System. Water Resources and Industry 31:100232. https://doi.org/10.1016/j.wri.2023.100232

Bagheri AR (2017) Comparative study on ultrasonic assisted adsorption of dyes from single system onto Fe_3O_4 magnetite nanoparticles loaded on activated carbon: Experimental design methodology. Ultrasonics Sonochemistry

Bagheri AR, Ghaedi M, Asfaram A, et al (2017) Comparative study on ultrasonic assisted adsorption of dyes from single system onto Fe_3O_4 magnetite nanoparticles loaded on activated carbon: Experimental design methodology. Ultrasonics Sonochemistry 34:294–304. https://doi.org/10.1016/j.ultsonch.2016.05.047

Barik AJ, Gogate PR (2018) Hybrid treatment strategies for 2,4,6-trichlorophenol degradation based on combination of hydrodynamic cavitation and AOPs. Ultrasonics Sonochemistry 40:383–394. https://doi.org/10.1016/j.ultsonch.2017.07.029

Bekakria H, Bendjeffal H, Djebli A, et al (2021) Heterogeneous sono-photo-Fenton degradation of methyl violet 10B using Fe_2O_3-Al_2O_3-Ga_2O_3 as a new photocatalyst. Inorganic and Nano-Metal Chemistry 51:1759–1774. https://doi.org/10.1080/24701556.2020.1852430

Bello MM, Raman AAA (2019) Synergy of adsorption and advanced oxidation processes in recalcitrant wastewater treatment. Environ Chem Lett 17:1125–1142. https://doi.org/10.1007/s10311-018-00842-0

Bethi B, Manasa V, Srinija K, Sonawane SH (2018) Intensification of Rhodamine-B dye removal using hydrodynamic cavitation coupled with hydrogel adsorption. Chemical Engineering and Processing - Process Intensification 134:51–57. https://doi.org/10.1016/j.cep.2018.10.017

Bethi B, Sonawane SH, Bhanvase BA, Gumfekar SP (2016) Nanomaterials-based advanced oxidation processes for wastewater treatment: A review. Chemical Engineering and Processing - Process Intensification 109:178–189. https://doi.org/10.1016/j.cep.2016.08.016

Bilinska L, Gmurek M, Ledakowicz S (2015) Application of Advanced Oxidation Technologies for Decolorization and Mineralization of Textile Wastewaters. Journal of Advanced Oxidation Technologies 18:185–194. https://doi.org/10.1515/jaots-2015-0202

BlakePerutz JR, Suslick KS, Didenko Y, et al (1999) Acoustic cavitation and its chemical consequences. Philosophical Transactions of the Royal Society of London Series A: Mathematical, Physical and Engineering Sciences 357:335–353. https://doi.org/10.1098/rsta.1999.0330

Bolton JR, Bircher KG, Tumas W, Tolman CA (2001) Figures-of-merit for the technical development and application of advanced oxidation technologies for both electric- and solar-driven systems (IUPAC Technical Report). Pure and Applied Chemistry 73:627–637. https://doi.org/10.1351/pac200173040627

Burzio E, Bersani F, Caridi GCA, et al (2020) Water disinfection by orifice-induced hydrodynamic cavitation. Ultrasonics Sonochemistry 60:104740. https://doi.org/10.1016/j.ultsonch.2019.104740

Cabana H, Jones JP, Agathos SN (2009) Utilization of cross-linked laccase aggregates in a perfusion basket reactor for the continuous elimination of endocrine-disrupting chemicals. Biotechnol Bioeng 102:1582–1592. https://doi.org/10.1002/bit.22198

Chakinala AG, Gogate PR, Burgess AE, Bremner DH (2008) Treatment of industrial wastewater effluents using hydrodynamic cavitation and the advanced Fenton process. Ultrasonics Sonochemistry 15:49–54. https://doi.org/10.1016/j.ultsonch.2007.01.003

Chakma S, Das L, Moholkar VS (2015a) Dye decolorization with hybrid advanced oxidation processes comprising sonolysis/Fenton-like/photo-ferrioxalate systems: A mechanistic investigation. Separation and Purification Technology 156:596–607. https://doi.org/10.1016/j.seppur.2015.10.055

Chakma S, Das L, Moholkar VS (2015b) Dye decolorization with hybrid advanced oxidation processes comprising sonolysis/Fenton-like/photo-ferrioxalate systems: A mechanistic investigation. Separation and Purification Technology 156:596–607. https://doi.org/10.1016/j.seppur.2015.10.055

Chakma S, Moholkar VS (2013) Physical mechanism of sono-Fenton process. AIChE Journal 59:4303–4313. https://doi.org/10.1002/aic.14150

Chakma S, Moholkar VS (2016) Investigations in sono-enzymatic degradation of ibuprofen. Ultrasonics Sonochemistry 29:485–494. https://doi.org/10.1016/j.ultsonch.2015.11.002

Chatel G, Valange S, Behling R, Colmenares JC (2017) A Combined Approach using Sonochemistry and Photocatalysis: How to Apply Sonophotocatalysis for Biomass Conversion? ChemCatChem 9:. https://doi.org/10.1002/cctc.201700297

Chauhan R, Dinesh GK, Alawa B, Chakma S (2021) A critical analysis of sono-hybrid advanced oxidation process of ferrioxalate system for degradation of recalcitrant pollutants. Chemosphere 277:130324. https://doi.org/10.1016/j.chemosphere.2021.130324

Chen H, Wang J (2019) Catalytic ozonation of sulfamethoxazole over Fe_3O_4/Co_3O_4 composites. Chemosphere 234:14–24. https://doi.org/10.1016/j.chemosphere.2019.06.014

Chen X (2024) Fabrication of Core-Shell Hydrogel Bead Based on Sodium Alginate and Chitosan for Methylene Blue Adsorption. JRM 12:815–826. https://doi.org/10.32604/jrm.2024.048470

Chen Z, Yao J, Ma B, et al (2022) A robust biocatalyst based on laccase immobilized superparamagnetic Fe_3O_4@SiO_2–NH_2 nanoparticles and its application for degradation of chlorophenols. Chemosphere 291:132727. https://doi.org/10.1016/j.chemosphere.2021.132727

Choudhury BJ, Roy K, Moholkar VS (2021) Improvement of Supercapacitor Performance through Enhanced Interfacial Interactions Induced by Sonication. Ind Eng Chem Res 60:7611–7623. https://doi.org/10.1021/acs.iecr.1c00279

Choudhury H, Malani R (2013) Acid catalyzed biodiesel synthesis from Jatropha oil: Mechanistic aspects of ultrasonic intensification. Chemical Engineering Journal (Amsterdam, Netherlands) 231:262–272. https://doi.org/10.1016/j.cej.2013.06.107

Chu J-H, Kang J-K, Park S-J, Lee C-G (2020) Application of magnetic biochar derived from food waste in heterogeneous sono-Fenton-like process for removal of organic dyes from aqueous solution. Journal of Water Process Engineering 37:101455. https://doi.org/10.1016/j.jwpe.2020.101455

Darandale GR, Jadhav MV, Warade AR, Hakke VS (2023) Hydrodynamic cavitation a novel approach in wastewater treatment: A review. Materials Today: Proceedings 77:960–968. https://doi.org/10.1016/j.matpr.2022.12.075

Das A, Singh J, K.N. Y (2017) Laccase immobilized magnetic iron nanoparticles: Fabrication and its performance evaluation in chlorpyrifos degradation. International Biodeterioration & Biodegradation 117:183–189. https://doi.org/10.1016/j.ibiod.2017.01.007

D'Cruz B, Madkour M, Amin MO, Al-Hetlani E (2020) Efficient and recoverable magnetic AC-Fe_3O_4 nanocomposite for rapid removal of promazine from wastewater. Materials Chemistry and Physics 240:122109. https://doi.org/10.1016/j.matchemphys.2019.122109

de Andrade FV, Augusti R, de Lima GM (2021) Ultrasound for the remediation of contaminated waters with persistent organic pollutants: A short review. Ultrasonics Sonochemistry 78:105719. https://doi.org/10.1016/j.ultsonch.2021.105719

Dehghani A, Baradaran S, Movahedirad S (2024) Synergistic degradation of Congo Red by hybrid advanced oxidation via ultraviolet light, persulfate, and hydrodynamic cavitation. Ecotoxicology and Environmental Safety 272:116042. https://doi.org/10.1016/j.ecoenv.2024.116042

Deng D, Huang T, Li Q, et al (2024a) Treatment of Coking Wastewater Using Hydrodynamic Cavitation Coupled with Fenton Oxidation Process. Molecules 29:1057. https://doi.org/10.3390/molecules29051057

Deng H, Jin Y, Yan B, et al (2024b) Degradation of tetracycline by heat/peroxymonosulfate and ultrasound/peroxymonosulfate systems: performance and kinetics. Water Science & Technology 89:421–433. https://doi.org/10.2166/wst.2024.004

Dey A, Gogate PR (2024) Comparative study of different ultrasound based hybrid oxidation approaches for treatment of real effluent from coke oven plant. Journal of

Environmental Management 352:120095. https://doi.org/10.1016/j.jenvman.2024.120095

Dhanke P, Wagh S (2020) Intensification of the degradation of Acid RED-18 using hydrodynamic cavitation. Emerging Contaminants 6:20–32. https://doi.org/10.1016/j.emcon.2019.12.001

Dietrich M, Franke M, Stelter M, Braeutigam P (2017) Degradation of endocrine disruptor bisphenol A by ultrasound-assisted electrochemical oxidation in water. Ultrasonics Sonochemistry 39:741–749. https://doi.org/10.1016/j.ultsonch.2017.05.038

Dil EA, Ghaedi M, Ghaedi A, et al (2016) Application of artificial neural network and response surface methodology for the removal of crystal violet by zinc oxide nanorods loaded on activate carbon: kinetics and equilibrium study. Journal of the Taiwan Institute of Chemical Engineers 59:210–220. https://doi.org/10.1016/j.jtice.2015.07.023

Duan Z, Zhang W, Lu M, et al (2020) Magnetic Fe_3O_4/activated carbon for combined adsorption and Fenton oxidation of 4-chlorophenol. Carbon 167:351–363. https://doi.org/10.1016/j.carbon.2020.05.106

El-Batal AI, ElKenawy NM, Yassin AS, Amin MA (2015) Laccase production by Pleurotus ostreatus and its application in synthesis of gold nanoparticles. Biotechnol Rep (Amst) 5:31–39. https://doi.org/10.1016/j.btre.2014.11.001

Estrada-Flórez SE, Serna-Galvis EA, Lee J, Torres-Palma RA (2024) Unraveling kinetic and synergistic effects during ultrasound-enhanced carbocatalysis for water remediation as a function of ultrasonic frequency. Journal of Environmental Management 350:119548. https://doi.org/10.1016/j.jenvman.2023.119548

Expósito AJ, Monteagudo JM, Durán A, Fernández A (2017) Dynamic behavior of hydroxyl radical in sono-photo-Fenton mineralization of synthetic municipal wastewater effluent containing antipyrine. Ultrasonics Sonochemistry 35:185–195. https://doi.org/10.1016/j.ultsonch.2016.09.017

Flores Alarcón MAD, Arenas Jarro RY, Ahmed MA, et al (2022) Intensification of Red-G dye degradation used in the dyeing of alpaca wool by advanced oxidation processes assisted by hydrodynamic cavitation. Ultrasonics Sonochemistry 89:106144. https://doi.org/10.1016/j.ultsonch.2022.106144

Fu M, Xing J, Ge Z (2019) Preparation of laccase-loaded magnetic nanoflowers and their recycling for efficient degradation of bisphenol A. Science of The Total Environment 651:2857–2865. https://doi.org/10.1016/j.scitotenv.2018.10.145

Gągol M, Przyjazny A, Boczkaj G (2018) Wastewater treatment by means of advanced oxidation processes based on cavitation – A review. Chemical Engineering Journal 338:599–627. https://doi.org/10.1016/j.cej.2018.01.049

Gałązka A, Jankiewicz U (2022) Endocrine Disrupting Compounds (Nonylphenol and Bisphenol A)–Sources, Harmfulness and Laccase-Assisted Degradation in the

Aquatic Environment. Microorganisms 10:2236. https://doi.org/10.3390/microorganisms10112236

Ganiyu SO, Martínez-Huitle CA, Rodrigo MA (2020) Renewable energies driven electrochemical wastewater/soil decontamination technologies: A critical review of fundamental concepts and applications. Applied Catalysis B: Environmental 270:118857. https://doi.org/10.1016/j.apcatb.2020.118857

Gawande G, Chougule S, Bangar S, et al (2024) Hydrodynamic cavitation and its hybridization with Fenton process as a promising AOP for dairy wastewater treatment. Materials Today: Proceedings S2214785324000324. https://doi.org/10.1016/j.matpr.2024.01.032

Ge H, Liu L, Li W, et al (2021) Hierarchical carbon fiber cloth (CFC)/Co_3O_4 composite with efficient photo-electrocatalytic performance towards water purification. Diamond and Related Materials 118:108537. https://doi.org/10.1016/j.diamond.2021.108537

Ghasemi M, Mashhadi S, Azimi-Amin J (2018) Fe_3O_4/AC nanocomposite as a novel nano adsorbent for effective removal of cationic dye: Process optimization based on Taguchi design method, kinetics, equilibrium and thermodynamics. J Water Environ Nanotechnol 3:. https://doi.org/10.22090/jwent.2018.04.005

Ghobashy MM, Elbarbary AM, Hegazy DE (2021) Synthesis of poly (vinylpyrrolidone)/Fe_3O_4@SiO_2 nanoporous catalyst by γ-rays and evaluation their sono-photo-Fenton degradation of toluidine blue under magnetic field. Applied Organometallic Chemistry 35:e6388. https://doi.org/10.1002/aoc.6388

Gogate PR (2002) Cavitation: an auxiliary technique in wastewater treatment schemes. Advances in Environmental Research 6:335–358. https://doi.org/10.1016/S1093-0191(01)00067-3

Gogate PR, Bhosale GS (2013) Comparison of effectiveness of acoustic and hydrodynamic cavitation in combined treatment schemes for degradation of dye wastewaters. Chemical Engineering and Processing: Process Intensification 71:59–69. https://doi.org/10.1016/j.cep.2013.03.001

Gogate PR, Pandit AB (2004) Sonophotocatalytic reactors for wastewater treatment: A critical review. AIChE Journal 50:1051–1079. https://doi.org/10.1002/aic.10079

Gogate PR, Pandit AB (2000) Engineering design methods for cavitation reactors II: Hydrodynamic cavitation. AIChE Journal 46:1641–1649. https://doi.org/10.1002/aic.690460815

Gonçalves I, Silva C, Cavaco-Paulo A (2015) Ultrasound enhanced laccase applications. Green Chem 17:1362–1374. https://doi.org/10.1039/C4GC02221A

Gong D, Yang P, Zhao J, Jia X (2024) Selective removal of thallium from water by MnO_2-doped magnetic beads: Performance and mechanism study. Journal of Environmental Management 353:120147. https://doi.org/10.1016/j.jenvman.2024.120147

Guo X, Mao F, Wang W, et al (2015) Sulfhydryl-Modified Fe_3O_4@SiO_2 Core/Shell Nanocomposite: Synthesis and Toxicity Assessment in Vitro. ACS Appl Mater Interfaces 7:14983–14991. https://doi.org/10.1021/acsami.5b03873

Hadjltaief HB, Bairq ZAS, Shi C, Benzina M (2021) Evaluation of sono-assisted solar/Fenton process for indigo carmine degradation over magnetic ZnO-Fe_3O_4 supported Tunisian kaolinite clay. Surfaces and Interfaces 26:101395. https://doi.org/10.1016/j.surfin.2021.101395

Harichandran G, Prasad S (2016) SonoFenton degradation of an azo dye, Direct Red. Ultrasonics Sonochemistry 29:178–185. https://doi.org/10.1016/j.ultsonch.2015.09.005

Hassani A, Malhotra M, Karim AV, et al (2022) Recent progress on ultrasound-assisted electrochemical processes: A review on mechanism, reactor strategies, and applications for wastewater treatment. Environmental Research 205:112463. https://doi.org/10.1016/j.envres.2021.112463

Ho Y-S (2006) Second-order kinetic model for the sorption of cadmium onto tree fern: A comparison of linear and non-linear methods. Water Research 40:119–125. https://doi.org/10.1016/j.watres.2005.10.040

Ho YS, McKay G (2000) The kinetics of sorption of divalent metal ions onto sphagnum moss peat. Water Research 34:735–742. https://doi.org/10.1016/S0043-1354(99)00232-8

Hoffmann MR, Hua I, Höchemer R (1996) Application of ultrasonic irradiation for the degradation of chemical contaminants in water. Ultrasonics Sonochemistry 3:S163–S172. https://doi.org/10.1016/S1350-4177(96)00022-3

Hou C, Wang Y, Ding Q, et al (2015) Facile synthesis of enzyme-embedded magnetic metal–organic frameworks as a reusable mimic multi-enzyme system: mimetic peroxidase properties and colorimetric sensor. Nanoscale 7:18770–18779. https://doi.org/10.1039/C5NR04994F

Hou L, Wang L, Royer S, Zhang H (2016) Ultrasound-assisted heterogeneous Fenton-like degradation of tetracycline over a magnetite catalyst. Journal of Hazardous Materials 302:458–467. https://doi.org/10.1016/j.jhazmat.2015.09.033

Hsing H-J, Chiang P-C, Chang E-E, Chen M-Y (2007) The decolorization and mineralization of Acid Orange 6 azo dye in aqueous solution by advanced oxidation processes: A comparative study. Journal of Hazardous Materials 141:8–16. https://doi.org/10.1016/j.jhazmat.2006.05.122

Hu J, Yuan B, Zhang Y, Guo M (2015) Immobilization of laccase on magnetic silica nanoparticles and its application in the oxidation of guaiacol, a phenolic lignin model compound. RSC Adv 5:99439–99447. https://doi.org/10.1039/C5RA14982G

Huang R, Fang Z, Yan X, Cheng W (2012a) Heterogeneous sono-Fenton catalytic degradation of bisphenol A by Fe_3O_4 magnetic nanoparticles under neutral condition. Chemical Engineering Journal 197:242–249. https://doi.org/10.1016/j.cej.2012.05.035

Huang R, Fang Z, Yan X, Cheng W (2012b) Heterogeneous sono-Fenton catalytic degradation of bisphenol A by Fe_3O_4 magnetic nanoparticles under neutral condition. Chemical Engineering Journal 197:242–249. https://doi.org/10.1016/j.cej.2012.05.035

Huang Y, Lapanje A, Parakhonskiy B, Skirtach AG (2024) Versatile and durable polyvinyl alcohol/alginate/gelatin/quaternary ammonium chitosan/Fe_3O_4 particles hybrid hydrogel beads: adsorption capabilities for cleaning pollutants. International Journal of Biological Macromolecules 280:135729. https://doi.org/10.1016/j.ijbiomac.2024.135729

Hussain A, Dubey SK, Kumar V (2015) Kinetic study for aerobic treatment of phenolic wastewater. Water Resources and Industry 11:81–90. https://doi.org/10.1016/j.wri.2015.05.002

Ince NH (2018) Ultrasound-assisted advanced oxidation processes for water decontamination. Ultrasonics Sonochemistry 40:97–103. https://doi.org/10.1016/j.ultsonch.2017.04.009

Ingole PM, Rathod VK (2023) Ultrasound-assisted enzymatic degradation of naproxen. Journal of the Indian Chemical Society 100:101040. https://doi.org/10.1016/j.jics.2023.101040

Ismail YH, Wang K, Shehhi MA, Hammadi AA (2024) Iodide ion-imprinted chitosan beads for highly selective adsorption for nuclear wastewater treatment applications. Heliyon 10:. https://doi.org/10.1016/j.heliyon.2024.e24735

Jaafarzadeh N, Takdastan A, Jorfi S, et al (2018) The performance study on ultrasonic/Fe_3O_4 /H_2O_2 for degradation of azo dye and real textile wastewater treatment. Journal of Molecular Liquids 256:462–470. https://doi.org/10.1016/j.molliq.2018.02.047

Jafarikojour M, Dabir B, Sohrabi M, Royaee SJ (2017) Evaluation and optimization of a new design photocatalytic reactor using impinging jet stream on a TiO_2 coated disc. Chemical Engineering and Processing: Process Intensification 121:215–223. https://doi.org/10.1016/j.cep.2017.08.011

Jamali M, Akbari A (2021) Facile fabrication of magnetic chitosan hydrogel beads and modified by interfacial polymerization method and study of adsorption of cationic/anionic dyes from aqueous solution. Journal of Environmental Chemical Engineering 9:105175. https://doi.org/10.1016/j.jece.2021.105175

John S, Rathinavelu S, Mary SMS, et al (2023) Solar-driven hybrid photo-Fenton degradation of persistent antibiotic ciprofloxacin by zinc ferrite-titania heterostructures: degradation pathway, intermediates, and toxicity analysis. Environ Sci Pollut Res 30:39605–39617. https://doi.org/10.1007/s11356-022-24926-1

Jonidi Jafari A, Kakavandi B, Jaafarzadeh N, et al (2017a) Fenton-like catalytic oxidation of tetracycline by AC@Fe_3O_4 as a heterogeneous persulfate activator: Adsorption and degradation studies. Journal of Industrial and Engineering Chemistry 45:323–333. https://doi.org/10.1016/j.jiec.2016.09.044

Jonidi Jafari A, Kakavandi B, Jaafarzadeh N, et al (2017b) Fenton-like catalytic oxidation of tetracycline by AC@Fe_3O_4 as a heterogeneous persulfate activator: Adsorption and degradation studies. Journal of Industrial and Engineering Chemistry 45:323–333. https://doi.org/10.1016/j.jiec.2016.09.044

Joshi S (2019) Applications of Fe_3O_4@AC nanoparticles for dye removal from simulated wastewater

Joshi SM, Gogate PR (2019) Intensification of industrial wastewater treatment using hydrodynamic cavitation combined with advanced oxidation at operating capacity of 70 L. Ultrasonics Sonochemistry 52:375–381. https://doi.org/10.1016/j.ultsonch.2018.12.016

Jung S, Jung M, Yoon J, et al (2024) Chitosan-derived activated carbon/chitosan composite beads for adsorptive removal of methylene blue and acid orange 7 dyes. Reactive and Functional Polymers 204:106028. https://doi.org/10.1016/j.reactfunctpolym.2024.106028

Kadam AA, Jang J, Lee DS (2017) Supermagnetically Tuned Halloysite Nanotubes Functionalized with Aminosilane for Covalent Laccase Immobilization. ACS Appl Mater Interfaces 9:15492–15501. https://doi.org/10.1021/acsami.7b02531

Kakama NK, Petrik LF, Ojumu TV (2024) The Optimization of Hydrodynamic Cavitation as an Advanced Oxidation Option for the Removal of Persistent Contaminants in Wastewater. Water Air Soil Pollut 235:193. https://doi.org/10.1007/s11270-024-06924-w

Kakavandi B (2016) Application of Fe_3O_4@C catalyzing heterogeneous UV-Fenton system for tetracycline removal with a focus on optimization by a response surface method

Kakavandi B, Jahangiri-rad M, Rafiee M, et al (2016) Development of response surface methodology for optimization of phenol and p -chlorophenol adsorption on magnetic recoverable carbon. Microporous and Mesoporous Materials 231:192–206. https://doi.org/10.1016/j.micromeso.2016.05.033

Kakavandi B, Kalantary RR, Jafari AJ, et al (2015) Pb(II) Adsorption Onto a Magnetic Composite of Activated Carbon and Superparamagnetic Fe_3O_4 Nanoparticles: Experimental and Modeling Study. CLEAN – Soil, Air, Water 43:1157–1166. https://doi.org/10.1002/clen.201400568

Kamali M, Khodaparast Z (2015) Review on recent developments on pulp and paper mill wastewater treatment. Ecotoxicology and Environmental Safety 114:326–342. https://doi.org/10.1016/j.ecoenv.2014.05.005

Kanafin YN, Makhatova A, Meiramkulova K, Poulopoulos SG (2022) Treatment of a poultry slaughterhouse wastewater using advanced oxidation processes. Journal of Water Process Engineering 47:102694. https://doi.org/10.1016/j.jwpe.2022.102694

Kanthale P, Pandey R, Thakur D, et al (2023) Application of combined hydrodynamic cavitation and Fenton reagent for COD reduction of cellulosic fiber industry effluents.

Journal of Water Process Engineering 56:104500. https://doi.org/10.1016/j.jwpe.2023.104500

Karaer H, Kaya İ (2016) Synthesis, characterization of magnetic chitosan/active charcoal composite and using at the adsorption of methylene blue and reactive blue4. Microporous and Mesoporous Materials 232:26–38. https://doi.org/10.1016/j.micromeso.2016.06.006

Kaur S, Rani S, Mahajan RK, et al (2015) Synthesis and adsorption properties of mesoporous material for the removal of dye safranin: Kinetics, equilibrium, and thermodynamics. Journal of Industrial and Engineering Chemistry 22:19–27. https://doi.org/10.1016/j.jiec.2014.06.019

Kausley SB, Desai KS, Shrivastava S, et al (2018) Mineralization of alkyd resin wastewater: Feasibility of different advanced oxidation processes. Journal of Environmental Chemical Engineering 6:3690–3701. https://doi.org/10.1016/j.jece.2017.04.001

Kaveh R, Bagherzadeh M (2022) Simultaneous removal of mercury ions and cationic and anionic dyes from aqueous solution using epichlorohydrin cross-linked chitosan @ magnetic Fe_3O_4/activated carbon nanocomposite as an adsorbent. Diamond and Related Materials 124:108923. https://doi.org/10.1016/j.diamond.2022.108923

Khataee A, Darvishi Cheshmeh Soltani R, Hanifehpour Y, et al (2014) Synthesis and Characterization of Dysprosium-Doped ZnO Nanoparticles for Photocatalysis of a Textile Dye under Visible Light Irradiation. Ind Eng Chem Res 53:1924–1932. https://doi.org/10.1021/ie402743u

Khataee A, Sheydaei M, Hassani A, et al (2015) Sonocatalytic removal of an organic dye using TiO_2/Montmorillonite nanocomposite. Ultrasonics Sonochemistry 22:404–411. https://doi.org/10.1016/j.ultsonch.2014.07.002

Kodavatiganti S, Bhat AP, Gogate PR (2021) Intensified degradation of Acid Violet 7 dye using ultrasound combined with hydrogen peroxide, Fenton, and persulfate. Separation and Purification Technology 279:119673. https://doi.org/10.1016/j.seppur.2021.119673

Kong J, Yu S (2007) Fourier transform infrared spectroscopic analysis of protein secondary structures. Acta Biochim Biophys Sin (Shanghai) 39:549–559. https://doi.org/10.1111/j.1745-7270.2007.00320.x

Kore VS, Manjare SD, Patil AD, Dhanke PB (2023) A parametric study on intensified degradation of textile dye water using hydrodynamic cavitation based hybrid technique. Chemical Engineering and Processing - Process Intensification 193:109550. https://doi.org/10.1016/j.cep.2023.109550

Korpe S, Bethi B, Sonawane SH, Jayakumar KV (2019) Tannery wastewater treatment by cavitation combined with advanced oxidation process (AOP). Ultrasonics Sonochemistry 59:104723. https://doi.org/10.1016/j.ultsonch.2019.104723

Korpe S, Rao PV, Sonawane SH (2023) Performance evaluation of hydrodynamic cavitation in combination with AOPs for degradation of tannery wastewater. Journal of

Environmental Chemical Engineering 11:109731. https://doi.org/10.1016/j.jece.2023.109731

Kumar A, Patra C, Rajendran HK, Narayanasamy S (2022) Activated carbon-chitosan based adsorbent for the efficient removal of the emerging contaminant diclofenac: Synthesis, characterization and phytotoxicity studies. Chemosphere 307:135806. https://doi.org/10.1016/j.chemosphere.2022.135806

Kurian M (2021) Advanced oxidation processes and nanomaterials -a review. Cleaner Engineering and Technology 2:100090. https://doi.org/10.1016/j.clet.2021.100090

Kurian M, Nair DS (2015) Heterogeneous Fenton behavior of nano nickel zinc ferrite catalysts in the degradation of 4-chlorophenol from water under neutral conditions. Journal of Water Process Engineering 8:e37–e49. https://doi.org/10.1016/j.jwpe.2014.10.011

Lai F, Tian F-X, Xu B, et al (2022) A comparative study on the degradation of phenylurea herbicides by UV/persulfate process: Kinetics, mechanisms, energy demand and toxicity evaluation associated with DBPs. Chemical Engineering Journal 428:132088. https://doi.org/10.1016/j.cej.2021.132088

Lakshmi NJ, Agarkoti C, Gogate PR, Pandit AB (2022) Acoustic and hydrodynamic cavitation-based combined treatment techniques for the treatment of industrial real effluent containing mainly pharmaceutical compounds. Journal of Environmental Chemical Engineering 10:108349. https://doi.org/10.1016/j.jece.2022.108349

Lakshmi NJ, Iyer AM, Gogate PR (2024) Treatment of wastewater containing ciprofloxacin using the hybrid treatment approach based on acoustic cavitation. The Canadian Journal of Chemical Engineering 102:2403–2417. https://doi.org/10.1002/cjce.25212

Le VT, Dao MU, Le HS, et al (2020) Adsorption of Ni(II) ions by magnetic activated carbon/chitosan beads prepared from spent coffee grounds, shrimp shells and green tea extract. Environmental Technology 41:2817–2832. https://doi.org/10.1080/09593330.2019.1584250

Li C, Zhong H, Wang S, et al (2015) Removal of basic dye (methylene blue) from aqueous solution using zeolite synthesized from electrolytic manganese residue. Journal of Industrial and Engineering Chemistry 23:344–352. https://doi.org/10.1016/j.jiec.2014.08.038

Li S, Qi B, Luo J, Wan Y (2022) Degradation of phenolic inhibitors by laccase immobilized on tannic acid/polyethylenimine modified magnetic nanoparticles. Results in Engineering 15:100585. https://doi.org/10.1016/j.rineng.2022.100585

Lin M, Ning X, An T, et al (2016) Degradation of polycyclic aromatic hydrocarbons (PAHs) in textile dyeing sludge with ultrasound and Fenton processes: Effect of system parameters and synergistic effect study. Journal of Hazardous Materials 307:7–16. https://doi.org/10.1016/j.jhazmat.2015.12.047

Liu L, Yang C, Tan W, Wang Y (2020) Degradation of Acid Red 73 by Activated Persulfate in a Heat/Fe_3O_4 @AC System with Ultrasound Intensification. ACS Omega 5:13739–13750. https://doi.org/10.1021/acsomega.0c00903

Liu X, Lei L, Li Y, et al (2011) Preparation of carriers based on magnetic nanoparticles grafted polymer and immobilization for lipase. Biochemical Engineering Journal 56:142–149. https://doi.org/10.1016/j.bej.2011.05.013

Liu Y, Shan H, Pang Y, et al (2023) Iron modified chitosan/coconut shell activated carbon composite beads for Cr(VI) removal from aqueous solution. International Journal of Biological Macromolecules 224:156–169. https://doi.org/10.1016/j.ijbiomac.2022.10.112

Lü C, Cui Z, Guan C, et al (2003) Research on Preparation, Structure and Properties of TiO_2/Polythiourethane Hybrid Optical Films with High Refractive Index. Macromolecular Materials and Engineering 288:717–723. https://doi.org/10.1002/mame.200300067

Lu X, Qiu W, Peng J, et al (2021) A Review on Additives-assisted Ultrasound for Organic Pollutants Degradation. Journal of Hazardous Materials 403:123915. https://doi.org/10.1016/j.jhazmat.2020.123915

Lu Y, Weavers LK (2002) Sonochemical desorption and destruction of 4-chlorobiphenyl from synthetic sediments. Environ Sci Technol 36:232–237. https://doi.org/10.1021/es010641+

Madhavan J, Grieser F, Ashokkumar M (2010) Degradation of orange-G by advanced oxidation processes. Ultrason Sonochem 17:338–343. https://doi.org/10.1016/j.ultsonch.2009.10.008

Madhavan J, Theerthagiri J, Balaji D, et al (2019) Hybrid Advanced Oxidation Processes Involving Ultrasound: An Overview. Molecules 24:3341. https://doi.org/10.3390/molecules24183341

Mahapatra K, Ramteke DS, Paliwal LJ (2012) Production of activated carbon from sludge of food processing industry under controlled pyrolysis and its application for methylene blue removal. Journal of analytical and applied pyrolysis

Mandal P, Dubey BK, Gupta AK (2017) Review on landfill leachate treatment by electrochemical oxidation: Drawbacks, challenges and future scope. Waste Manag 69:250–273. https://doi.org/10.1016/j.wasman.2017.08.034

Maroudas A, Pandis PK, Chatzopoulou A, et al (2021) Synergetic decolorization of azo dyes using ultrasounds, photocatalysis and photo-fenton reaction. Ultrasonics Sonochemistry 71:105367. https://doi.org/10.1016/j.ultsonch.2020.105367

Medina-Collana JT, Sejje Suárez WD, Anyosa Cáceres N, et al (2023) Intensification of Lead, Copper and Antimony Removal Using Brown Algae Adsorption Coupled to Hydrodynamic Cavitation. Sustainability 15:3453. https://doi.org/10.3390/su15043453

Mehdaoui R, Agren S, El Haskouri J, et al (2022) An optimized sono-heterogeneous Fenton degradation of olive-oil mill wastewater organic matter by new magnetic glutarlaldehyde-crosslinked developed cellulose. Environ Sci Pollut Res 30:20450–20468. https://doi.org/10.1007/s11356-022-23276-2

Mehrizad A, Behnajady MA, Gharbani P, Sabbagh S (2019) Sonocatalytic degradation of Acid Red 1 by sonochemically synthesized zinc sulfide-titanium dioxide nanotubes: Optimization, kinetics and thermodynamics studies. Journal of Cleaner Production 215:1341–1350. https://doi.org/10.1016/j.jclepro.2019.01.172

Mehrkhah R, Park SY, Lee JH, et al (2024) A comparative study of advanced oxidation-based hybrid technologies for industrial wastewater treatment: An engineering perspective. Chemical Engineering Science 286:119675. https://doi.org/10.1016/j.ces.2023.119675

Miljevic B, Hedayat F, Stevanovic S, et al (2014) To Sonicate or Not to Sonicate PM Filters: Reactive Oxygen Species Generation Upon Ultrasonic Irradiation. Aerosol Science and Technology 48:1276–1284. https://doi.org/10.1080/02786826.2014.981330

Mirzajani R, Karimi S (2019) Ultrasonic assisted synthesis of magnetic Ni-Ag bimetallic nanoparticles supported on reduced graphene oxide for sonochemical simultaneous removal of sunset yellow and tartrazine dyes by response surface optimization: Application of derivative spectrophotometry. Ultrasonics Sonochemistry 50:239–250. https://doi.org/10.1016/j.ultsonch.2018.09.022

Mohan D, Sarswat A, Singh VK, et al (2011) Development of magnetic activated carbon from almond shells for trinitrophenol removal from water. Chemical engineering journal

Moholkar VS, Sable SP, Pandit AB (2000) Mapping the cavitation intensity in an ultrasonic bath using the acoustic emission. AIChE Journal 46:684–694. https://doi.org/10.1002/aic.690460404

Moholkar VS, Warmoeskerken MMCG (2003) Integrated approach to optimization of an ultrasonic processor. AIChE Journal 49:2918–2932. https://doi.org/10.1002/aic.690491121

Mohseni-Bandpi A, Kakavandi B, Kalantary RR, et al (2015) Development of a novel magnetite–chitosan composite for the removal of fluoride from drinking water: adsorption modeling and optimization. RSC Adv 5:73279–73289. https://doi.org/10.1039/C5RA11294J

Momin RF, Gogate PR (2024) Degradation of Procion Brilliant Purple H-3R using ultrasound coupled with advanced oxidation processes. Journal of Environmental Management 350:119642. https://doi.org/10.1016/j.jenvman.2023.119642

Nigussie W, Zewge F, Chandravanshi BS (2007) Removal of excess fluoride from water using waste residue from alum manufacturing process. Journal of Hazardous Materials 147:954–963. https://doi.org/10.1016/j.jhazmat.2007.01.126

Pandey D, Daverey A, Dutta K, Arunachalam K (2023) Dye removal from simulated and real textile effluent using laccase immobilized on pine needle biochar. Journal of Water Process Engineering 53:103710. https://doi.org/10.1016/j.jwpe.2023.103710

Patil AL, Patil PN, Gogate PR (2014) Degradation of imidacloprid containing wastewaters using ultrasound based treatment strategies. Ultrason Sonochem 21:1778–1786. https://doi.org/10.1016/j.ultsonch.2014.02.029

Patil Y, Sonawane SH, Shyam P, et al (2023) Hybrid hydrodynamic cavitation (HC) technique for the treatment and disinfection of lake water. Ultrasonics Sonochemistry 97:106454. https://doi.org/10.1016/j.ultsonch.2023.106454

Peng S, Meng H, Ouyang Y, Chang J (2014) Nanoporous Magnetic Cellulose–Chitosan Composite Microspheres: Preparation, Characterization, and Application for Cu(II) Adsorption. Industrial & Engineering Chemistry Research 53:2106–2113. https://doi.org/10.1021/ie402855t

Peng ZG, Hidajat K, Uddin MS (2004) Adsorption of bovine serum albumin on nanosized magnetic particles. Journal of Colloid and Interface Science 271:277–283. https://doi.org/10.1016/j.jcis.2003.12.022

Pinjari DV, Pandit AB (2010) Cavitation milling of natural cellulose to nanofibrils. Ultrasonics Sonochemistry 17:845–852. https://doi.org/10.1016/j.ultsonch.2010.03.005

Prakash LV, Gopinath A, Gandhimathi R, et al (2021) Ultrasound aided heterogeneous Fenton degradation of Acid Blue 15 over green synthesized magnetite nanoparticles. Separation and Purification Technology 266:118230. https://doi.org/10.1016/j.seppur.2020.118230

Priyan V V, Kumar N, Narayanasamy S (2022) Toxicological assessment and adsorptive removal of lead (Pb) and Congo red (CR) from water by synthesized iron oxide/activated carbon (Fe_3O_4/AC) nanocomposite. Chemosphere 294:133758. https://doi.org/10.1016/j.chemosphere.2022.133758

Pu S, Ma H, Zinchenko A, Chu W (2017) Novel highly porous magnetic hydrogel beads composed of chitosan and sodium citrate: an effective adsorbent for the removal of heavy metals from aqueous solutions. Environ Sci Pollut Res 24:16520–16530. https://doi.org/10.1007/s11356-017-9213-0

Pulicharla R, Das RK, Kaur Brar S, et al (2018) Degradation kinetics of chlortetracycline in wastewater using ultrasonication assisted laccase. Chemical Engineering Journal 347:828–835. https://doi.org/10.1016/j.cej.2018.04.162

Qiu X, Wang Y, Xue Y, et al (2020) Laccase immobilized on magnetic nanoparticles modified by amino-functionalized ionic liquid via dialdehyde starch for phenolic compounds biodegradation. Chemical Engineering Journal 391:123564. https://doi.org/10.1016/j.cej.2019.123564

Quesada HB, De Araújo TP, Cusioli LF, et al (2022) Caffeine removal by chitosan/activated carbon composite beads: Adsorption in tap water and synthetic hospital wastewater.

Chemical Engineering Research and Design 184:1–12. https://doi.org/10.1016/j.cherd.2022.05.044

Rabiee F, Sarkhosh M, Azizi S, et al (2024) The superior decomposition of 2,4-Dinitrophenol under ultrasound-assisted Fe_3O_4@TiO_2 magnetic nanocomposite: Process modeling and optimization, Effect of various oxidants and Degradation pathway studies. International Journal of Environmental Analytical Chemistry 104:1243–1265. https://doi.org/10.1080/03067319.2022.2034798

Rahmi, Fathurrahmi, Lelifajri, et al (2019) Preparation of Magnetic Chitosan Beads for Heavy Metal Ions Removal from Water. IOP Conf Ser: Earth Environ Sci 276:012004. https://doi.org/10.1088/1755-1315/276/1/012004

Raj A, Bethi B, Sonawane SH (2018) Investigation of removal of crystal violet dye using novel hybrid technique involving hydrodynamic cavitation and hydrogel. Journal of Environmental Chemical Engineering 6:5311–5319. https://doi.org/10.1016/j.jece.2018.08.016

Rajoriya S, Bargole S, George S, et al (2019) Synthesis and characterization of samarium and nitrogen doped TiO_2 photocatalysts for photo-degradation of 4-acetamidophenol in combination with hydrodynamic and acoustic cavitation. Separation and Purification Technology 209:254–269. https://doi.org/10.1016/j.seppur.2018.07.036

Rajoriya S, Bargole S, George S, Saharan VK (2018) Treatment of textile dyeing industry effluent using hydrodynamic cavitation in combination with advanced oxidation reagents. Journal of Hazardous Materials 344:1109–1115. https://doi.org/10.1016/j.jhazmat.2017.12.005

Rashid SS, Mustafa AH, Ab Rahim MH (2022) Ferromagnetic nanoparticles synthesis and functionalization for laccase enzyme immobilization. Materials Today: Proceedings 48:916–919. https://doi.org/10.1016/j.matpr.2021.03.661

Reddy DHK, Lee S-M (2013) Application of magnetic chitosan composites for the removal of toxic metal and dyes from aqueous solutions. Advances in Colloid and Interface Science 201–202:68–93. https://doi.org/10.1016/j.cis.2013.10.002

Rezgui S, Amrane A, Fourcade F, et al (2018) Electro-Fenton catalyzed with magnetic chitosan beads for the removal of Chlordimeform insecticide. Applied Catalysis B: Environmental 226:346–359. https://doi.org/10.1016/j.apcatb.2017.12.061

Rodrigues CSD, Soares OSGP, Pinho MT, et al (2017) p-Nitrophenol degradation by heterogeneous Fenton's oxidation over activated carbon-based catalysts. Applied Catalysis B: Environmental 219:109–122. https://doi.org/10.1016/j.apcatb.2017.07.045

Rodríguez-Couto S (2018) Solid-State Fermentation for Laccases Production and Their Applications. In: Current Developments in Biotechnology and Bioengineering. Elsevier, pp 211–234

Rodríguez-Narváez OM, Picos AR, Bravo-Yumi N, et al (2021) Electrochemical oxidation technology to treat textile wastewaters. Current Opinion in Electrochemistry 29:100806. https://doi.org/10.1016/j.coelec.2021.100806

Rostami MS, Khodaei MM, Benassi E (2024) Surface modified of chitosan by TiO_2@MWCNT nanohybrid for the efficient removal of organic dyes and antibiotics. International Journal of Biological Macromolecules 274:133382. https://doi.org/10.1016/j.ijbiomac.2024.133382

Rouhani S, Azizi S, Maaza M, et al (2021) Covalent immobilization of laccase on Fe_3O_4-graphene oxide nanocomposite for biodegradation of phenolic compounds. Environ Protect Eng 47:. https://doi.org/10.37190/epe210107

Roy K, Moholkar VS (2020) Sulfadiazine degradation using hybrid AOP of heterogeneous Fenton/persulfate system coupled with hydrodynamic cavitation. Chemical Engineering Journal 386:121294. https://doi.org/10.1016/j.cej.2019.03.170

Sadeghzadeh S, Ghobadi Nejad Z, Ghasemi S, et al (2020) Removal of bisphenol A in aqueous solution using magnetic cross-linked laccase aggregates from Trametes hirsuta. Bioresource Technology 306:123169. https://doi.org/10.1016/j.biortech.2020.123169

Sajjadi S, Khataee A, Kamali M (2017) Sonocatalytic degradation of methylene blue by a novel graphene quantum dots anchored CdSe nanocatalyst. Ultrasonics Sonochemistry 39:676–685. https://doi.org/10.1016/j.ultsonch.2017.05.030

Salem DB, Ouakouak A, Touahra F, et al (2023) Easy separable, floatable, and recyclable magnetic-biochar/alginate bead as super-adsorbent for adsorbing copper ions in water media. Bioresource Technology 383:129225. https://doi.org/10.1016/j.biortech.2023.129225

Sancheti SV, Saini C, Ambati R, Gogate PR (2018) Synthesis of ultrasound assisted nanostuctured photocatalyst (NiO supported over CeO_2) and its application for photocatalytic as well as sonocatalytic dye degradation. Catalysis Today 300:50–57. https://doi.org/10.1016/j.cattod.2017.02.047

Santana Cadaval TR, Camara AS, Dotto GL, Pinto LADA (2013) Adsorption of Cr (VI) by chitosan with different deacetylation degrees. Desalination and Water Treatment 51:7690–7699. https://doi.org/10.1080/19443994.2013.778797

Santhosh C, Velmurugan V, Jacob G, et al (2016) Role of nanomaterials in water treatment applications: A review. Chemical Engineering Journal 306:1116–1137. https://doi.org/10.1016/j.cej.2016.08.053

Sharifi N, Nasiri A, Silva Martínez S, Amiri H (2022) Synthesis of Fe_3O_4@activated carbon to treat metronidazole effluents by adsorption and heterogeneous Fenton with effluent bioassay. Journal of Photochemistry and Photobiology A: Chemistry 427:113845. https://doi.org/10.1016/j.jphotochem.2022.113845

Sheldon RA, van Pelt S (2013) Enzyme immobilisation in biocatalysis: why, what and how. Chem Soc Rev 42:6223–6235. https://doi.org/10.1039/c3cs60075k

Shen S, Fu JJ, Wang HB (2021) Unravelling the favorable photocatalytic effect of hydrogenation process on the novel g-C_3N_4-TiO_2 catalysts for water purification. Diamond and Related Materials 114:108292. https://doi.org/10.1016/j.diamond.2021.108292

Shi L, Xu F, Gao J, et al (2020) Nanostructured boron-doped diamond electrode for degradation of the simulation wastewater of phenol. Diamond and Related Materials 109:108098. https://doi.org/10.1016/j.diamond.2020.108098

Shirgaonkar IZ, Pandit AB (1997) Degradation of aqueous solution of potassium iodide and sodium cyanide in the presence of carbon tetrachloride. Ultrasonics Sonochemistry 4:245–253. https://doi.org/10.1016/S1350-4177(97)00022-9

Sivasankar T, Moholkar VS (2009a) Physical insights into the sonochemical degradation of recalcitrant organic pollutants with cavitation bubble dynamics. Ultrasonics Sonochemistry 16:769–781. https://doi.org/10.1016/j.ultsonch.2009.02.009

Sivasankar T, Moholkar VS (2009b) Mechanistic approach to intensification of sonochemical degradation of phenol. Chemical Engineering Journal 149:57–69. https://doi.org/10.1016/j.cej.2008.10.004

Sivasankar T, Paunikar AW, Moholkar VS (2007) Mechanistic approach to enhancement of the yield of a sonochemical reaction. AIChE Journal 53:1132–1143. https://doi.org/10.1002/aic.11170

Souza FS, Da Silva VV, Rosin CK, et al (2018) Determination of pharmaceutical compounds in hospital wastewater and their elimination by advanced oxidation processes. Journal of Environmental Science and Health, Part A 53:213–221. https://doi.org/10.1080/10934529.2017.1387013

Sun H, Yuan F, Jia S, et al (2023) Laccase encapsulation immobilized in mesoporous ZIF-8 for enhancement bisphenol A degradation. Journal of Hazardous Materials 445:130460. https://doi.org/10.1016/j.jhazmat.2022.130460

Taghiloo B, Shahnazi A, Nabid MR (2024) Construction of nanocomposite hydrogel by TiO_2-carbon quantum dots encapsulated in alginate with a highly efficient adsorption and photodegradation of dye pollutants. Journal of Alloys and Compounds 1005:175859. https://doi.org/10.1016/j.jallcom.2024.175859

Tuomela M, Hatakka A (2019) Oxidative Fungal Enzymes for Bioremediation. In: Comprehensive Biotechnology. Elsevier, pp 224–239

Vasseghian Y, Almomani F, Le VT, et al (2022) Decontamination of toxic Malathion pesticide in aqueous solutions by Fenton-based processes: Degradation pathway, toxicity assessment and health risk assessment. Journal of Hazardous Materials 423:127016. https://doi.org/10.1016/j.jhazmat.2021.127016

Verma K, Moholkar VS (2023) Mineralization of Industrial Wastewater by a Hybrid Technique of Adsorption (Fe_3O_4@AC Nanocomposite) + Heterogeneous Fenton + Sonication and Discernment of Synergistic Effects. Ind Eng Chem Res acs.iecr.3c00427. https://doi.org/10.1021/acs.iecr.3c00427

Verma K, Moholkar VS (2024) Investigations in Sonoenzymatic Treatment of Industrial Wastewater Using Fe_3O_4@Laccase Nanocomposites. ACS EST Water 4:1637–1646. https://doi.org/10.1021/acsestwater.3c00697

Verma M, Haritash AK (2019) Degradation of amoxicillin by Fenton and Fenton-integrated hybrid oxidation processes. Journal of Environmental Chemical Engineering 7:102886. https://doi.org/10.1016/j.jece.2019.102886

Viikari L, Suurnäkki A, Grönqvist S, et al (2009) Forest Products: Biotechnology in Pulp and Paper Processing. In: Encyclopedia of Microbiology. Elsevier, pp 80–94

Voinov MA, Sosa Pagán JO, Morrison E, et al (2011) Surface-mediated production of hydroxyl radicals as a mechanism of iron oxide nanoparticle biotoxicity. J Am Chem Soc 133:35–41. https://doi.org/10.1021/ja104683w

Wanchai K, Pichon R (2020) Synthesis of Fe_3O_4@chitosan beads for degradation of sulfanilamide using photo-fenton process. Pattaya, Thailand, p 130002

Wang B, Su H, Zhang B (2021a) Hydrodynamic cavitation as a promising route for wastewater treatment – A review. Chemical Engineering Journal 412:128685. https://doi.org/10.1016/j.cej.2021.128685

Wang B, Wang T, Su H (2022) A dye-methylene blue (MB)-degraded by hydrodynamic cavitation (HC) and combined with other oxidants. Journal of Environmental Chemical Engineering 10:107877. https://doi.org/10.1016/j.jece.2022.107877

Wang D, Lou J, Yuan J, et al (2021b) Laccase immobilization on core-shell magnetic metal-organic framework microspheres for alkylphenol ethoxylate compound removal. Journal of Environmental Chemical Engineering 9:105000. https://doi.org/10.1016/j.jece.2020.105000

Wang W, Liu Y, Li T, Zhou M (2014) Heterogeneous Fenton catalytic degradation of phenol based on controlled release of magnetic nanoparticles. Chemical Engineering Journal 242:1–9. https://doi.org/10.1016/j.cej.2013.12.080

Wang Y, Chang M, Pan Y, et al (2019) Performance analysis and optimization of ammonium removal in a new biological folded non-aerated filter reactor. Sci Total Environ 688:505–512. https://doi.org/10.1016/j.scitotenv.2019.06.188

Wang Y, Li B, Zhou Y, Jia D (2008) Chitosan-induced synthesis of magnetite nanoparticles via iron ions assembly. Polymers for Advanced Techs 19:1256–1261. https://doi.org/10.1002/pat.1121

Wang Y, Yang W, Yin X, Liu Y (2016) The role of Mn-doping for catalytic ozonation of phenol using Mn/γ-Al_2O_3 nanocatalyst: Performance and mechanism. Journal of Environmental Chemical Engineering 4:3415–3425. https://doi.org/10.1016/j.jece.2016.07.016

Wang Z, Lin X, Li P, et al (2012) Effects of low intensity ultrasound on cellulase pretreatment. Bioresource Technology 117:222–227. https://doi.org/10.1016/j.biortech.2012.04.015

Wei H, Hu D, Su J, Li K (2015) Intensification of levofloxacin sono-degradation in a US/H_2O_2 system with Fe_3O_4 magnetic nanoparticles. Chinese Journal of Chemical Engineering 23:296–302. https://doi.org/10.1016/j.cjche.2014.11.011

Xu R, Bi H, He G, et al (2014) Synthesis of Cu-Fe_3O_4@graphene composite: A magnetically separable and efficient catalyst for the reduction of 4-nitrophenol. Materials Research Bulletin 57:190–196. https://doi.org/10.1016/j.materresbull.2014.05.045

Yadav D, Ranjan B, Mchunu N, et al (2021) Enzymatic treatment of phenolic pollutants by a small laccase immobilized on APTES-functionalised magnetic nanoparticles. 3 Biotech 11:302. https://doi.org/10.1007/s13205-021-02854-0

Yang J, Lin Y, Yang X, et al (2017) Degradation of tetracycline by immobilized laccase and the proposed transformation pathway. Journal of Hazardous Materials 322:525–531. https://doi.org/10.1016/j.jhazmat.2016.10.019

Yegane Badi M, Azari A, Pasalari H, et al (2018) Modification of activated carbon with magnetic Fe_3O_4 nanoparticle composite for removal of ceftriaxone from aquatic solutions. Journal of Molecular Liquids 261:146–154. https://doi.org/10.1016/j.molliq.2018.04.019

Yosofi Y, Mousavi SA (2020) Sono-photo-Fenton degradation of Reactive Black 5 from aqueous solutions: performance and kinetics. Desalination and Water Treatment 174:354–360. https://doi.org/10.5004/dwt.2020.24843

Yurtseven A, Ince B, Nas MS, Calimli MH (2023) Sonocatalytic Degradation of Methylene Blue by a Novel SnO_2-Fe_3O_4@MWCNT Hybrid Nanocatalyst Under Ultrasonic Irradiation. Catal Lett. https://doi.org/10.1007/s10562-023-04347-6

Zanias A, Frontistis Z, Vakros J, et al (2020) Degradation of methylparaben by sonocatalysis using a Co–Fe magnetic carbon xerogel. Ultrasonics Sonochemistry 64:105045. https://doi.org/10.1016/j.ultsonch.2020.105045

Zhang X, Hao C, Ma C, et al (2019) Studied on sonocatalytic degradation of Rhodamine B in aqueous solution. Ultrasonics Sonochemistry 58:104691. https://doi.org/10.1016/j.ultsonch.2019.104691

Zhao M, Zhang X, Deng C (2015) Rational synthesis of novel recyclable Fe_3O_4@MOF nanocomposites for enzymatic digestion. Chem Commun 51:8116–8119. https://doi.org/10.1039/C5CC01908G

Zheng ng, Jiang Y (2012) 260365 Biomimetic Synthesis of Magnetic Composite Particles for Laccase Immobilization

Zhu A, Yuan L, Liao T (2008) Suspension of Fe_3O_4 nanoparticles stabilized by chitosan and o-carboxymethylchitosan. Int J Pharm 350:361–368. https://doi.org/10.1016/j.ijpharm.2007.09.004

CHAPTER 2

Mineralization of industrial wastewater by a hybrid technique of adsorption (Fe_3O_4@AC nanocomposite) + heterogeneous Fenton + sonication and discernment of synergistic effects

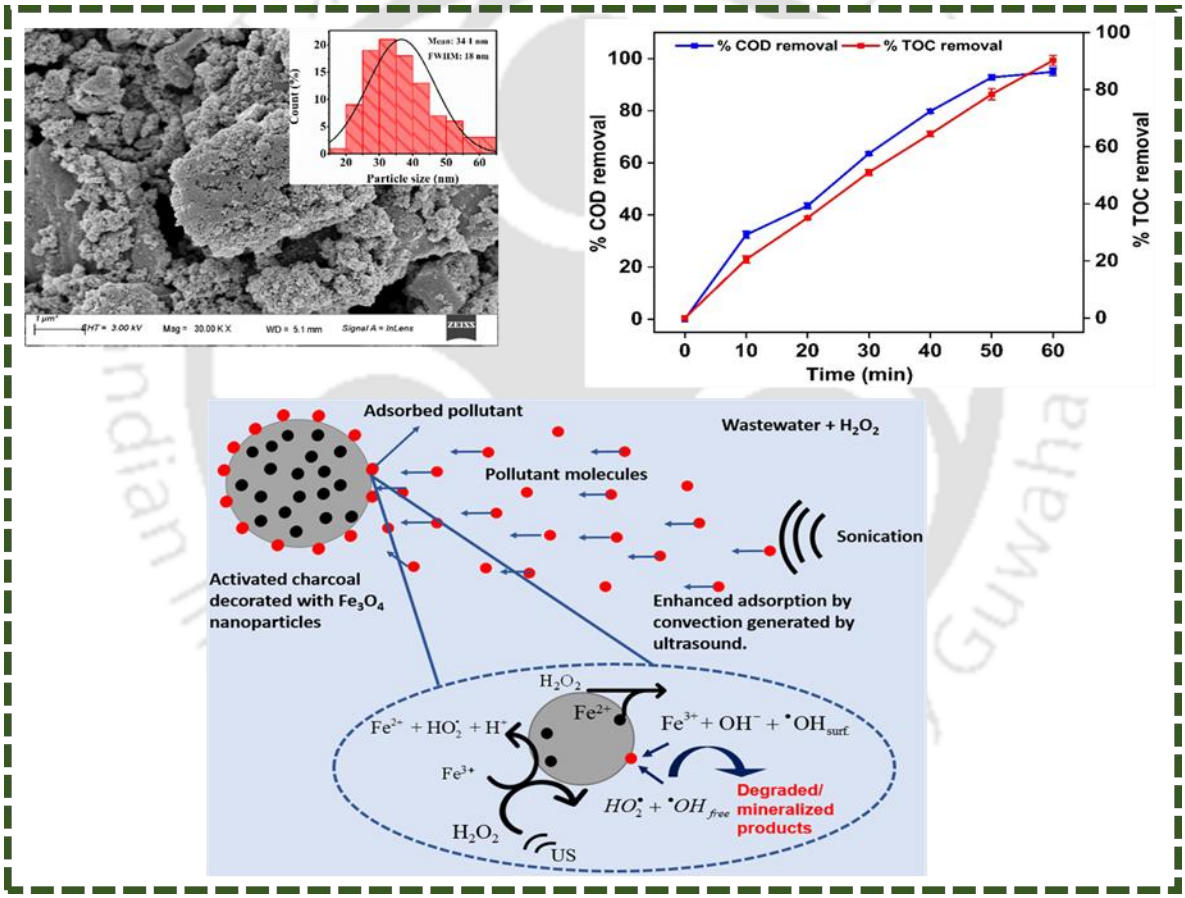

***Online*:** Verma, K., Moholkar, V. S. Mineralization of Industrial Wastewater by a Hybrid Technique of Adsorption (Fe_3O_4@AC Nanocomposite) + Heterogeneous Fenton + Sonication and Discernment of Synergistic Effects. *Industrial and Engineering Chemistry Research*, doi.org/10.1021/acs.iecr.3c00427.

CHAPTER 2

MINERALIZATION OF INDUSTRIAL WASTEWATER BY A HYBRID TECHNIQUE OF ADSORPTION (Fe_3O_4@AC NANOCOMPOSITE) + HETEROGENEOUS FENTON + SONICATION AND DISCERNMENT OF SYNERGISTIC EFFECTS

2.1 Introduction

Effective treatment and mineralization of industrial wastewater before its disposal into natural water bodies like rivers and lakes is challenging for process industries. The wastewater discharge from chemical process industries like refineries, petrochemicals, fertilizer, pharmaceuticals, pesticides, and dyestuff industries often contains recalcitrant organic pollutants that are not effectively degraded by conventional techniques like microbial processes. Even the advanced oxidation processes (AOPs) such as Fenton reactions, photocatalysis, ozonation, H_2O_2 treatment, or sonication do not adequately mineralize the wastewater (Bilinska et al. 2015; Souza et al. 2018; Kausley et al. 2018; Korpe et al. 2019; Kanafin et al. 2022). Therefore, significant research has been published in the last two decades on hybrid techniques that combine two or more AOPs (Bagal and Gogate 2014b; Bethi et al. 2016; Gągol et al. 2018; Madhavan et al. 2019; Chauhan et al. 2021). Another technique for removing pollutants from wastewater is adsorption. Numerous carbonaceous adsorbents -

especially activated charcoals - have been used to remove organic contaminants from wastewater. However, this technique does not lead to complete mineralization of the pollutants (Hsing et al. 2007; Aleboyeh et al. 2008). Proper disposal of the contaminants after desorption (for recycling the adsorbent) remains a challenge. Several authors have combined the physical technique of adsorption and AOPs (e.g., Fenton, photocatalysis, sonication, and ozonation) to enhance wastewater treatment efficiency. Bello and Raman (2019) have given a review and analysis of adsorption-AOP hybrid techniques.

In the present chapter, we have used a ternary hybrid technique, viz. adsorption + heterogeneous Fenton process + sonication, to treat and mineralize wastewater from a combined discharge of local industries and academic institutions (including our institute) into a local water body. Before stating the rationale underlying combining the three techniques, we would like to state the following individual features of these techniques: (1) The AOP of sonication essentially works on generating oxidizing radicals ($^{\bullet}OH$, $^{\bullet}O$ and $HO_2^{\bullet}$) through the transient collapse of cavitation bubbles driven by the ultrasound waves. However, the occurrence of transient cavitation events in the wastewater volume is rather sporadic - in both time and space domains. The net utility of the radicals generated through cavitation bubbles depends on the probability of their interaction with the pollutant molecules. The radicals are highly unstable and do not diffuse into the liquid from their point of generation (Sivasankar et al. 2007; Sivasankar and Moholkar 2009a). Thus, most of these radicals recombine - for example, $^{\bullet}OH$ radicals recombine to generate H_2O_2 – which is a loss of oxidation efficiency. Thus, augmenting the probability of radical-pollutant interaction is necessary for boosting sonication efficiency. In addition to the chemical effect of generating oxidizing radicals, the sonication also has the physical effect of creating intense turbulence or micro-mixing in the medium. This enhances the mass transfer in heterogeneous or multiphase (liquid-liquid or

solid-liquid) systems. (2) The conventional homogeneous Fenton process ($FeCl_2 + H_2O_2$) for wastewater treatment results in the retention of dissolved iron (Fe^{2+}) in treated water, which results in the production of excessive sludge when discharged to the environment. This problem can be avoided by using a Fenton reagent in heterogeneous forms such as Fe_3O_4 particles. The surface leaching of the Fe_3O_4 particle can generate Fe^{2+} ions, and these particles can be separated after treatment using stirrers with magnetic surfaces. (3) The most widely used adsorbent in wastewater treatment is activated charcoal (AC). However, separating the activated charcoal particles before the discharge of the treated water is also problematic. The usual techniques, such as filtration or sedimentation, have limitations when applied to large volumes. Therefore, a nanocomposite of Fe_3O_4@AC has been employed by previous authors (Kakavandi 2016; Kakavandi et al. 2016; Bagheri et al. 2017; Jonidi Jafari et al. 2017a; Joshi 2019; Liu et al. 2020). The ferromagnetic properties of the Fe_3O_4 help in the easy separation of the adsorbent. Moreover, the presence of Fe_3O_4 nanoparticles on the surface of activated charcoal enhances the adsorption of pollutants due to the presence of O_2^- sites around Fe^{2+} and Fe^{3+} atoms. The adsorption of organic pollutants on the surface of Fe_3O_4@AC nanocomposite may involve several mechanisms, such as hydrophobic interactions, H-bond formation, and π-π stacking interactions.

The hypothesis underlying this study is as follows: the adsorption of the pollutants onto Fe_3O_4@AC nanocomposite will generate a high surface concentration of the pollutants, and leaching of Fe^{2+}/Fe^{3+} ions from Fe_3O_4 particles can initiate Fenton reactions on the surface that generate the $^{\bullet}OH$ and $HO_2^{\bullet}$ radicals through following reactions:

$$Fe^{2+} + H_2O_2 \longrightarrow Fe^{3+} + HO^{\bullet} + OH^- \quad (2.1)$$

$$Fe^{3+} + H_2O_2 \longrightarrow Fe^{2+} + HO_2^{\bullet} + H^+ \quad (2.2)$$

The probability of interaction among the pollutant molecules and the radicals is expected to be high, leading to effective degradation and mineralization of the organic pollutants. The sonication can enhance the mass transfer in the system leading to saturation of the adsorbent surface and the inner pores. The radicals generated through transient cavitation may degrade the pollutant in bulk liquid, but this contribution is small compared to the degradation/ mineralization through Fenton reactions (Chakma and Moholkar 2013). The in-situ generated H_2O_2 by the combination of the $^{\bullet}OH$ radicals generated by transient cavitation can further aid the surface Fenton reactions on the Fe_3O_4@AC nanocomposite.

This chapter has the following components: (1) synthesis of Fe_3O_4@AC nanocomposite using co-precipitation method, (2) characterization of the Fe_3O_4@AC nanocomposite using standard techniques of FTIR, FE-SEM, EDX, TEM, BET surface area analysis, XRD and magnetic property determination using VSM, (3) statistical optimization of the process parameters of wastewater treatment using COD removal as the response variable and compositional assessment of treated water using LC-MS, (4) assessment of adsorption characteristics and kinetics of the Fe_3O_4@AC nanocomposite, (5) estimation of toxicity reduction at conditions of optimum treatment. As described in subsequent sections, the ternary hybrid technique combining adsorption, the Fenton process, and sonication leads to almost complete wastewater mineralization (or TOC removal).

2.2 Materials and Methods

2.2.1 Reagents

The following chemicals have been used in this study: Activated charcoal powder (AC), Ferric chloride hexahydrate ($FeCl_3 \cdot 6H_2O$), sulfuric acid (H_2SO_4; 98%), ferrous sulfate heptahydrate ($FeSO_4 \cdot 7H_2O$), hydrogen peroxide (H_2O_2; 30% v/v), potassium permanganate ($KMnO_4$), and hydrochloric acid (HCl; 35%) were purchased from Himedia Ltd. (India). Hydrazine hydrate (N_2H_4, 50-60%) and sodium carbonate anhydrous (Na_2CO_3) were obtained from Sigma-Aldrich (India). The chemicals used in the COD analysis, i.e., ferrous ammonium sulfate heptahydrate ($Fe(NH_4)_2(SO_4)_2 \cdot 7H_2O$), potassium dichromate ($K_2Cr_2O_7$), mercuric sulfate ($HgSO_4$), silver sulfate (Ag_2SO_4), conc. H_2SO_4 (98%) and ferroin indicator were analytical grade Himedia Ltd.(India) reagents. The following chemicals for BOD analysis were procured from Sigma Aldrich: sodium thiosulfate ($Na_2S_2O_3$), alkali iodide azide, manganese sulfate ($MnSO_4$), starch, potassium dihydrogen phosphate (KH_2PO_4), dipotassium hydrogen orthophosphate (K_2HPO_4), disodium hydrogen phosphate (Na_2HPO_4), ammonium chloride (NH_4Cl), calcium chloride ($CaCl_2$), magnesium sulfate ($MgSO_4$) and ferric chloride ($FeCl_3$). The activated carbon was extensively washed with distilled water till the neutral pH of wash water and then dried in an oven at 80^oC overnight. All reagents were of analytical grade and used as received without further purification. The wastewater (WW) was obtained from the combined discharge from local industries and academic institutions (including our institute) into a local water body. The WW was filtered and stored in sealed bottles in a dark, 4 ^oC refrigerator. The WW samples were diluted using deionized water to obtain the required initial COD values. The physicochemical composition of the effluent was analyzed, and the results are shown in Table 2.1.

2.2.2 Synthesis of Fe_3O_4@AC nanocomposite

Fe_3O_4 nanoparticles were prepared using the co-precipitation method, as reported in Choudhury et al. (2021), with minor modifications. In a typical process to fabricate magnetite (Fe_3O_4) nanoparticles, a sonication bath was used to dissolve $FeCl_3 \cdot 6H_2O$ (2.2 g) completely and $FeSO_4 \cdot 7H_2O$ (1.2 g) in 100 mL of DI water. After gradually adding sodium carbonate (10.6 g, 100 mL) to the solution, as mentioned above, hydrazine hydrate (5 mL) was added dropwise in the presence of sonication.

Table 2.1. Characteristics of industrial wastewater

Parameter	Value
pH	9.31 ± 0.85
Color	Mustard Yellow
Initial COD	3246 ± 20 mg/L
Initial TOC	2500 ± 16 mg/L
Initial BOD	1000 ±12 mg/L
Biodegradability index (BOD_5: COD)	0.31 ± 0.05

The values given in the table are averages of triplets.

The solution was transferred to an oil bath and continuously stirred at 80 °C, followed by another 15 min sonication. After one hour, the solution was removed from the oil bath and cooled to room temperature. A permanent magnet was employed to gather the Fe_3O_4 nanoparticles that precipitated as an agglomerated black mass. This black mass was washed many times with deionized water, and the resulting Fe_3O_4 nanoparticles were dried for 12 h at 70 °C under a vacuum. Next, activated carbon (3 g) was dispersed into 100 mL of DI water

using a sonication bath for 30 min. The synthesized Fe_3O_4 nanoparticles (500 mg) were added to this suspension (which makes the Fe_3O_4:AC ratio = 5:30), and the mixture was stirred for one hour at 600 rpm in an oil bath at 80°C. The solution was cooled to room temperature, and the Fe_3O_4@AC nanocomposite particles were separated using a magnet. These particles were washed 3× with DI water to bring the pH of the wash water to a neutral level, followed by vacuum-drying for 12 h at 70°C.

2.2.3 Characterization of Fe_3O_4@AC

A Rigaku powder X-ray diffractometer (model Smart Lab, Cu K_α, λ = 1.54178 Å) was used to analyze the crystal structures of Fe_3O_4@AC nanocomposite. A Micromeritics surface area analyzer was used to perform the precise surface area measurements using the Brunauer-Emmett-Teller (BET) method (model Tristar II). The surface morphologies of the produced nanomaterials were examined using a Zeiss field emission scanning electron microscope (FE-SEM; model Sigma 300) and a JEOL transmission electron microscope (TEM; model JEM 2100). A Lakeshore vibrating sample magnetometer was used to assess the magnetic behavior of the Fe_3O_4 and Fe_3O_4@AC nanocomposite (model 7410 series). The functional groups of the Fe_3O_4@AC nanocomposite were studied using an FTIR spectrophotometer [Spectrum Two, PerkinElmer] in the wavenumber range of 4000-400 cm^{-1}. The elemental makeup of the Fe_3O_4@AC nanocomposite was ascertained by an energy-dispersive X-ray (EDX) examination [Sigma, Zeiss]. The COD and BOD analysis was carried out using standard methods. Biological oxygen demand after five days (BOD_5) was measured according to method 5210 D. As per method 5220 D, chemical oxygen demand (COD) was calculated using the acidic digestion (closed reflux) method with potassium dichromate as the oxidant at 150 °C for two hours (Merck, ECO25 Thermoreactor VELP SCIETIFICA) (Association et al. 1995). The total organic carbon (TOC) of the wastewater after treatment was determined using a TOC analyzer (Shimadzu, Model: TOC-LCPN+SSM). The wastewater was analyzed using HR-LCMS at the

advanced analytical instrument facility of NIPER Guwahati. LC-ESI-MS/MS analysis was conducted with a ZORBAX Eclipse C_{18} (4.6× 100 mm, 3.5 µm) from Agilent Technologies (Santa Clara, US). The details of the instrumentation and mobile phase composition are given in Table 2.2. In the mass spectrophotometer, the spray and cone voltages applied were ±4500 V and ±1000 V, respectively. The drying gas flow rate was 12 L/min (593 K), and the nebulizer pressure was 3.4 bar (50 psi). The oxidant (H_2O_2) consumption in the solution was evaluated using 1,5- diphenyl carbazide, which is oxidized to 1,5- diphenyl carbazone. 1,5- diphenyl carbazone formation can be determined by absorption at the wavelength of 563 nm (Rodrigues et al. 2017).

2.2.4 Experimental setup and procedure

A microprocessor-controlled ultrasound probe (Sonics and Materials Inc., Model: VCX 500; Frequency 20 kHz; Max power 500 W) was used for sonication. The ultrasound probe was operated at 40% of maximum power (acoustic intensity = 74548 $W/m^{2,}$ pressure amplitude = 470 kPa or 4.7 bar). Fig. 2.1 shows the schematic diagram of the experimental setup. Experiments of sonocatalytic degradation were conducted in a 250 mL borosilicate glass beaker.

Table 2.2. The details of the instrumentation and mobile phase composition

Instrument	1290 Infinity HPLC system with 6545 Quadrupole-Time OF Flight
Column temperature	45°C
Mobile Phase	Positive Mode A Milli-Q water with 0.1%FA B Methanol with 0.1% FA Negative Mode A Milli-Q water with 1% MeOH B Methanol with 10% H_2O
Flow rate	0.4 ml/min- Positive Mode 0.5 ml/min- Negative Mode
Mode	Gradient

The total sonication time of the reaction mixture was one hour in all experiments. The temperature of the reaction mixture in the beaker was maintained at 25 ^{o}C using a circulating water bath. We would like to note that an important parameter of the synthesis of Fe_3O_4@AC nanocomposite is the Fe_3O_4:AC ratio. To deduce the influence of this parameter on the efficacy of wastewater treatment (%COD removal), preliminary experiments were conducted using nanocomposites synthesized with varying Fe_3O_4:AC ratios. The results of these experiments are depicted in Fig. 2.2(a). It could be seen that COD removal increases proportionately with the Fe_3O_4:AC ratio. However, a leveling-off of the COD removal is seen after the Fe_3O_4:AC ratio of 5:30. Given this result, we have used the Fe_3O_4@AC nanocomposites with Fe_3O_4:AC ratio of 5:30 in this study. Preliminary experiments were conducted to deduce the effect of theoretical power input to ultrasound probe on %COD removal, as depicted in Fig. 2.2(b). It could be seen that the % COD removal increases proportionately with the input power of the ultrasound probe. All experiments were done in triplicate to assess the reproducibility of the results. The following parameters were used for the statistical design of experiments (DoE): adsorbent dose, pH, and H_2O_2 loading. The response variable of the statistical DoE was %COD removal.

In a typical experiment, 150 mL of wastewater was taken in the glass beaker. The solution pH was adjusted using 1 M HCl or 1 M NaOH. After the addition of the desired doses of H_2O_2 and Fe_3O_4@AC nanocomposite, the solution was subjected to sonication. Aliquots of the solution (3 mL) were withdrawn at 10 min intervals and centrifuged at 5000 rpm for 10 min. The supernatant was then analyzed to measure %COD removal. The control experiments were performed using native Fe_3O_4 nanoparticles. After completion of sonication, the Fe_3O_4@AC nanocomposites were magnetically separated and washed several times with DI water to remove the adsorbed pollutants that may not have been degraded. The wash water was added to the wastewater, and the final mixed solution was subjected to COD and TOC analysis.

Concurrent with sonication experiments, the adsorption characteristics of the Fe_3O_4@AC nanocomposites were also studied. Adsorption isotherms were obtained using 50 mg of the adsorbent Fe_3O_4@AC added to 150 mL solution with varying initial COD values at pH 4.2. Finally, the reusability and stability of Fe_3O_4@AC nanocomposite were evaluated in five consecutive cycles of wastewater treatment. The adsorption capacity (mg/g) of the Fe_3O_4@AC nanocomposite at any time (t) and the % COD removal can be deduced as:

$$q_t = \frac{(C_o - C_t)}{m} V \tag{2.3}$$

$$\%\text{COD removal} = \frac{(C_o - C_t)}{C_o} \times 100 \tag{2.4}$$

where C_o and C_t are the initial and instantaneous (at any time t) COD values of the solution, respectively; V is the solution volume (L), and m is the mass of the Fe_3O_4@AC nanocomposite (g). The equilibrium adsorption capacity (q_e) and final %COD removal is calculated by replacing C_t with C_e, the equilibrium COD value (mg/L).

2.2.5 Statistical design of experiments

Principal physical parameters that influence the COD removal during treatment are (1) adsorbent dose, (2) initial pH of the solution, and (3) H_2O_2 loading or dosage. Central Composite Design (CCD), a statistical design of experiments (DoE), was employed to deduce the optimum combination of the values of these parameters. A 3 factor – 3 level design was used using the following ranges of the parameters: (1) Adsorbent dose (X_1): 0.06-0.34 g/L; (2) pH (X_2): 2-10, and (3) H_2O_2 loading (X_3): 0.28 – 1.42 M. The ranges of the optimization parameters were determined on the basis of some preliminary trial experiments. The complete experimental design comprised 20 runs: 8 factorials, 6 axial points, and 6 replicates at the center

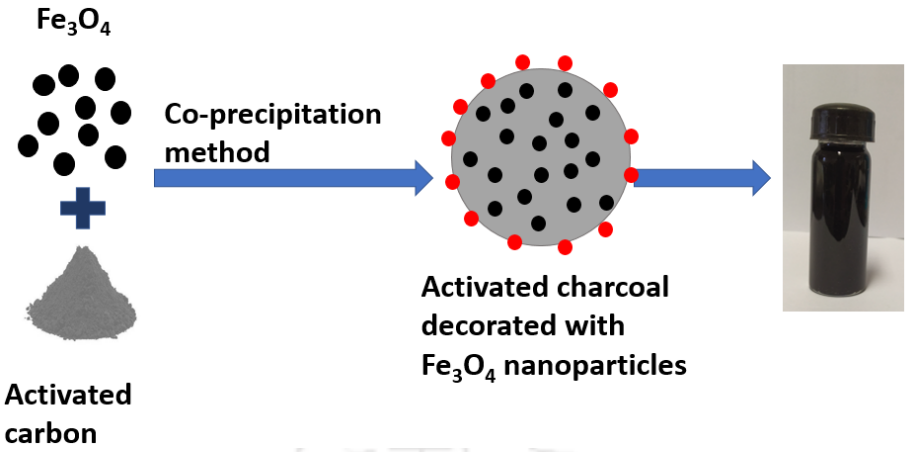

(a)

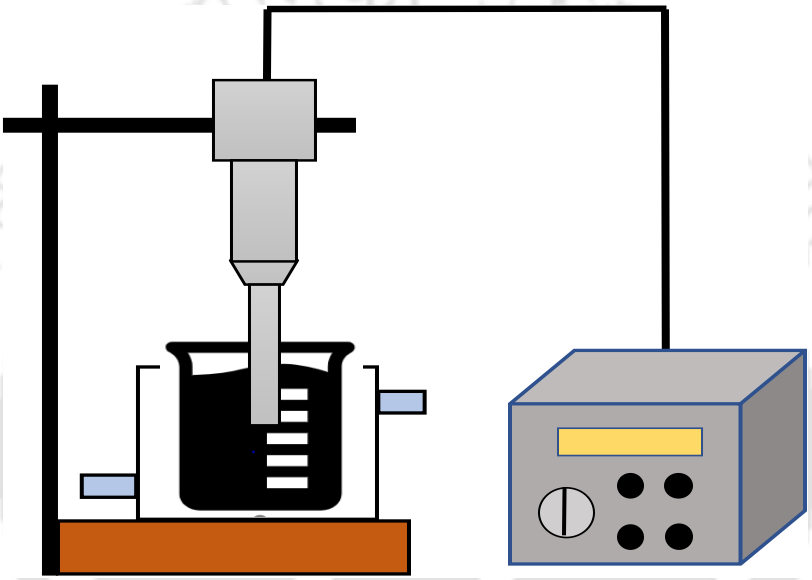

(b)

Figure 2.1. Schematic diagram of the (a) fabrication of Fe_3O_4@AC nanocomposite (b) experimental setup

point. The results of the statistical DoE were analyzed using response surface methodology by fitting a quadratic equation (2.5) to the data as follows (Ansari et al. 2016).

$$Y = \beta_0 + \sum_{i=1}^{k} \beta_i X_i + \sum_{i=1}^{k} \sum_{j=1}^{k} \beta_{ij} X_i X_j + \sum_{i=1}^{k} \beta_{ii} X_i^2 + \varepsilon \qquad (2.5)$$

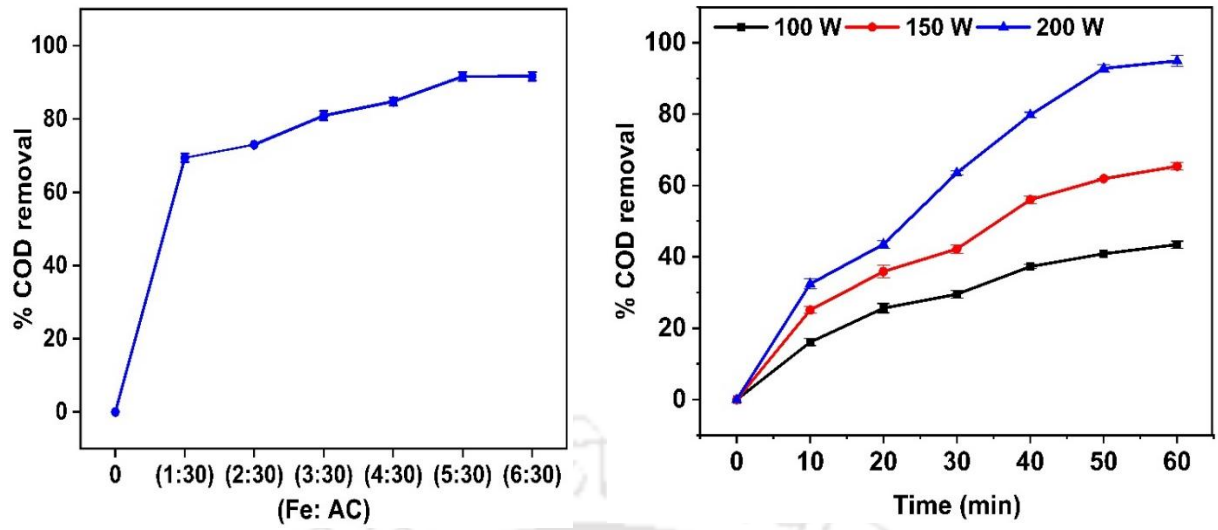

(a) (b)

Figure 2.2 (a) COD removal with varying Fe_3O_4:AC ratios. (b) COD removal at various levels of theoretical power input (pH = 4.2; adsorbent loading (Fe_3O_4@AC) = 0.34 g/L; H_2O_2 loading = 0.71 M)

Y is the response variable (% COD removal), β_0 is the constant coefficient, β_i are the linear coefficients, β_{ii} are the quadratic coefficients, β_{ij} are the interaction coefficients, X_i, X_j are the coded values of the independent process variables, k is the total number of independent variables, and ε is the residual error. The quality of the quadratic equation fitted to experimental data was determined using analysis of variance (ANOVA) and the response surfaces and contour plots. Tables 2.3 and 2.4 give the details of the statistical DoE.

Table 2.3. Factors and their levels for the design of experiments

Factor	Unit	Level		
		Low (-1)	Middle (0)	High (+1)
Adsorbent dose (X_1)	g/L	0.06	0.2	0.34
pH (X_2)	-	2	6	10
H_2O_2 loading (X_3)	M	0.28	0.85	1.42

2.2.6 Adsorption characteristics of Fe_3O_4@AC nanocomposite

Concurrently with the wastewater treatment experiments, the adsorption characteristics of the Fe_3O_4@AC nanocomposites were determined using the following pseudo-1st order pseudo-2nd order and intraparticle diffusion kinetic model expressions (Ho and McKay 2000; Ho 2006).

$$q_t = q_e(1-e^{k_1 t}) \tag{2.6}$$

$$q_t = \frac{q_e^2 k_2 t}{1+q_t k_2 t} \tag{2.7}$$

$$q_t = k_{diff} t^{1/2} + C \tag{2.8}$$

q_e = equilibrium adsorption capacity of Fe_3O_4@AC nanocomposite; q_t = instantaneous adsorption capacity (at time t), k_1 (min^{-1}) is the pseudo-1st order rate constant, k_2 (g/mg min) is the pseudo-2nd order rate constant, k_{diff} (mg/g min$^{1/2}$) is the initial rate of intraparticle diffusion and C (mg/g) is the intercept.

The adsorption behavior and the interactions between the adsorbent and pollutants for Fe_3O_4@AC nanocomposite were determined using a non-linear Langmuir and Freundlich adsorption isotherm.

$$q = \frac{q_m k_L C_e}{1+k_L C_e} \tag{2.9}$$

$$q_e = k_F C_e^{1/n} \tag{2.10}$$

where C_e is the COD value of the solution in equilibrium with the adsorbent (at a capacity of q_e), k_L (L/mg) is the Langmuir constant, q_m (mg/g) is the maximum monolayer adsorption capacity, and k_F. (mg/g) (mg/L)$^{-1/n}$ is the Freundlich constant. The non-dimensional separation factor (R_L) for Langmuir isotherm (Nigussie et al. 2007) is defined as:

$$R_L = \frac{1}{1 + k_L C_o} \tag{2.11}$$

where C_o is the initial COD value (mg/L). The separation factor determines the nature of the adsorption process as unfavorable ($R_L > 1$), favorable ($0 < R_L < 1$), linear ($R_L = 1$), or irreversible ($R_L = 0$) (Nigussie et al. 2007).

The isotherms were determined for varying initial CODs of the wastewater solution (150 mL) at the following conditions: pH = 4.2, H_2O_2 loading = 0.71 M, equilibrium time = 60 min.

2.2.7 Toxicity analysis

The relative reduction in wastewater toxicity was analyzed by seed toxicity test as reported in previous literature Kumar et al. (2022). The seeds used in this study were of the *Vigna radiata* (K-851) genre. The seeds were washed with 1% sodium hypochlorite (NaOCl) solution to prevent fungus growth. The seeds were then rinsed in deionized water to remove minuscule dust particles. The experiment was carried out on a 24-well plate. Ten seeds were germinated in a 24-well plate with deionized water (blank), before treatment (control), and after treatment (test) as the medium. The seeds were then incubated for three days in a dark environment, followed by four days at ambient temperature with a 16-hour photoperiod. Following incubation, the number of seeds germinating in each sample was determined as the experiment's response.

Table 2.4. Central composite design matrix and observed/predicted values for %COD removal

Run	Adsorbent dose (X_1), g/L	pH (X_2) (-)	H_2O_2 dose (X_3), M	%COD removal (Exp.)	%COD removal (Pred.)
1	0.2	6	0.28	93.25	92.51
2	0.2	6	0.85	90.77	94.51
3	0.06	6	0.85	85.76	85.29
4	0.2	6	0.85	90.75	94.51
5	0.2	6	0.85	95.45	94.51
6	0.06	2	1.42	74.38	76.26
7	0.06	2	0.28	79.97	81.21
8	0.06	10	0.28	50.74	49.58
9	0.2	6	0.85	95.57	94.51
10	0.2	10	0.85	57.35	62.07
11	0.34	2	0.28	83.98	85.99`
12	0.2	6	0.85	94.97	94.51
13	0.2	2	0.85	97.98	91.16
14	0.34	2	1.42	79.35	81.03
15	0.06	10	1.42	54.72	53.23
16	0.2	6	0.85	95.35	94.51
17	0.34	10	1.42	55.19	54.47
18	0.34	10	0.28	52.19	50.84
19	0.34	6	1.42	93.2	91.85
20	0.34	6	0.85	89.94	88.31

2.3 Results and Discussion

2.3.1 Characterization of Fe_3O_4@AC nanocomposite

X-ray diffractograms were used to investigate the phase purity and crystallinity of the AC, Fe_3O_4 native particles, and Fe_3O_4@AC nanocomposite before and after the experiment. XRD analysis was performed at 25 °C (λ = 1.54) in the 10-80^o (2θ) range. The XRD patterns shown in Fig. 2.3 confirm the synthesis of Fe_3O_4@AC composite and the crystalline nature of the composite. The untreated activated carbon displayed two broad peaks at 25° and 44° indicative of amorphous materials. The sharp peak at 26.1° corresponding to the (0 0 2) plane confirms the presence of a highly graphitized percentage. However, when compared to the pure AC, the (0 0 2) peak for Fe_3O_4@AC is sharper with reduced intensity (Fig. 2.3). According to JCPDS (No. 19-0629), the sharp peaks at 2θ values of 30.07 (2 2 0), 35.44 (311), 43.15 (4 0 0), 54.6 (4 2 2), 56.99 (5 1 1), and 62.6 (4 4 0) are related to the cubic phase Fe_3O_4. The X-ray diffractogram of Fe_3O_4@AC comprises all the above-mentioned peaks, as seen in Fig. 2.3. Moreover, there is no appreciable change in the fundamental AC and Fe_3O_4 diffraction peaks, suggesting no discernible damage was done to the AC and Fe_3O_4 framework during the nanocomposite formation. This reaffirms the deposition of the Fe_3O_4 nanoparticles on the AC surface. The XRD patterns of Fe_3O_4@AC nanocomposite after completion of sonication treatment also show all of the above peaks, albeit with some reduced intensity. This indicates no significant alteration of the structure and composition of the nanocomposite during treatment and confirms its reusability in successive treatment cycles.

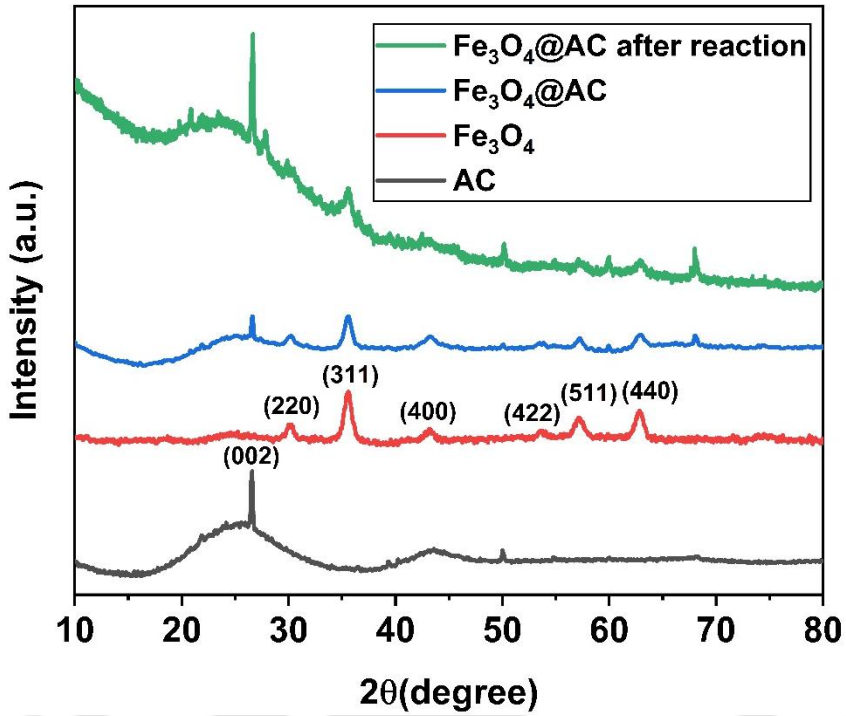

Figure 2.3. XRD patterns of AC, Fe_3O_4 nanoparticles, and Fe_3O_4@AC nanocomposite before and after the reaction

The VSM magnetization curves of Fe_3O_4 and Fe_3O_4@AC nanoparticles at ambient temperature in a ±15 kOe magnetic field are shown in Fig 2.4. Very high magnetization saturation (83.32 emu/g) was attained for Fe_3O_4, whereas for Fe_3O_4@AC, the saturation declined to 72.80 emu/g. This can be ascribed to the inclusion of Fe_3O_4 nanoparticles in the surface texture of non-magnetic AC. Nonetheless, the saturation magnetization value of Fe_3O_4@AC nanocomposite is still sufficient for magnetic separation of the nanocomposites. Additionally, it was noted that the catalyst demonstrated a strong magnetic response when positioned close to a magnet (inset Fig. 2.4).

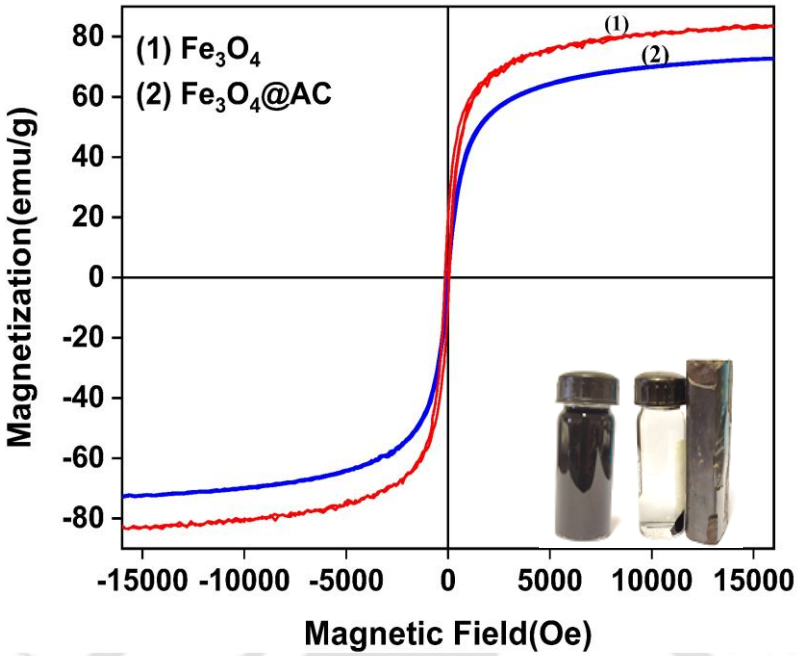

Figure 2.4. Magnetization vs. applied magnetic field for Fe_3O_4 and Fe_3O_4@AC

The Brunauer-Emmett-Teller (BET) technique was used for specific surface area, volume, and average pore diameter of the activated charcoal, Fe_3O_4 nanoparticles, and Fe_3O_4@AC nanocomposite. The N_2 adsorption-desorption curves for the Fe_3O_4 nanoparticles and Fe_3O_4@AC nanocomposite at 77.3 K are shown in Fig. 2.5. The N_2 adsorption/desorption isotherms of mesoporous Fe_3O_4 nanoparticles and Fe_3O_4@AC nanocomposite are of type IV, as illustrated in Fig. 2.5, and the hysteresis loops between the adsorption and desorption curves at a medium relative pressure demonstrate the high quality of mesoporous materials (Babaei et al. 2017).

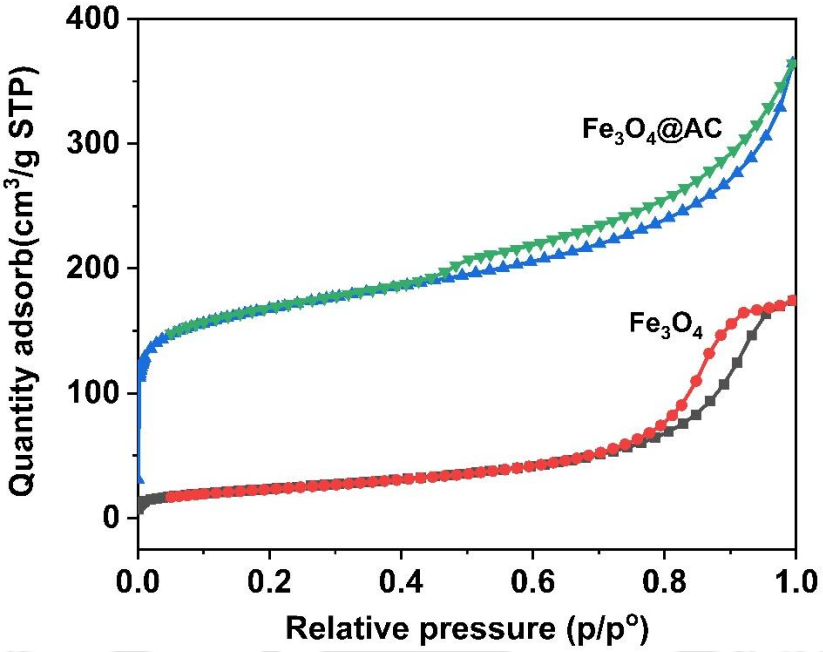

Figure 2.5. Nitrogen adsorption-desorption isotherm plot of Fe_3O_4 and Fe_3O_4@AC

The results of the BET analysis are given in Table 2.5. Fe_3O_4 and Fe_3O_4@AC nanocomposite structures were typically mesoporous and represented by an isotherm type IV (Jonidi Jafari et al. 2017b). The specific surface area of activated charcoal (605.35 m^2/g) reduces after forming the Fe_3O_4@AC nanocomposite (538.88 m^2/g). This observation is in concurrence with previous literature Mohseni-Bandpi et al. (2015). This result could be a consequence of blockage of some of the active sites and pores of activated charcoal due to the deposition of the Fe_3O_4 particles with a significantly smaller surface area (85.32 m^2/g). According to the IUPAC classification, the average pore diameters of the three adsorbents were 2 – 50 nm, placing them in the mesopores category (Mohan et al. 2011). The previous authors have also synthesized Fe_3O_4@AC with surface areas of 572.6 m^2/g, Babaei et al. (2017) 210.95 m^2/g, Sharifi et al. (2022) and 473 m^2/g, Duan et al. (2020) respectively.

Table 2.5. Textural characteristics of AC, Fe_3O_4, and Fe_3O_4@AC

Sample	BET surface area (m^2/g)	Pore volume (cm^3/g)	Average pore diameter (nm)	Pore structure
AC	605.35	0.55	3.66	Mesoporous
Fe_3O_4	85.32	0.27	12.55	Mesoporous
Fe_3O_4@AC	538.88	0.55	4.08	Mesoporous

The surface functional groups of the Fe_3O_4@AC before and after the wastewater treatment process were examined using FTIR spectroscopy, and the results are shown in Fig. 2.6. The broad peak in the range 3250-3750 cm^{-1} can be attributed to the stretching vibration of the hydroxyl (-OH) group (Mahapatra et al. 2012; Bagheri et al. 2017). The peaks at 3435, 1725, 1629, 1373, and 1213 cm^{-1} correspond to the O-H stretching, C=O stretching, C=C stretching, CH_3 in-phase bending, and C-C vibration mode, respectively, demonstrating the existence of activated charcoal in the magnetic nanocomposite (Priyan V et al. 2022; Sharifi et al. 2022). In addition, the FTIR spectrum of Fe_3O_4@AC nanocomposite before treatment showed a strong and overlapped peak at 570.34 cm^{-1}, corresponding to the Fe-O bond vibration in Fe_3O_4 present in the nanocomposite (Bagheri et al. 2017; D'Cruz et al. 2020). The intensities of the bands dropped following the wastewater treatment that involves adsorption and the Fenton process. A new broad and strong band developed at 3420 cm^{-1}, which can be attributed to -OH stretching caused by adsorbed water or hydroxyl groups. Additional peaks are seen at 1561.13 cm^{-1} and 1168.87 cm^{-1}. The formation of new peaks and the elimination of previous ones indicate possible interactions of the Fe_3O_4@AC nanocomposite with the Fenton reagent.

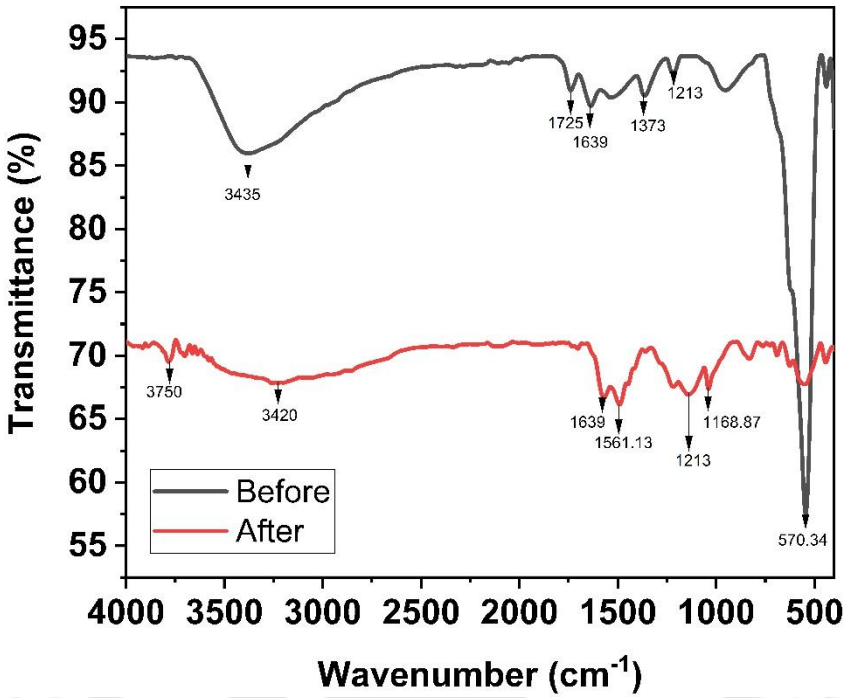

Figure 2.6. FTIR spectra of Fe_3O_4@AC before and after the reaction

FESEM studied the surface morphologies of activated carbon, Fe_3O_4, and Fe_3O_4@AC nanocomposite, and the micrographs are displayed in Fig. 2.7(a-c). The surface of the AC is visibly smooth and has a layered structure, whereas the surface of the Fe_3O_4@AC nanocomposite is somewhat rough due to the impregnation of iron oxide. The size of the Fe_3O_4@AC nanocomposite was measured as less than 34±1 nm (inset of Fig. 2.7(c)). FETEM micrograph shows a uniform distribution of Fe_3O_4 nanoparticles on the surface of AC (Fig. 2.7(d)). The Fe_3O_4@AC nanocomposite's selected area diffraction (SAED) pattern, as depicted in Fig. 2.7(e), suggests that the composite is polycrystalline. The SAED pattern of the composite revealed the Fe_3O_4 planes (2 2 0), (3 1 1), (4 0 0), and (4 2 2) that may be correlated to the X-ray diffractograms discussed in the preceding section. The high-resolution TEM images (HR-TEM) of the Fe_3O_4@AC nanocomposite Fig. 2.7(f) indicate a fringe spacing of ~ 0.24 nm.

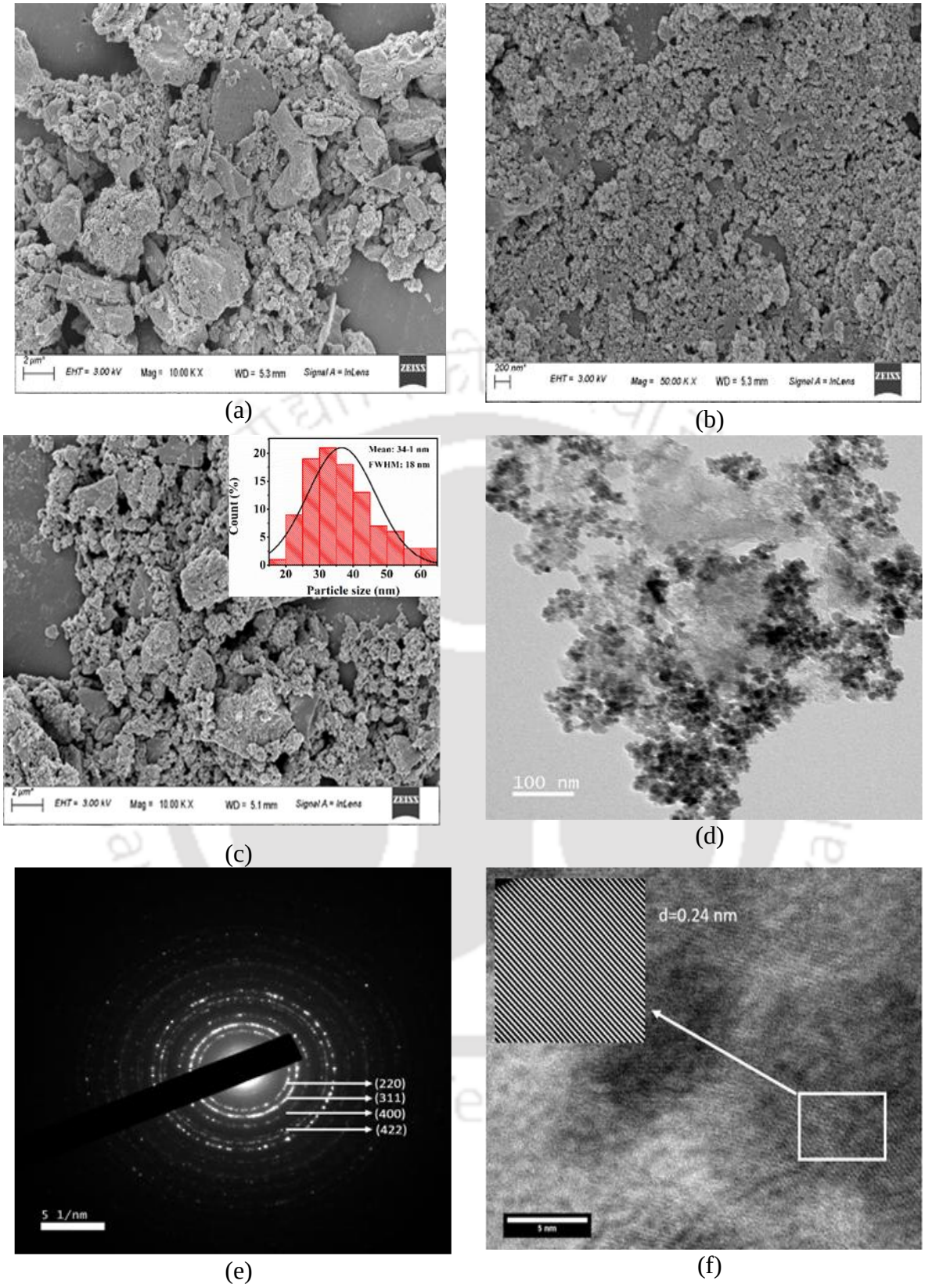

Figure 2.7. SEM images of (a) AC, (b) Fe_3O_4 nanoparticles, and (c) Fe_3O_4@AC nanocomposite; (d) FE-TEM image of Fe_3O_4@AC (e) SAED pattern of Fe_3O_4@AC nanocomposite and (f) HR-TEM of nanocomposite

Energy dispersive X-ray spectroscopy (EDX), in conjunction with FESEM, was used to characterize the elemental composition of the Fe_3O_4@AC. According to the findings of the EDX examination (Table 2.6), the Fe_3O_4@AC nanocomposite contains 82.2% carbon, 9.8% oxygen, and 8.1% iron, suggesting that iron and oxygen were the primary components of the coating. Additionally, the EDX spectra of the nanocomposite Fig. 2.8 show no distinctive impurity peaks, which indicates excellent purity of the Fe_3O_4@AC nanocomposite.

Table 2.6. EDX elemental composition of Fe_3O_4 and Fe_3O_4@AC nanocomposite

Sample	C (wt%)	Fe (wt%)	O (wt%)
Fe_3O_4	-	74.8	25.2
Fe_3O_4@AC	82.2	8.1	9.7

2.3.2 Results of Central Composite Design for wastewater treatment

The result of the central composite design (CCD) of experiments for wastewater treatment using three process parameters, viz. adsorbent dose (X_1), pH (X_2), and H_2O_2 loading (X_3), as optimization variables, are shown in Table 2.3. The second-order polynomial equation correlating the response variable (removal percentage of COD) to the optimization variables is expressed as:

$$\%\text{COD removal} = 54.56 + 1298X_1 + 9.31X_2 + 1.72X_3 - 19268X_1^2 - 1.118X_2^2 - 0.583X_3^2 - 11.0X_1X_2 - 0.1X_1X_3 + 0.269X_2X_3 \quad (2.12)$$

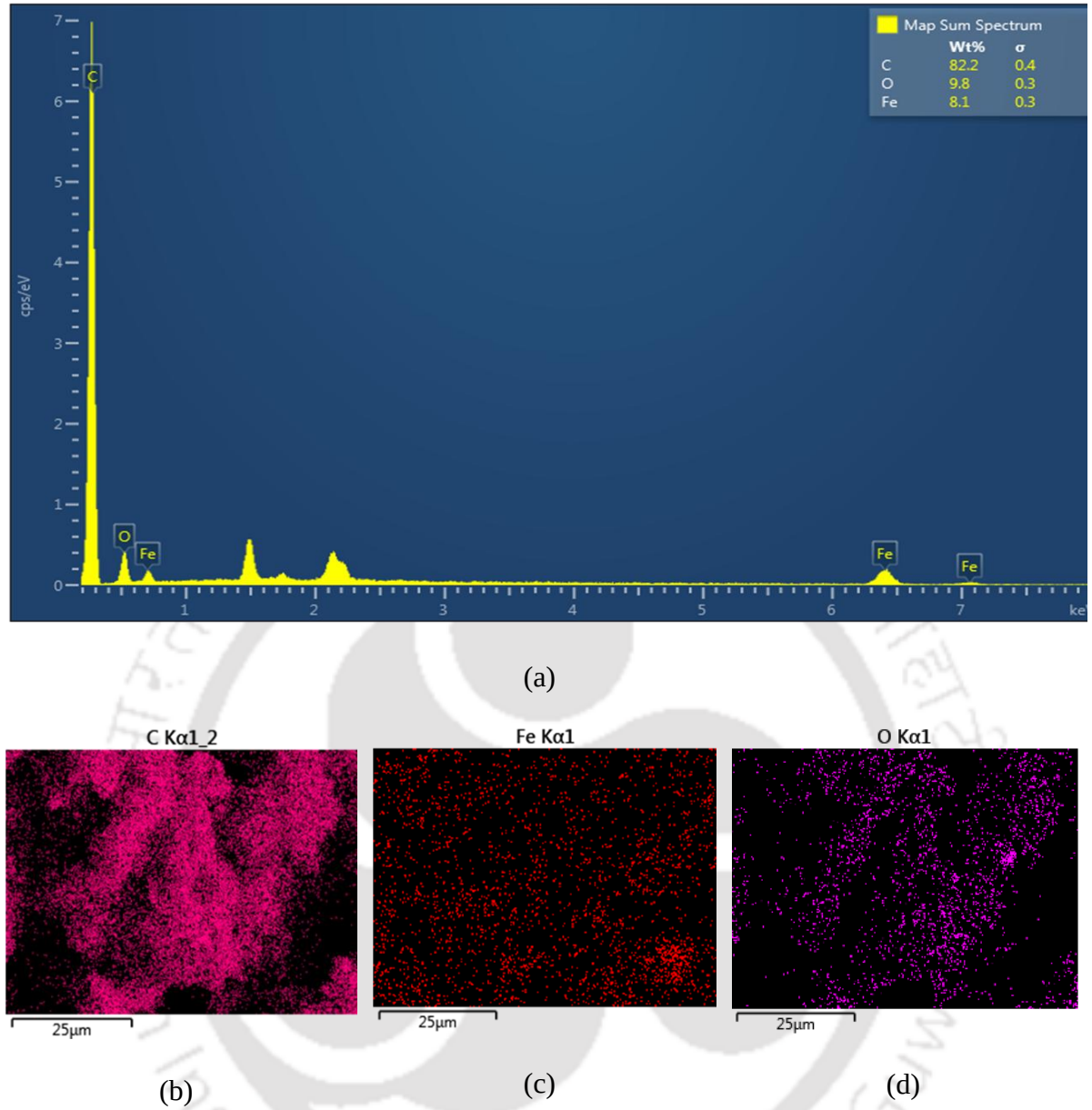

Figure 2.8. (a) EDX spectra of Fe_3O_4@AC nanocomposite and (b-d) Elemental mapping of Fe_3O_4@AC nanocomposite

The statistical design of experiments predicted the following set of parameters for maximum COD removal of 94.75%: pH = 4.2, adsorbent dose = 0.34 g/L, and H_2O_2 loading = 0.71 M. The analysis of variance (ANOVA) for the CCD experimental design is given in Table A2.1 in the Appendix (A2). ANOVA shows a high *F*-value (47.86) and very low *p*-value (< 0.0001) for the overall model, which is indicative of the best fit of the model. Regarding the influences

of individual parameters on response variables, only pH has a *p*-value < 0.0001 that indicates its significance. The other two variables (adsorbent dose and H_2O_2 loading) have *p*-values of 0.204 and 0.773, indicating their insignificance within the ranges or levels used in the experimental design. Interestingly, all the binary coefficients (X_1X_2, X_1X_3, and X_2X_3) also have large *p*-values indicating their insignificance. This means that within the ranges used in the statistical experimental design, the optimization variables have an almost independent influence on the response variables, and interaction among them is negligible. Section A2.1 (Appendix A2) represents the RSM 3D surface plot and desirability plot for a better understanding of the interaction between the variables.

2.3.3 Physical explanation of results of statistical experimental design

A plausible explanation for these results can be given as follows: pH influences the process of degradation and mineralization in various ways: (1) The Fenton reactions are affected by the pH of the solution. The Fe^{2+}/Fe^{3+} conversion is most favored in the pH range of approx. 3 to 4. Higher pH can lead to precipitation of Fe^{3+} as FeO(OH), whereas the reactivity of Fe^{2+} is slowed down at lower pH; (2) The oxidation potential of the OH radicals also reduces at higher pH (2.65 to 2.8 eV at pH 3 and 1.9 eV at pH 7) Rodrigues et al. (2017); (3) The adsorption of the pollutant molecules on the activated charcoal is also influenced by the pH. At low pH, the surface of the activated charcoal containing oxygen groups will be protonated or positively charged. If the pollutant molecules in the wastewater are anionic, they could have either a negative charge or be in molecular form if their pKa > pH. These factors render pH as the significant variable influencing the %COD removal and mineralization process.

Both adsorbent dose and H_2O_2 loadings have been revealed to be insignificant variables in the treatment process. To explain this result, we would like to take an OVAT (one-variable-at-a-

time) approach. Consider the following results extracted from Table 4: (1) Adsorbent dose = 0.06 g/L, pH = 2, H_2O_2 loading = 0.28 M, % COD removal = 79.97%, and (2) Adsorbent dose = 0.34 g/L, pH = 2, H_2O_2 loading = 0.28 M, % COD removal = 83.98%. A 5-fold rise in adsorbent dose resulted in a 4% rise in COD removal. Similarly, consider the following results extracted from Table 3: (1) Adsorbent dose = 0.2 g/L, pH = 6, H_2O_2 loading = 0.28 M, % COD removal = 93.25%; (2) Adsorbent dose = 0.2 g/L, pH = 6, H_2O_2 loading = 1.42 M, % COD removal = 93.2%. In this case, a negligible change in %COD removal is seen with a 5-fold rise in H_2O_2 loading.

A rise in the adsorbent dose would increase the area for adsorption for the pollutant molecules, and the amount of Fe^{2+}/Fe^{3+} ions leached into the solution from the surface of Fe_3O_4 nanoparticles. Similarly, a rise in H_2O_2 loading is expected to increase not only the rate of Fenton reactions but also the scavenging of the $^{\bullet}OH$ radicals through reactions:

$$^{\bullet}OH + H_2O_2 \longrightarrow HO_2^{\bullet} + H_2O \qquad (2.13)$$

$$HO_2^{\bullet} + {}^{\bullet}OH \longrightarrow H_2O + O_2 \qquad (2.14)$$

A minuscule rise in %COD removal with 5× rise in the adsorbent dose and H_2O_2 loading could be a consequence of the following causes:

(1) Due to the very large surface area (538 m^2/g) of the mesoporous Fe_3O_4@AC adsorbent, effective adsorption of the pollutant molecules is achieved with a minimal quantity of 0.06 g/L of adsorbent. In addition, intense microconvection generated by sonication causes effective mass transfer (adsorption/desorption) through the mesopores of the Fe_3O_4@AC adsorbent. This contributed to the effective utilization of the surface area of the adsorbent. Thus, any further increase in adsorbent dose is not manifested in a marked rise in the extent of %COD removal.

(2) As the Fenton reactions occur on the surface of the Fe_3O_4@AC adsorbent, where the pollutant molecules are adsorbed, the probability of the interactions between $^{\bullet}OH$ radicals and the pollutant molecules is relatively high. Thus, most radicals are utilized for oxidative degradation of the pollutants – instead of recombining and/or being scavenged by the excess H_2O_2 in the bulk solution. Thus, a 5-fold increase in H_2O_2 loading also does not result in any marked rise in %COD removal.

2.3.3.1 Validation experiment

A validation experiment was performed (in triplicate to ensure reproducibility of results) for the wastewater treatment using the ternary AOP at the optimum conditions predicted by the statistical design of experiments (adsorbent dose = 0.34 g/L, pH = 4.2, H_2O_2 loading = 0.71 M). The results of this experiment are shown in Fig. 2.9(a). The %COD removal at optimum conditions was 94.75%, which is in close agreement with the predicted value of 92.32% by the statistical design. The TOC removal for these conditions was 89%. The time profiles of the oxidant (H_2O_2) were also monitored, and the results are given in Fig. 2.9(b). It could be seen that the entire H_2O_2 is consumed during the 60 min treatment.

Confirmation of the synergistic effects in the ternary hybrid AOP: For confirmation of the hypothesis of synergistic interactions in the ternary AOP used in the present study, we performed several blank experiments (at optimum values of all parameters determined in the statistical design of experiments) as follows: (1) mere sonication of wastewater; (2) sonication with the addition of H_2O_2 (0.71 M); (3) sonication with 0.71 M H_2O_2 and 4 mg Fe_3O_4 particles in native (or freely suspended) form; (4) stirring (300 rpm) with the addition of 41 mg activated charcoal; (5) stirring (300 rpm) with the addition of 50 mg of Fe_3O_4@AC nanocomposite. The quantities of Fe_3O_4 particles and activated charcoal were determined based on the percentage composition of C (82.2%) and Fe (8.1%) in the nanocomposite, as revealed by the EDX

analysis shown in Fig. 2.8. The volume of wastewater used in all blank experiments was 150 mL and the time of treatment was 60 min. The results of the blank experiment are shown in Fig. 2.9(c). The COD removal with mere sonication was 18.9%, which increased to 30.75% with the addition of H_2O_2. Further addition of 4 mg of Fe_3O_4 nanoparticles – which triggered the Fenton reactions – enhanced the COD removal to 35.8%.

On the other hand, adding activated charcoal to the wastewater resulted in 20.19% COD removal, while adding Fe_3O_4@AC nanocomposite augments the COD removal to 45.75%. It should be noted that the blank experiments with sonication involve the removal of pollutants by oxidative degradation (leading to mineralization). In contrast, the experiments with stirring involve the removal of contaminants through adsorption (not leading to mineralization). Comparison of the results of all blank experiments with the results of the validation experiment (COD removal = 94.75%, TOC removal = 89%) essentially confirms the hypothesis of synergistic interactions among individual processes of adsorption, sonication, and Fenton reactions (stated in the Introduction section) that lead to enhanced COD removal with complete mineralization of the pollutants, as indicated by TOC removal.

2.3.4 Determination of adsorption behavior of the Fe_3O_4@AC nanocomposites

We also assessed the adsorption behavior of the Fe_3O_4@AC nanocomposite at the optimum conditions of %COD and TOC removal. Fig. 2.10(a) shows the time profile of adsorption of pollutants onto 0.05 g Fe_3O_4@AC added to 150 mL of the solution at a pH of 4.2 in the presence of 20 kHz sonication at 40% theoretical power. The adsorption profile was fitted to the pseudo 1^{st} order, pseudo 2^{nd} order, and intraparticle diffusion model (Fig. 2.10(a)) kinetic model. The data was also fitted to Langmuir and Freundlich adsorption isotherm (Fig. 2.10(b)) after determining the q_e and C_e values. The results of this analysis are depicted in Table 2.7. It can

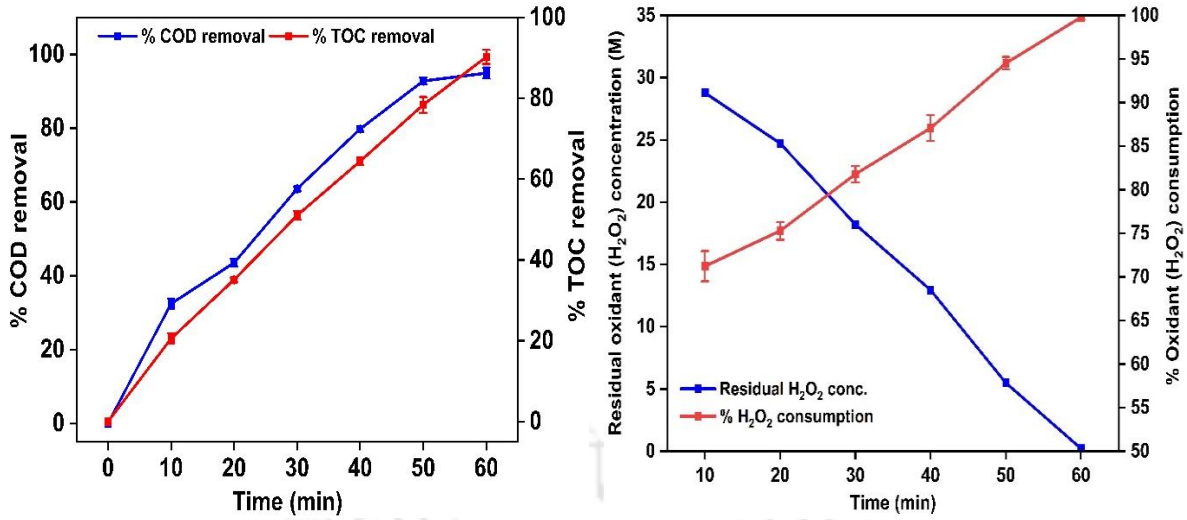

(a) (b)

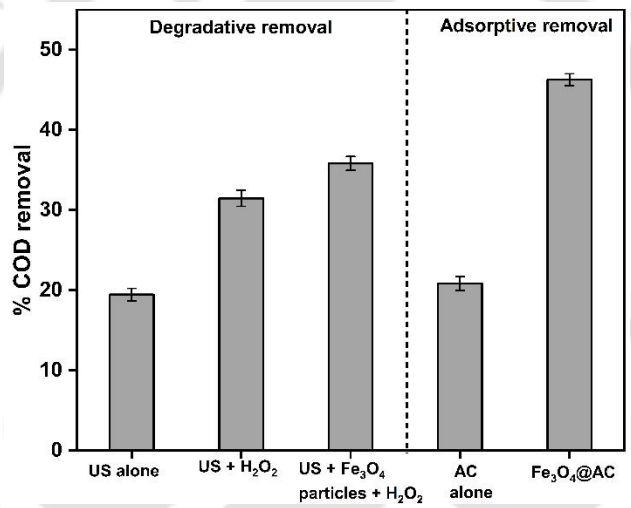

(c)

Figure 2.9. Results of validation experiment: (a) Time profile of %COD and % TOC removal using Fe_3O_4@AC nanocomposite, (b) Time profile for H_2O_2 consumption; (c) Results of blank experiments for assessment of synergistic effects in ternary hybrid AOP used in this study

be seen that the adsorption profile of pollutants on the Fe_3O_4@AC nanocomposite is best suited for second-order use. kinetics (R^2 = 0.99) with q_e value of 215.75 mg/g and second order kinetic constant of 0.0523 (g/mg min). The results of this investigation are consistent with those of earlier research that looked at the adsorption of dyes onto different adsorbents (Kaur et al. 2015;

Li et al. 2015). The value of R_L (separation factor) is determined as 0.0016, which indicates a strongly favored isotherm. These results represent the efficacy of the Fe_3O_4@AC nanocomposite for the adsorption of pollutants (Kakavandi et al. 2015). The nature of interactions of pollutants with adsorbent can be identified using FTIR spectra of the Fe_3O_4@AC nanocomposite before and after treatment. A shift of peak at 3435 cm^{-1} to 3420 cm^{-1} after treatment, corresponding to stretching vibrations of O-H, implied the existence of hydrogen bond interactions between the Fe_3O_4@AC adsorbent and pollutant molecules. The peak at 1639 cm^{-1} (attributed to stretching vibration of C=C groups in the aromatic ring) in the spectrum of adsorbent, both before and after treatment, indicated the π-π interactions between pollutant molecules and adsorbent. After treatment, the new peaks at 1168 and 1561 cm^{-1} in the adsorbent spectrum showed some combinations of pollutant molecules and adsorbent through chemisorption.

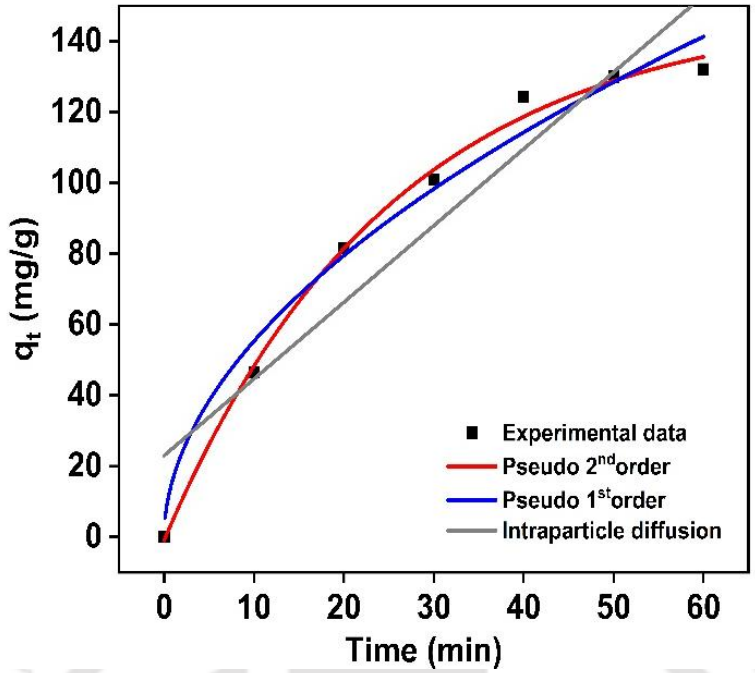

(a)

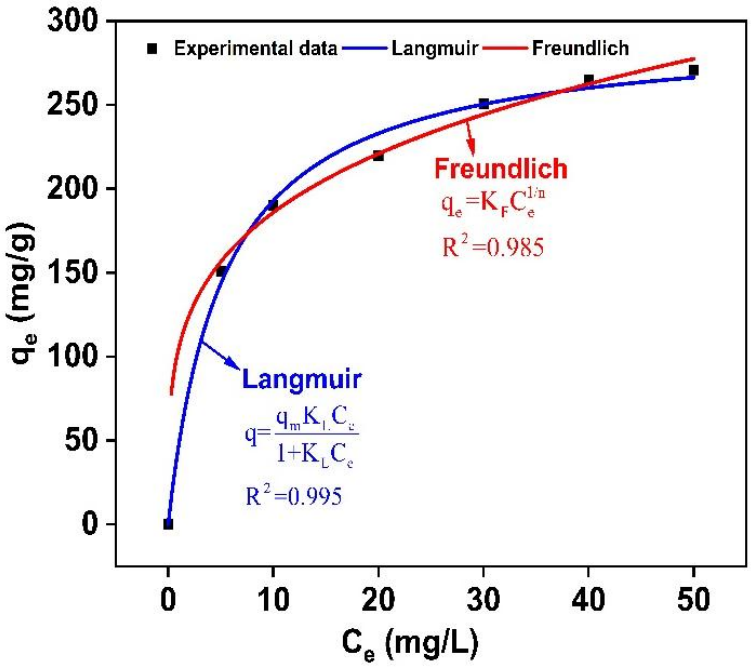

(b)

Figure 2.10. (a) Time profiles of pollutants adsorption on Fe_3O_4@AC nanocomposites and fitting of non-linear adsorption kinetics; (b) Plot of q_e vs. C_e and fitting of non-linear adsorption isotherms on Fe_3O_4@AC nanocomposite (at optimum conditions: adsorbent dose = 0.34 g/L, pH = 4.2 and H_2O_2 loading =0.71 M).

Table 2.7. Adsorption behavior of Fe_3O_4@AC under sonication

Adsorption kinetics	Parameters	Value
Pseudo-first order model	$q_{e,cal}$ (mg/g)	149.72
	k_1 (min^{-1})	0.039
	R^2	0.95
Pseudo- second order model	$q_{e,cal}$ (mg/g)	215.75
	k_2 (g/mg min)	0.0523
	R^2	0.99
	$q_{e,exp}$.(mg/g)	220.78
Intra-particle diffusion model	k_{diff} (mg/g $min^{1/2}$)	2.15
	C (mg/g)	12.32
	R^2	0.89
Langmuir Adsorption isotherm	q_{max} (mg/g)	294.31
	k_L (L/mg)	0.189
	R^2	0.99
	R_L	0.0016
Freundlich Adsorption isotherm	k_F (mg/g) $(mg/L)^{-1/n}$	104.80
	1/n	0.25
	R^2	0.99

A summary of the literature on wastewater treatment using Fe_3O_4@AC nanocomposite as an adsorbent is presented in the Appendix A2 (Table A2.2). The % removal of a particular pollutant or % COD/TOC removal (as applicable) and q_{max} values of the Fe_3O_4@AC adsorbent have been listed in Table A2.2 and compared against those obtained in the present study.

2.3.5 LC-ESI MS/MS analysis of the original and treated wastewater

The chromatograms of wastewater before and after treatment are shown in Fig. 2.11. The list of degraded contaminants (identified from LC-ESI MS/MS analysis) in the original wastewater during the treatment with ternary hybrid AOP technique is listed in Table A2.3 (provided in the Appendix A2). The major organic contaminants which were degraded up to 75 % and more are listed as follows: Arginine 15N (96.42%), Diethatyl-ethyl (93.35 %), Fenthion sulfoxide (92.14%), Di-p-cresyl phosphate (90.86%), Phthalimidoacetic acid (85.46%), Acenaphthylene (85.04%), Ferimzone (82.55%), Haloxyfop-r-methyl (80.78%), Aniline, 5-chloro-2-methyl (80.06%), 2,2',3,3',4,5,5',6-Octachlorobiphenyl (79.91%), Sethoxydim (79.33%), Diacetoxyscirpenol (78.95%), Thiacloprid (77.93%), Trinexapac-ethyl (75.65%) and Fluazifop (75.64%). Most of these contaminants are herbicides and pesticides.

2.3.6 Toxicity of Wastewater

The results of the toxicity experiments, i.e., germination of seeds in deionized water, original wastewater, and treated wastewater, are shown in Fig. 2.12. The number of seeds germinating in each sample was counted as a relative measure of toxicity. It could be seen that all seeds in deionized water grew well. None of the seeds in untreated or original wastewater grew, whereas 60% grew in treated wastewater. This essentially signifies that the relative toxicity of the original wastewater was reduced up to 60% post-treatment using ternary hybrid AOP.

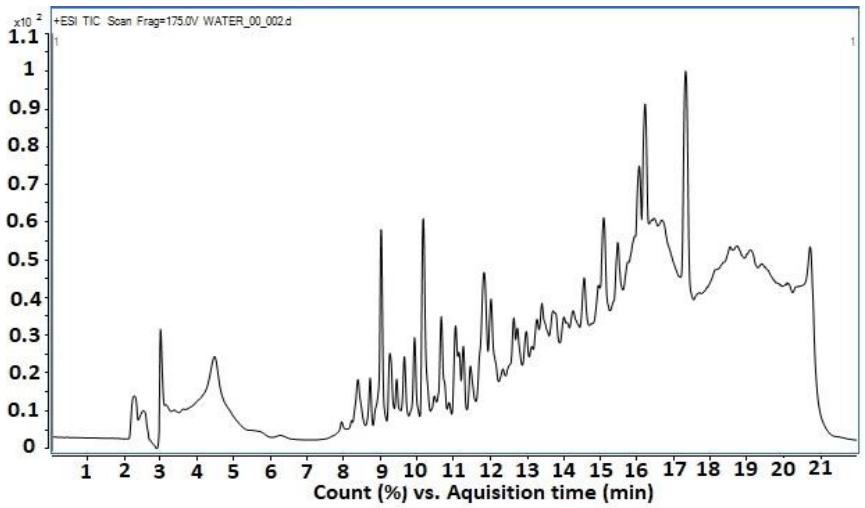

(a)

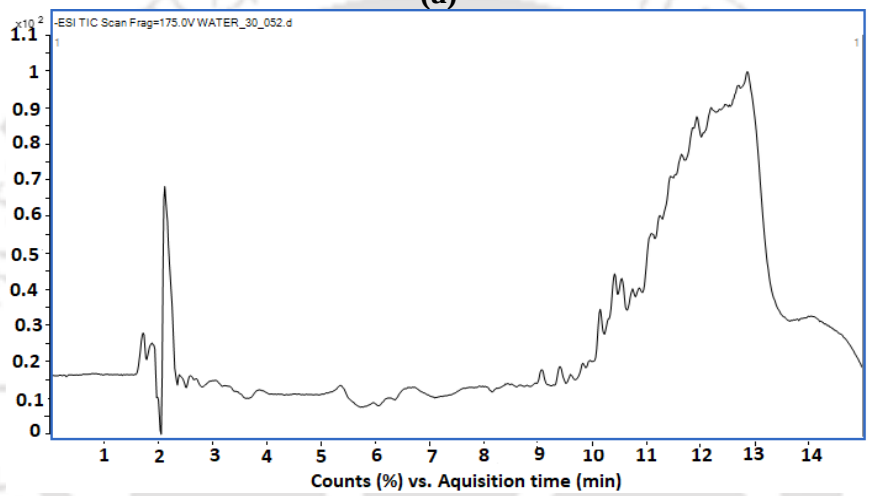

(b)

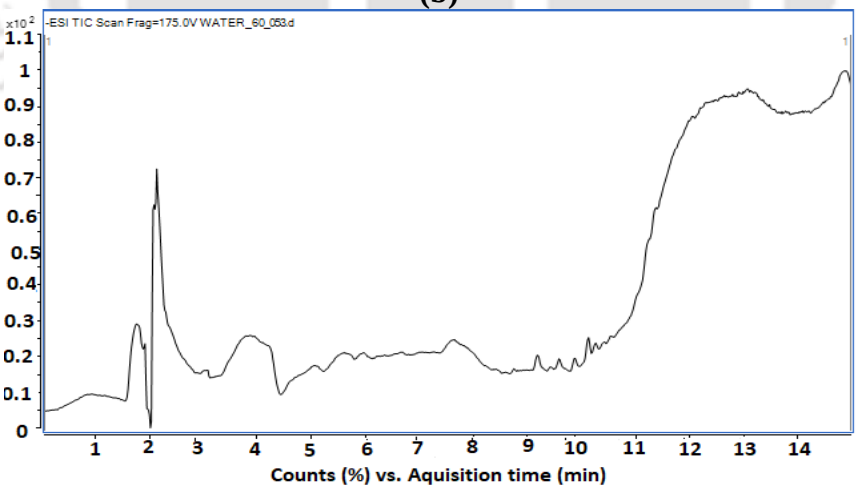

(c)

Figure 2.11. LC-MS chromatogram of (a) original (untreated) wastewater, (b) wastewater after 30 min treatment, (c) wastewater after 60 min treatment

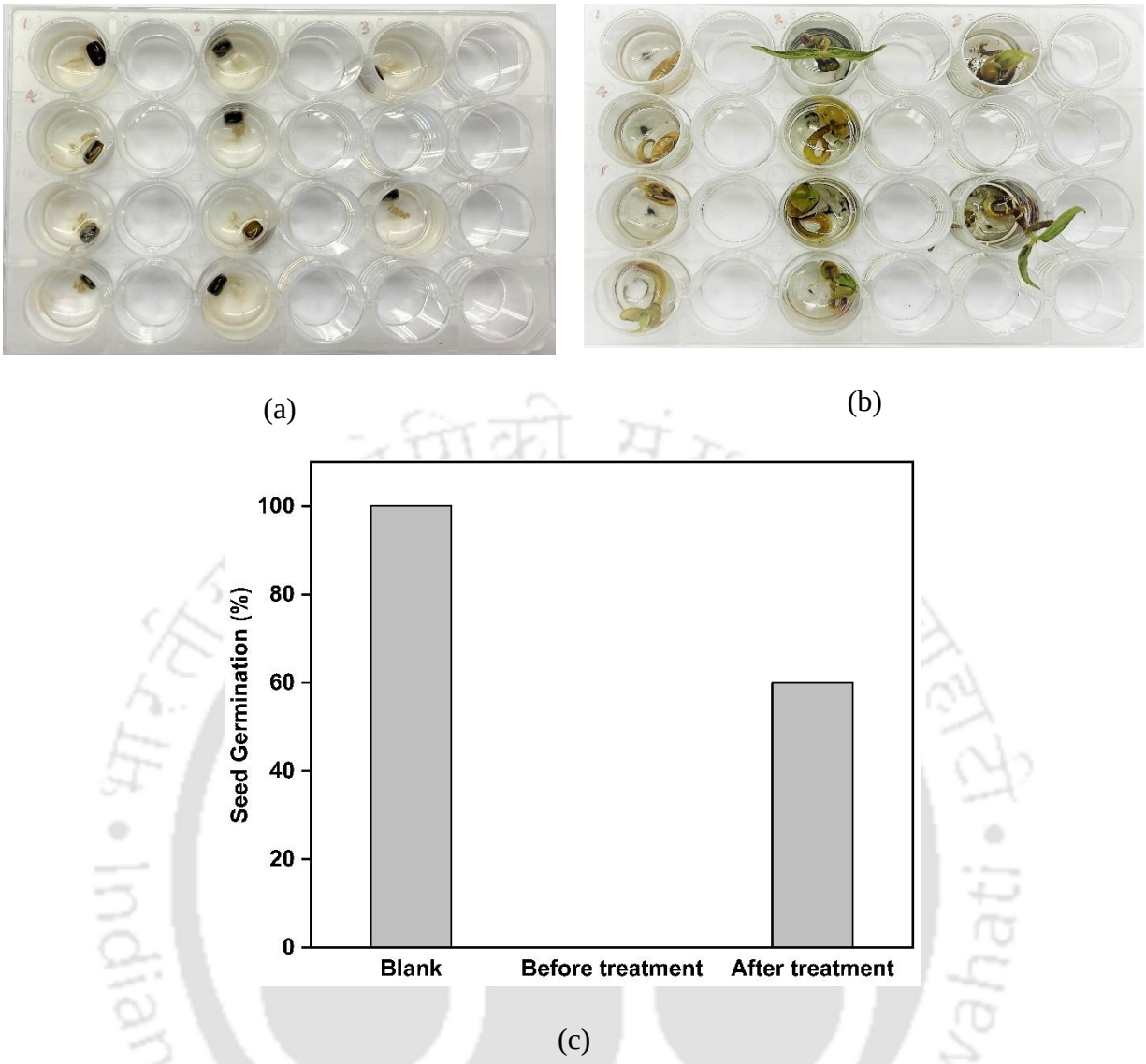

Figure 2.12 Toxicity assay of wastewater using seed germination technique. (a) seed germination in original wastewater, (b) seed germination in wastewater after treatment, (c) assessment of toxicity reduction based on relative seed germination rate.

2.3.7 Reusability and stability of magnetic Fe_3O_4@AC nanocomposite

The recyclability and reusability of the Fe_3O_4@AC nanocomposites were assessed for five consecutive cycles. The recyclability of the nanocomposite was measured as the percentage recovery of the initial nanocomposite added to the solution after the treatment. At the same time, the reusability was evaluated as %COD removal in successive cycles of treatment. In a typical experiment, Fe_3O_4@AC nanocomposite in the solution was collected using a filter

paper (0.25 µm) after the treatment, rinsed multiple times with DI-water, and added to another batch of 150 mL solution for the next cycle of treatment. This cycle was repeated five times. The results of this analysis are shown in Fig. 2.13. It could be seen that the recovery of Fe_3O_4@AC nanocomposite was more than 98 wt% in successive cycles of treatment. This indicates that the Fe_3O_4@AC adsorbent could be easily and effectively recycled. The %COD removal in the first treatment cycle was 94.75%, which reduced to 90% in the fifth cycle. This means that the Fe_3O_4@AC nanocomposite retained its catalytic ability very well through 5 cycles of recovery and recycling.

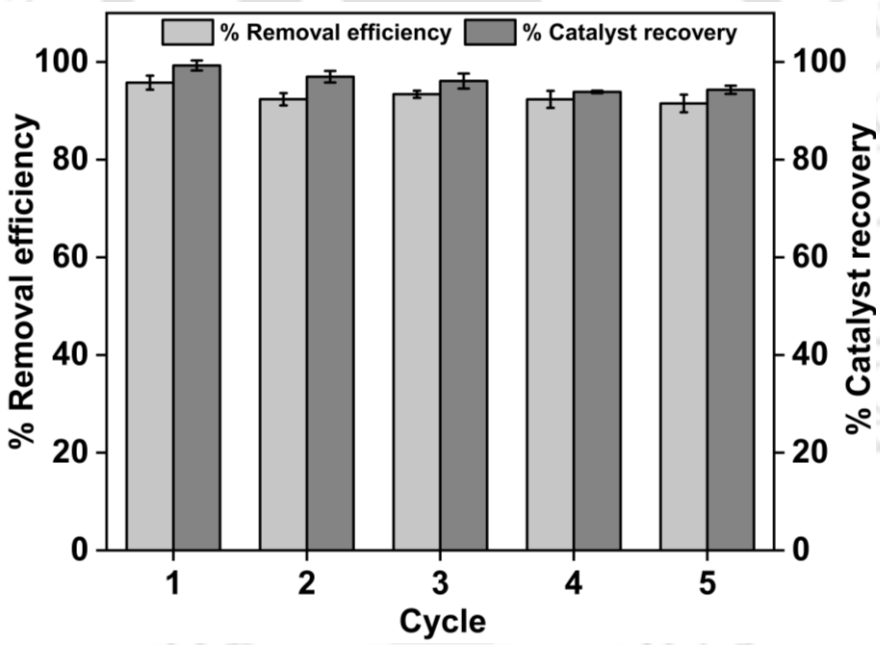

Figure 2.13. Reusability and stability analysis of Fe_3O_4@AC nanocomposite within five successive cycles (under the optimum condition: adsorbent dose = 0.34 g/L, pH =4.2, and H_2O_2 loading=0.71 M).

2.4 Conclusion

This chapter has demonstrated the efficacy of the ternary hybrid AOP of sonication + Fenton + adsorption using the Fe_3O_4@AC nanocomposites to mineralize wastewater from discharge from local industries and academic institutions into a local water body. As much as 94.75% COD removal and 89% TOC removal were achieved in just 1 hour of treatment. LC-MS analysis revealed effective (> 50%) degradation of more than 25 significant contaminants (in the form of herbicides and pesticides) after the treatment with ternary hybrid AOP. Similarly, the toxicity analysis test using the seed germination technique revealed a ~ 60% reduction in the toxicity of the wastewater after treatment. This result is essentially a consequence of synergistic interactions among the adsorption of pollutants onto activated charcoal and surface Fenton reactions induced due to the leaching of Fe^{2+}/Fe^{3+} ions from the Fe_3O_4 nanoparticles. Microconvection generated due to sonication assisted faster mass transport (adsorption/desorption) of pollutants between Fe_3O_4@AC nanocomposite and the solution. The net result of this synergism was high interactions and reactions among $^{\bullet}OH$ and $HO_2^{\bullet}$ radicals and pollutants that resulted in the effective mineralization of wastewater. This synergy is schematically explained in Fig. 2.14. The Fe_3O_4@AC nanocomposites also showed excellent recovery and catalytic activity retention for five consecutive treatment cycles. The ternary AOP presented in this study can also be applied to wastewater discharges from other chemical and process industries.

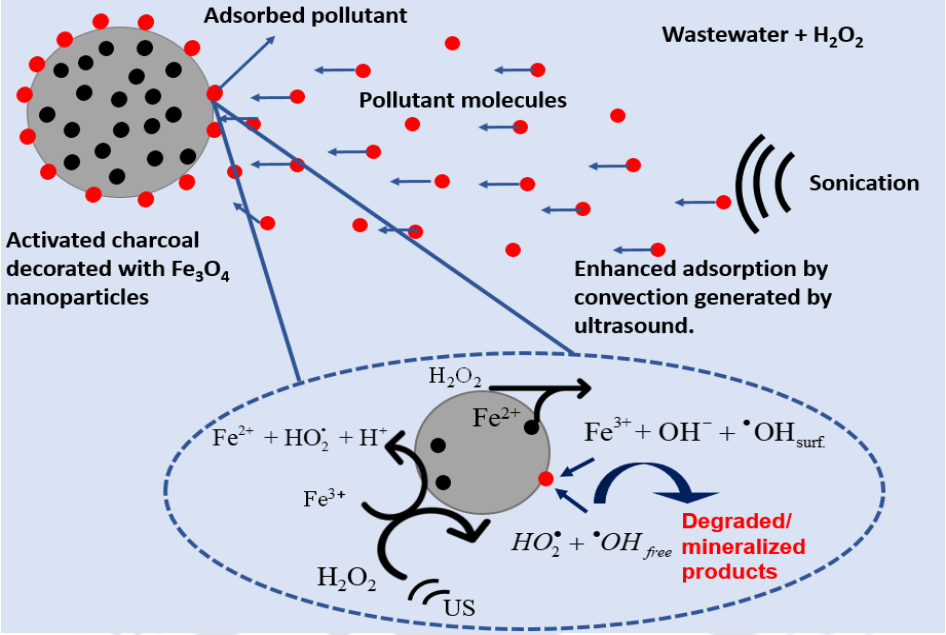

Figure 2.14. Schematic of the synergistic interactions in the ternary hybrid AOP using Fe_3O_4@AC nanocomposite for wastewater treatment

References

Aleboyeh A, Olya ME, Aleboyeh H (2008) Electrical energy determination for an azo dye decolorization and mineralization by UV/H_2O_2 advanced oxidation process. Chem Eng J 137:518–524. https://doi.org/10.1016/j.cej.2007.05.016

Ansari F, Ghaedi M, Taghdiri M, Asfaram A (2016) Application of ZnO nanorods loaded on activated carbon for ultrasonic assisted dyes removal: Experimental design and derivative spectrophotometry method. Ultrason Sonochem 33:197–209. https://doi.org/10.1016/j.ultsonch.2016.05.004

American Public Health Association. (1926). *Standard methods for the examination of water and wastewater* (Vol. 6). American Public Health Association.

Babaei AA, Kakavandi B, Rafiee M, et al (2017) Comparative treatment of textile wastewater by adsorption, Fenton, UV-Fenton and US-Fenton using magnetic nanoparticles-functionalized carbon (MNPs@C). J Ind Eng Chem 56:163–174. https://doi.org/10.1016/j.jiec.2017.07.009

Bagal MV, Gogate PR (2014) Wastewater treatment using hybrid treatment schemes based on cavitation and Fenton chemistry: A review. Ultrason Sonochem 21:1–14. https://doi.org/10.1016/j.ultsonch.2013.07.009

Bagheri AR, Ghaedi M, Asfaram A, et al (2017) Comparative study on ultrasonic assisted adsorption of dyes from single system onto Fe_3O_4 magnetite nanoparticles loaded on activated carbon: Experimental design methodology. Ultrason Sonochem 34:294–304. https://doi.org/10.1016/j.ultsonch.2016.05.047

Bello MM, Raman AAA (2019) Synergy of adsorption and advanced oxidation processes in recalcitrant wastewater treatment. Environ Chem Lett 17:1125–1142. https://doi.org/10.1007/s10311-018-00842-0

Bethi B, Sonawane SH, Bhanvase BA, Gumfekar SP (2016) Nanomaterials-based advanced oxidation processes for wastewater treatment: A review. Chem Eng Process - Process Intensif 109:178–189. https://doi.org/10.1016/j.cep.2016.08.016

Bilinska L, Gmurek M, Ledakowicz S (2015) Application of Advanced Oxidation Technologies for Decolorization and Mineralization of Textile Wastewaters. J Adv Oxid Technol 18:185–194. https://doi.org/10.1515/jaots-2015-0202

Chakma S, Moholkar VS (2013) Physical mechanism of sono-Fenton process. AIChE J 59:4303–4313. https://doi.org/10.1002/aic.14150

Chauhan R, Dinesh GK, Alawa B, Chakma S (2021) A critical analysis of sono-hybrid advanced oxidation process of ferrioxalate system for degradation of recalcitrant pollutants. Chemosphere 277:130324. https://doi.org/10.1016/j.chemosphere.2021.130324

Choudhury BJ, Roy K, Moholkar VS (2021) Improvement of Supercapacitor Performance through Enhanced Interfacial Interactions Induced by Sonication. Ind Eng Chem Res 60:7611–7623. https://doi.org/10.1021/acs.iecr.1c00279

D'Cruz B, Madkour M, Amin MO, Al-Hetlani E (2020) Efficient and recoverable magnetic AC-Fe_3O_4 nanocomposite for rapid removal of promazine from wastewater. Mater Chem Phys 240:122109. https://doi.org/10.1016/j.matchemphys.2019.122109

Duan Z, Zhang W, Lu M, et al (2020) Magnetic Fe_3O_4/activated carbon for combined adsorption and Fenton oxidation of 4-chlorophenol. Carbon 167:351–363. https://doi.org/10.1016/j.carbon.2020.05.106

Gągol M, Przyjazny A, Boczkaj G (2018) Wastewater treatment by means of advanced oxidation processes based on cavitation – A review. Chem Eng J 338:599–627. https://doi.org/10.1016/j.cej.2018.01.049

Ho Y-S (2006) Second-order kinetic model for the sorption of cadmium onto tree fern: A comparison of linear and non-linear methods. Water Res 40:119–125. https://doi.org/10.1016/j.watres.2005.10.040

Ho YS, McKay G (2000) The kinetics of sorption of divalent metal ions onto sphagnum moss peat. Water Res 34:735–742. https://doi.org/10.1016/S0043-1354(99)00232-8

Hsing H-J, Chiang P-C, Chang E-E, Chen M-Y (2007) The decolorization and mineralization of Acid Orange 6 azo dye in aqueous solution by advanced oxidation processes: A comparative study. J Hazard Mater 141:8–16. https://doi.org/10.1016/j.jhazmat.2006.05.122

Jonidi Jafari A, Kakavandi B, Jaafarzadeh N, et al (2017a) Fenton-like catalytic oxidation of tetracycline by AC@Fe_3O_4 as a heterogeneous persulfate activator: Adsorption and degradation studies. J Ind Eng Chem 45:323–333. https://doi.org/10.1016/j.jiec.2016.09.044

Jonidi Jafari A, Kakavandi B, Jaafarzadeh N, et al (2017b) Fenton-like catalytic oxidation of tetracycline by AC@Fe_3O_4 as a heterogeneous persulfate activator: Adsorption and degradation studies. J Ind Eng Chem 45:323–333. https://doi.org/10.1016/j.jiec.2016.09.044

Joshi S (2019) Applications of Fe_3O_4@AC nanoparticles for dye removal from simulated wastewater

Kakavandi B (2016) Application of Fe_3O_4@C catalyzing heterogeneous UV-Fenton system for tetracycline removal with a focus on optimization by a response surface method

Kakavandi B, Jahangiri-rad M, Rafiee M, et al (2016) Development of response surface methodology for optimization of phenol and p -chlorophenol adsorption on magnetic recoverable carbon. Microporous Mesoporous Mater 231:192–206. https://doi.org/10.1016/j.micromeso.2016.05.033

Kakavandi B, Kalantary RR, Jafari AJ, et al (2015) Pb(II) Adsorption Onto a Magnetic Composite of Activated Carbon and Superparamagnetic Fe_3O_4 Nanoparticles: Experimental and Modeling Study. CLEAN – Soil Air Water 43:1157–1166. https://doi.org/10.1002/clen.201400568

Kanafin YN, Makhatova A, Meiramkulova K, Poulopoulos SG (2022) Treatment of a poultry slaughterhouse wastewater using advanced oxidation processes. J Water Process Eng 47:102694. https://doi.org/10.1016/j.jwpe.2022.102694

Kaur S, Rani S, Mahajan RK, et al (2015) Synthesis and adsorption properties of mesoporous material for the removal of dye safranin: Kinetics, equilibrium, and thermodynamics. J Ind Eng Chem 22:19–27. https://doi.org/10.1016/j.jiec.2014.06.019

Kausley SB, Desai KS, Shrivastava S, et al (2018) Mineralization of alkyd resin wastewater: Feasibility of different advanced oxidation processes. J Environ Chem Eng 6:3690–3701. https://doi.org/10.1016/j.jece.2017.04.001

Korpe S, Bethi B, Sonawane SH, Jayakumar KV (2019) Tannery wastewater treatment by cavitation combined with advanced oxidation process (AOP). Ultrason Sonochem 59:104723. https://doi.org/10.1016/j.ultsonch.2019.104723

Kumar A, Patra C, Rajendran HK, Narayanasamy S (2022) Activated carbon-chitosan based adsorbent for the efficient removal of the emerging contaminant diclofenac: Synthesis, characterization and phytotoxicity studies. Chemosphere 307:135806. https://doi.org/10.1016/j.chemosphere.2022.135806

Li C, Zhong H, Wang S, et al (2015) Removal of basic dye (methylene blue) from aqueous solution using zeolite synthesized from electrolytic manganese residue. J Ind Eng Chem 23:344–352. https://doi.org/10.1016/j.jiec.2014.08.038

Liu L, Yang C, Tan W, Wang Y (2020) Degradation of Acid Red 73 by Activated Persulfate in a Heat/Fe_3O_4@AC System with Ultrasound Intensification. ACS Omega 5:13739–13750. https://doi.org/10.1021/acsomega.0c00903

Madhavan J, Theerthagiri J, Balaji D, et al (2019) Hybrid Advanced Oxidation Processes Involving Ultrasound: An Overview. Molecules 24:3341. https://doi.org/10.3390/molecules24183341

Mahapatra K, Ramteke DS, Paliwal LJ (2012) Production of activated carbon from sludge of food processing industry under controlled pyrolysis and its application for methylene blue removal. J Anal Appl Pyrolysis

Mohan D, Sarswat A, Singh VK, et al (2011) Development of magnetic activated carbon from almond shells for trinitrophenol removal from water. Chem Eng J

Mohseni-Bandpi A, Kakavandi B, Kalantary RR, et al (2015) Development of a novel magnetite–chitosan composite for the removal of fluoride from drinking water: adsorption modeling and optimization. RSC Adv 5:73279–73289. https://doi.org/10.1039/C5RA11294J

Nigussie W, Zewge F, Chandravanshi BS (2007) Removal of excess fluoride from water using waste residue from alum manufacturing process. J Hazard Mater 147:954–963. https://doi.org/10.1016/j.jhazmat.2007.01.126

Priyan V V, Kumar N, Narayanasamy S (2022) Toxicological assessment and adsorptive removal of lead (Pb) and Congo red (CR) from water by synthesized iron oxide/activated carbon (Fe_3O_4/AC) nanocomposite. Chemosphere 294:133758. https://doi.org/10.1016/j.chemosphere.2022.133758

Rodrigues CSD, Soares OSGP, Pinho MT, et al (2017) p-Nitrophenol degradation by heterogeneous Fenton's oxidation over activated carbon-based catalysts. Appl Catal B Environ 219:109–122. https://doi.org/10.1016/j.apcatb.2017.07.045

Sharifi N, Nasiri A, Silva Martínez S, Amiri H (2022) Synthesis of Fe_3O_4@activated carbon to treat metronidazole effluents by adsorption and heterogeneous Fenton with effluent bioassay. J Photochem Photobiol Chem 427:113845. https://doi.org/10.1016/j.jphotochem.2022.113845

Sivasankar T, Moholkar VS (2009) Physical insights into the sonochemical degradation of recalcitrant organic pollutants with cavitation bubble dynamics. Ultrason Sonochem 16:769–781. https://doi.org/10.1016/j.ultsonch.2009.02.009

Sivasankar T, Paunikar AW, Moholkar VS (2007) Mechanistic approach to enhancement of the yield of a sonochemical reaction. AIChE J 53:1132–1143. https://doi.org/10.1002/aic.11170

Souza FS, Da Silva VV, Rosin CK, et al (2018) Determination of pharmaceutical compounds in hospital wastewater and their elimination by advanced oxidation processes. J Environ Sci Health Part A 53:213–221. https://doi.org/10.1080/10934529.2017.1387013

Appendix (A2)

Table A2.1. Analysis of variance (ANOVA) for the response surface quadratic model

Source	Degree of freedom	Sum of square	Mean square	*F*-value	*p*-value
Model	9	5293.69	588.19	47.86	<0.0001
X_1	1	22.74	22.74	1.85	0.204
X_2	1	2116.15	2116.15	172.17	<0.0001
X_3	1	1.08	1.08	0.09	0.773
X_1X_1	1	163.36	163.36	13.29	0.004
X_2X_2	1	880.37	880.37	71.63	<0.0001
X_3X_3	1	14.96	14.96	1.22	0.296
X_1X_2	1	6.23	6.23	0.51	0.493
X_1X_3	1	0	0	0	0.998
X_2X_3	1	36.98	36.98	3.01	0.113
Error	10	122.91	12.29		
Lack-of-Fit	5	94.8	18.96	3.37	0.104
Pure Error	5	28.11	5.62		
Total	19	5416.6			
Quality of quadratic model					
R^2				0.983	
Adjusted R^2				0.9676	
Predicted R^2				0.8994	

Section A2.1. RSM 3D surface plot which represents the interaction between response variable to optimized parameters

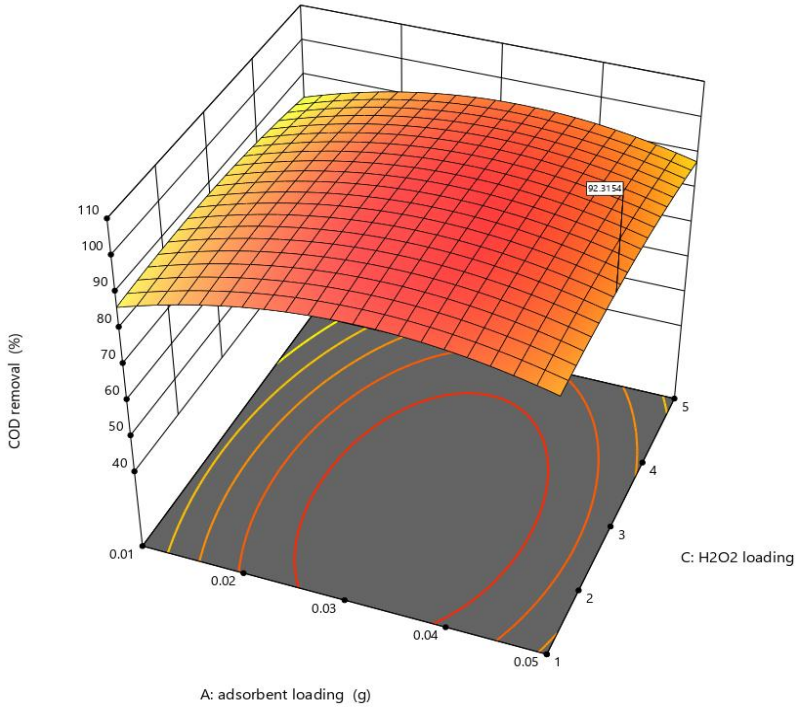

(a)

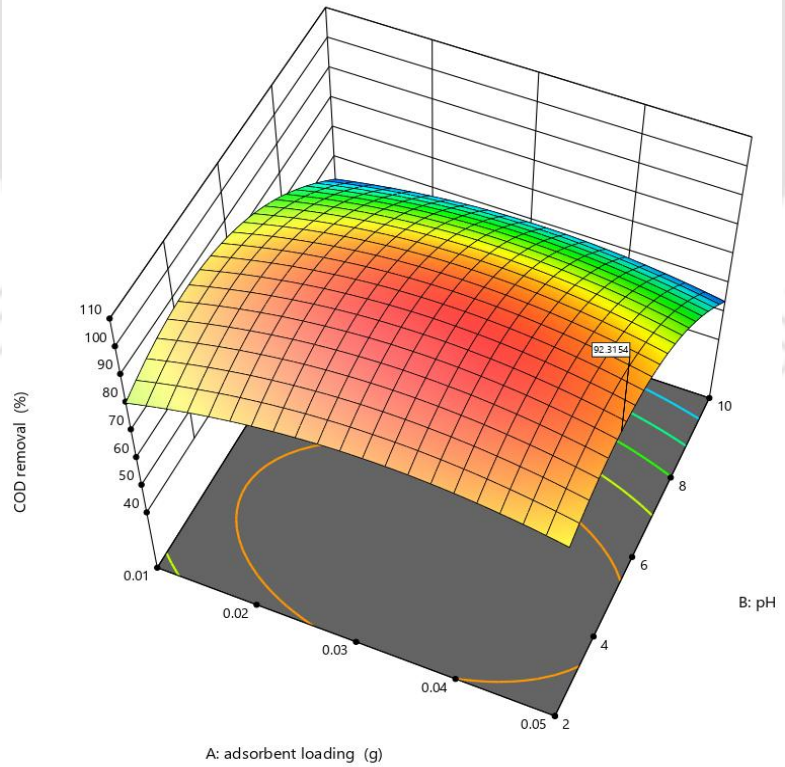

(b)

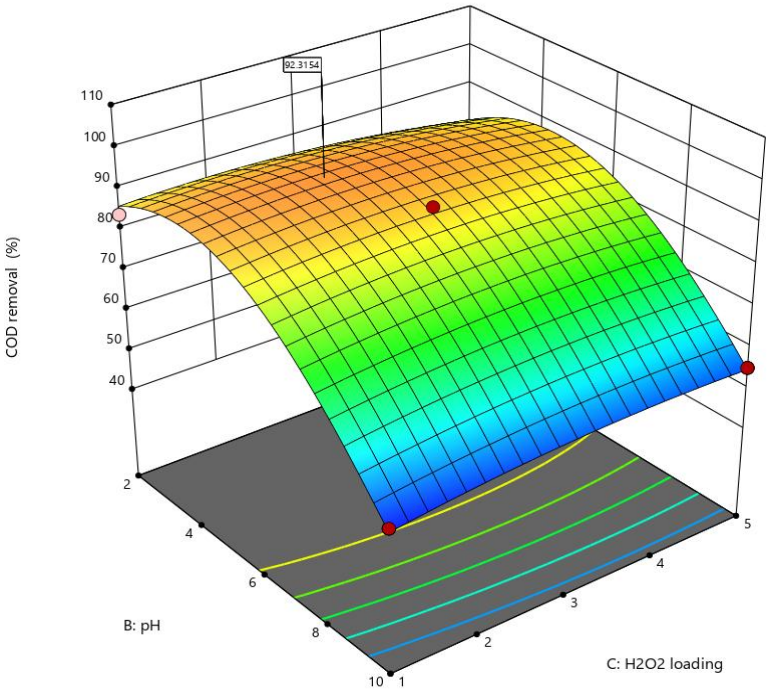

(c)

Desirability plot

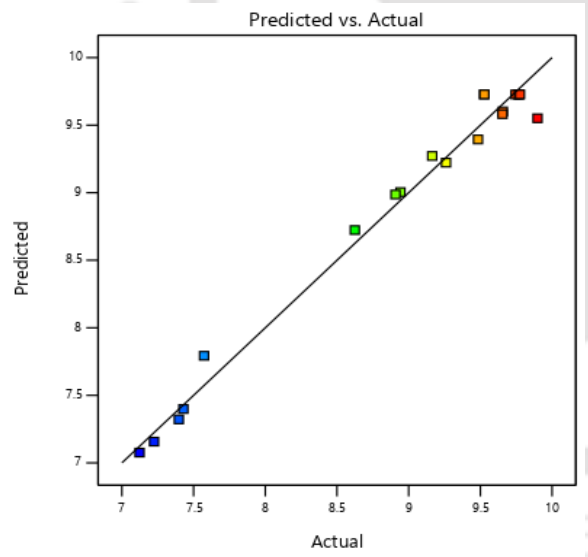

(a)

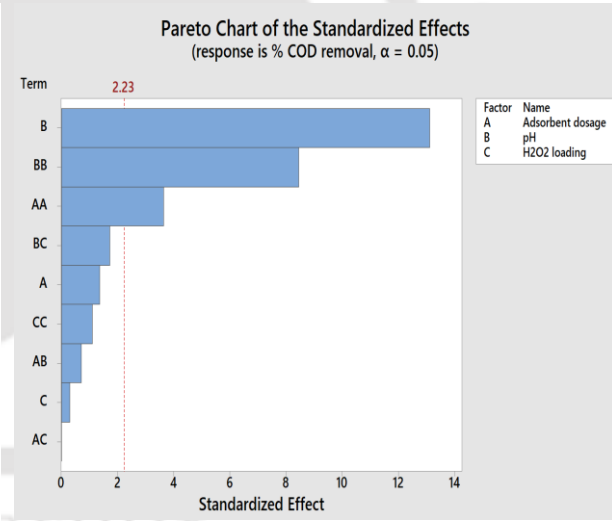

(b)

Table A2.2. Summary of representative literature on wastewater treatments using Fe_3O_4@AC adsorbent

Compound	Experimental condition	% Removal of pollutants	TOC/COD removal	q_{max} (mg/g)	Reference
Industrial WW	Initial COD: 3246 mg/L Initial TOC: 2500 mg/L pH: 4.2, Adsorbent: 0.34 g/L H_2O_2 loading: 0.71 M	**Not applicable**	**89% TOC and 94.75% COD removal**	270.27	**This study**
Tetracycline	Initial [TC]: 30 mg/L pH: 5.5±0.3, PS: 30 mM Fe_3O_4@AC: 0.2 g/L	99.8% TC removal	50.6% TOC removal	158.7	(Jonidi Jafari et al. 2017b)
DR16 dye	Initial conc.: 20-100 mg/L pH: 2±0.3, Fe_3O_4@AC: 1g/L Time: 30 min	99.9 % removal using (UV-fenton)	Not reported	96.15	(Babaei et al. 2017)
Promazine	Initial conc.: 40 mg/L pH: 8.5, Adsorbent: 10 mg	99.97 % removal	Not reported	101.01	(D'Cruz et al. 2020)
Sunset Yellow	Initial conc.: 15 mg/L pH: 4, Adsorbent: 0.04 g	96.63 % removal	Not reported	76.37	(Bagheri 2017)
Metronidazole	Initial conc.: 5-30 mg/L pH: 3-11,	74.75 % removal from real WW;	Not reported	56.18	(Sharifi et al. 2022)

	Adsorbent: 0.1-1 g/L H_2O_2 conc.: 5-30 mmol/L Temp.: 20-60 ^oC, Time: 5-60 min	98.03% removal from synthetic WW			
Ceftriaxone	Initial Conc.: 10-100 mg/L Adsorbent : 1.05-2 g/L pH: 3-11 Temp.: 298-313 K	97.18% removal	Not reported	28.93	(Yegane Badi et al. 2018)
Methylene Blue dye	Initial conc.: 25 mg/L pH: 7, Adsorbent : 0.03 g Time: 30 min, Temp.: 298 K	96.2 % removal	Not reported	384.6	(Ghasemi et al. 2018)

Table A2.3: List of major organic contaminants degraded by a hybrid technique of adsorption (Fe_3O_4@AC nanocomposite) + heterogeneous Fenton + sonication

Compound name	Chemical formula	Retention time (min)	Mass (g/mol)	% Reduction
Arginine 15N	$C_6 H_{14} [15N] N_3 O_2$	9.505	175.11	96.42
Diethatyl-ethyl	$C_{16} H_{22} Cl N O_3$	9.777	311.13	93.35
Fenthion sulfoxide	$C_{10} H_{15} O_4 P S_2$	11.973	294.01	92.14
Di-p-cresylphosphate (DpCP)	$C_{21} H_{21} O_4 P$	1.733	368.12	90.86
Phthalimidoacetic acid	$C_{10} H_7 N O_4$	15.721	205.04	85.46
Acenaphthylene	$C_{12} H_8$	2.692	152.06	85.04
Ferimzone	$C_{15} H_{18} N_4$	3.213	254.15	82.55
Haloxyfop-r-methyl	$C_{16} H_{13} Cl F_3 N O_4$	8.978	375.05	80.78
Aniline, 5-chloro-2-methyl	$C_9 H_9 Cl F_3 N$	3.51	223.04	80.06
2,2',3,3',4,5,5',6-Octachlorobiphenyl (PCB 199)	$C_{12} H_2 Cl_8$	9.779	425.77	79.91
Sethoxydim	$C_{17} H_{29} N O_3 S$	10.121	327.19	79.33
Diacetoxyscirpenol	$C_{19} H_{26} O_7$	3.223	366.17	78.95
Thiacloprid	$C_{10} H_9 Cl N_4 S$	13.957	252.03	77.93
Trinexapac-ethyl	$C_{13} H_{16} O_5$	13.062	252.10	75.65
Fluazifop	$C_{15} H_{12} F_3 N O_4$	2.557	327.07	75.64
Phenkapton	$C_{15} H_{12} N_2 O_2$	2.404	252.09	73.79
Naphthalenol, 1-	$C_{16} H_{11} N_3 O_3$	14.025	293.08	73.56
3,4,4',5-Tetrachlorobiphenyl (PCB 81)	$C_{12} H_6 Cl_4$	2.301	311.91	72.17
DMST (Tolylfluanid metabolite)	$C_9 H_{14} N_2 O_2 S$	9.81	214.08	67.17
Flurtamone	$C_{18} H_{14} F_3 N O_2$	8.117	333.10	67.06
Rimsulfuron	$C_{14} H_{17} N_5 O_7 S_2$	2.29	431.06	65.89
Nicotine-N'-oxide	$C_{10} H_{16} Cl_2 N_2 O$	12.175	250.07	65.80
Ethylaluminum sesquichloride	$C_6 H_{15} Al_2 Cl_3$	11.753	245.99	65.51

Dazomet	$C_5 H_{10} N_2 S_2$	13.946	162.03	63.78
4-Hydroxyphenanthrene	$C_{14} H_{10} O$	7.866	194.08	61.38
Anthracene	$C_{14} H_{10}$	8.5	178.08	53.77
Alachlor	$C_{14} H_{20} Cl N O_2$	12.45	269.12	53.75
Methidathion	$C_6 H_{11} N_2 O_4 P S_3$	20.85	301.96	53.53
Bentazone	$C_{10} H_{12} N_2 O_3 S$	3.354	240.06	52.39
Methacrifos	$C_7 H_{13} O_5 P S$	8.956	240.02	50.24
5-Nitro-o-toluidine	$C_7 H_8 N_2 O_2$	10.757	152.06	49.85
Diethyldithiophosphate (DEDTP)	$C_4 H_{11} O_2 P S_2$	8.903	185.99	49.66
Anthraquinone	$C_{14} H_8 O_2$	2.301	208.06	48.04
Carbophenothion-Methyl	$C_9 H_{12} Cl O_2 P S_3$	20.875	313.95	45.30
Bisphenol AF	$C_{15} H_{10} F_6 O_2$	2.16	336.06	44.98
Methylcholanthrene, 3-	$C_{21} H_{16}$	13.984	268.13	42.41
Dimethipin	$C_6 H_{10} O_4 S_2$	21.011	210.00	40.78
2,6-Dimethylaniline	$C_8 H_{11} N$	9.461	143.07	38.8
Cyhalothrin	$C_{23} H_{19} Cl F_3 N O_3$	8.929	449.11	37.29
4-methylbenzophenone	$C_{14} H_{12} O$	2.386	196.09	36.07
Pyroquilon	$C_{11} H_{11} N O$	16.059	173.08	36.06
3-Hydroxycarbofuran	$C_{12} H_{15} N O_4$	16.131	254.13	34.67
Bis(1-chloro-2-propyl) phosphate (BCPP)	$C_6 H_{13} Cl_2 O_4 P$	13.955	249.99	34.03
1-Hydroxypyrene	$C_{16} H_{10} O$	11.066	218.08	33.94
Quinoclamine	$C_{10} H_6 Cl N O_2$	8.924	207.01	33.88
Diclocymet II	$C_{15} H_{18} Cl_2 N_2 O$	8.916	312.08	33.67
Tebupirimfos	$C_{13} H_{23} N_2 O_3 P S$	16.617	318.12	32.44
1,2,3,4,7,8,9-Heptachlorodibenzofuran (HPCDF)	$C_{12} H Cl_7 O$	15.667	405.79	31.68
Dibenz[a,c]anthracene	$C_{22} H_{14}$	14.449	278.11	30.48

References

Babaei AA, Kakavandi B, Rafiee M, et al (2017) Comparative treatment of textile wastewater by adsorption, Fenton, UV-Fenton and US-Fenton using magnetic nanoparticles-functionalized carbon (MNPs@C). J Ind Eng Chem 56:163–174. https://doi.org/10.1016/j.jiec.2017.07.009

Bagheri AR (2017) Comparative study on ultrasonic assisted adsorption of dyes from single system onto Fe_3O_4 magnetite nanoparticles loaded on activated carbon: Experimental design methodology. Ultrason Sonochem

D'Cruz B, Madkour M, Amin MO, Al-Hetlani E (2020) Efficient and recoverable magnetic AC-Fe_3O_4 nanocomposite for rapid removal of promazine from wastewater. Mater Chem Phys 240:122109. https://doi.org/10.1016/j.matchemphys.2019.122109

Ghasemi M, Mashhadi S, Azimi-Amin J (2018) Fe_3O_4/AC nanocomposite as a novel nano adsorbent for effective removal of cationic dye: Process optimization based on Taguchi design method, kinetics, equilibrium and thermodynamics. J Water Environ Nanotechnol 3:. https://doi.org/10.22090/jwent.2018.04.005

Jonidi Jafari A, Kakavandi B, Jaafarzadeh N, et al (2017) Fenton-like catalytic oxidation of tetracycline by AC@Fe_3O_4 as a heterogeneous persulfate activator: Adsorption and degradation studies. J Ind Eng Chem 45:323–333. https://doi.org/10.1016/j.jiec.2016.09.044

Sharifi N, Nasiri A, Silva Martínez S, Amiri H (2022) Synthesis of Fe_3O_4@activated carbon to treat metronidazole effluents by adsorption and heterogeneous Fenton with effluent bioassay. J Photochem Photobiol Chem 427:113845. https://doi.org/10.1016/j.jphotochem.2022.113845

Yegane Badi M, Azari A, Pasalari H, et al (2018) Modification of activated carbon with magnetic Fe_3O_4 nanoparticle composite for removal of ceftriaxone from aquatic solutions. J Mol Liq 261:146–154. https://doi.org/10.1016/j.molliq.2018.04.019

CHAPTER 3

Investigations in sonoenzymatic treatment of industrial wastewater using Fe_3O_4@Laccase nanocomposite

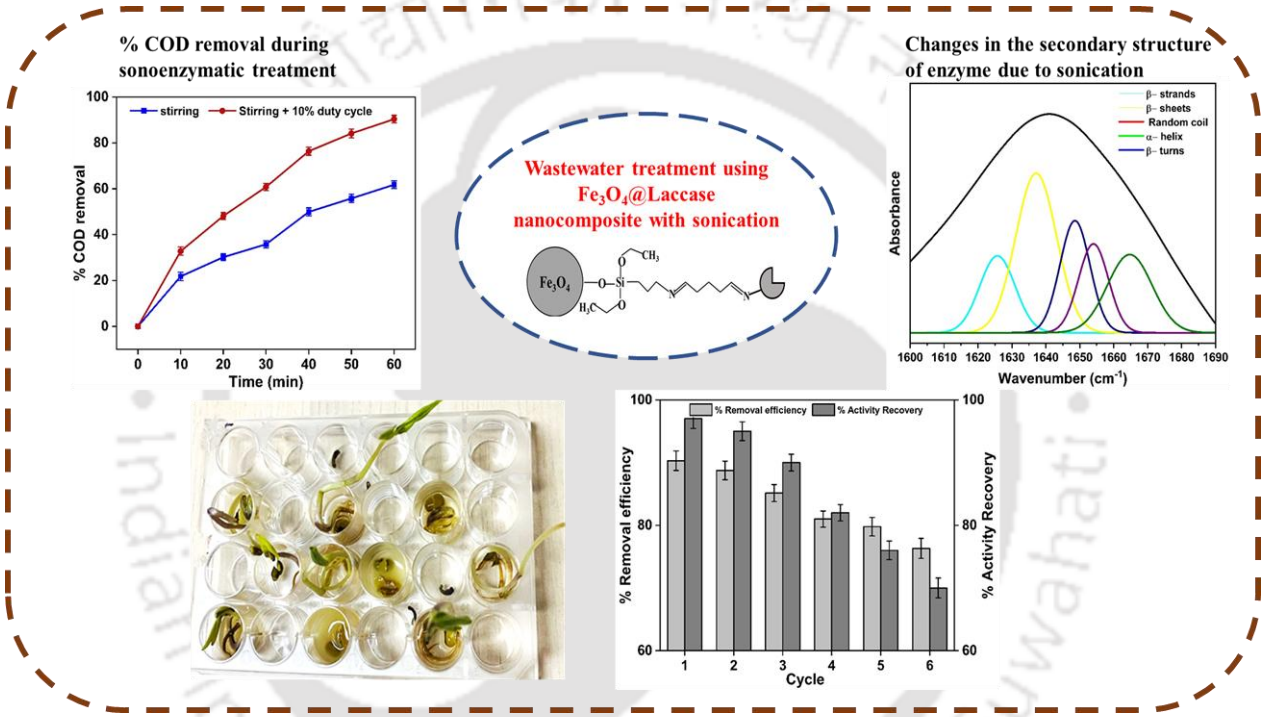

***Online*:** Verma, K., Moholkar, V. S. Investigations in Sonoenzymatic Treatment of Industrial Wastewater Using Fe_3O_4@Laccase Nanocomposites. *ACS ES&T Water,* doi.org/10.1021/acsestwater.3c00697

CHAPTER 3

INVESTIGATIONS IN SONOENZYMATIC TREATMENT OF INDUSTRIAL WASTEWATER USING Fe_3O_4@LACCASE NANOCOMPOSITE

3.1 Introduction

Wastewater discharges from different sources like process industries, agricultural and poultry runoffs, academic and research institutions, and domestic sectors (sewage) often comprise organic contaminants that are not degraded by the conventional anaerobic digestion technique. Effective degradation and mineralization of these pollutants in wastewater requires advanced oxidation processes (AOP) that are based on oxidative radicals ($^{\bullet}O$, $^{\bullet}OH$, $HO_2^{\bullet}$). Sonication (or ultrasound irradiation) is a relatively new AOP in which the oxidizing radicals are generated through the transient collapse of cavitation bubbles. Sonication also induces intense microturbulence (or micromixing) in the bulk liquid medium due to the oscillatory motion of the liquid elements induced during propagation of the ultrasound in the form of a longitudinal wave. However, in many situations, sonication alone is not able to completely degrade and mineralize the contaminants in wastewater (Choudhury and Malani 2013). Sonication is, therefore, coupled with other AOPs such as Fenton, photocatalysis, ozonation, H_2O_2, etc. More recently, the application of green biocatalysts from the oxidase family, including peroxidase,

laccase, glucose oxidase, phenol oxidase, etc., has been investigated for the degradation of various pollutants in wastewater (Rouhani et al. 2021). These biocatalysts have shown promising efficacy for oxidative degradation of organic pollutants. Laccase, classified as a multi-copper oxidase, exhibits the ability to catalyze the oxidation of diverse aromatic substrates, such as phenol derivatives, benzenethiols, polyphenols, and polycyclic aromatic hydrocarbons (PAHs), through the reduction of molecular oxygen to water. Enzymatic degradation of pollutants suffers from two demerits, viz. slow kinetics, and recovery (and reuse) of the enzyme. In actual industrial wastewater containing numerous contaminants, some contaminants may act as enzyme inhibitors. Several previous authors have used immobilized laccases on suitable supports for inorganic materials (Fe_3O_4 nanoparticles, GO, carbon nanotubes), organic materials (polymeric materials like PMMA, alginate chitosan and polyaniline), and hybrids (MOFs) for wastewater treatments (Zhao et al. 2015; Hou et al. 2015; Santhosh et al. 2016; Wang et al. 2021b). The immobilized enzymes can be recovered after treatment and reused. Among different supports employed for immobilization, the magnetic Fe_3O_4 nanoparticles are of special interest due to their easy separation using a magnet. Previous authors have reported marked enhancement in the kinetics of degradation of pollutants using either free or immobilized oxidase enzyme with the application of sonication (Gonçalves et al. 2015; Chakma and Moholkar 2016; Pulicharla et al. 2018; Ingole and Rathod 2023). Although these authors have reported recovery of the immobilized enzyme after treatment and reuse, these studies have focused on the degradation of a specific pollutant, not real wastewater generated from the process industry. Table A3.1 (provided in Appendix A3) summarizes the previous literature on the degradation of biorecalcitrant pollutants using free and immobilized laccase on different supports.

The present chapter has addressed the treatment of industrial effluent for COD reduction using immobilized laccase in the form of Fe_3O_4@Laccase nanocomposite. The

wastewater treatment has been carried out in the presence of sonication to enhance the kinetics. The major components of this study are (1) synthesis of Fe_3O_4@Laccase nanocomposite by immobilization of laccase on magnetic Fe_3O_4 nanoparticles and its characterization; (2) optimization of the physical parameters of sonoenzymatic effluent treatment using the statistical technique of CCD (central composite design); (3) kinetic analysis of the sonoenzymatic treatment to quantify the enhancement effect of ultrasound; (4) deduction of the synergism between enzymatic oxidation and sonication using analysis of the secondary structure of enzyme proteins; (5) LC-MS analysis of the wastewater before and after treatment for identification of major contaminants; (6) analysis of the toxicity reduction of wastewater after treatment; (7) analysis of the separation and reusability of Fe_3O_4@Laccase nanocomposite.

3.2 Materials and Methods

3.2.1 Reagents

The following chemicals have been used in this study: A Laccase from *Trametes versicolor* was purchased from Sigma Aldrich. Ferric chloride hexahydrate ($FeCl_3 \cdot 6H_2O$), sulfuric acid (H_2SO_4; 98%), ferrous sulfate heptahydrate ($FeSO_4 \cdot 7H_2O$), hydrogen peroxide (H_2O_2; 30% v/v), potassium permanganate ($KMnO_4$), and hydrochloric acid (HCl; 35%) were purchased from Himedia Ltd. (India). Hydrazine hydrate (N_2H_4, 50-60%) and sodium carbonate anhydrous (Na_2CO_3) were obtained from Sigma-Aldrich (India). The chemicals used in the COD analysis, i.e., ferrous ammonium sulfate heptahydrate ($Fe(NH_4)_2(SO_4)_2 \cdot 7H_2O$), potassium dichromate ($K_2Cr_2O_7$), mercuric sulfate ($HgSO_4$), silver sulfate (Ag_2SO_4), conc. H_2SO_4 (98%) and ferroin indicator were analytical grade Himedia Ltd.(India) reagents. The following chemicals for BOD analysis were procured from Sigma Aldrich: sodium thiosulfate

($Na_2S_2O_3$), alkali iodide azide, manganese sulfate ($MnSO_4$), starch, potassium dihydrogen phosphate (KH_2PO_4), dipotassium hydrogen orthophosphate (K_2HPO_4), disodium hydrogen phosphate (Na_2HPO_4), ammonium chloride (NH_4Cl), calcium chloride ($CaCl_2$), magnesium sulfate ($MgSO_4$) and ferric chloride ($FeCl_3$). (3-aminopropyl) trimethoxysilane (APTMS, 97%), Glutaraldehyde (25%), 2, 2- azino- bis (3- ethylbenzothiazoline -6-sulfonic acid) (ABTS) were purchased from Sigma Aldrich. All reagents were of analytical grade and used as received without further purification. The wastewater (WW) was obtained from the combined discharge from local (small-scale) industries and academic institutions (including our institute) into a local water body. The WW was filtered and stored in sealed bottles in a dark, 4 ^oC refrigerator. The WW samples were diluted using deionized water to obtain the required initial COD values.

3.2.2 Functionalization of Fe_3O_4 nanoparticles

Fe_3O_4 nanoparticles were synthesized using the co-precipitation method described in our earlier work by Verma and Moholkar (2023). The surface modification of Fe_3O_4 nanoparticles is synthesized with minor changes according to previously reported literature (Rashid et al. 2022). To achieve amino functionalization of the synthesized ferromagnetic nanoparticles, 3-aminopropyltrimethoxysilane (APTMS) was used. The procedure involved dispersing the iron oxide nanoparticles (0.2 g) in 100 mL of ethanol solution (67% v/v). After the suspension of Fe_3O_4 nanoparticles in the ethanol-water solution, it was subjected to sonication for 30 min at room temperature. Following sonication, 1 mL of APTMS was added to the solution, and the mixture was mechanically stirred at 150 rpm for a period of 6 h. Subsequently, the amino-functionalized magnetic nanoparticles (AF-MNPs) were separated from the solution using magnetic decantation. Once the liquid was removed, the AF-MNPs were subjected to washing with deionized water (3 × 100 mL) and ethanol (3 × 100 mL) until a neutral pH value was achieved. After the washing process, the AF-MNPs were dried in a vacuum oven at 70 °C for

a duration of 24 h. Finally, the dried AF-MNPs were stored in a refrigerator at 4 °C for further use.

3.2.3 Immobilization of Laccase onto functionalized Fe_3O_4 nanoparticles

The immobilization of laccase involves two steps: the co-precipitation process of AF-MNPs followed by the cross-linking process. In the first step, 50 mg of AF-MNPs and 2.4% (w/w) laccase were suspended in 10 mL of chilled 2-propanol along with 1 mL of deionized water. This suspension was sonicated for 45 min at room temperature. In the second step, 10 mL of glutaraldehyde (5%, v/v) was added dropwise to the solution at room temperature. The mixture was then mechanically stirred at 200 rpm for an additional 4 h. The resulting solid obtained from the immobilization process was separated using magnetic decantation. The separated solids were then rinsed with phosphate-buffered saline (PBS, 0.1 mol/L, pH 7, 2 × 100 mL) and deionized water (2 × 100 mL). This rinsing step was performed to remove any residual glutaraldehyde from the immobilized laccase and kept at 4 ^oC for further use. Fig. 3.1 represents the schematic diagram of the immobilization of laccase.

3.2.4 Characterization techniques

The crystal structures of the Fe_3O_4, Fe_3O_4-NH_2, and Fe_3O_4@Laccase nanocomposite were analyzed using a Rigaku powder X-ray diffractometer (model Smart Lab) with Cu K_α radiation (λ = 1.54178 Å). To determine the precise surface area, a Micromeritics surface area analyzer (model Tristar II) was utilized, employing the Brunauer-Emmett-Teller (BET) method. The surface morphologies of the nanomaterials were examined using a Zeiss field emission scanning electron microscope (FE-SEM; model Sigma 300) and a JEOL transmission electron microscope (TEM; model JEM 2100). The magnetic behavior of both Fe_3O_4, Fe_3O_4-NH_2, and Fe_3O_4@Laccase nanocomposite was assessed using a Lakeshore vibrating sample magnetometer (model 7410 series). To study the functional group present in the free laccase and Fe_3O_4@Laccase nanocomposite, an FTIR spectrophotometer (Spectrum Two,

PerkinElmer) was employed, covering the wavenumber range of 4000-400 cm^{-1}.

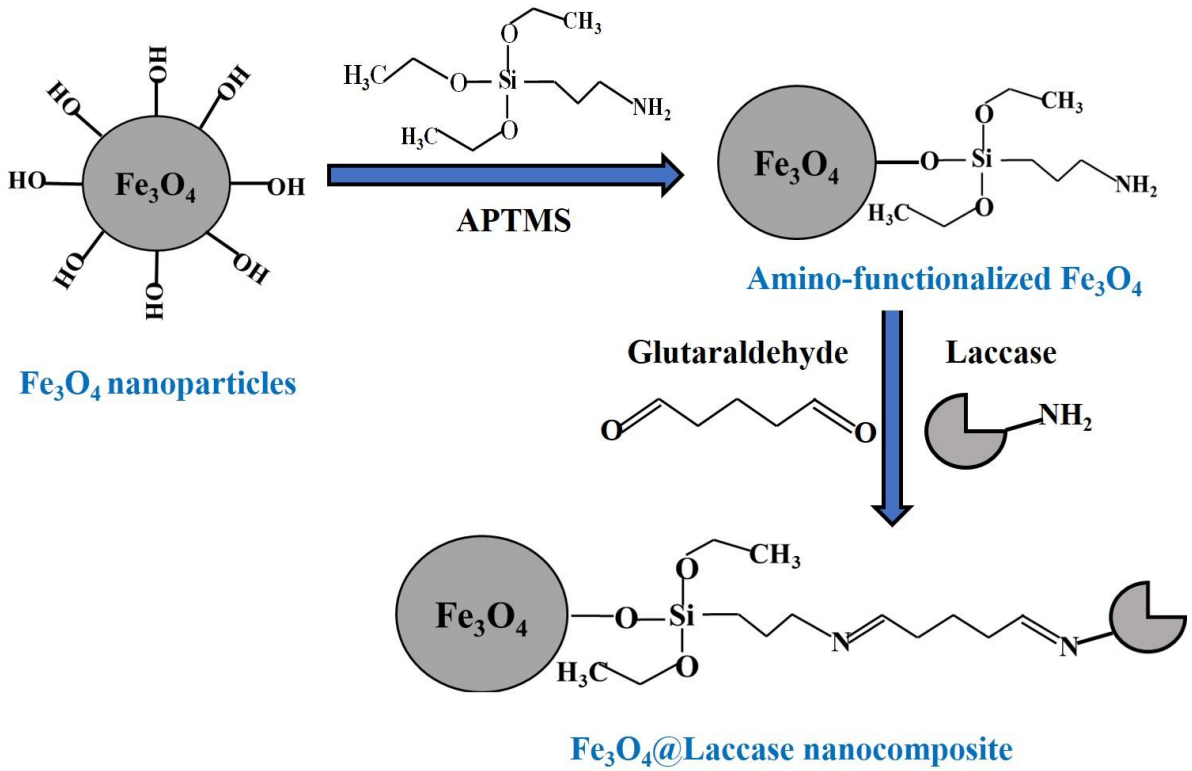

Figure 3.1. Schematic diagram of the fabrication of Fe_3O_4@Laccase nanocomposite

The elemental composition of the Fe_3O_4@Laccase nanocomposite was determined through energy-dispersive X-ray (EDX) examination using a Sigma Zeiss instrument. Furthermore, the analysis of chemical oxygen demand (COD) and biological oxygen demand (BOD) was conducted according to standard methods. The BOD_5 (biological oxygen demand after 5 days) was measured following method 5210 D, while the COD was calculated using the acidic digestion (closed reflux) method with potassium dichromate as the oxidant at 150 °C for 2 h, following Method 5220 D (Merck, ECO25 Thermoreactor VELP SCIETIFICA) (Association et al. 1995). The total organic carbon (TOC) of wastewater before and after treatment was determined by TOC analyzer (Analytikjena, multi N/C model: 2100 S). LC-MS analysis was

determined through LCMS/QTOF (Agilent 1100/1200/1260/1290 LC). The details of the instrumentation and mobile phase are listed in Table A3.2 (provided in Appendix A3).

3.2.5 Experimental setup and procedure

The optimization of the experimental parameters with immobilized laccase (Fe_3O_4@Laccase) was conducted under mechanical stirring. The reaction solution was stirred at 300 rpm using a magnetic bar (length = 1 cm, dia. = 0.5 cm). The experiments of intensification of COD removal using sonication were conducted at the optimum set of parameters obtained from the central composite experimental design. The sonication of the reaction solution was done using a 1.5 L ultrasound bath (Elma, Germany, Model: T460, 35 kHz, 35 W). The ultrasound bath was filled with water that acted as a medium for transmission of ultrasound waves. The glass beaker containing the reaction mixture was positioned precisely at the center of the ultrasound bath and immersed to approximately 75% of its height. This arrangement guaranteed that the entire reaction mixture within the glass beaker was uniformly exposed to the ultrasound waves. To maintain consistency and prevent any artifacts arising from spatial variations in acoustic intensity, the position of the glass beaker in the bath was meticulously maintained throughout all experiments (Moholkar et al. 2000). The sonication of the enzymatic reaction mixture was conducted using a duty cycle of 10%, which involved 1 min of sonication followed by 9 min of mechanical stirring within every 10 min interval of the reaction. Water circulation was employed to control the temperature rise during sonication. A temperature-controlled cooling water circulating bath (Amkette Analytics, Model: WB2000) was used for this purpose. In a typical experiment, the total volume and treatment time of the reaction solution was 50 mL and 60 min, respectively. The pH of the solution was adjusted to the desired value by adding either 1 M HCl or 1 M NaOH. 3 mL aliquots of the reaction solution were withdrawn at intervals of 10 min, followed by centrifugation at 5000 rpm for another 10 min. The resulting supernatant was analyzed to determine the percentage of COD (Chemical Oxygen Demand) removal. After

completion of the treatment, the Fe_3O_4@Laccase nanocomposites were magnetically separated and subjected to several washes with DI water to desorb any adsorbed but un-degraded pollutants. The wash water was added to the reaction solution, which was analyzed for the final COD value. The weight ratio of enzyme to immobilization support is an important factor governing the efficacy of the nanocomposite and, hence, COD removal during wastewater treatment. Another important factor that affects the activity of the enzyme is pH. This factor also needs to be optimized after the immobilization of the enzyme on the given support. We conducted several preliminary experiments to decide the optimum enzyme/immobilization support weight ratio values and the solution pH. The results of these preliminary experiments are represented in Fig. 3.2. To assess the impact of the laccase loading on the effectiveness of wastewater treatment (%COD removal), preliminary experiments were conducted using Fe_3O_4@Laccase nanocomposites synthesized with varying doses. This allowed us to deduce the influence of this parameter on the overall efficacy of the wastewater treatment process. The precise amount of enzyme required for achieving the maximum extent of degradation is a crucial factor in enzymatic-catalyzed degradation reactions, particularly when considering the commercial aspect of such processes. Fig. 3.2(a) depicted that % COD removal increases with the laccase loading. From the results, it has been observed that the maximum %COD removal is 78% with laccase loading approximately 24.89 mg/g, whereas activity recovery attained to 76%. Further, increase in laccase loading there is decrease in %COD removal as well as in activity recovery because of excess loading leads to the formation of enzyme aggregates that hinders the active sites. Hence, an optimum laccase loading (~24.9 mg/g) has been used for the all the experiments. Fig. 3.2(b) showed that the effect of pH on the enzyme activity for both free and immobilized laccase. It revealed that immobilized laccase (pH=5 at which enzyme activity is 96%) shows a broader range for pH than free laccase (pH=4 at which enzyme activity is 75%), which could be due to the interaction of laccase to the functional group of Fe_3O_4

nanoparticles. The procedure used for assessing enzyme activity assay for laccase has been provided in Appendix A3 Section A.3.1 It was observed that the activity of free laccase was 56.8 U, while after immobilization, the activity of Fe_3O_4@Laccase nanocomposite was 46.7 U.

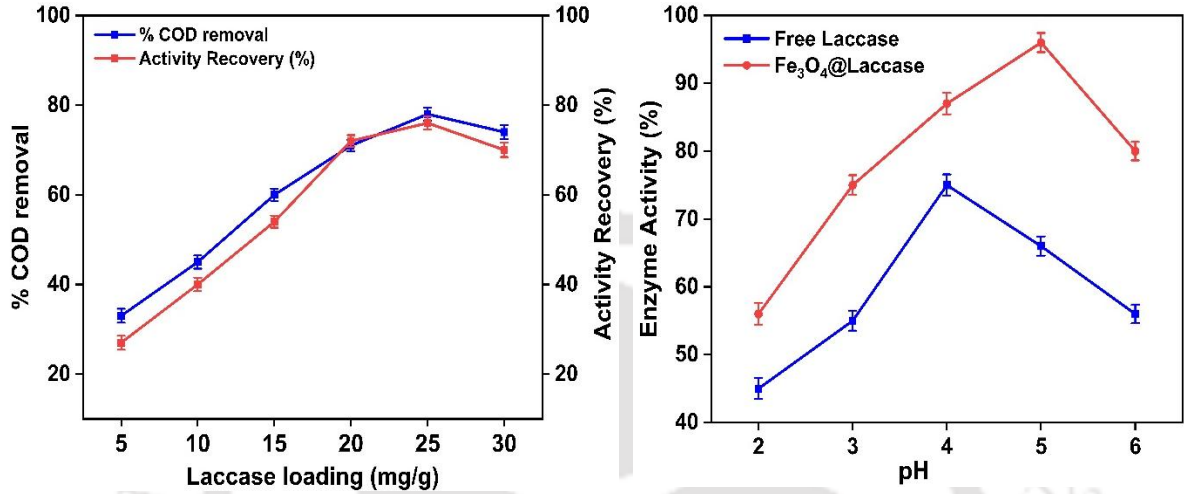

(a) (b)

Figure 3.2. (a) The effect of laccase loading on %COD removal and Activity recovery. (b) The effect of pH on enzyme activity

***Control experiments*:** In the present experimental system, there could be alternate parallel pathways for degrading organic contaminants in wastewater and reducing COD. Sonication alone can generate $^{\bullet}OH$ and $O_2^{\bullet-}$ which can oxidize and degrade the contaminants (Miljevic et al. 2014). Moreover, sonication in the presence of Fe_3O_4 nanoparticles can also generate radicals that can lead to COD reduction (Verma and Moholkar 2023). In order to isolate these effects and distinguish the efficacy of Fe_3O_4@Laccase nanocomposite for COD reduction, we conducted two control experiments as follows:

1. Wastewater treatment with only sonication: 7.6% COD removal

2. Sonication with magnetite nanoparticles: 68.7% COD removal.

3.2.6 Statistical design of experiments

The extent of COD removal during treatment is influenced by several physical parameters. The principal parameters among these are (1) nanocomposite dose (or biocatalyst loading), (2) initial pH of the solution, and (3) temperature. We employed a statistical design for the experiments, viz. Central Composite Design (CCD) is used to optimize these parameters simultaneously. A 3-factor-3-level experimental design was utilized, with the following ranges for each parameter: (1) Fe_3O_4@Lacasse (X_1): 0.2-2 g/L, (2) pH (X_2): 2-6, and (3) Temperature (X_3): 30-70 ^oC. The factors and their levels are given in Table 3.1. These ranges were fixed on some preliminary trial experiments. The complete experimental design consisted of a total of 20 runs, which included 8 factorial points, 6 axial points, and 6 replicates at the center point. This design allows for a comprehensive exploration of the parameter space to identify the optimum conditions for COD removal. The results of the statistical DoE were analyzed using response surface methodology by fitting a quadratic equation (3.1) to the data as follows.

$$Y = \beta_0 + \sum_{i=1}^{k} \beta_i X_i + \sum_{i=1}^{k} \sum_{j=1}^{k} \beta_{ij} X_i X_j + \sum_{i=1}^{k} \beta_{ii} X_i^2 + \varepsilon \qquad (3.1)$$

Y is the response variable (% COD removal), β_0 is the constant coefficient, β_i are the linear coefficients, β_{ii} are the quadratic coefficients, β_{ij} are the interaction coefficients, X_i, X_j are the coded values of the independent process variables, k is the total number of independent variables, and ε is the residual error. The quality of the quadratic equation fitted to experimental data was determined using analysis of variance (ANOVA). Table 3.2 give the details of the statistical DoE.

Table 3.1. Factors and their level for the Design of Experiments(DoE)

Factor	Unit	Level		
		Low (-1)	Middle (0)	High (+1)
Fe_3O_4@Laccase (X_1)	g/L	0.2	1.1	2
pH (X_2)	-	2	4	6
Temperature (X_3)	^oC	30	50	70

3.2.7 Kinetic models

For the assessment of maximum reaction rate or velocity (V_{max}, mg/ L min) at varying initial substrate concentrations ([S_0], mg/ L), various kinetic models are reported in the literature. In this typical method, the substrate concentration is obtained by varying the initial COD value of the wastewater solution at optimum conditions. Several different kinetic substrate utilization and inhibition models have been employed to explain and characterize the dynamic behavior of laccase enzymes, which is explained by equations (3.2-3.4).

Michaelis Menten equation (Chen et al. 2022): $$v\big|_{[S_0]} = v_0 = \frac{V_{max}[S_0]}{K_m + [S_0]} \quad (3.2)$$

The values of the Michaelis-Menten constant (K_m) and maximum velocity (V_{max}) for the free as well as immobilized laccase enzyme were determined through a series of enzymatic reactions using different substrate concentrations.

Haldane equation:(Hussain et al. 2015) $$v\big|_{[S_0]} = v_0 = \frac{V_{max}[S_0]}{K_m + [S_0] + \frac{[S_0]^2}{K_i}} \quad (3.3)$$

Yano and Koga model:(Agarry et al. 2009): $$v\big|_{[S_0]} = v_0 = \frac{V_{max}[S_0]}{K_m + [S_0] + \frac{[S_0]^2}{K_i}\left(1 + \frac{[S_0]}{K_i}\right)} \quad (3.4)$$

From these models, V_{max} (mg/ L min), K_m (mg/ L) and K_i (mg/ L) were calculated and the best fit was obtained from the R^2 value.

Table 3.2. Central composite design matrix and observed/predicted values for %COD removal

Run	Fe_3O_4@Laccase (X_1), g/L	pH (X_2)	Temperature (X_3),°C	% COD removal (Exp.)	% COD removal (Pred.)
1	2.0	4	50	60.2	59.1
2	1.1	4	50	62.8	62.4
3	1.1	4	30	59.8	56.1
4	1.1	4	50	59.5	62.4
5	1.1	2	50	50.2	48.0
6	0.2	2	70	30.8	30.6
7	2.0	2	30	37.4	38.8
8	1.1	4	50	65.0	62.4
9	1.1	4	50	60.5	62.4
10	2.0	2	70	45.2	45.0
11	0.2	2	30	23.2	24.3
12	0.2	6	30	33.8	34.3
13	2.0	6	30	48.8	49.3
14	1.1	4	70	61	63.1
15	1.1	4	50	62.8	62.4
16	0.2	6	70	43	42
17	2.0	6	70	57.8	57
18	1.1	6	50	58.4	59.0
19	0.2	4	50	44.8	44.4
20	1.1	4	50	60.8	62.4

3.2.8 Toxicity analysis

To assess the relative reduction in wastewater toxicity, a seed toxicity test was performed using *Vigna radiata* (K-851) seeds, as described in our previous chapter (Verma and Moholkar 2023).

The seeds were treated to prevent fungus growth by washing them with a 1% sodium hypochlorite (NaOCl) solution. They were then rinsed with deionized water to remove any dust particles. The experiment was conducted using a 24-well plate, where ten seeds were germinated in deionized water (blank), before treatment (control), and after treatment (test) as the growth medium. The seeds were incubated for 3 days in a dark environment, followed by 4 days at ambient temperature with a 16 h photoperiod. After incubation, the number of germinated seeds in each sample were recorded as the response of the experiment.

3.3 Results and Discussions

3.3.1 Characterization

The phase purity and crystallinity of Fe_3O_4 native particles, Fe_3O_4-NH_2, and Fe_3O_4@laccase nanocomposite were investigated using X-ray diffractograms shown in Fig. 3.3. The XRD investigation was conducted at 25°C (λ = 1.54 nm) in the 10-80° (2θ) range. According to JCPDS (no. 19−0629), the sharp peaks at 2θ values of 30.07 (2 2 0), 35.44 (3 1 1), 43.15 (4 0 0), 54.6 (4 2 2), 56.99 (5 1 1), and 62.6 (4 4 0) are related to the cubic phase Fe_3O_4.(Xu et al. 2014). The peaks of Fe_3O_4 nanoparticles, amino-functionalized Fe_3O_4 nanoparticles, and Fe_3O_4@Laccase were distinct and consistent with the usual pattern for Fe_3O_4, indicating that particle modification did not affect the crystalline structure.

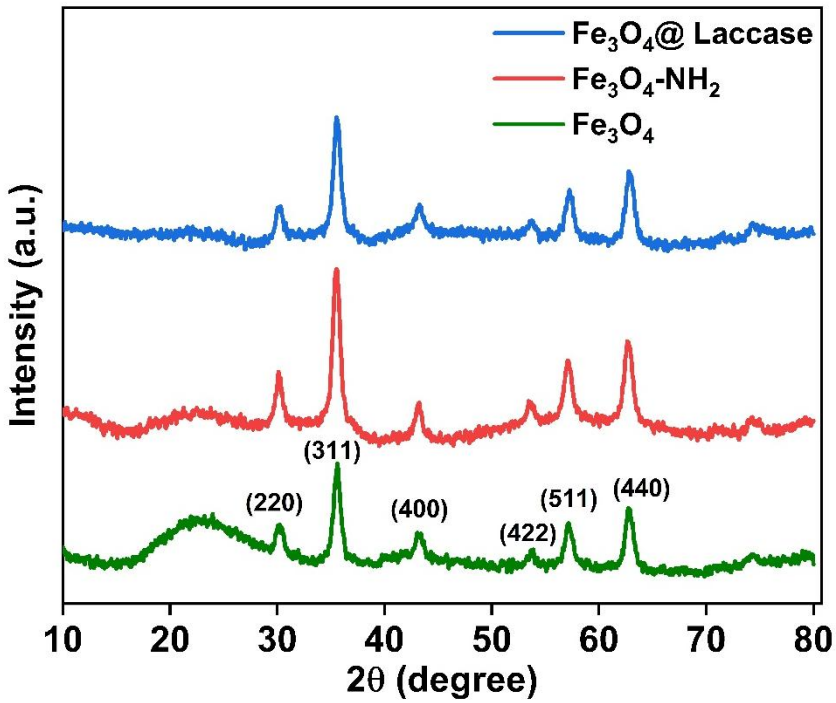

Figure 3.3. XRD patterns of Fe_3O_4 nanoparticles, amino-functionalized Fe_3O_4 (Fe_3O_4-NH_2) and Fe_3O_4@Laccase nanocomposite

Figure. 3.4 depicts the change in magnetization of Fe_3O_4, Fe_3O_4-NH_2, and Fe_3O_4@Laccase nanoparticles. The saturation magnetization value of Fe_3O_4 NPs was calculated to be 49.77 emu/g, while that of Fe_3O_4-NH_2 NPs and Fe_3O_4@Laccase was lowered to 47.28 and 40.46 emu/g, respectively. The decrease in saturation magnetization values could be due to the increasing fraction of other components on the surface of Fe_3O_4 NPs throughout the modification process and the successful loading of laccase. Similar outcomes are obtained with other magnetic nanoparticles treated with other polymers (Liu et al. 2011; Guo et al. 2015). Additionally, it should be noted that there was no hysteresis in the magnetic hysteresis loops with very low coercivity, which was much lower than the value predicted for superparamagnetic particles ($Hc \leq 5$ mT = 50 Oe), demonstrating that these magnetic NPs are superparamagnetic at room temperature (Kadam et al. 2017). Fe_3O_4@Laccase is highly susceptible to external magnetic fields due to its high magnetization value and

superparamagnetic properties. It can be quickly separated from the aqueous solution and redispersed easily and evenly once the external magnetic field is removed (Inset Fig 3.4), making it cost-effective and reusable for practical applications.

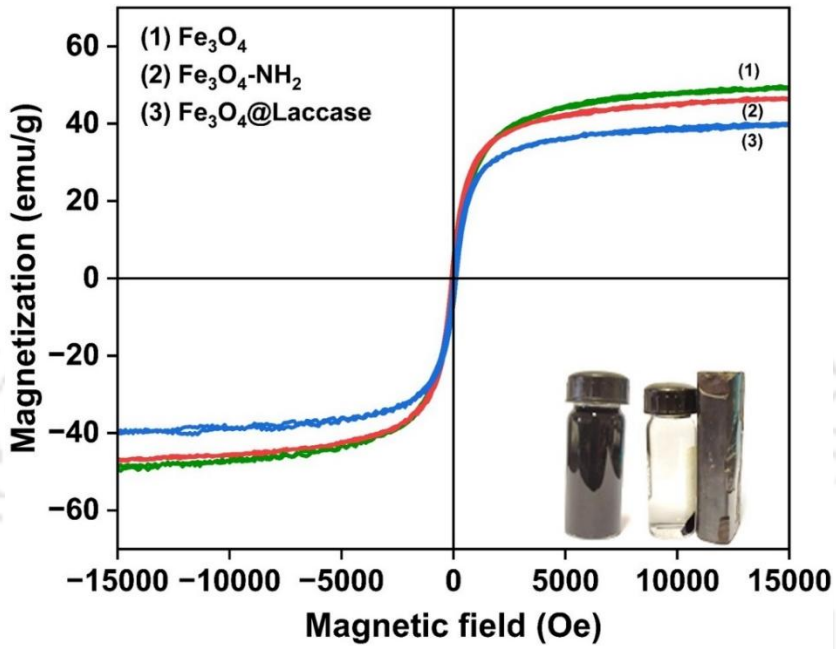

Figure 3.4. VSM plot (M-H) of Fe_3O_4, Fe_3O_4-NH_2 and Fe_3O_4@Laccase nanocomposite

The specific surface area, volume, and average pore diameter of two materials—Fe_3O_4 nanoparticles, and the Fe_3O_4@Laccase nanocomposite—were determined using the Brunauer−Emmett−Teller (BET) technique. To achieve this, N_2 adsorption−desorption experiments were conducted at a temperature of 77.3 K. The resulting adsorption and desorption curves for Fe_3O_4 nanoparticles and the Fe_3O_4@Laccase nanocomposite are visually represented in Fig. 3.5. The N_2 adsorption/desorption isotherms observed for both the mesoporous Fe_3O_4 nanoparticles and the Fe_3O_4@Laccase nanocomposite confirm to type IV, as depicted in Fig. 3.5. Notably, the presence of hysteresis loops between the adsorption and desorption curves at moderate relative pressures is indicative of the high-quality mesoporous

characteristics of these materials (Babaei et al. 2017). The Fe_3O_4 nanoparticles possessed a mesoporous structure with BET surface area = 85.32 m^2·/g, pore volume = 0.27 cm^3/g, and average pore diameter = 12.55 nm. Whereas Fe_3O_4@Laccase nanocomposite also possessed a mesoporous structure with BET surface area = 44.66 m^2·/g, pore volume = 0.12 cm^3/g and average pore diameter = 11.09 nm. This high surface area of Fe_3O_4 nanoparticles facilitates substantial enzyme loading. Reduction in BET surface area and pore diameter indicates immobilization of laccase onto Fe_3O_4 nanoparticles (represented as Fe_3O_4@Laccase).

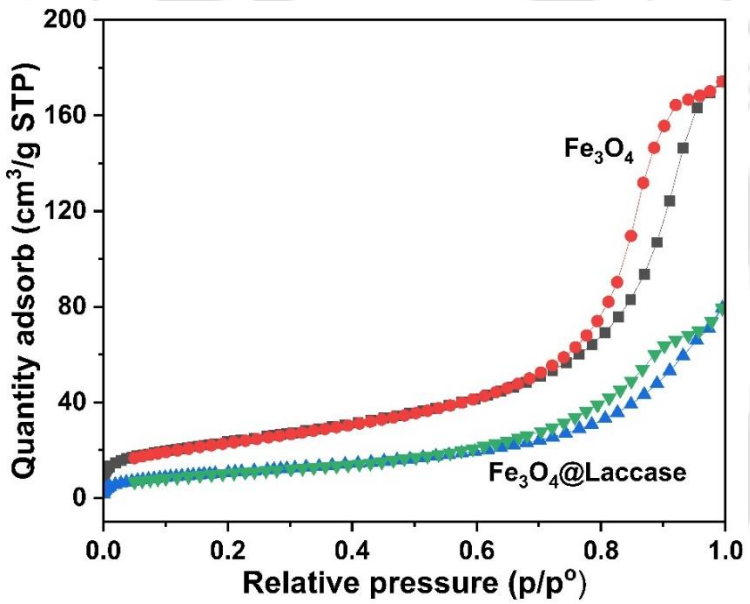

Figure 3.5. BET surface area plots (Nitrogen adsorption-desorption isotherm plots)

FTIR analysis was used to assess the immobilization of laccase on magnetic nanoparticles. According to Fig. 3.6, the FTIR spectra of Fe_3O_4 nanoparticles, free laccase, and amino-functionalized Fe_3O_4 nanoparticles with amine groups before immobilization, and the same Fe_3O_4 nanoparticles following laccase immobilization are all represented. Before and after the experiment, the typical characteristic peaks of 576, 571, and 570 cm^{-1} were noticed in the spectra of Fe_3O_4, Fe_3O_4-NH_2, and Fe_3O_4@Laccase, which are attributed to vibration of the Fe-

O bond in Fe_3O_4 (Zhu et al. 2008). The peaks in Fig. 3.6 (i) at 3417 and 1626 cm^{-1} were assigned to O-H stretching and deformation, respectively (Lü et al. 2003; Peng et al. 2004). Fig. 3.6 (ii) shows the FTIR spectra of amino-functionalized Fe_3O_4 in which the peak at 796 cm^{-1} corresponds to the Si-O-Fe bond, indicating the chemical binding of SiO_2 to Fe_3O_4. The strong band at 1037 cm^{-1} is due to the stretching vibration of Si-O-Si, whereas the band at 1616 cm^{-1} is attributed to Si-OH group vibration (Zheng and Jiang 2012). The band at 1523 cm^{-1} corresponds to the bending vibration of the N–H in primary amine. The strong absorption band at 3364 cm^{-1} in Fig. 3.6 (ii) is probably caused by free amino groups and overlaps with O–H stretching vibration (Hu et al. 2015). This result shows the successful attachment of amine groups onto the surfaces of the Fe_3O_4 nanoparticles via the silanization reaction. Laccase characteristic bands Fig. 3.6 (iv) were found at 3300 cm^{-1} (OH stretch and/or N-H stretching vibration), 2800 cm^{-1} (C-H stretch), 1630 cm^{-1} (carbonyl group, attributed to secondary amide structure (CO-NH), and 1100 cm^{-1} (C-O-C) (El-Batal et al. 2015).

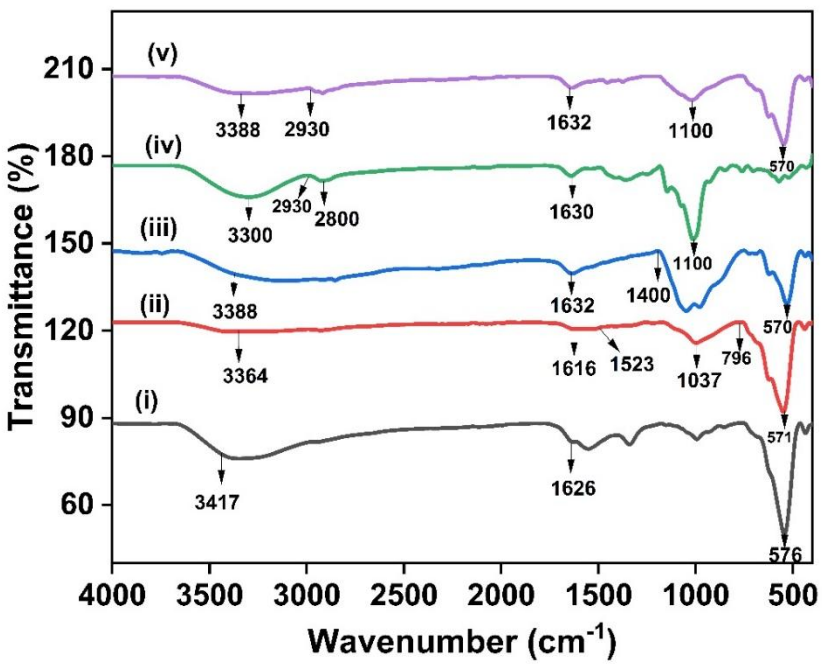

Figure 3.6. FTIR spectra of (i) Fe_3O_4, (ii) (Fe_3O_4-NH_2), (iii) Fe_3O_4@Laccase before reaction, (iv) Free laccase and (v) Fe_3O_4@Laccase after reaction.

The surface morphologies of native Fe_3O_4, amino-functionalized Fe_3O_4, and Fe_3O_4@Laccase nanocomposite are shown in the FE-SEM micrographs Figure. 3.7. Comparative assessment of FE-SEM micrographs of native and amino-functionalized Fe_3O_4 particles reveals no morphological alternations post-silanization. From Fig. 3.7 (a-c), the average nanoparticles size of Fe_3O_4 nanoparticles was 34.1 nm while immobilized Fe_3O_4@Laccase was about 60 nm, respectively, which shows that laccase has been immobilized on amino-functionalized Fe_3O_4 nanoparticles successfully. Fig. 3.7 (d) shows the TEM image of Fe_3O_4@Laccase nanocomposites. Spherical geometry, along with the homogeneous distribution of the Fe_3O_4@Laccase nanocomposites, can be observed in the TEM micrograph. The TEM micrograph can also observe a noticeable agglomeration among the Fe_3O_4@Laccase nanoparticles due to strong, attractive forces. The SAED pattern of the Fe_3O_4@Laccase nanocomposites shown in Fig. 3.7 (e) reveals Fe_3O_4 planes (2 2 0), (3 1 1), (4 0 0), and (4 2 2). These planes may be related to the X-ray diffractograms of Fe_3O_4@Laccase nanocomposites reported in the previous section. Fig. 3.7 (f) shows the HR-TEM image of the Fe_3O_4@Laccase nanocomposite.

The formation of Fe_3O_4@Laccase nanocomposite (or immobilization of laccase on Fe_3O_4-NH_2 particles) was also confirmed using energy-dispersive X-ray (EDX) analysis. Copper is a characteristic component of the laccase enzyme. The presence of copper in the EDX spectrum shown in Fig. 3.8 confirmed the immobilization of the laccase enzyme onto the surface of Fe_3O_4-NH_2 particles. The elemental composition of Fe_3O_4 nanoparticles was: Fe = 74.8%, O = 25.2%, whereas the composition of Fe_3O_4@Laccase was: Fe = 62.9%, N = 1.3%, O = 28.5%, Si = 5.1%, Cu = 2.5%.

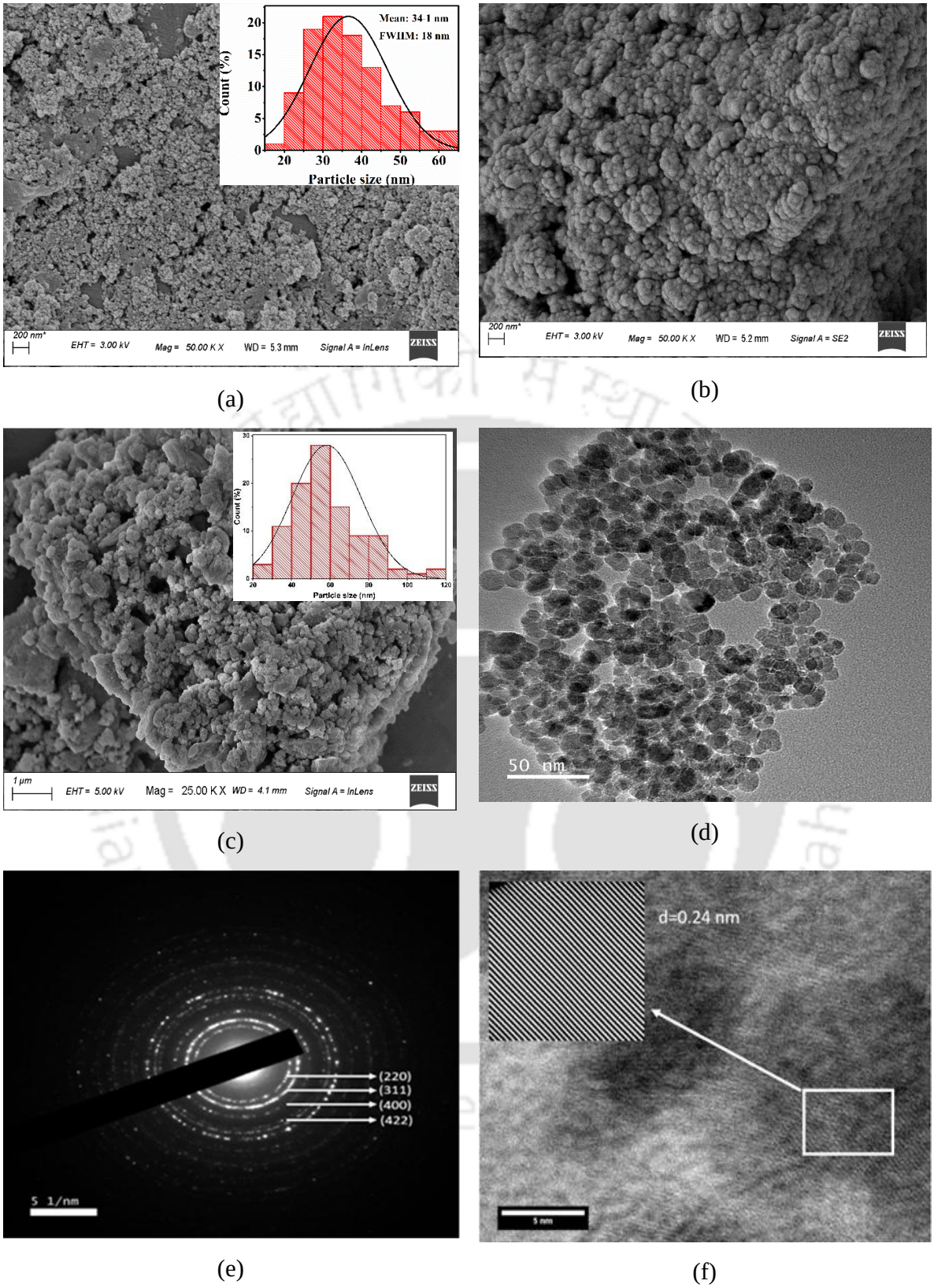

Figure 3.7. FE-SEM micrographs of (a) Fe_3O_4 nanoparticles, (b) Fe_3O_4-NH_2, and (c) Fe_3O_4@Laccase nanocomposite; (d) FE-TEM micrograph of Fe_3O_4@Laccase (e) SAED pattern of Fe_3O_4@Laccase nanocomposite, and (f) HR-TEM of Fe_3O_4@Laccase nanocomposite

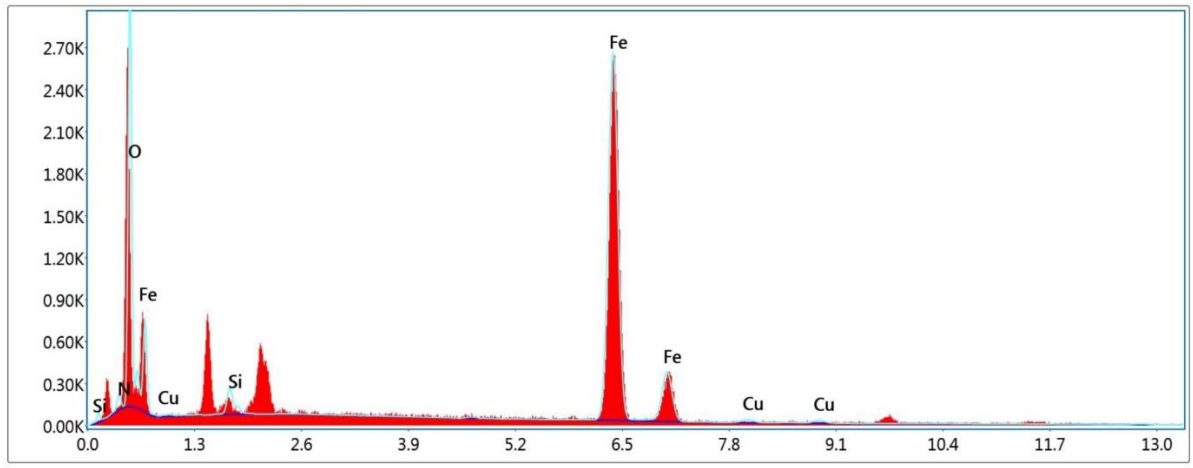

(a)

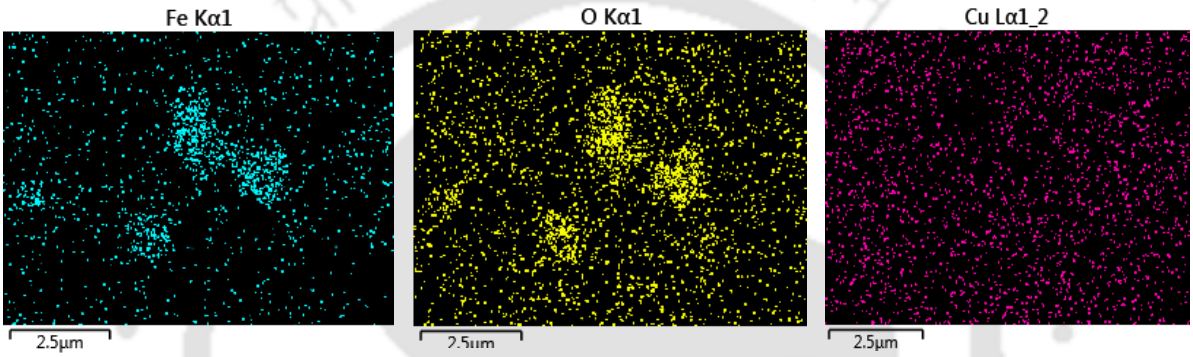

(b) (c) (d)

Figure 3.8. (a) EDX spectrum of Fe_3O_4@Laccase and (b-d) elemental mapping of Fe_3O_4@Laccase nanocomposite

3.3.2 Results of optimization using response surface methodology

The experimental results obtained from the Central Composite Design (CCD) for wastewater treatment, considering three process parameters as optimization variables (Fe_3O_4@Laccase dose - X_1, pH - X_2, and Temperature - X_3), are presented in Table 3.2. The relationship between the response variable (removal percentage of COD) and the optimization variables can be described by a second-order polynomial equation:

$$\%\ COD\ removal = 62.41 + 7.38\,X_1 + 5.49\,X_2 + 3.47\,X_3 + 0.1475\,X_1\,X_2 + 0.0050\,X_1\,X_3 + 0.3350\,X_2\,X_3 - 10.65\,X_1^2 - 8.85\,X_2^2 - 2.76\,X_3^2$$

The statistical design of experiments yielded the following set of optimum parameters for maximum predicted COD removal of 65.6 %: pH = 4.5, Fe_3O_4@Laccase dose = 1.46 g/L, and temperature = 66.5 ^oC. The analysis of variance (ANOVA) for the Central Composite Design (CCD) is presented in Table 3.3. The ANOVA results indicate a high *F*-value of 47.70 and an extremely low *p*-value (<0.0001) for the overall model. These findings indicate that the model fits the data very well.

Validation experiment: A validation experiment was conducted in triplicate at the optimum set of parameters predicted by the statistical design of experiments. The time profile of COD removal in the validation experiment is shown in Fig. 3.9. The final COD removal was 61.7%, which is in close agreement with the predicted COD removal of 65.6% obtained from the statistical experimental design.

Intensification of COD removal using sonication

Post optimization of the parameters for the wastewater treatment using Fe_3O_4@Laccase, experiments were conducted with the application of 35 kHz sonication (10% duty cycle) to the reaction solution using an ultrasound bath with a theoretical power rating of 35 W, as stated earlier. The time profiles of COD removal are shown in Fig. 3.9. The final COD removal after 1 h treatment was 90.3%, corresponding to 46.3% enhancement over the COD removal obtained with mechanical agitation. Table 3.4 represents the characteristics of wastewater before and after the treatment.

Table 3.3. The ANOVA for the central composite design

Source	Degree of freedom	Sum of square	Mean square	*F*-value	*p*-value	
Model	9	2853.49	317.05	47.70	< 0.0001	Significant
X_1	1	545.23	545.23	82.02	< 0.0001	
X_2	1	301.07	301.07	45.29	< 0.0001	
X_3	1	120.69	120.69	18.16	0.0017	
X_1X_1	1	0.1740	0.1740	0.0262	0.8747	Insignificant
X_2X_2	1	0.0002	0.0002	0.0000	0.9957	Insignificant
X_3X_3	1	0.8978	0.8978	0.1351	0.7209	Insignificant
X_1X_2	1	311.83	311.83	46.91	< 0.0001	
X_1X_3	1	215.56	215.56	32.43	0.0002	
X_2X_3	1	20.93	20.93	3.15	0.1064	Insignificant
Error	10	66.47	6.65			
Lack-of-Fit	5	30.67	6.13	0.8564	0.5655	Not significant
Pure Error	5	35.81	7.16			
Total	19	2919.96				
Quality of quadratic model						
R^2				0.977		
Adjusted R^2				0.956		
Predicted R^2				0.908		

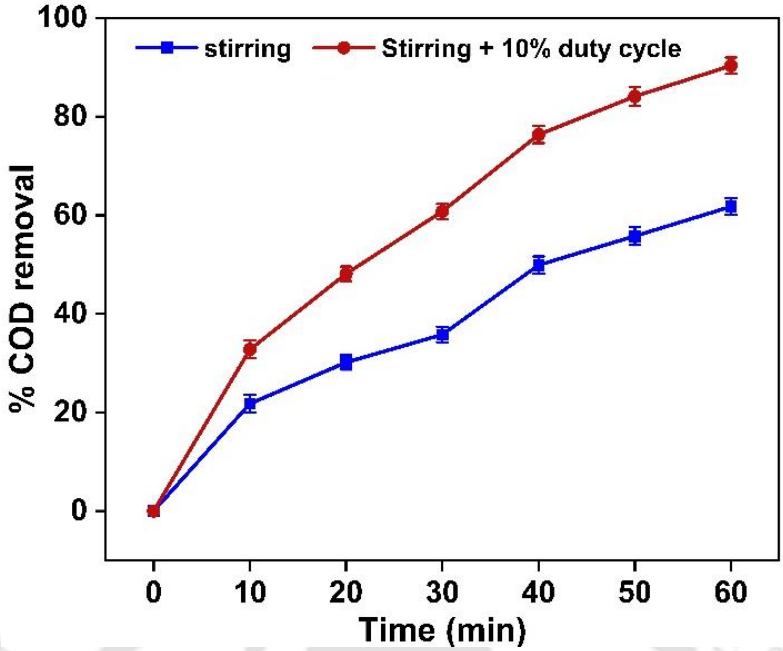

Figure 3.9. Time profiles of COD removal in validation experiment (with mechanical stirring of solution) and sonication experiment (mechanical stirring + sonication @10% duty cycle). Other experimental conditions: Fe_3O_4@Laccase dose = 1.46 g/L; pH = 4.5 and temperature = 66.5 ^oC

Table 3.4. Physico-chemical characteristics of WW before and after treatment

Parameter	Before treatment	After treatment
pH	8.31 ± 0.85	6.78 ± 0.28
Color	Mustard Yellow	Colourless
Initial COD	3246 ± 20 mg/L	314.54 ± 10 mg/L
Initial BOD	1000 ±12 mg/L	238.34 ± 8 mg/L
Initial TOC	1098 ± 10 mg/L	182.2 ± 12 mg/L
Biodegradability index (BOD_5: COD)	0.31 ± 0.05	0.75 ± 0.04

The values given in the table are averages of triplets.

3.3.3 Kinetics of COD removal using Fe_3O_4@Laccase nanocomposite

Experiments were conducted using wastewater with different initial COD values to obtain the kinetic parameters of sono-enzymatic removal of COD using Fe_3O_4@Laccase nanocomposite.

The reaction velocity at initial substrate concentration ($v_0 = v|_{[S_0]}$) was obtained from the time profiles of COD removal with time. The data of v_0 vs [S_0] was fitted with mathematical expressions of different kinetic models (viz. Michaelis-Menten, Haldane and Yano and Koga). This yielded maximum reaction velocity (V_{max}), the Michaelis constant (K_m), and the inhibition constant (K_i). The results of the fitting of kinetic expressions are given in Table 3.5, whereas the fitting of different kinetic expressions to the experimental data is shown in Fig. 3.10. It could be seen that Haldane kinetic model, which accounts for the substrate inhibition, fits well with the data in both control and test experiments. Comparison of the values of Haldane kinetic model parameters (V_{max}, K_m, and K_i) for control and test experiments reveals that V_{max} increases while K_m reduces with the application of sonication in the test experiments. A rise in V_{max} indicates a faster reduction of COD, while a reduction in K_m indicates higher enzyme-substrate affinity. The values of the inhibition constant K_i, viz. 11.67 and 13.45 mg/L for control and test experiments, reveal that substrate inhibition reduces in the presence of sonication. Nonetheless, the K_i values are relatively small compared to the initial COD levels used in this study. The initial COD values of the wastewater used in the experiments ranged from 40 to 200 mg/L. This essentially means that laccase suffers from significant substrate inhibition during the treatment. Thus, the sonication-induced enhancement of COD reduction in test experiments is strongly limited by the substrate inhibition of laccase. To obtain greater insight into the sonication-induced enhancement of COD removal, we have done the secondary structure analysis of the immobilized laccase enzyme, as described in the next section.

Table 3.5. Modeling of the enzyme kinetics in control and test experiments

Model name	Parameters	Control[#]	Test[#]
Michaelis – Menten	V_{max} (mg/L min)	0.021	0.045
	K_m (mg/L)	147.2	136.46
	R^2	0.97	0.99
Haldane	V_{max} (mg/L min)	0.014	0.019
	K_m (mg/L)	90	81
	K_i (mg/L)	11.67	13.45
	R^2	0.99	0.98
Yano and Koga	V_{max} (mg/L min)	0.010	0.013
	K_m (mg/L)	33.9	31.18
	K_i (mg/L)	1.1	1.9
	R^2	0.9459	0.9423

Control experiments – mechanical stirring @ 300 rpm, Test experiments – mechanical stirring with sonication @ 10% duty cycle.

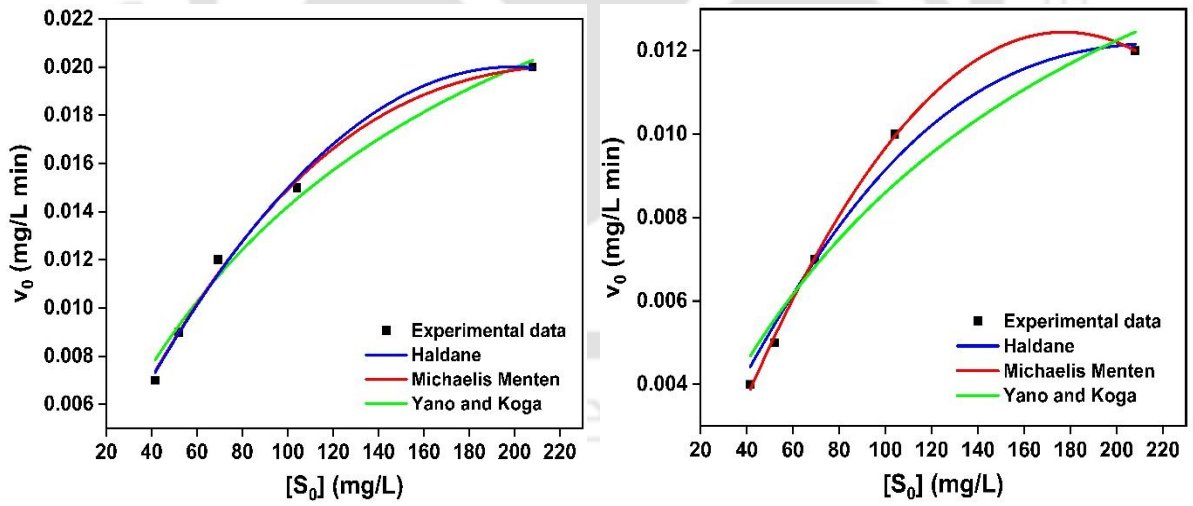

Figure 3.10. The fitting of different kinetic expression to the experimental data (a) control experiment and (b) test experiment

3.3.4 Secondary structure analysis of immobilized laccase

The catalytic efficiency of an enzyme is strongly connected to its secondary structure. Exposure to sonication induces significant changes in the secondary structure of laccase. Deconvolution of the FTIR spectrum using multi-peak fitting of the Gaussian function of laccase before and after sonication helps deduce the secondary structure changes. The amide-I band (1700-1600 cm^{-1}) is the most sensitive spectral region in the FTIR spectrum of enzymes; it represents the secondary structural components of proteins. The deconvolutions of the FTIR spectrum of Fe_3O_4@Laccase nanocomposite in the control and test experiments are shown in Fig. 3.11. For deconvolution of FTIR spectra, the selected spectral regions corresponding to different components (or fractions) of the secondary structure of the enzyme were as follows: β-strands (1627 ± 2.0 cm^{-1}), β-sheets (1638 ± 2.0 cm^{-1}), random coils (1648 ± 2.0 cm^{-1}), α-helix (1656 ± 2.0 cm^{-1}) and β-turns (1664 - 1690 cm^{-1}) (Kong and Yu 2007). The deconvolution results revealed significant alterations in the secondary structure of the enzyme. Percentages (or fractions) of secondary structure components of enzyme in Fe_3O_4@Laccase were as follows: Control experiment: β-strands = 10.5%, β-sheets = 30.8%, random coils = 16.6%, α-helix = 18.5% and β-turns = 23.6%, Test experiment: β-strands = 14.6%, β-sheets = 34.7%, random coils = 24.6%, α-helix = 10.8% and β-turns = 15.4%. These results clearly show that sonication induces marked change in the secondary structure of the enzyme. A major change in the secondary structure of laccase is the rise in random coil content (from 16.6% to 24.6%), along with a minor rise in β-strands and β-sheets. The α-helix and β-turns content is reduced by 41.6% and 34.7%, respectively. Significant changes in the secondary structure of the enzyme after immobilization and sonication result in a marked shift in its catalytic activity (Wang et al. 2012). A rise in random coil content with concurrent lessening of α-helix content causes relaxation of the enzyme structure with widening or enlargement of the binding pocket. This provides easier access to the substrate's binding pocket and stabilizes the substrate-enzyme

complex. These effects are manifested in terms of enhancement in enzyme efficiency and faster kinetics of COD reduction.

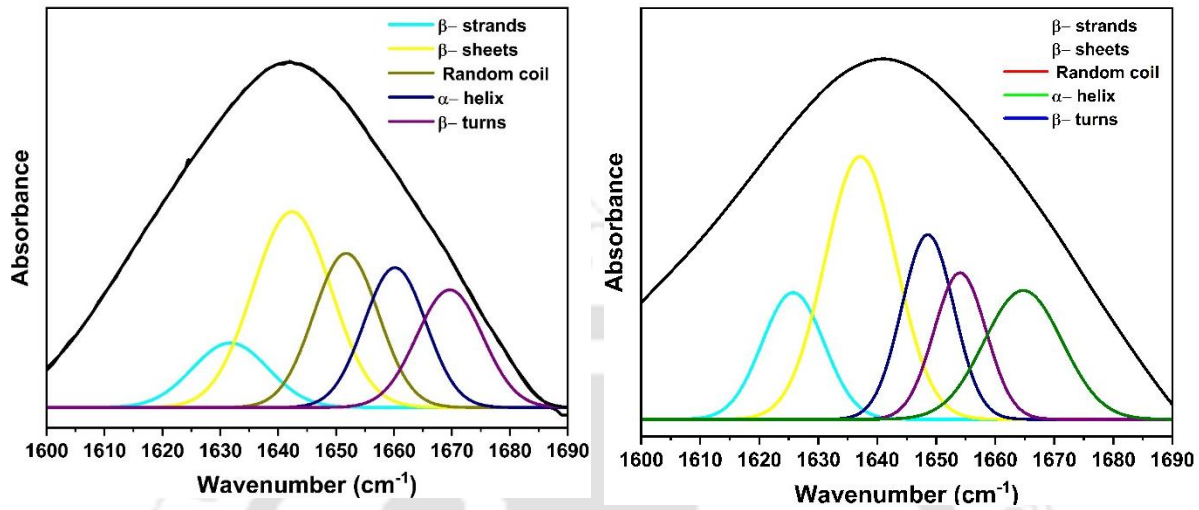

Figure 3.11. Secondary structure of (a) control and (b) test (Control experiments – mechanical stirring @ 300 rpm, Test experiments – mechanical stirring with sonication @ 10% duty cycle)

3.3.5 LC-MS analysis

Figure 3.12 shows the LC-MS chromatograms of wastewater samples before and after treatment. The list of identified contaminants in original wastewater through LC-MS/QTOF analysis is presented in Table A3.3 provided in the Appendix A3 The major contaminants that get degraded ≥ 75% are: 3,4-methylene-dioxymethamphetamine (76.1%), 6,12-diazaanthanthrene (77.5%), 2,2-diethylpent-4-enamide (80.4%), 2-aminoundecanoic acid (82.6%), 1,1,2-triethoxyethane (83.8%), anapheline (86%), octan-2-amine (88.7%), 1-dodecanamine (89.7%) and bis(methoxymethyl)-melamine (97.6%). These contaminants have rather diverse origins, such as pharmaceutical and organic and inorganic compounds.

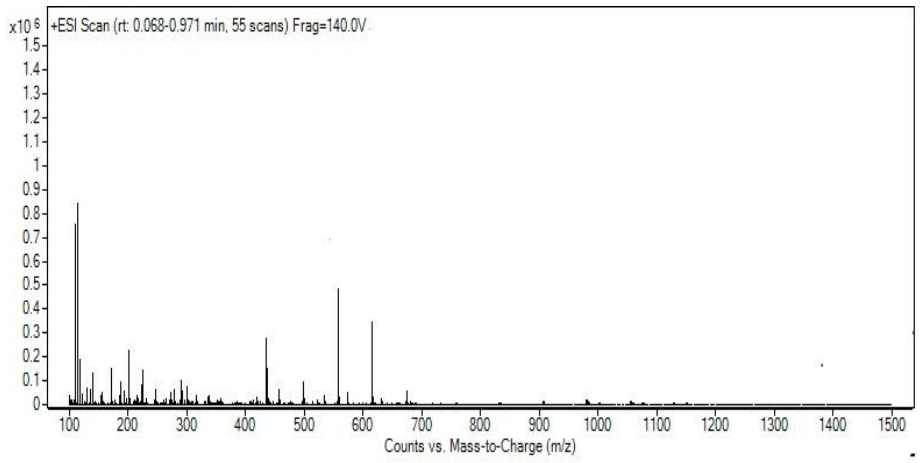

(a)

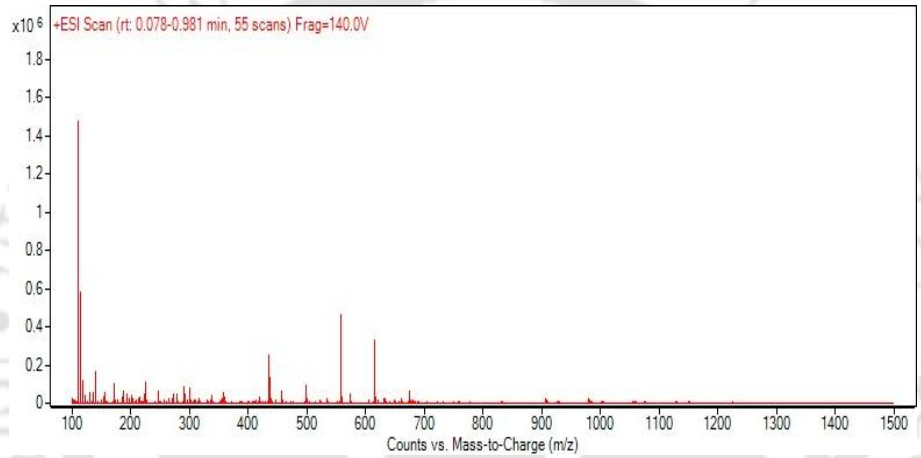

(b)

Figure 3.12. LC-MS chromatogram of (a) original (untreated) wastewater, (b) wastewater after 60 min treatment

3.3.6 Toxicity analysis

Reduction in the toxicity of wastewater during the sonoenzymatic treatment was assessed using seed germination technique. The seeds of *Vigna radiata* were grown in original and treated wastewater samples, as shown in Fig. 3.13. The germination percentage was used as a measure of reduction in toxicity. As a control experiment, the seeds were also grown in deionized water. Observations revealed that all seeds in deionized water showed healthy growth with 100% germination. Conversely, none of the seeds in untreated or original wastewater showed any

growth (0% germination), while 70% of seeds in treated wastewater underwent germination. These findings reveal that sonoenzymatic treatment using Fe_3O_4@Laccase effectively mitigated the toxicity of the wastewater.

(a) (b)

Figure 3.13. Toxicity assay of wastewater using seed germination technique. (a) seed germination in original wastewater, (b) seed germination in wastewater after treatment

3.3.7 Reusability and stability of Fe_3O_4@Laccase

One of the primary benefits of immobilized enzymes is their effective separation and reuse in consecutive wastewater treatment cycles. In a typical experiment, following the completion of treatment, the Fe_3O_4@Laccase nanocomposite particles in the solution were collected and separated using an external magnet, rinsed several times with DI water, and added to another batch of 50 mL solution for the next cycle of treatment. The % COD removal reduced marginally in six successive treatment cycles as 90.3% > 88.8% >85.1% > 81% > 79.8% > 76.3%. Similarly, the enzymatic activity of Fe_3O_4@Laccase reduced in the order 97% > 95% > 90% > 82% > 76% > 70% in six treatment cycles. The remarkable stability of immobilized laccase can be attributed to the glutaraldehyde linkage, which allows for multi-point attachment of the enzyme to Fe_3O_4 nanoparticles, resulting in the biocatalyst's structural rigidity (Cabana

et al. 2009). These findings also indicate the ability of immobilized laccase (Fe_3O_4@Laccase) for long-term use, which is essential from the viewpoint of industrial application. A graphical schematic of the COD removal and activity recovery is given in Fig. 3.14.

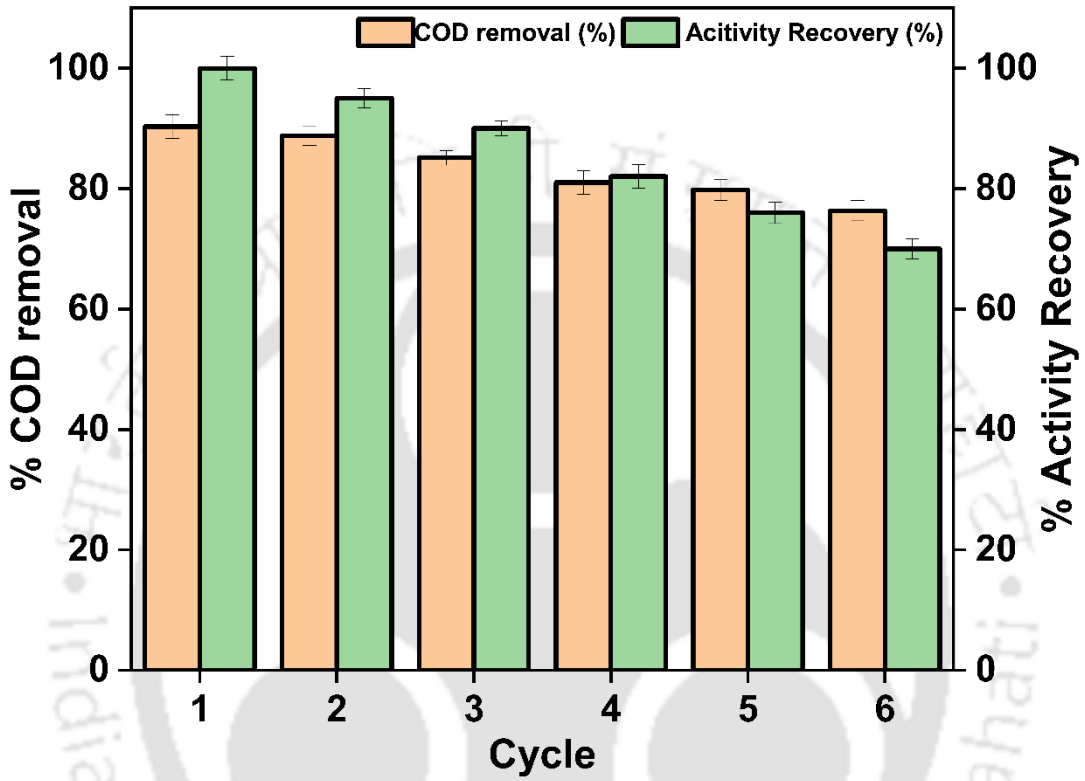

Figure 3.14. Reusability and stability analysis of Fe_3O_4@Laccase nanocomposite within six successive cycles (under the optimum condition: Fe_3O_4@Lacacse dose = 1.46 g/L, pH =4.5, and Temperature=66.5 ^oC

3.4. Conclusion

This study has demonstrated effective COD reduction of industrial wastewater using sonoenzymatic treatment. Laccase immobilized on magnetic Fe_3O_4 particles (Fe_3O_4@Laccase) was used as the biocatalyst for treatment. Fe_3O_4 was synthesized using the coprecipitation technique followed by amino-functionalization of the particle surface. Laccase was immobilized on the surface of these particles using glutaraldehyde cross-linking. Optimization

of the physical parameters pH, temperature, and Fe_3O_4@Laccase loading with 300 rpm mechanical stirring achieved 61.7% COD removal. Applying 35 kHz sonication (10% duty cycle) during treatment enhanced the COD removal to 90.3%. Kinetic analysis of the enzymatic treatment using the Haldane model revealed enhancement of substrate affinity of the enzyme and reduction in substrate inhibition with the application of sonication. Analysis of the secondary structure of immobilized laccase using deconvolution of FTIR spectra revealed significant changes in the secondary structure composition with a reduction in α-helix and β-turn content and a rise in random coil content. These changes lead to the relaxation of the enzyme with the widening of binding pockets, manifested in the enhancement of kinetics. The exact mechanism of laccase was depicted in section A3.2 (in Appendix A3). Toxicity assessment using the seed germination technique revealed a ~ 70% reduction in toxicity. The Fe_3O_4@Laccase biocatalyst also showed excellent recoverability and retention of enzymatic activity till 6 consecutive treatment cycles. These results clearly show the potential of Fe_3O_4@Laccase nanocomposite as a green catalyst for the effective treatment and mineralization of industrial wastewater.

References

Agarry SE, Audu TOK, Solomon BO (2009) Substrate inhibition kinetics of phenol degradation by Pseudomonas fluorescence from steady state and wash-out data. Int J Environ Sci Technol 6:443–450. https://doi.org/10.1007/BF03326083

American Public Health Association. (1926). *Standard methods for the examination of water and wastewater* (Vol. 6). American Public Health Association.

Babaei AA, Kakavandi B, Rafiee M, et al (2017) Comparative treatment of textile wastewater by adsorption, Fenton, UV-Fenton, and US-Fenton using magnetic nanoparticles-

functionalized carbon (MNPs@C). J Ind Eng Chem 56:163–174. https://doi.org/10.1016/j.jiec.2017.07.009

Cabana H, Jones JP, Agathos SN (2009) Utilization of cross-linked laccase aggregates in a perfusion basket reactor for the continuous elimination of endocrine-disrupting chemicals. Biotechnol Bioeng 102:1582–1592. https://doi.org/10.1002/bit.22198

Chakma S, Moholkar VS (2016) Investigations in sono-enzymatic degradation of ibuprofen. Ultrason Sonochem 29:485–494. https://doi.org/10.1016/j.ultsonch.2015.11.002

Chen Z, Yao J, Ma B, et al (2022) A robust biocatalyst based on laccase immobilized superparamagnetic Fe_3O_4@SiO_2–NH_2 nanoparticles and its application for degradation of chlorophenols. Chemosphere 291:132727. https://doi.org/10.1016/j.chemosphere.2021.132727

Choudhury H, Malani R (2013) Acid catalyzed biodiesel synthesis from Jatropha oil: Mechanistic aspects of ultrasonic intensification. Chem Eng J Amst Neth 231:262–272. https://doi.org/10.1016/j.cej.2013.06.107

El-Batal AI, ElKenawy NM, Yassin AS, Amin MA (2015) Laccase production by Pleurotus ostreatus and its application in synthesis of gold nanoparticles. Biotechnol Rep Amst Neth 5:31–39. https://doi.org/10.1016/j.btre.2014.11.001

Gonçalves I, Silva C, Cavaco-Paulo A (2015) Ultrasound enhanced laccase applications. Green Chem 17:1362–1374. https://doi.org/10.1039/C4GC02221A

Guo X, Mao F, Wang W, et al (2015) Sulfhydryl-Modified Fe_3O_4@SiO_2 Core/Shell Nanocomposite: Synthesis and Toxicity Assessment in Vitro. ACS Appl Mater Interfaces 7:14983–14991. https://doi.org/10.1021/acsami.5b03873

Hou C, Wang Y, Ding Q, et al (2015) Facile synthesis of enzyme-embedded magnetic metal–organic frameworks as a reusable mimic multi-enzyme system: mimetic peroxidase properties and colorimetric sensor. Nanoscale 7:18770–18779. https://doi.org/10.1039/C5NR04994F

Hu J, Yuan B, Zhang Y, Guo M (2015) Immobilization of laccase on magnetic silica nanoparticles and its application in the oxidation of guaiacol, a phenolic lignin model compound. RSC Adv 5:99439–99447. https://doi.org/10.1039/C5RA14982G

Hussain A, Dubey SK, Kumar V (2015) Kinetic study for aerobic treatment of phenolic wastewater. Water Resour Ind 11:81–90. https://doi.org/10.1016/j.wri.2015.05.002

Ingole PM, Rathod VK (2023) Ultrasound-assisted enzymatic degradation of naproxen. J Indian Chem Soc 100:101040. https://doi.org/10.1016/j.jics.2023.101040

Kadam AA, Jang J, Lee DS (2017) Supermagnetically Tuned Halloysite Nanotubes Functionalized with Aminosilane for Covalent Laccase Immobilization. ACS Appl Mater Interfaces 9:15492–15501. https://doi.org/10.1021/acsami.7b02531

Kong J, Yu S (2007) Fourier transform infrared spectroscopic analysis of protein secondary structures. Acta Biochim Biophys Sin 39:549–559. https://doi.org/10.1111/j.1745-7270.2007.00320.x

Liu X, Lei L, Li Y, et al (2011) Preparation of carriers based on magnetic nanoparticles grafted polymer and immobilization for lipase. Biochem Eng J 56:142–149. https://doi.org/10.1016/j.bej.2011.05.013

Lü C, Cui Z, Guan C, et al (2003) Research on Preparation, Structure and Properties of TiO_2/Polythiourethane Hybrid Optical Films with High Refractive Index. Macromol Mater Eng 288:717–723. https://doi.org/10.1002/mame.200300067

Miljevic B, Hedayat F, Stevanovic S, et al (2014) To Sonicate or Not to Sonicate PM Filters: Reactive Oxygen Species Generation Upon Ultrasonic Irradiation. Aerosol Sci Technol 48:1276–1284. https://doi.org/10.1080/02786826.2014.981330

Moholkar VS, Sable SP, Pandit AB (2000) Mapping the cavitation intensity in an ultrasonic bath using the acoustic emission. AIChE J 46:684–694. https://doi.org/10.1002/aic.690460404

Peng ZG, Hidajat K, Uddin MS (2004) Adsorption of bovine serum albumin on nanosized magnetic particles. J Colloid Interface Sci 271:277–283. https://doi.org/10.1016/j.jcis.2003.12.022

Pulicharla R, Das RK, Kaur Brar S, et al (2018) Degradation kinetics of chlortetracycline in wastewater using ultrasonication assisted laccase. Chem Eng J 347:828–835. https://doi.org/10.1016/j.cej.2018.04.162

Rashid SS, Mustafa AH, Ab Rahim MH (2022) Ferromagnetic nanoparticles synthesis and functionalization for laccase enzyme immobilization. Mater Today Proc 48:916–919. https://doi.org/10.1016/j.matpr.2021.03.661

Rouhani S, Azizi S, Maaza M, et al (2021) Covalent immobilization of laccase on Fe_3O_4-graphene oxide nanocomposite for biodegradation of phenolic compounds. Environ Prot Eng 47:. https://doi.org/10.37190/epe210107

Santhosh C, Velmurugan V, Jacob G, et al (2016) Role of nanomaterials in water treatment applications: A review. Chem Eng J 306:1116–1137. https://doi.org/10.1016/j.cej.2016.08.053

Verma K, Moholkar VS (2023) Mineralization of Industrial Wastewater by a Hybrid Technique of Adsorption (Fe_3O_4@AC Nanocomposite) + Heterogeneous Fenton + Sonication and Discernment of Synergistic Effects. Ind Eng Chem Res acs.iecr.3c00427. https://doi.org/10.1021/acs.iecr.3c00427

Wang D, Lou J, Yuan J, et al (2021) Laccase immobilization on core-shell magnetic metal-organic framework microspheres for alkylphenol ethoxylate compound removal. J Environ Chem Eng 9:105000. https://doi.org/10.1016/j.jece.2020.105000

Wang Z, Lin X, Li P, et al (2012) Effects of low intensity ultrasound on cellulase pretreatment. Bioresour Technol 117:222–227. https://doi.org/10.1016/j.biortech.2012.04.015

Xu R, Bi H, He G, et al (2014) Synthesis of Cu-Fe_3O_4@graphene composite: A magnetically separable and efficient catalyst for the reduction of 4-nitrophenol. Mater Res Bull 57:190–196. https://doi.org/10.1016/j.materresbull.2014.05.045

Zhao M, Zhang X, Deng C (2015) Rational synthesis of novel recyclable Fe_3O_4@MOF nanocomposites for enzymatic digestion. Chem Commun 51:8116–8119. https://doi.org/10.1039/C5CC01908G

Zheng ng, Jiang Y (2012) 260365 Biomimetic Synthesis of Magnetic Composite Particles for Laccase Immobilization

Zhu A, Yuan L, Liao T (2008) Suspension of Fe_3O_4 nanoparticles stabilized by chitosan and o-carboxymethylchitosan. Int J Pharm 350:361–368. https://doi.org/10.1016/j.ijpharm.2007.09.004

Appendix A3

Table A3.1. Summary of the previous literature on degradation of biorecalcitrant pollutants using free as well as immobilized laccase

Specific Pollutants	Method/ catalyst	Process parameters	Results	References
Naproxen	Sono-enzymatic/ Free laccase	Laccase conc. = 0.15% (w/v), Power = 50 W, T = 40 ^{o}C and t = 150 min	96 % degradation and 80-85 % Toxicity reduced	(Ingole and Rathod 2023)
Bisphenol A	Batch study/ Laccase immobilized on MOF	FL@ZIF-8(PA) dose= 0.4 g/g, pH = 5, T = 30 ^{o}C and t = 12 h	90.3 % degradation was achieved	(Sun et al. 2023)
Malachite green dye	Incubator shaker/ Laccase immobilized on biochar	Dye conc. = 50 mg/L, speed = 180 rpm, T = 30^{o}C and t = 24 h	73.8 % degradation was obtained	(Pandey et al. 2023)
Congo red dye		Dye conc. = 50 mg/L, speed = 180 rpm, T = 30^{o}C and t = 24 h	88.1 % degradation was obtained	
Phenolic compounds	Mechanical Shaker/ Fe_3O_4@Laccase	Laccase loading = 39.9 mg/g, pH = 4 , T = 25 ^{o}C and t = 12 h	Removal efficiency was obtained at 9.8% for vanillin, 67.3% for syringaldehyde, 100% for ferulic acid and 38.5% for p-coumaric acid	(Li et al. 2022)
Phenolic compounds	Mechanical stirring/ Lac/Fe_3O_4/GO	Lac/Fe_3O_4/GO dose = 45 mg, pH = 5 and t = 8 h.	74, 8, and 88%, degradation of phenol, *p*-chlorophenol, and 2,4-	(Rouhani et al. 2021)

			dichlorophenol and 86% activity recovery were obtained	
Phenolic pollutants	Mechanical incubator/ MNP-rSLAC	Laccase = 2U/mL, pH = 8, T = 37 ^{o}C, speed = 50 rpm and t = 2 h	100% degradation and 73% of initial activity was reatined	(Yadav et al. 2021)
Direct Red 23 dye	Batch study/ Fe_3O_4@Laccase	Fe_3O_4@Laccase dose = 300 mg/L, pH = 5, T = 50^{o}C and t = 60 min	83 % degradation was obtained and 70% decolorization after sixth cycle	(Alsaiari et al. 2021)
Bisphenol A	Magnetic stirrer/ Fe_3O_4@Laccase	BPA conc. = 60 ppm, pH = 7, T = 45 ^{o}C and t = 11 h	87.3 % BPA removal was obtained	(Sadeghzadeh et al. 2020)
Bisphenol A	Incubator shaker/ MNFs	BPA conc. = 25 mg/L, MNFs conc. = 0.6 g/L, pH = 5.5, speed = =120rpm and t = 45 min	100 % degradation was achieved	(Fu et al. 2019)
Chlortetracycline	Sono-enzymatic/ free laccase	Laccase conc.= 0.5 U L^{-1}, CTC conc.= 2 mg/L, pH = 4.5 and t = 2h	80 % degradation of CTC	(Pulicharla et al. 2018)
Chlorpyrifos	Batch study/ Fe_3O_4@Laccase	Fe_3O_4@Laccase dose = 10 mg, pH = 7, T = 60 ^{o}C, Mechanical shaking = 150 rpm and t = 12 h	99 % degradation and 95 % activity recovery were obtained	(Das et al. 2017)
Tetracycline	Incubator shaker/ Fe_3O_4@Laccase	TC conc. = 100 µg/mL, Fe_3O_4@Laccase dose = 10 U/mL, pH = 6, T = 25 ^{o}C and t =12 h	80% removal was obtained	(Yang et al. 2017)
Industrial effluent	**Sono-enzymatic/ Fe_3O_4@Laccase**	**Fe_3O_4@Laccase dose = 1.46 g/L, pH = 4.5, T = 66.5 ^{o}C, 10 % duty cycle and t= 60 min**	**61.7% COD removal obtained with stirring whereas with 10% duty cycle 90.3% COD removal was obtained and 70% reduction in toxicity with 70% activity recovery**	**This study**

Table A3.2. The details of the instrumentation and mobile phase composition

Instrument	LCMS/QTOF (Agilent 1100/1200/1260/1290 LC).
Nebulizer pressure (psi)	20
Gas temperature (°C)	325
Sheath gas flow rate (l/min)	12
Mode	Gradient

A3.1 Enzyme activity assay

For the laccase activity assay, the ABTS (2,2-azino-bis(3-ethylbenzothiazoline-6-sulfonic acid)) oxidation rate was measured following a previously described method (Qiu et al. 2020). In brief, the reaction mixture consisted of an appropriate amount of either free laccase or immobilized laccase (1 mL) and ABTS solution (1 mM, 450 µL) prepared using acetate buffer solution (0.1 M, 500 µL) at the optimal pH value for each case. The reaction mixture was allowed to react for 5 minutes. Following the reaction, the supernatant was separated using a magnet, and the absorbance was measured at 420 nm using a UV-visible spectrometer. The laccase activity was determined by defining one unit (1 U) as the amount of laccase required to catalyze the conversion of 1 µmol of ABTS within one minute. The formulas for calculating laccase activity were as follows:

$$\text{Expressed activity (U/g biocatalyst)} = \frac{A \times 10^6 \times V_t}{\varepsilon \times t \times m_1} \quad (1)$$

Where, A – absorbance of $ABTS^{2+}$ at 420 nm; V_t – volume of reaction system (L); ε – molar extinction coefficient of $ABTS^{2+}$ (36000 M^{-1} cm^{-1}); t – reaction time (min); m_1 – amount of immobilized laccase (g).

The activity recovery of the immobilized enzyme was calculated using the formula proposed

by Sheldon and van Pelt (Sheldon and van Pelt 2013).

$$\text{Activity Recovery (\%)} = \frac{\text{Free Enzyme Activity before Immobilization}}{\text{Immobilized Enzyme Activity}} \times 100 \qquad (2)$$

In this equation, the Free Enzyme Activity before Immobilization refers to the activity of the enzyme prior to its immobilization, and Immobilized Enzyme Activity represents the activity of the enzyme after immobilization. The protein content was determined according to Bradford method (Zheng and Jiang 2012).

Table A3.3. List of identified contaminants in the wastewater using LC-MS/ QTOF that get degraded ≥ 75% during sono-enzymatic treatment

Compound name	Chemical formula	m/z	Mass (g/mol)	% Reduction
Pyridine-3,4-diamine	[C_5 H_7 N_3]	110.071	109.13	60.8
Octan-2-amine	[C_8 H_{19} N]	130.1589	129.24	88.7
1-Cyclopentylpiperazine	[C_9 H_{18} N_2]	155.1544	154.24	67.1
Methyl 2-amino-3-hydroxy propanoate hydrochloride	[C_4 H_{10} Cl N O_3]	156.0423	155.58	65.1
2,2-diethylpent-4-enamide	[C_9 H_{17} N O]	156.1384	155.24	80.4
N-(3-(Dimethylamino)propyl) Methacrylamide	[C_9 H_{18} N_2 O]	171.1493	170.25	79.5
1,1,2-triethoxyethane	[C_8 H_{18} O_3]	185.1149	162.23	83.8
1-Dodecanamine	[C_{12} H_{27} N]	186.2218	185.35	89.7
3,4-methylenedioxymethamphet Amine	[C_{11} H_{15} N O_2]	194.1177	193.24	76.1
2-aminoundecanoic acid	[C_{11} H_{23} N O_2]	202.1804	201.31	82.6
Bis(methoxymethyl)melamine	[C_7 H_{14} N_6 O_2]	215.1256	214.2%3	97.6
3-cyanopropyl(3-phenylpropyl) Azanide	[C_{13} H_{17} N_2]	224.1283	201.29	74.9
Anapheline	[C_{13} H_{24} N_2 O]	225.1964	224.34	86
6,12-Diazaanthanthrene	[C_{20} H_{10} N_2]	279.0936	278.3	77.5

A3.2. Mechanism of laccase-induced COD reduction

COD reduction by laccase enzyme essentially occurs due to oxidative degradation of the organic contaminants present in water. The wastewater used in this study contains numerous contaminants, and hence, it will be difficult for us to describe the mechanism of laccase specific to any particular compound. In such difficulty, we describe herewith the general mechanism of laccase-induced oxidation of the contaminants. Laccases are enzymes characterized by the presence of four copper atoms distributed across different binding sites, classified into three types: one Cu-type 1 (T1), one Cu-type 2 (T2), and two Cu-type 3 (T3) (Rodríguez-Couto 2018). Various 3-D structures of laccases have been documented. The typical reaction catalyzed by laccase involves the oxidation of a phenolic compound accompanied by the simultaneous reduction of molecular oxygen to water. This process entails four cycles of single-electron oxidations leading to the formation of free radicals. Subsequently, the enzyme facilitates the reduction of one molecule of oxygen, resulting in the generation of two water molecules. To achieve this, the enzyme must store four electrons before the reduction of oxygen. The reduction of oxygen is likely to occur in two steps involving bound oxygen intermediates. During laccase-catalyzed oxidation, the substrate loses a single electron, forming a free radical. The aryl radicals formed as a result of laccase activity are unstable and may undergo subsequent non-enzymatic oxidation or reduction reactions. These radicals can also couple with other phenolic structures or undergo polymerization, resulting in the production of vividly colored products. Laccases exhibit broad substrate specificities, capable of oxidizing a diverse range of compounds including di- and polyphenols, aromatic amines, and various other compounds (Tuomela and Hatakka 2019). Their ability to oxidize multiple substrates contributes to their significance in various biological and industrial processes. During the substrate oxidation process facilitated by laccase enzymes, the four copper ions situated in the enzyme's active site play a crucial role in transferring electrons involved in the

reaction. It's believed that the T1 copper site initially accepts electrons from the reducing substrates. These electrons are then conveyed to the three-nuclear copper cluster site (T2/T3), where the reduction of oxygen to water takes place. Consequently, this process leads to the oxidation of four substrate molecules into four radicals and the simultaneous reduction of one oxygen molecule into two water molecules as depicted in Figure A1 (Viikari et al. 2009).

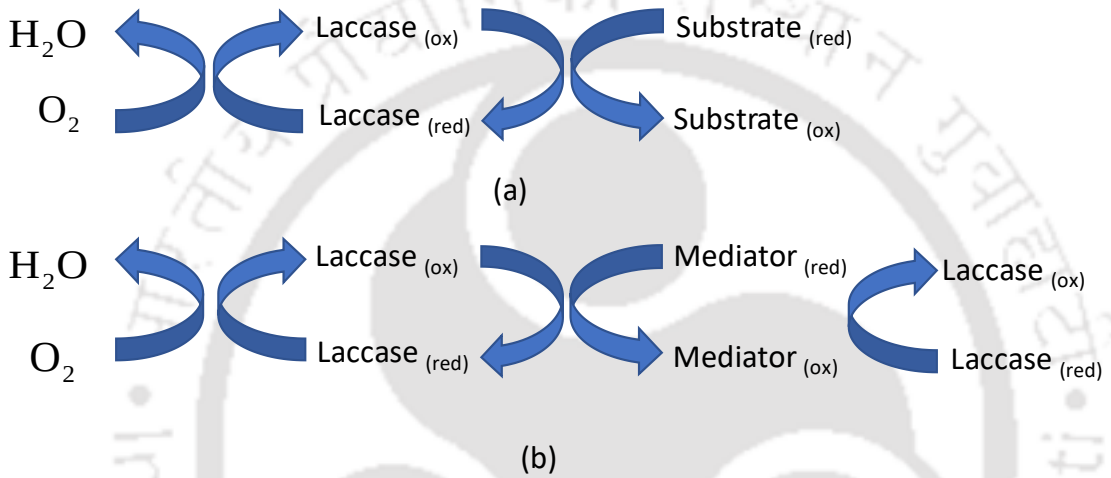

Figure A1. Schematic depiction of Laccase-catalyzed Redox Reactions for Substrate Oxidation: Absence (a) and Presence (b) of Redox Mediators (re-drawn from Rodriguez – Couto (Rodríguez-Couto 2018))

References

Alsaiari NS, Amari A, Katubi KM, et al (2021) The Biocatalytic Degradation of Organic Dyes Using Laccase Immobilized Magnetic Nanoparticles. Appl Sci 11:8216. https://doi.org/10.3390/app11178216

Das A, Singh J, K.N. Y (2017) Laccase immobilized magnetic iron nanoparticles: Fabrication and its performance evaluation in chlorpyrifos degradation. Int Biodeterior Biodegrad 117:183–189. https://doi.org/10.1016/j.ibiod.2017.01.007

Fu M, Xing J, Ge Z (2019) Preparation of laccase-loaded magnetic nanoflowers and their recycling for efficient degradation of bisphenol A. Sci Total Environ 651:2857–2865. https://doi.org/10.1016/j.scitotenv.2018.10.145

Ingole PM, Rathod VK (2023) Ultrasound-assisted enzymatic degradation of naproxen. J Indian Chem Soc 100:101040. https://doi.org/10.1016/j.jics.2023.101040

Li S, Qi B, Luo J, Wan Y (2022) Degradation of phenolic inhibitors by laccase immobilized on tannic acid/polyethylenimine modified magnetic nanoparticles. Results Eng 15:100585. https://doi.org/10.1016/j.rineng.2022.100585

Pandey D, Daverey A, Dutta K, Arunachalam K (2023) Dye removal from simulated and real textile effluent using laccase immobilized on pine needle biochar. J Water Process Eng 53:103710. https://doi.org/10.1016/j.jwpe.2023.103710

Pulicharla R, Das RK, Kaur Brar S, et al (2018) Degradation kinetics of chlortetracycline in wastewater using ultrasonication assisted laccase. Chem Eng J 347:828–835. https://doi.org/10.1016/j.cej.2018.04.162

Qiu X, Wang Y, Xue Y, et al (2020) Laccase immobilized on magnetic nanoparticles modified by amino-functionalized ionic liquid via dialdehyde starch for phenolic compounds biodegradation. Chem Eng J 391:123564. https://doi.org/10.1016/j.cej.2019.123564

Rodríguez-Couto S (2018) Solid-State Fermentation for Laccases Production and Their Applications. In: Current Developments in Biotechnology and Bioengineering. Elsevier, pp 211–234

Rouhani S, Azizi S, Maaza M, et al (2021) Covalent immobilization of laccase on Fe_3O_4-graphene oxide nanocomposite for biodegradation of phenolic compounds. Environ Prot Eng 47:. https://doi.org/10.37190/epe210107

Sadeghzadeh S, Ghobadi Nejad Z, Ghasemi S, et al (2020) Removal of bisphenol A in aqueous solution using magnetic cross-linked laccase aggregates from Trametes hirsuta. Bioresour Technol 306:123169. https://doi.org/10.1016/j.biortech.2020.123169

Sheldon RA, van Pelt S (2013) Enzyme immobilisation in biocatalysis: why, what and how. Chem Soc Rev 42:6223–6235. https://doi.org/10.1039/c3cs60075k

Sun H, Yuan F, Jia S, et al (2023) Laccase encapsulation immobilized in mesoporous ZIF-8 for enhancement bisphenol A degradation. J Hazard Mater 445:130460. https://doi.org/10.1016/j.jhazmat.2022.130460

Tuomela M, Hatakka A (2019) Oxidative Fungal Enzymes for Bioremediation. In: Comprehensive Biotechnology. Elsevier, pp 224–239

Viikari L, Suurnäkki A, Grönqvist S, et al (2009) Forest Products: Biotechnology in Pulp and Paper Processing. In: Encyclopedia of Microbiology. Elsevier, pp 80–94

Yadav D, Ranjan B, Mchunu N, et al (2021) Enzymatic treatment of phenolic pollutants by a small laccase immobilized on APTES-functionalised magnetic nanoparticles. 3 Biotech 11:302. https://doi.org/10.1007/s13205-021-02854-0

Yang J, Lin Y, Yang X, et al (2017) Degradation of tetracycline by immobilized laccase and the proposed transformation pathway. J Hazard Mater 322:525–531. https://doi.org/10.1016/j.jhazmat.2016.10.019

Zheng ng, Jiang Y (2012) 260365 Biomimetic Synthesis of Magnetic Composite Particles for Laccase Immobilization

CHAPTER 4

COD and toxicity reduction of wastewater using a hybrid advanced oxidation process of sonication with chitosan-based hydrogel beads

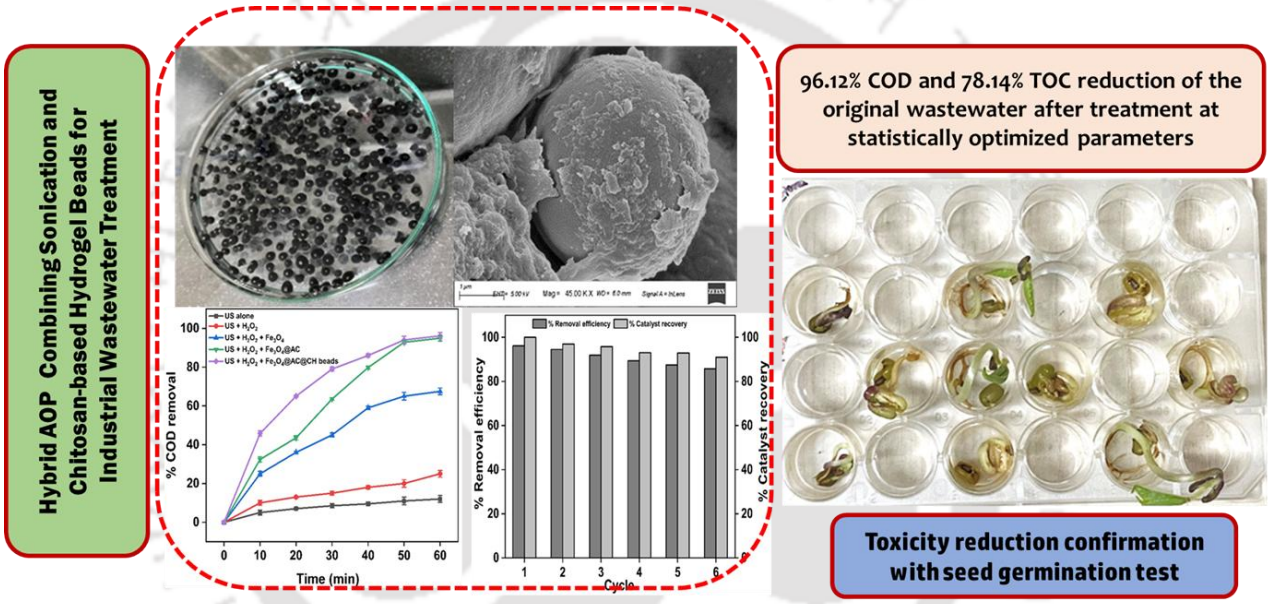

***Online*:** Verma, K., Moholkar, V. S. COD and toxicity reduction of wastewater using a hybrid advanced oxidation process of sonication with chitosan-based hydrogel beads. *Process Safety and Environmental Protection*. https://doi.org/10.1016/j.psep.2024.11.024.

CHAPTER 4

COD AND TOXICITY REDUCTION OF WASTEWATER USING A HYBRID ADVANCED OXIDATION PROCESS OF SONICATION WITH CHITOSAN-BASED HYDROGEL BEADS

4.1 Introduction

The rapid industrialization of developing economies like India, along with population rise, has posed significant challenges in terms of air, water, and terrestrial ecosystem pollution. Industrial, domestic, and agricultural sectors produce substantial quantities of wastewater (WW). This WW discharge includes a variety of persistent pollutants, such as pesticides, insecticides, dyes, pharmaceutical residues, and carbon-based compounds. Even at low concentrations, these contaminants can pose significant risks to human health (Shi et al. 2020; Shen et al. 2021; Ge et al. 2021). Advanced Oxidation Processes (AOPs) have been widely used to eliminate toxic recalcitrant contaminants from WW (Chakma et al. 2015b). AOPs are based on oxidative degradation of the contaminants induced by radical species like O, $^{\bullet}$OH $HO_2^{\bullet}$ and $O_2^{\bullet-}$ (Sivasankar and Moholkar 2009b). A variety of AOPs have been utilized for degrading organic contaminants, such as ultra-violet processes, Fenton oxidation, ozone treatments, persulfate oxidation, ultrasound irradiation, and electrochemical methods (Hassani et al. 2022). In many situations, it has been observed that a single AOP is not sufficient to

effectively degrade and mineralize the pollutants that yield the required reduction in COD and TOC content of WW. Therefore, combined or hybrid AOPs have also been widely used. For more effective implementation of the hybrid AOPs, it is essential to understand the synergism of the hybrid AOP (or the mutual interactions among different individual AOPs combined in the hybrid process). Table A4.1 (provided in Appendix A4) summarizes a few representative recent studies on the degradation/mineralization of recalcitrant pollutants using different hybrid AOPs.

In a previous chapter, we showed the performance of the ternary hybrid AOP incorporating adsorption (nanocomposite Fe_3O_4@AC) + heterogeneous Fenton + sonication for effective WW treatment. This ternary hybrid AOP achieved more than a 90% lowering in COD and TOC in WW released from local industries and educational institutions in a mere 1 h of treatment. More recently, hydrogel beads synthesized from organic materials such as biochar, alginate, and chitosan have been used for adsorptive WW treatment (Afzal et al. 2022; Liu et al. 2023; Salem et al. 2023). These hydrogel beads act as adsorbents for the contaminants in WW. Most of the literature published in the area of WW treatment using hydrogel beads is based on the adsorptive separation of pollutants (Chen 2024; Ismail et al. 2024; Gong et al. 2024; Rostami et al. 2024; Anulekshmi et al. 2024; Huang et al. 2024; Jung et al. 2024; Taghiloo et al. 2024). Table A4.2 (provided in Appendix A4) summarizes the literature on removing organic pollutants using chitosan composites with different filler materials. A few authors have demonstrated that hydrogels can be used in hybrid AOPs for simultaneous adsorption and degradation of pollutants. Afzal et al. (2022) have reported sonocatalytic degradation of the pharmaceutical pollutant ciprofloxacin using hydrogel beads of TiO_2-incorporated biochar and chitosan. Wanchai and Pichon (2020) reported sulphanilamide degradation using magnetic chitosan beads in a photo-Fenton process.

In this chapter, we report our studies in WW treatment with a sono-Fenton process in which the hydrogel beads of Fe_3O_4@AC nanocomposite and chitosan are used. Henceforth, these beads are denoted as Fe_3O_4@AC@CH. Previous authors have used Chitosan-based hydrogels mainly for the adsorptive removal of pollutants from WW.

The roles of the individual components of the Fe_3O_4@AC@CH hydrogel beads in the process of WW treatment are as follows: (1) Chitosan, obtained via deacetylation of chitin, is essentially a polysaccharide with N-acetyl glucosamine and glucosamine as primary components. It has large numbers of active –OH and $–NH_2$ groups. One $–NH_2$ and two –OH groups on each glucosamine unit constitute an adsorption site. Thus, the main role of chitosan is the adsorption of the organic contaminants present in the WW. Linked chitosan particles in the bead matrix can also trap the Fe_3O_4@AC nanocomposite particles, which gives mechanical strength to the beads; (2) Activated carbon, recognized for its porous structure, extensive surface area, and diverse functional groups (-CH, -OH, C–O, -COO-, etc.), efficiently adsorbs organic contaminants. This process facilitates the transfer of these pollutants from a dilute solution onto the carbon's surface; (3) Fe_3O_4 particles act as heterogeneous Fenton agents. Surface leaching of the Fe_3O_4 particles, caused by strong microconvection generated by sonication, can release Fe^{2+}/Fe^{3+} ions, which, after reacting with H_2O_2, can induce Fenton reactions to generate $^{\bullet}OH$ and $HO_2^{\bullet}$ radicals. H_2O_2 may be externally added to the medium or generated in situ through the transient cavitation events. The principal advantage of using the Fe_3O_4@AC nanocomposite in the form of Fe_3O_4@AC@CH hydrogel beads is a marked rise in the possibility of interaction between reactive radicals and contaminant molecules due to surface adsorption as well as absorption due to swelling of the chitosan matrix, as compared to using the Fe_3O_4@AC nanocomposite in bare or native form. Moreover, due to low density, the Fe_3O_4@AC@CH hydrogel beads float over the water surface and, thus, can be easily separated and recycled after every treatment cycle with almost complete recovery and no loss of material.

As against this, the Fe_3O_4@AC nanoparticles were not completely recoverable even when using a magnetic stirrer bar, with some loss in between treatment cycles (Verma and Moholkar 2023). To our knowledge, floatable Fe_3O_4@AC@CH hydrogel beads have not previously been used in a hybrid AOP to treat real industrial WW. As described in subsequent sections of this chapter, these hydrogel beads have the potential for rapid degradation of organic contaminants in the WW. This chapter has following objectives: (1) synthesis and characterization of Fe_3O_4@AC@CH hydrogel beads, (2) statistical optimization of WW treatment process parameters, (3) LC-MS analysis to identify major contaminants in both original and treated WW, (4) evaluation of the adsorption properties and kinetics of the Fe_3O_4@AC@CH hydrogel beads, and (5) assessment of toxicity minimization of WW after treatment.

4.2. Materials and methods

4.2.1 Reagents

The chemicals used in this study and their sources are given below:

Activated charcoal powder, Ferric chloride hexahydrate ($FeCl_3 \cdot 6H_2O$), sulfuric acid (H_2SO_4; 98%), ferrous sulfate heptahydrate ($FeSO_4 \cdot 7H_2O$), hydrogen peroxide (H_2O_2; 30%), potassium permanganate ($KMnO_4$), hydrochloric acid (HCl; 35%), ferrous ammonium sulfate heptahydrate ($Fe(NH_4)_2(SO_4)_2 \cdot 7H_2O$), potassium dichromate ($K_2Cr_2O_7$), mercuric sulfate ($HgSO_4$), silver sulfate (Ag_2SO_4), conc. H_2SO_4 (98%) and ferroin indicator were purchased from Himedia Ltd. (India). All reagents were of analytical grade and used without additional purification.

Hydrazine hydrate (N_2H_4, 50-60%), sodium carbonate anhydrous (Na_2CO_3), chitosan (CH), glutaraldehyde, acetic acid, sodium thiosulfate ($Na_2S_2O_3$), manganese sulfate ($MnSO_4$), potassium dihydrogen phosphate (KH_2PO_4), dipotassium hydrogen orthophosphate (K_2HPO_4),

disodium hydrogen phosphate (Na_2HPO_4), ammonium chloride (NH_4Cl), calcium chloride ($CaCl_2$), magnesium sulfate ($MgSO_4$) and ferric chloride ($FeCl_3$) were obtained from Sigma-Aldrich (India). All reagents were used as received without any additional treatment or purification.

4.2.2 Synthesis of Fe_3O_4@AC@CH hydrogel beads

Using the co-precipitation method detailed in our earlier work, the Fe_3O_4@AC nanocomposites were synthesized (Verma and Moholkar 2023). In a sequence of steps, 0.5 g of chitosan powder was added to 60 mL of acetic acid solution (2% v/v) and stirred vigorously for 45 minutes to ensure complete dissolution. Next, 1 g of Fe_3O_4@AC was introduced into the solution, and magnetic stirring was maintained for an additional 30 minutes. The solution's color changed from yellow to black. The prepared suspension was slowly dripped into a 100 mL NaOH solution (2.5% w/v) using a syringe to form hydrogel beads and then allowed to stand overnight. Before adding the above suspension, 400 µL of 25% glutaraldehyde was mixed into the NaOH solution to facilitate cross-linking of the chitosan chains. The cross-linking of chitosan chains imparts mechanical strength to the hydrogel beads during WW treatment. The NaOH solution was decanted, and the formed spherical Fe_3O_4@AC@CH hydrogel beads underwent thorough washing with deionized water to eliminate excess NaOH and residual cross-linker. This washing process was repeated until the water pH reached 7. Finally, the beads were dried through freeze-drying for 24 hours. Figure 4.1 schematically represents the procedure for the synthesis of Fe_3O_4@AC@CH hydrogel beads.

4.2.3 Water content in Fe_3O_4@AC@CH beads

Approximately 7 g Fe_3O_4@AC@CH beads underwent freeze-drying for a period of 12 h, during which a weight reduction was observed, reflecting the removal of water content from Fe_3O_4@AC@CH beads. The physical dimensions of the catalyst beads remained unaltered throughout the freeze-drying process (Afzal et al. 2022).

$$\text{Water content} = \frac{W_2 - W_3}{W_2 - W_1} \times 100 \qquad (4.1)$$

W_1 = weight of the empty container, W_2, and W_3 denote the weights of hydrogel beads + container before and after the freeze-drying process.

4.2.4 Characterization of Fe_3O_4@AC@CH hydrogel beads

The crystal structures of Fe_3O_4@AC@CH hydrogel beads were analyzed using an XRD (Rigaku powder X-ray diffractometer Model Smart Lab, Cu K_α, λ = 1.54178 Å). The BET (model Tristar II) determined the surface area and pore size. The structural morphologies of the hydrogel beads were investigated by a Zeiss field emission scanning electron microscope (FE-SEM; Model Sigma 300) and a JEOL transmission electron microscope (TEM; Model JEM 2100). The magnetic behavior of Fe_3O_4@AC@CH beads was assessed by the Lakeshore vibrating sample magnetometer (Model 7410 series). The FTIR spectrophotometer (PerkinElmer) was used to study functional groups of the Fe_3O_4@AC@CH hydrogel beads in the wavenumber range of 4000-400 cm^{-1}. The elemental composition of the Fe_3O_4@AC@CH hydrogel beads was identified by EDX analysis (Sigma, Zeiss). The COD and BOD analysis was carried out using standard methods. (Association et al. 1995). The TOC analysis of the WW pre- and post-treatment was ascertained by the TOC analyzer (Shimadzu, Model: TOC-LCPN+SSM). Appendix A4 gives greater details of the TOC analysis procedure (sections A4.1 and Table A4 3).

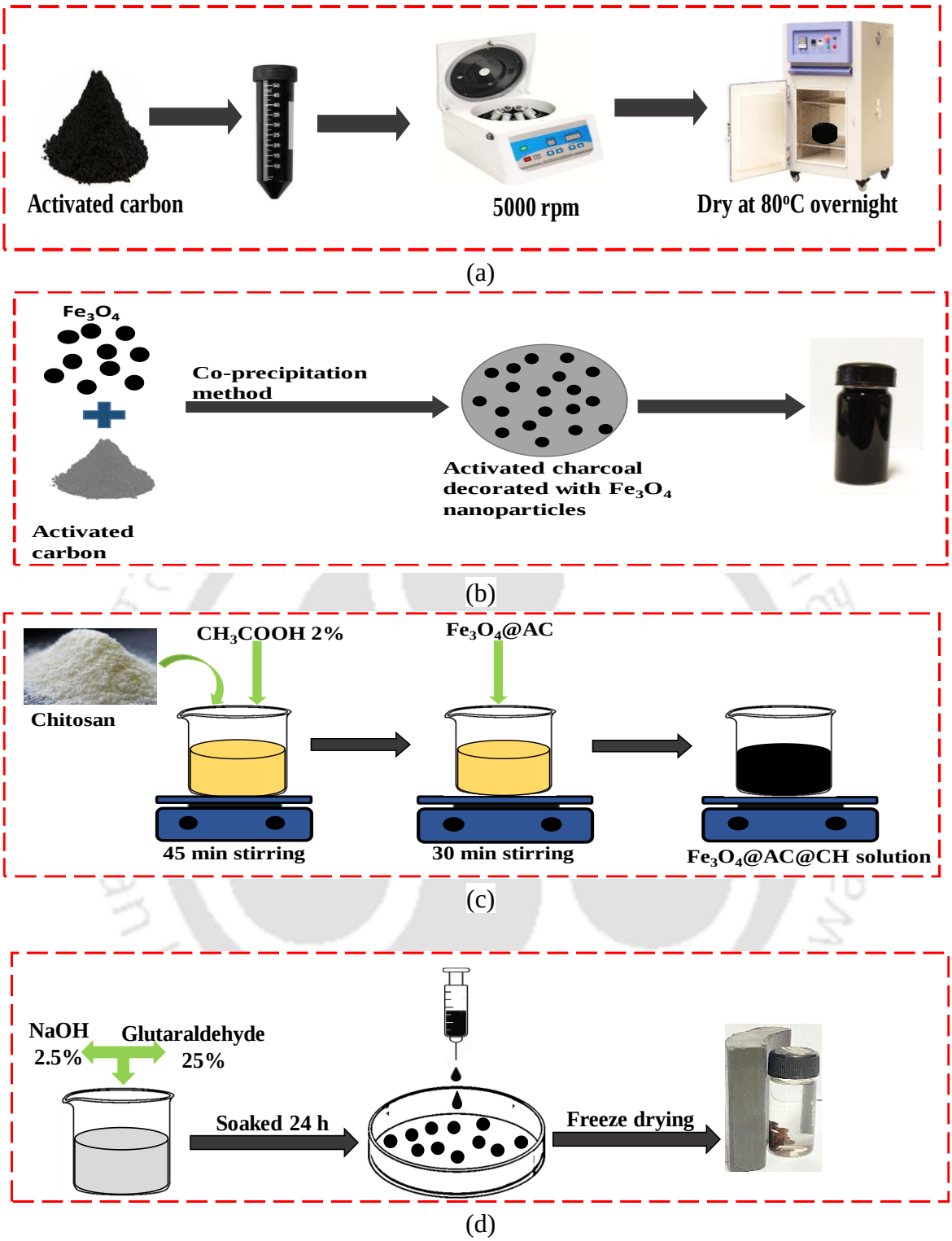

Figure 4.1. Schematic representation of the synthesis procedure for Fe_3O_4@AC@CH hydrogel beads (a) Scheme for the preparation of activated carbon, (b) synthesis of Fe_3O_4@AC nanocomposite, (c) scheme for the preparation of Fe_3O_4@AC@CH solution, and (d) cross-linking and freeze drying of Fe_3O_4@AC@CH hydrogel beads

4.2.5 Experimental procedure

The sonication of the WW solution after the addition of the hydrogel beads was carried out using a probe-type sonicator, as described in greater detail in our previous paper (Verma and Moholkar 2023). A microprocessor-controlled ultrasound probe (Sonics and Materials Inc., Model: VCX 500; Frequency 20 kHz; Max power 500 W) was used for sonication. The ultrasound probe was operated at 40% of maximum power (acoustic intensity = 74548 W/m^2, pressure amplitude = 470 kPa or 4.7 bar) and reaction volume 150 mL. Figure A4.1 (provided in Appendix A4) represents the schematic of the experimental setup. The sonication process lasted for one hour in all experiments, and the temperature of the solution was maintained at 25 °C using a circulating water bath. All experiments were conducted in triplicate for result reproducibility. The optimization parameters in the Design of experiments (DoE) were Fe_3O_4@AC@CH hydrogel beads dose, pH, and H_2O_2 loading, while the response variable was % COD removal. Sonication was applied to the solution after the addition of H_2O_2 and Fe_3O_4@AC@CH hydrogel beads in desired quantities. 5 mL samples of the WW solution were withdrawn at 10 min intervals and centrifuged, and the supernatant was analyzed to determine the %COD removal. The control experiments were performed with sonication in the presence of native Fe_3O_4 nanoparticles. Post-sonication, Fe_3O_4@AC@CH hydrogel beads were magnetically separated by using an external magnet and washed with deionized water, and the WW was mixed with wash water for COD analysis. Concurrently, the adsorption characteristics of Fe_3O_4@AC@CH hydrogel beads were also studied in separate experiments. Adsorption isotherms were generated using 1 g/L of Fe_3O_4@AC@CH hydrogel beads added in a 150 mL solution at pH 5.12 with varying initial COD values. Lastly, the reusability and stability of the Fe_3O_4@AC@CH hydrogel beads were evaluated in the sixth consecutive WW treatment cycle. The reusability of the hydrogel beads was assessed by recovering the beads with a magnet followed by washing them with DI water, and reusing them in identical

conditions for the next experiment. The response variable (% COD removal), presented as mean values, was obtained in duplicated experiments. The adsorption capacity (mg/g) of the Fe_3O_4@AC@CH hydrogel beads and the % COD removal can be determined by:

$$q_t = \frac{(C_o - C_t)}{m} V \tag{4.2}$$

$$\%\text{COD removal} = \frac{(C_o - C_t)}{C_o} \times 100 \tag{4.3}$$

Where C_o and C_t represent the initial and instantaneous COD values of the WW solution, respectively, V (L) is the volume of solution, and m (g) mass of the Fe_3O_4@AC@CH hydrogel beads. The q_e and %COD removal are calculated by substituting C_t with C_e.

4.2.6 Statistical experimental design (DoE)

The physical parameters affecting the %COD removal include (1) the dosage of hydrogel beads, (2) the initial pH of the solution, and (3) the dosage of H_2O_2. A Central Composite Design (CCD) was employed to determine the optimal combination of these parameters. A three-factor, three-level design was utilized, incorporating the following parameter ranges: (1) Fe_3O_4@AC@CH hydrogel beads dose (X_1): 0.34 - 1 g/L; (2) pH (X_2): 2 - 7; and (3) H_2O_2 loading (X_3): 0.28 - 0.85 M. These ranges were established based on preliminary experiments. The results were examined by using response surface methodology, in which the quadratic equation (4.4) was fitted to the experimental data (Ansari et al. 2016).

$$Y = \beta_0 + \sum_{i=1}^{k} \beta_i X_i + \sum_{i=1}^{k} \sum_{j=1}^{k} \beta_{ij} X_i X_j + \sum_{i=1}^{k} \beta_{ii} X_i^2 + \varepsilon \tag{4.4}$$

where Y = response variable (% COD removal), β_0 = constant coefficient, β_i = linear coefficients, β_{ii} = quadratic coefficients, β_{ij} = interaction coefficients, X_i X_j = independent

variables, k = total number of independent variables, and ε = residual error. The description of the statistical DoE is given in Table 4.1.

Table 4.1. Experimental design: variables and their levels

Variables	Unit	Level		
		Low (-1)	Middle (0)	High (+1)
Fe_3O_4@AC@CH hydrogel beads dose (X_1)	g/L	0.34	0.67	1
pH (X_2)	-	2	4.5	7
H_2O_2 loading (X_3)	M	0.28	0.57	0.85

4.2.7 Adsorption characteristics of Fe_3O_4@AC@CH hydrogel beads

The adsorption characteristics of the Fe_3O_4@AC@CH hydrogel beads were determined using pseudo-first order, pseudo-second order, and intra-particle diffusion kinetic models (Ho and McKay 2000; Ho 2006).

$$q_t = q_e(1-e^{k_1 t}) \quad (4.5)$$

$$q_t = \frac{q_e^2 k_2 t}{1+q_t k_2 t} \quad (4.6)$$

$$q_t = k_{diff} t^{1/2} + C \quad (4.7)$$

q_e = equilibrium adsorption capacity of Fe_3O_4@AC@CH hydrogel beads; q_t = instantaneous adsorption capacity, k_1 = pseudo-first-order kinetic rate constant, k_2 = pseudo-second-order kinetic rate constant, k_{diff} = rate constant of intra-particle diffusion and C = intercept. The adsorption isotherm (Langmuir and Freundlich) was used to characterize the interactions between the adsorbent and contaminants for Fe_3O_4@AC@CH hydrogel beads.

$$q_e = \frac{q_m k_L C_e}{1 + k_L C_e} \tag{4.8}$$

$$q_e = k_F C_e^{1/n} \tag{4.9}$$

where C_e = equilibrium COD of the solution, k_L = Langmuir constant, q_m = maximum adsorption capacity, k_F. = Freundlich constant. The separation factor (R_L) for Langmuir isotherm Nigussie et al. (2007) is deduced as:

$$R_L = \frac{1}{1 + k_L C_o} \tag{4.10}$$

Where C_o is the initial COD of solution (mg/L). The nature of adsorption was determined by separation factors like unfavorable ($R_L > 1$) and favorable ($0 < R_L < 1$) (Nigussie et al. 2007). These isotherms were conducted by varying initial CODs of the 150 mL solution at optimum conditions: pH = 5.12, H_2O_2 loading = 0.75 M, and time of 60 min.

4.2.8 Toxicity analysis

The relative reduction in toxicity of WW was assessed through a seed germination test, as outlined in a prior publication (Kumar et al. 2022). The percentage of seed germinated counted as a relative reduction in the toxicity of WW.

4.3. Results and Discussion

4.3.1 Characterization of Fe_3O_4@AC@CH hydrogel beads

The crystalline structure of native Fe_3O_4 nanoparticles and the Fe_3O_4@AC@CH hydrogel beads were assessed using X-ray diffractograms. XRD analysis was conducted in the 2θ range of 10-80°. The XRD peaks depicted in Figure 4.2 provide evidence of the synthesis of the Fe_3O_4@AC@CH hydrogel beads and affirm the crystalline nature of the hydrogel beads. As per the JCPDS (No. 19-0629) reference, distinct peaks at 2θ values of 30.07 (2 2 0), 35.44 (311), 43.15 (4 0 0), 54.6 (4 2 2), 56.99 (5 1 1), and 62.6 (4 4 0) are indicative of the cubic phase Fe_3O_4. These characteristic peaks are evident in the X-ray diffractogram of Fe_3O_4@AC@CH hydrogel beads, as illustrated in Fig. 4.2. Additionally, a faint diffraction peak at $2\theta = 22.92°$ is likely attributed to the (0 0 2) plane of the cellulose I structure in chitosan (JCPDS no. 03-0226) (Agani et al. 2020). Notably, there is no significant alteration in the primary Fe_3O_4 nanoparticle diffraction peaks, suggesting a minimal impact on the structural integrity of AC Chitosan and Fe_3O_4 during the formation of hydrogel beads. Furthermore, the absence of activated carbon peaks in the Fe_3O_4@AC@CH hydrogel beads pattern underscores the amorphous nature of the carbonaceous material in the hydrogel beads (Anfar et al. 2020).

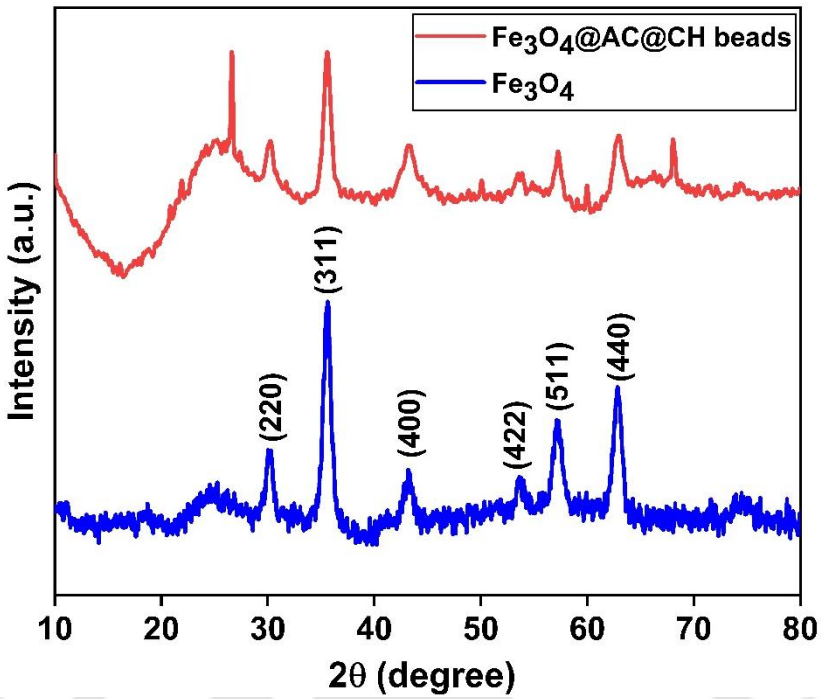

Figure 4.2. XRD patterns of Fe_3O_4 nanoparticles, and Fe_3O_4@AC@CH hydrogel beads

To assess the recovery capability of Fe_3O_4@AC@CH hydrogel beads through an external magnetic field after treatment, the saturated magnetization (Ms) value becomes crucial. The magnetic properties of the synthesized Fe_3O_4@AC@CH hydrogel beads stem from the presence of Fe_3O_4 nanoparticles embedded in activated carbon and chitosan. The magnetization characteristics were explored using VSM at ambient temperature within the range of ± 15 kOe, magnetic field, and the findings are depicted in Figure 4.3. In Figure 4.3, the observed hysteresis loops, resembling an S-curve, signify the super magnetization of the synthesized samples, with saturation magnetizations of 74.28 and 53.24 emu/g for Fe_3O_4 and Fe_3O_4@AC@CH hydrogel beads, respectively. The magnetic saturation of the hydrogel beads was notably lower than that of Fe_3O_4 nanoparticles, possibly due to the presence of activated carbon powder and the non-magnetic matrix of chitosan. These values, either higher or comparable to those of other magnetic bio adsorbents based on chitosan, indicate the efficacy

of the Fe_3O_4@AC@CH hydrogel beads (Jamali and Akbari 2021; Kaveh and Bagherzadeh 2022). Contemplating all the aforementioned findings, the saturation magnetization of the hydrogel beads is deemed sufficient for prompt response to the magnet, facilitating their easy removal from the aqueous solution (inset Fig. 4.3).

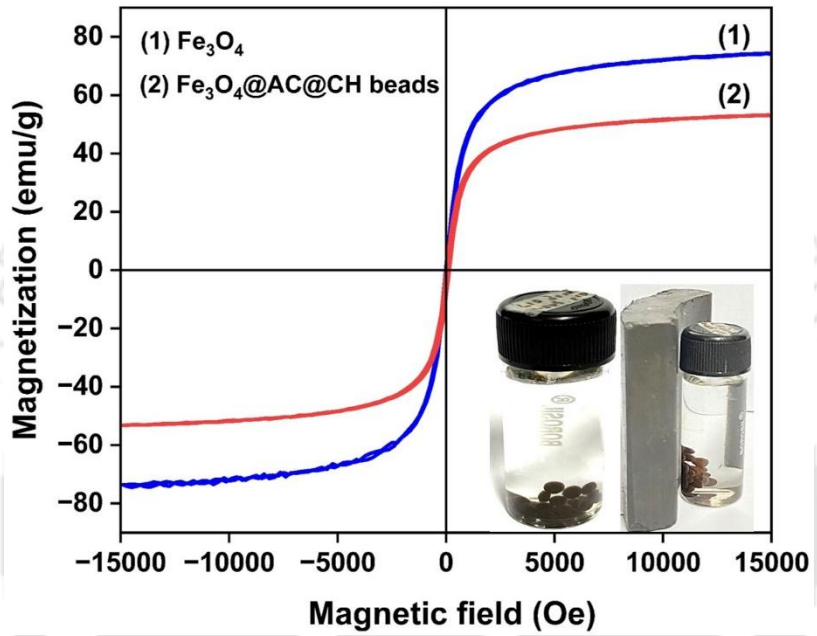

Figure 4.3. VSM plot for Fe_3O_4 and Fe_3O_4@AC@CH hydrogel beads

The nitrogen adsorption-desorption isotherms for Fe_3O_4@AC and Fe_3O_4@AC@CH hydrogel beads are depicted in Figure 4.4, all exhibiting type IV isotherms. Textural parameters reveal surface areas of 605.34, 538.88, 3.07, and 312.61 m^2/g for AC, Fe_3O_4@AC, CH, and Fe_3O_4@AC@CH beads, respectively, based on BET measurements (Table 4.2). The surface area of Fe_3O_4@AC nanocomposite is lower than that of AC, attributed to the presence of Fe_3O_4 nanoparticles. Additionally, the reduction of surface area with the incorporation of chitosan suggests that chitosan obstructs the pores of the Fe_3O_4@AC nanocomposite. The elevated surface area of Fe_3O_4@AC@CH hydrogel beads (312.61 m^2/g) is linked to the inclusion of AC

within the chitosan matrix. Following the IUPAC classification for mesoporous materials, Fe_3O_4@AC@CH hydrogel beads are identified as Type IV mesoporous material (d = 2–50 nm). Furthermore, the specific surface area of Fe_3O_4@AC@CH hydrogel beads synthesized in this study was higher than that reported by previous authors, Le et al. (2020); Jamali and Akbari (2021) viz. 264.97 and 105.74 m^2/g for magnetic activated carbon chitosan beads.

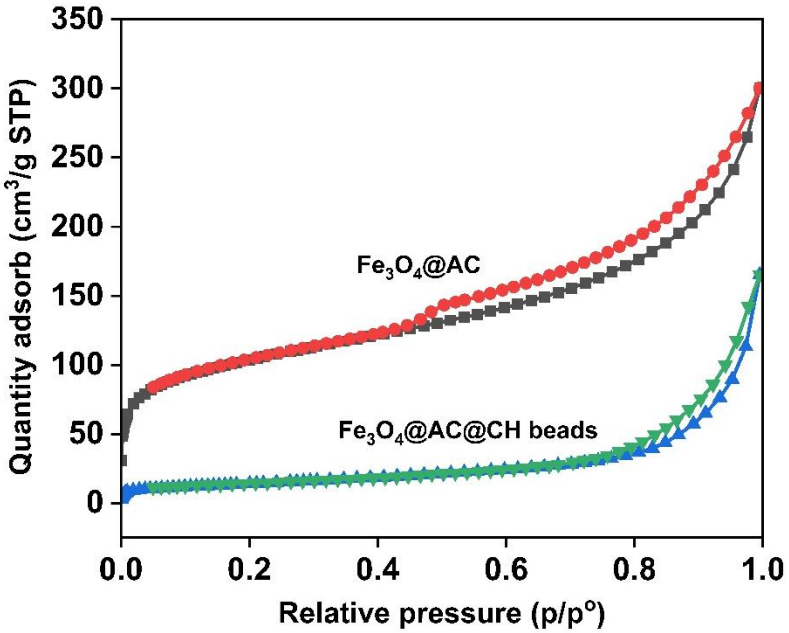

Figure 4.4. BET plot of Fe_3O_4@ACand Fe_3O_4@AC@CH hydrogel beads

Table 4.2. Textural properties of Fe_3O_4@AC@CH hydrogel beads

	AC	Fe_3O_4@AC	CH	Fe_3O_4@AC@CH beads
BET surface area (m^2/g)	605.34	538.88	3.07	312.61
Total pore volume (cm^3/g)	0.55	0.29	0.013	0.19
Mean pore diameter (nm)	3.66	4.08	58.49	3.25

The Fourier-transform infrared spectroscopy (FTIR) was used to identify functional groups in the Fe_3O_4@AC@CH hydrogel beads shown in Figure 4.5. It can be observed that the positions and intensities of characteristic peaks in the FTIR spectra of the hydrogel beads changed after the treatment. It could be due to the interaction of the beads with various organic pollutants present in the WW. The broad peak at 3430 cm^{-1} corresponded to –OH and $–NH_2$ stretching vibrations, which revealed the presence of chitosan (Wang et al. 2008). However, the addition of iron led to a significant decrease in transmittance at 3430 cm^{-1}, indicating the formation of metal-NH_2 bonds (Santana Cadaval et al. 2013). The absorption peak at 2845 cm^{-1} was attributed to C–H vibrations (Kaveh and Bagherzadeh 2022). Additionally, peaks at 1594 cm^{-1} and 1643 cm^{-1} were assigned to C═O bending vibration and N–H stretching, respectively (Peng et al. 2014). The absorption peaks at 1419 cm^{-1} and 1382 cm^{-1} were attributed to the C–N stretching and –C–O stretching of the primary alcohol group. Furthermore, the 1074 cm^{-1} peak was attributed to C–O stretching in the CH_2–OH group (Reddy and Lee 2013). It is evident that in the spectrum of the magnetic hydrogel beads (before and after treatment), intrinsic peaks persisted, which revealed a new band in the low-frequency region (1000–500 cm^{-1}) corresponding to the Fe_3O_4 skeleton (Fe-O stretching vibration). This shows the structural stability of the hydrogel beads with no detachment of Fe oxide nanoparticles during sonication (Rezgui et al. 2018).

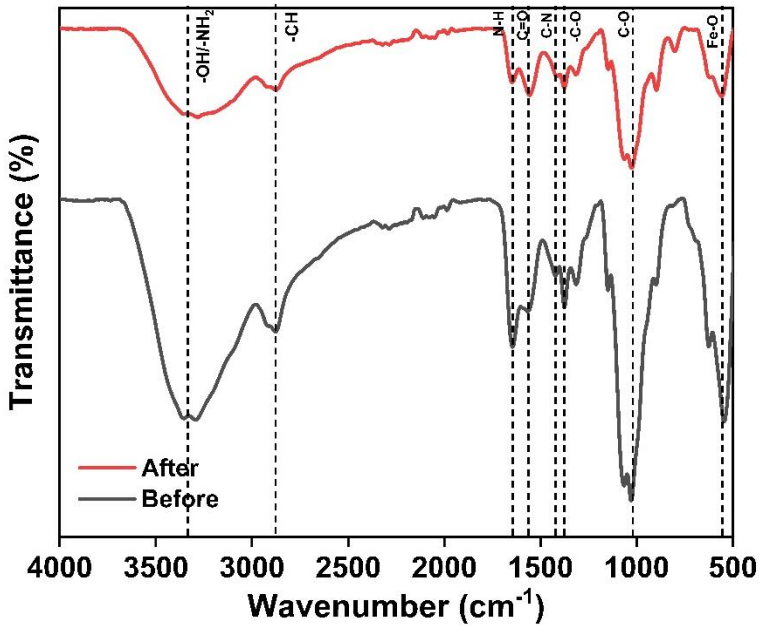

Figure 4.5. FTIR spectra of Fe_3O_4@AC@CH hydrogel beads before and after the reaction

The surface morphology of magnetic chitosan-based hydrogel beads was depicted by using FE-SEM and FE-TEM analysis. In Figure 4.6 (a, b), photographic images depict spherical shapes of wet and floatable chitosan and Fe_3O_4@AC@CH beads. Figure 4.6 (c) illustrates that the hydrogel beads can be easily separated by placing a magnet beside the solution. These beads can be easily recycled after separation and reused.

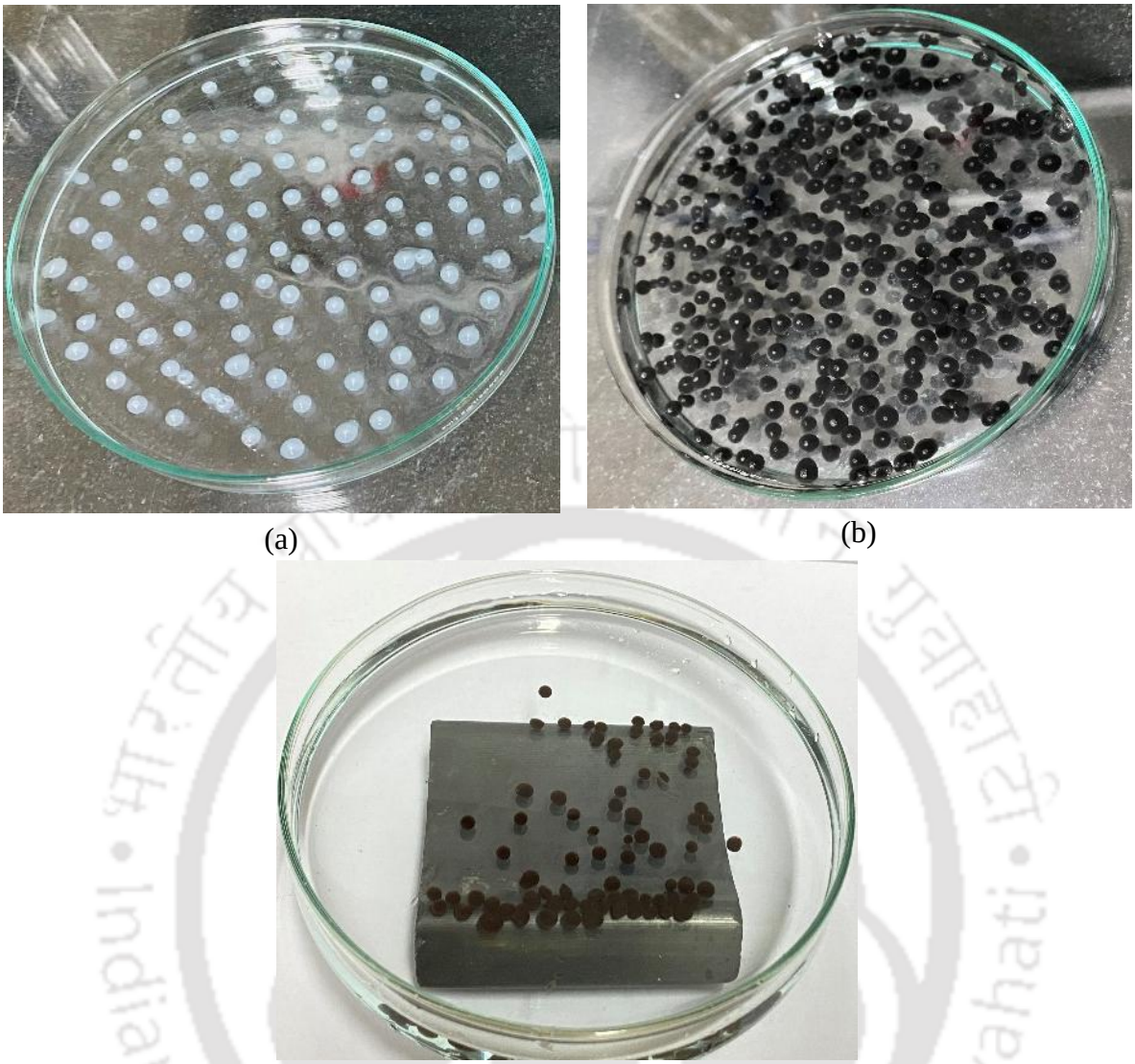

Figure 4.6. (a-c) Photographic images of chitosan and Fe_3O_4@AC@CH hydrogel beads

Figures 4.7 (a-c) illustrate the surface morphology of Fe_3O_4@AC nanocomposite, CH beads, and Fe_3O_4@AC@CH hydrogel beads. All samples exhibit a spherical morphology but with distinguishable surface features. The FE-SEM image of the Fe_3O_4@AC nanocomposite (Fig. 4.7a) reveals the presence of Fe_3O_4 particles on the AC surface. Figure 4.7 (b) displays the smooth and non-porous surface of pure chitosan beads, while Figure 4.7 (c) depicts the rough and heterogeneous surface of Fe_3O_4@AC@CH hydrogel beads, which indicates the presence of iron oxide (Fe_3O_4) nanoparticles on the surface of the chitosan beads, in addition to the

nanoparticles that are embedded inside the hydrogel matrix. The water content in pure chitosan beads was 96% while it reduced to 65% for Fe_3O_4@AC@CH hydrogel beads (calculated by eq. 4.1). Figure 4.7 (d) shows the pore size distribution of hydrogel beads with an average pore size of 41 nm.

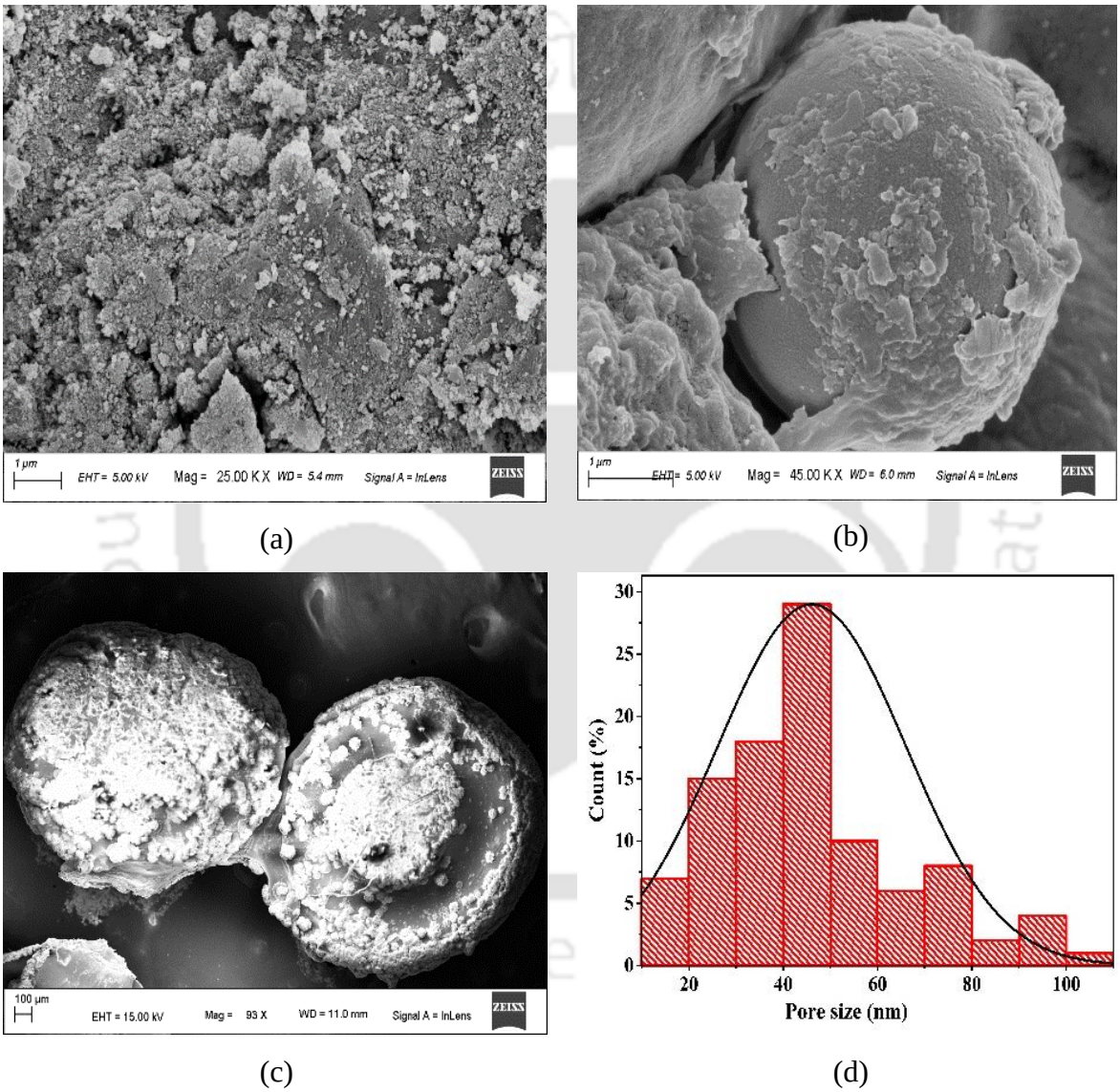

Figure 4.7. (a-c) FE-SEM images of Fe_3O_4@AC, pure chitosan beads, and Fe_3O_4@AC@CH hydrogel beads; (d) pore size distribution of hydrogel beads

EDX coupled with field-emission scanning electron microscopy (FESEM) was used for the elemental characterization of the Fe_3O_4@AC@CH hydrogel beads. The EDX analysis (refer to Table 4.3) revealed that the Fe_3O_4@AC@CH hydrogel beads comprised 33.8% carbon, 29.2% oxygen, 24.2% iron, and 12.7% nitrogen, which are the primary elements in the beads. This also confirms the presence of chitosan, activated carbon, and Fe_3O_4 in the beads. Furthermore, the EDX spectra for the hydrogel beads (shown in Figure 4.8) displayed an absence of distinct impurity peaks, underscoring the exceptional purity of the Fe_3O_4@AC@CH hydrogel beads.

Table 4.3. EDX elemental composition of Fe_3O_4@AC@CH hydrogel beads

Sample	C (wt%)	O (wt%)	Fe (wt%)	N (wt%)
Fe_3O_4	-	25.2	74.8	-
Fe_3O_4@AC	82.2	9.8	8.1	-
CH	50.3	23.5	-	26.2
Fe_3O_4@AC@CH beads	33.9	29.2	24.2	12.7

4.3.2 Outcome of Central Composite Design (CCD) of Experiments

As previously mentioned, a statistical experimental design (CCD) was used to optimize the process parameters for WW treatment. The statistical DoE helps in the identification of the optimum parameters while taking into consideration the interactions among these parameters represented by Table 4.4 The optimization parameters were: Fe_3O_4@AC@CH hydrogel beads dose (X_1), pH (X_2), and H_2O_2 loading (X_3), while the response variable was the percentage of COD removal. A quadratic model (Eq. 4.4) was fitted to the data obtained through statistical DoE. The model fitness was assessed using Analysis of Variance (ANOVA).

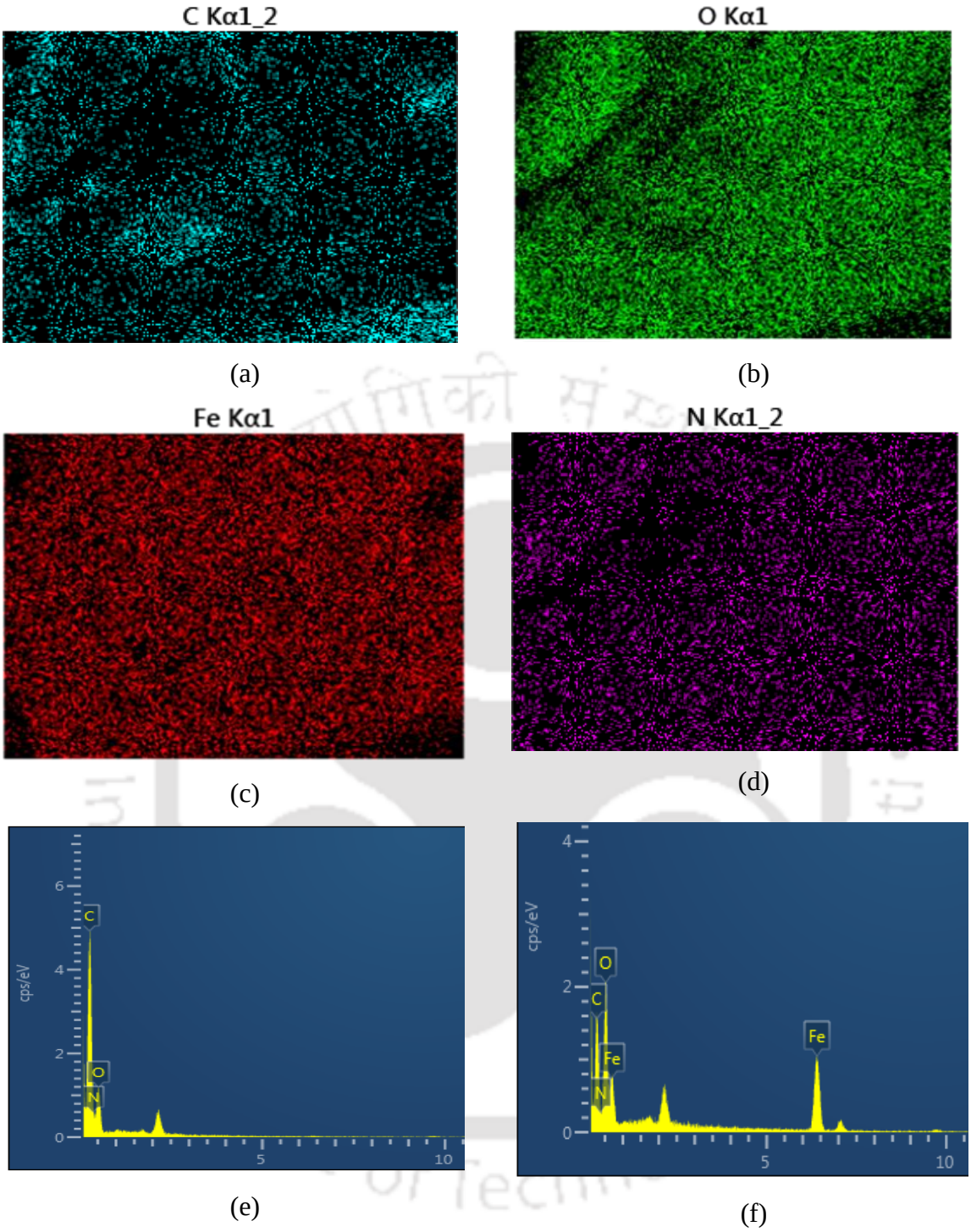

Figure 4.8. (a-d) Elemental mapping of Fe_3O_4@AC@CH hydrogel beads; EDX spectra of (e) chitosan and (f) Fe_3O_4@AC@CH hydrogel beads

$$\% \text{ COD removal} = 95.40 + 7.38X_1 + 5.50X_2 + 3.48X_3 + 0.1362X_1X_2 - 0.0063X_1X_3 + 0.3462X_2X_3 - 10.64X_1^2 - 8.85X_2^2 - 2.75X_3^2 \quad (4.11)$$

The statistical DoE predicted the optimal parameters for maximum COD removal of 96.12%: pH = 5.12, Fe_3O_4@AC@CH beads dose = 1 g/L, and H_2O_2 loading = 0.75 M.

Table 4.4. Central Composite Design (CCD) matrix for %COD Removal

Run	Fe_3O_4@AC@CH hydrogel beads dose (X_1) (g/L)	pH (X_2) (-)	H_2O_2 loading (X_3) (M)	% COD removal (experimental)	% COD removal (predicted)
1	0.34	2	0.85	63.8	63.6
2	0.67	4.5	0.28	92.8	89.2
3	1	7	0.85	90.8	89.9
4	0.67	7	0.57	91.4	92.1
5	1	4.5	0.57	93.2	92.1
6	0.67	2	0.57	83.2	81.1
7	0.67	4.5	0.57	95.8	95.4
8	1	7	0.28	81.8	82.3
9	0.67	4.5	0.57	91.5	95.4
10	0.67	4.5	0.85	93.9	96.1
11	0.34	7	0.28	66.8	67.3
12	0.67	4.5	0.57	98.5	95.4
13	0.34	4.5	0.57	77.8	77.4
14	0.34	7	0.85	75.9	74.9
15	0.67	4.5	0.57	93.9	95.4
16	0.34	2	0.28	56.2	57.3
17	0.67	4.5	0.57	92.8	95.4
18	0.67	4.5	0.57	97.2	95.4
19	1	2	0.28	70.4	71.8
20	1	2	0.85	78.2	78.0

The analysis of variance (ANOVA) for the CCD is detailed in Table A4.4 (Appendix A4). ANOVA unveils a high *F*-value of 47.54 and a very low *p*-value (< 0.0001) for the overall quadratic model, indicating a strong fit. The lack of fit value of 0.5630 suggests that it is not significantly different from pure error. Additionally, the standard deviation of 2.29 and a precision of 21.284 also highlight the reliability of the results.

4.3.3. Validation experiment

A validation experiment was conducted to confirm the results of the statistical DoE. This experiment was conducted at the optimum set of parameters obtained from statistical DoE: Fe_3O_4@AC@CH beads dose = 1 g/L, pH = 5.12, H_2O_2 loading = 0.75 M. The experimental results revealed 96.12% COD removal at the optimum conditions, closely aligning with the value of 94.20% predicted by the DoE. Additionally, the TOC removal under the optimized conditions was 78.14%. The physicochemical composition of the WW before and after treatment is shown in Table 4.5.

Table 4.5. Characteristics of industrial wastewater pre and post-treatment

Parameter	Before treatment	After treatment
pH	9.31 ± 0.85	7.3 ± 0.46
Color	Mustard Yellow	Colourless
Initial COD (mg/L)	3246 ± 20	125.94 ± 10
Initial TOC (mg/L)	1098 ± 16	240 ± 12
Initial BOD (mg/L)	1000 ±12	238.34 ± 10
Biodegradability index (BOD_5: COD)	0.31 ± 0.05	0.75 ± 0.03

The values given in the table are averages of triplets.

Validation of Synergistic Effects in the Advanced Oxidation Process. To confirm the synergistic interactions employed in this study, a series of control experiments were conducted under optimal conditions determined by the statistical DoE. The experiments included: (1) only sonication; (2) sonication with H_2O_2 (0.75 M); (3) sonication with 0.71 M H_2O_2 and 0.24 g/L Fe_3O_4 nanoparticles in their native (freely suspended) form; (4) sonication with Fe_3O_4@AC nanocomposite with H_2O_2, and (5) sonication with 0.75 M H_2O_2 and 1 g/L Fe_3O_4@AC@CH hydrogel beads The quantity of Fe_3O_4 was determined from the percentage elemental

composition of Fe (24.2%) in the Fe_3O_4@AC@CH hydrogel beads, as shown in EDX analysis shown in Table 4.3. All other conditions of the validation experiments were the same as the statistical DoE. The results of the control experiments are illustrated in Figure 4.9

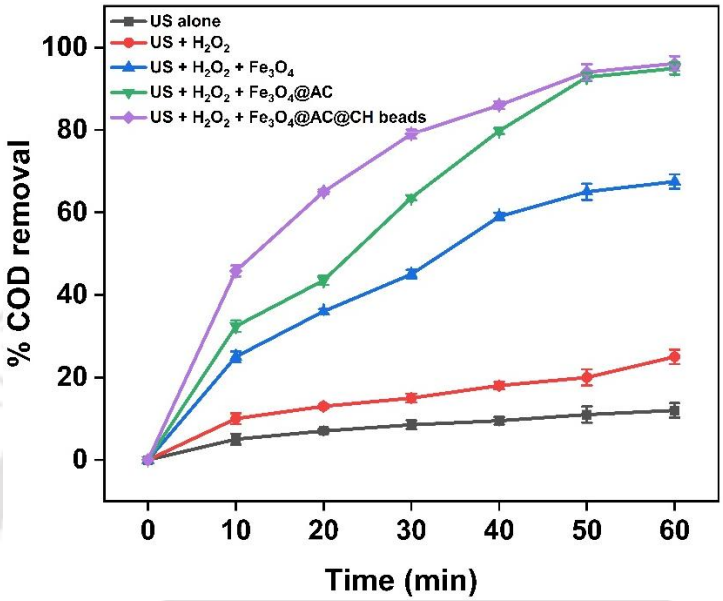

Figure 4.9. Results of validation studies as %COD removal (at optimized condition: Fe_3O_4@AC@CH beads dose = 1 g/L, pH = 5.12, H_2O_2 loading = 0.75 M)

Identification of synergistic interactions and their influence on COD removal: WW treatment with only sonication resulted in less than 15% removal efficiency. This outcome underscores the inefficacy of transient cavitation and in-situ generation of oxidizing radicals for the degradation of pollutants present in WW. The COD removal increased ~2× for the US + H_2O_2 system (25%) as compared to sonication alone (12%). This improvement can probably be attributed to the generation of additional oxidizing radical species (particularly radicals) in WW through the dissociation of externally added H_2O_2 inside the cavitation bubble (Acisli et al. 2017). However, on an absolute basis, the COD removal efficiency of 25% for the US+H_2O_2 system is rather marginal. This could be a consequence of the low evaporation of H_2O_2 within cavitation bubbles, owing to its low volatility and acidic pH (Huang et al. 2012b). The system

of US+Fe_3O_4+H_2O_2 (with Fe_3O_4 0.24 g/L) enhanced the COD removal significantly to 67.5%. The system of US+Fe_3O_4@AC+H_2O_2 gave COD removal of 93.25%. This enhancement is attributed to the substantial rise in the generation of oxidizing radicals due to Fenton reactions between hydrogen peroxide and Fe_3O_4 nanoparticles (NPs) (Expósito et al. 2017). The high shear rate in the liquid due to intense microconvection generated by sonication results in surface leaching of Fe_3O_4 nanoparticles and release of Fe^{2+} and Fe^{3+} ions, which induce Fenton reactions (Roy and Moholkar 2020; Hassani et al. 2022). The highest COD removal of 96.12% was achieved for the system with magnetic synthesized hydrogel beads Fe_3O_4@AC@CH (1 g/L) in addition to US + H_2O_2. This result is a consequence of multiple phenomena that simultaneously occur in the reaction system. The surface and porous matrix of the hydrogels adsorbs large quantities of (mostly organic) pollutants. The Fenton reactions induced by H_2O_2 in the medium and Fe_3O_4@AC nanoparticles on the surface of the hydrogel beads generate the oxidizing $^{\bullet}OH$ and $HO_2^{\bullet}$ radicals (Voinov et al. 2011). Due to the very close proximity of the sites (or spots) of the generation of radicals and the adsorbed pollutants on the surface of the hydrogel beads, the probability of interaction between the radicals and pollutant molecules is very high. Thus, the $^{\bullet}OH$ and $HO_2^{\bullet}$ radicals can easily oxidize and mineralize the adsorbed pollutants. Further, the intense micro-mixing and microconvection generated by sonication enhance the mass transfer between the bulk medium and the surface/pores of the hydrogel beads. Moreover, the micromixing also prevents agglomeration between the hydrogel beads and assists their uniform dispersion in the reaction medium. The positive synergy between these phenomena leads to effective degradation and mineralization of persistent pollutants in WW and almost complete COD removal (Khataee et al. 2014; Hou et al. 2016).

Role of sonication: For identification of the contribution of sonication in COD removal, a control experiment was performed using hydrogel beads of Fe_3O_4@AC@CH with mechanical stirring. All other conditions of this experiment were the same as the validation experiment (at

optimum conditions) stated previously. The COD removal achieved in this experiment was 79%. With the application of sonication, the COD removal increased to 96.1%, which is a rise of 21.5%. As noted earlier, this rise essentially is a consequence of the faster mass transfer of pollutant molecules between hydrogel beads and the bulk medium.

Comparison with previous literature: As mentioned earlier in the Introduction section, most of the previous studies on WW treatment using hydrogel beads are based on adsorptive removal of the pollutants. Relatively little literature is available on the use of hydrogel beads for the degradation of pollutants in WW. Afzal et al. (2022) achieved 85.23% degradation of ciprofloxacin in a sonocatalytic process using hydrogel beads of TiO_2-incorporated biochar and chitosan. Similarly, Wanchai and Pichon (2020) reported 84.2% sulphanilamide degradation using magnetic chitosan beads in a photo-Fenton process. Mehdaoui et al. (2022) have reported 75% degradation of olive oil mill WW in a sono-heterogeneous Fenton process using magnetic glutaraldehyde cross-linked developed cellulose (GTA-[PDA-g-DAC]@Fe_3O_4).

4.3.4 Investigation of adsorption behavior of the Fe_3O_4@AC@CH hydrogel beads

Simultaneously with the WW treatment experiments, the adsorption behavior of the Fe_3O_4@AC@CH hydrogel beads was evaluated. Figure 4.10a represents the time profile of pollutant adsorption onto 1 g/L Fe_3O_4@AC@CH beads in a 150 mL solution at pH 5.12, subjected to 20 kHz sonication. Since the WW contains a mixture of components, the degradation and adsorption are based on %COD removal. The time profiles of adsorption were analyzed using pseudo-first-order, pseudo-second-order, and intraparticle diffusion models. Additionally, Langmuir and Freundlich adsorption isotherms were also fitted to the data (Figure 4.10b) after determining q_e and C_e values, and the results are presented in Table 4.6. The analysis revealed that the adsorption profile of pollutants on the Fe_3O_4@AC@CH beads

best fits the second-order kinetics (R^2 = 0.99), with a q_e value of 215.94 mg/g, which was close to experimental q_e (230.56 mg/g), and a second-order rate constant of 0.55 (g/mg min). Furthermore, Langmuir adsorption isotherm best fitted the experimental data with R^2 = 0.99, and the maximum adsorption capacity was found to be 279.68 mg/g. The R_L (separation factor) was calculated as 0.0021, indicating a strongly preferred isotherm. These findings underscore the efficiency of the Fe_3O_4@AC@CH hydrogel beads in adsorbing pollutants, subsequently degraded by radicals generated through Fenton reactions on or near the adsorbent surface.

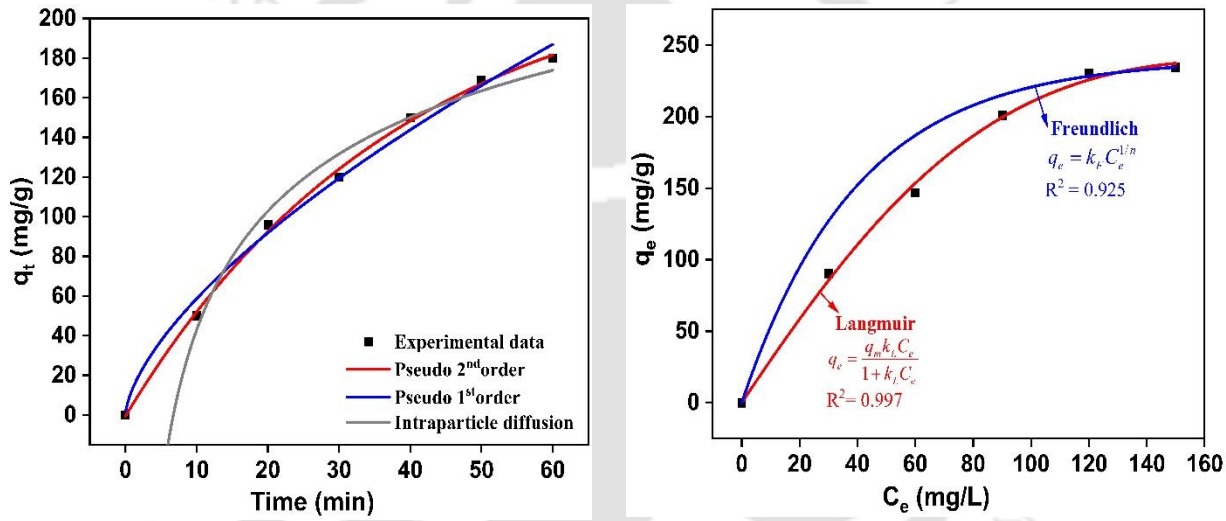

(a) (b)

Figure 4.10. (a) The effect of time on adsorption of pollutants and fitting of non-linear adsorption kinetics on Fe_3O_4@AC@CH beads; (b) Plot of q_e vs. C_e and adsorption isotherms on Fe_3O_4@AC@CH beads (at the optimum condition: Fe_3O_4@AC@CH beads dose = 1 g/L, pH = 5.12, H_2O_2 loading = 0.75 M).

Table 6. Adsorption behaviour of Fe_3O_4@AC@CH hydrogel beads

Adsorption kinetics	Parameters	Value
Pseudo- first-order model	$q_{e,cal}$ (mg/g)	154.56
	k_1 (min^{-1})	0.019
	R^2	0.94
Pseudo- second order model	$q_{e,cal}$ (mg/g)	215.94
	k_2 (g/mg min)	0.55
	R^2	0.99
	$q_{e,exp}$.(mg/g)	230.56
Intra-particle diffusion model	k_{diff} (mg/g $min^{1/2}$)	0.038
	C (mg/g)	10.153
	R^2	0.89
Langmuir Adsorption isotherm	q_{max} (mg/g)	279.68
	k_L (L/mg)	0.149
	R^2	0.99
	R_L	0.0021
Freundlich Adsorption isotherm	k_F (mg/g) $(mg/L)^{-1/n}$	39.78
	1/n	0.34
	R^2	0.92

The optimized condition: Fe_3O_4@AC@CH beads dose = 1 g/L, pH = 5.12, H_2O_2 loading = 0.75 M.

4.3.5 LC-MS/MS analysis of the wastewater

Figure 4.11 displays the chromatograms of WW pre and post-treatment. Table A4.5 (available in Appendix A4) provides a list of organic pollutants identified from LC-MS/MS analysis. The organic contaminants that were degraded > 90% are listed as follows: benzyl butyl phthalate (100%), endrin (100%), 2,3,4,5-tetrabromobenzoic acid (TBBA) (99%), 2,3,4,5-tetrachlroanisole (99%), 2-isopropoxyphenol (99.9%), pentachloroaniline (99.9%), bensulfuron-methyl (99.9%), benzene (99.9%), and *p*-cresol (94.8%). Most of these

contaminants are toxic pollutants, which are used in PVC production, textile industry, industrial bleaching, dye and rubber manufacturing, herbicides, and pesticides, and some are adhesive and used as plasticizers in polymer.

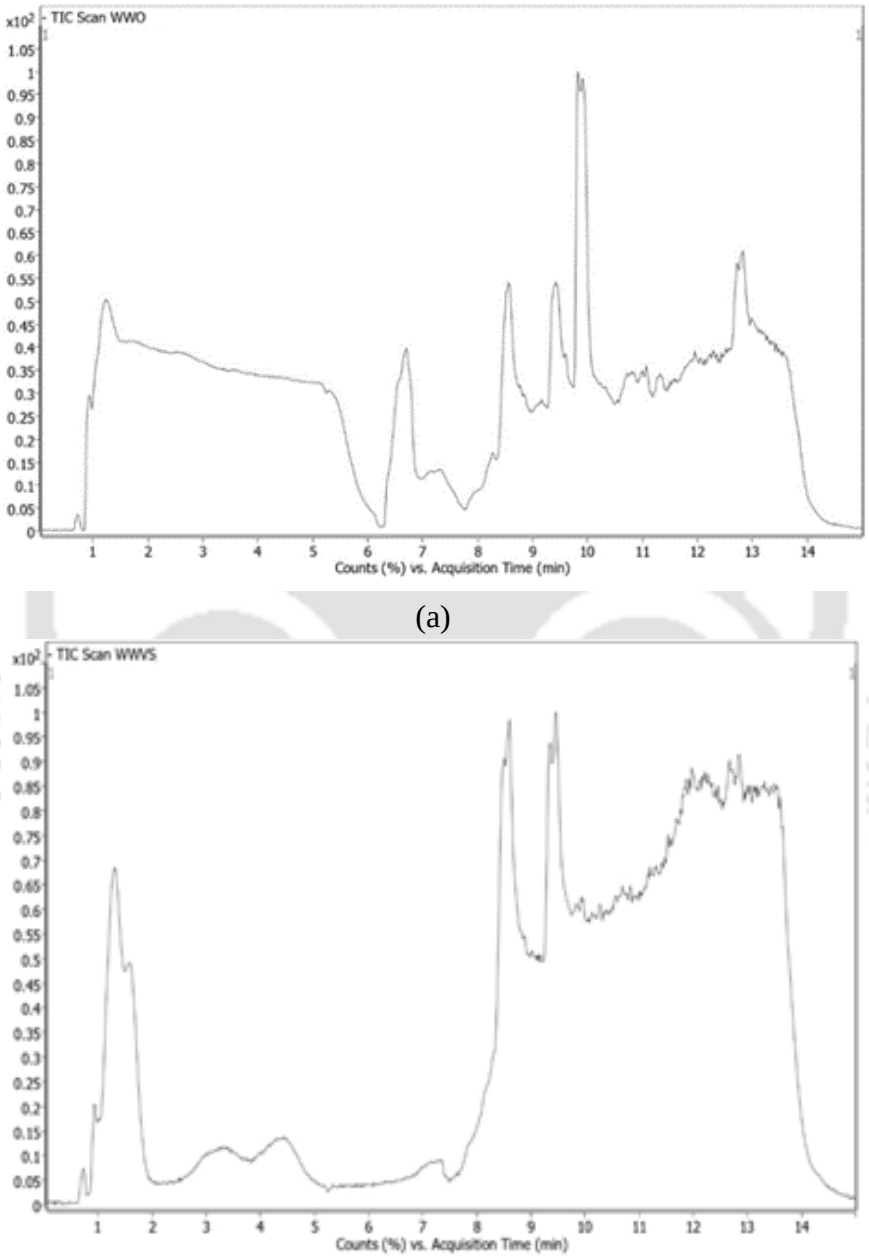

Figure 4.11. LC-MS/MS chromatogram of wastewater (a) pre and (b) post treatment (at optimized condition: Fe_3O_4@AC@CH beads dose = 1 g/L, pH = 5.12, H_2O_2 loading = 0.75 M)

4.3.6 Toxicity of Wastewater

The effectiveness of the ultrasonic treatment of WW with Fe_3O_4@AC@CH hydrogel beads in reducing the toxicity of WW was evaluated through a seed germination technique using *Vigna radiata* seeds (Fig. 4.12). In comparison to the 100% germination observed in the control group grown in deionized water, the original WW exhibited no seed growth (0% germination). However, the seeds in the after-treatment WW displayed a significant improvement with a 70% germination rate. These results affirm the successful mitigation of WW toxicity through the application of sonication.

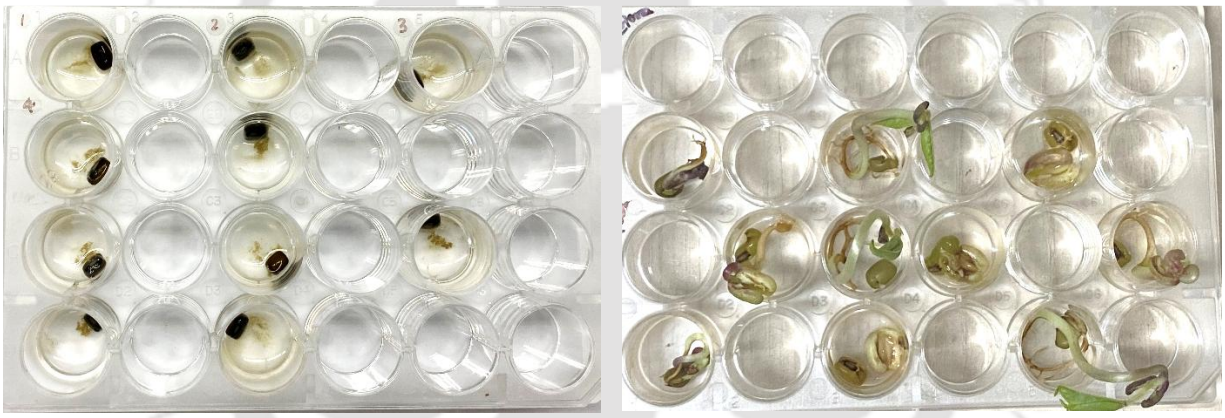

(a) (b)

Figure 4.12. Toxicity assay of WW (a) before treatment and (b) after treatment (at the optimized condition: Fe_3O_4@AC@CH beads dose = 1 g/L, pH = 5.12, H_2O_2 loading = 0.75 M)

4.3.7 Reusability and stability of Fe_3O_4@AC@CH hydrogel beads

The recyclability and reusability of the Fe_3O_4@AC@CH beads were evaluated over six consecutive treatment cycles. Recyclability was gauged by calculating the percentage recovery of the initial weight of the hydrogel beads introduced into the solution, while reusability was assessed based on the %COD removal in successive treatments. In a usual experiment, the

Fe_3O_4@AC@CH beads, suspended in the solution after sonication treatment, were collected using a magnet, rinsed thoroughly with DI water, and then introduced into another 150 mL solution for a subsequent 60-min sonication treatment. This cycle was repeated 6×. Figure 4.13 illustrates the results of this analysis conducted at optimum conditions of pH, Fe_3O_4@AC@CH beads dose, and H_2O_2 loading. The findings indicate that the recovery of the Fe_3O_4@AC@CH beads exceeded 95 wt% over successive treatment cycles, affirming its excellent recyclability. The %COD removal was 96.12% in the initial treatment cycle, slightly decreasing to 89% in the sixth cycle. This implies that the catalytic ability of the Fe_3O_4@AC@CH hydrogel beads remained highly effective across the sixth cycle of stability and recovery.

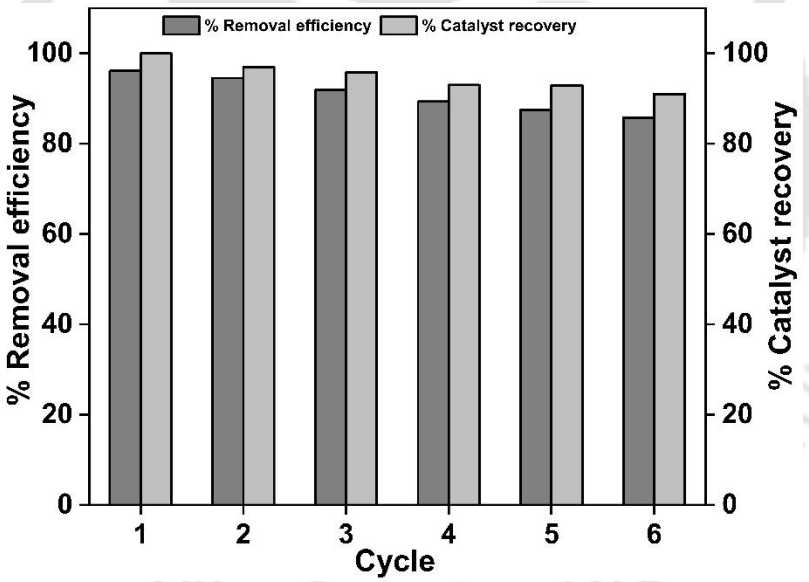

Figure 4.13. Reusability and stability of Fe_3O_4@AC@CH hydrogel beads within sixth consecutive cycles (at optimum condition: Fe_3O_4@AC@CH beads dose = 1 g/L, pH = 5.12, H_2O_2 loading = 0.75 M).

4.4 Conclusion

In this chapter, we have reported the treatment of industrial WW using sonication in the presence of floatable chitosan-based hydrogel beads. As filler material, these hydrogel beads were synthesized with Fe_3O_4 decorated activated charcoal nanoparticles (Fe_3O_4@AC nanocomposites). These beads were characterized for physicochemical properties and surface and structural morphologies using FTIR. XRD, BET, VSM, FE-SEM, EDX, and FE-TEM techniques. The Fe_3O_4@AC@CH hydrogel beads acted as both adsorbents and heterogeneous Fenton reagents. Statistical optimization of the hybrid AOP was done using the RSM technique. At optimum conditions (0.75 M H_2O_2, 1 g/L Fe_3O_4@AC@CH beads, pH 5.12), a COD removal of 96.12% and TOC removal of 78.14% was achieved in 1 h treatment. Several control experiments were performed simultaneously to deduce synergism in the hybrid AOPs. The COD removal in these experiments was as follows: sonication (US) alone = 12%, US + H_2O_2 = 25%, US + Fe_3O_4 +H_2O_2 = 67.5%, US + Fe_3O_4@AC +H_2O_2 = 93.25%, and Fe_3O_4@AC@CH hydrogel beads + mechanical stirring + H_2O_2 = 79%. The synergistic interactions in the hybrid AOP were identified as follows: the surface and porous matrix of the hydrogels adsorbed large quantities of pollutants. Fenton reactions were induced on the surface of the hydrogel beads due to H_2O_2 added to the medium and Fe-ions released in the medium due to surface leaching of Fe_3O_4 nanoparticles. These Fenton reactions generated $^{\bullet}OH$ and $HO_2^{\bullet}$ radicals that effectively degraded and mineralized adsorbed pollutants. Sonication induced intense micro-mixing in the medium, enhancing mass transfer between bulk medium and surface/pores of hydrogel beads. The toxicity of WW was reduced by ~70% after treatment. Major contaminants in the WW degraded during treatment were identified using LC−MS analysis. More than 25 pollutants were degraded entirely during the treatment of WW. Fe_3O_4@AC@CH hydrogel beads had excellent recyclability till six consecutive treatment cycles. In summary,

the Fe_3O_4@AC@CH hydrogel beads, when used with sonication, have remarkable potential for reduction in COD and TOC of actual WW.

References

Acisli O, Khataee A, Karaca S, et al (2017) Combination of ultrasonic and Fenton processes in the presence of magnetite nanostructures prepared by high energy planetary ball mill. Ultrason Sonochem 34:754–762. https://doi.org/10.1016/j.ultsonch.2016.07.011

Afzal MZ, Zu P, Zhang C-M, et al (2022) Sonocatalytic degradation of ciprofloxacin using hydrogel beads of TiO_2 incorporated biochar and chitosan. J Hazard Mater 434:128879. https://doi.org/10.1016/j.jhazmat.2022.128879

Agani I, K. Fatombi J, A. Osseni S, et al (2020) Removal of atrazine from aqueous solutions onto a magnetite/chitosan/activated carbon composite in a fixed-bed column system: optimization using response surface methodology. RSC Adv 10:41588–41599. https://doi.org/10.1039/D0RA07873E

Anfar Z, Amedlous A, Majdoub M, et al (2020) New amino group functionalized porous carbon for strong chelation ability towards toxic heavy metals. RSC Adv 10:31087–31100. https://doi.org/10.1039/D0RA05220E

Ansari F, Ghaedi M, Taghdiri M, Asfaram A (2016) Application of ZnO nanorods loaded on activated carbon for ultrasonic assisted dyes removal: Experimental design and derivative spectrophotometry method. Ultrason Sonochem 33:197–209. https://doi.org/10.1016/j.ultsonch.2016.05.004

Anulekshmi PS, Nithya K, Kumar PS, et al (2024) Design of biocompatible gelatin hydrogels reinforced with magnetite nanoparticles: Effective removal of chromium from water environment. Environ Res 260:119768. https://doi.org/10.1016/j.envres.2024.119768

American Public Health Association. (1926). *Standard methods for the examination of water and wastewater* (Vol. 6). American Public Health Association.

Chakma S, Das L, Moholkar VS (2015) Dye decolorization with hybrid advanced oxidation processes comprising sonolysis/Fenton-like/photo-ferrioxalate systems: A

mechanistic investigation. Sep Purif Technol 156:596–607. https://doi.org/10.1016/j.seppur.2015.10.055

Chen X (2024) Fabrication of Core-Shell Hydrogel Bead Based on Sodium Alginate and Chitosan for Methylene Blue Adsorption. J Renew Mater 12:815–826. https://doi.org/10.32604/jrm.2024.048470

Expósito AJ, Monteagudo JM, Durán A, Fernández A (2017) Dynamic behavior of hydroxyl radical in sono-photo-Fenton mineralization of synthetic municipal wastewater effluent containing antipyrine. Ultrason Sonochem 35:185–195. https://doi.org/10.1016/j.ultsonch.2016.09.017

Ge H, Liu L, Li W, et al (2021) Hierarchical carbon fiber cloth (CFC)/Co_3O_4 composite with efficient photo-electrocatalytic performance towards water purification. Diam Relat Mater 118:108537. https://doi.org/10.1016/j.diamond.2021.108537

Gong D, Yang P, Zhao J, Jia X (2024) Selective removal of thallium from water by MnO_2-doped magnetic beads: Performance and mechanism study. J Environ Manage 353:120147. https://doi.org/10.1016/j.jenvman.2024.120147

Hassani A, Malhotra M, Karim AV, et al (2022) Recent progress on ultrasound-assisted electrochemical processes: A review on mechanism, reactor strategies, and applications for wastewater treatment. Environ Res 205:112463. https://doi.org/10.1016/j.envres.2021.112463

Ho Y-S (2006) Second-order kinetic model for the sorption of cadmium onto tree fern: A comparison of linear and non-linear methods. Water Res 40:119–125. https://doi.org/10.1016/j.watres.2005.10.040

Ho YS, McKay G (2000) The kinetics of sorption of divalent metal ions onto sphagnum moss peat. Water Res 34:735–742. https://doi.org/10.1016/S0043-1354(99)00232-8

Hou L, Wang L, Royer S, Zhang H (2016) Ultrasound-assisted heterogeneous Fenton-like degradation of tetracycline over a magnetite catalyst. J Hazard Mater 302:458–467. https://doi.org/10.1016/j.jhazmat.2015.09.033

Huang R, Fang Z, Yan X, Cheng W (2012) Heterogeneous sono-Fenton catalytic degradation of bisphenol A by Fe_3O_4 magnetic nanoparticles under neutral condition. Chem Eng J 197:242–249. https://doi.org/10.1016/j.cej.2012.05.035

Huang Y, Lapanje A, Parakhonskiy B, Skirtach AG (2024) Versatile and durable polyvinyl alcohol/alginate/gelatin/quaternary ammonium chitosan/Fe_3O_4 particles hybrid hydrogel beads: adsorption capabilities for cleaning pollutants. Int J Biol Macromol 280:135729. https://doi.org/10.1016/j.ijbiomac.2024.135729

Ismail YH, Wang K, Shehhi MA, Hammadi AA (2024) Iodide ion-imprinted chitosan beads for highly selective adsorption for nuclear wastewater treatment applications. Heliyon 10:. https://doi.org/10.1016/j.heliyon.2024.e24735

Jamali M, Akbari A (2021) Facile fabrication of magnetic chitosan hydrogel beads and modified by interfacial polymerization method and study of adsorption of

cationic/anionic dyes from aqueous solution. J Environ Chem Eng 9:105175. https://doi.org/10.1016/j.jece.2021.105175

Jung S, Jung M, Yoon J, et al (2024) Chitosan-derived activated carbon/chitosan composite beads for adsorptive removal of methylene blue and acid orange 7 dyes. React Funct Polym 204:106028. https://doi.org/10.1016/j.reactfunctpolym.2024.106028

Kaveh R, Bagherzadeh M (2022) Simultaneous removal of mercury ions and cationic and anionic dyes from aqueous solution using epichlorohydrin cross-linked chitosan @ magnetic Fe_3O_4/activated carbon nanocomposite as an adsorbent. Diam Relat Mater 124:108923. https://doi.org/10.1016/j.diamond.2022.108923

Khataee A, Darvishi Cheshmeh Soltani R, Hanifehpour Y, et al (2014) Synthesis and Characterization of Dysprosium-Doped ZnO Nanoparticles for Photocatalysis of a Textile Dye under Visible Light Irradiation. Ind Eng Chem Res 53:1924–1932. https://doi.org/10.1021/ie402743u

Kumar A, Patra C, Rajendran HK, Narayanasamy S (2022) Activated carbon-chitosan based adsorbent for the efficient removal of the emerging contaminant diclofenac: Synthesis, characterization and phytotoxicity studies. Chemosphere 307:135806. https://doi.org/10.1016/j.chemosphere.2022.135806

Le VT, Dao MU, Le HS, et al (2020) Adsorption of Ni(II) ions by magnetic activated carbon/chitosan beads prepared from spent coffee grounds, shrimp shells and green tea extract. Environ Technol 41:2817–2832. https://doi.org/10.1080/09593330.2019.1584250

Liu Y, Shan H, Pang Y, et al (2023) Iron modified chitosan/coconut shell activated carbon composite beads for Cr(VI) removal from aqueous solution. Int J Biol Macromol 224:156–169. https://doi.org/10.1016/j.ijbiomac.2022.10.112

Mehdaoui R, Agren S, El Haskouri J, et al (2022) An optimized sono-heterogeneous Fenton degradation of olive-oil mill wastewater organic matter by new magnetic glutarlaldehyde-crosslinked developed cellulose. Environ Sci Pollut Res 30:20450–20468. https://doi.org/10.1007/s11356-022-23276-2

Nigussie W, Zewge F, Chandravanshi BS (2007) Removal of excess fluoride from water using waste residue from alum manufacturing process. J Hazard Mater 147:954–963. https://doi.org/10.1016/j.jhazmat.2007.01.126

Peng S, Meng H, Ouyang Y, Chang J (2014) Nanoporous Magnetic Cellulose–Chitosan Composite Microspheres: Preparation, Characterization, and Application for Cu(II) Adsorption. Ind Eng Chem Res 53:2106–2113. https://doi.org/10.1021/ie402855t

Reddy DHK, Lee S-M (2013) Application of magnetic chitosan composites for the removal of toxic metal and dyes from aqueous solutions. Adv Colloid Interface Sci 201–202:68–93. https://doi.org/10.1016/j.cis.2013.10.002

Rezgui S, Amrane A, Fourcade F, et al (2018) Electro-Fenton catalyzed with magnetic chitosan beads for the removal of Chlordimeform insecticide. Appl Catal B Environ 226:346–359. https://doi.org/10.1016/j.apcatb.2017.12.061

Rostami MS, Khodaei MM, Benassi E (2024) Surface modified of chitosan by TiO_2@MWCNT nanohybrid for the efficient removal of organic dyes and antibiotics. Int J Biol Macromol 274:133382. https://doi.org/10.1016/j.ijbiomac.2024.133382

Roy K, Moholkar VS (2020) Sulfadiazine degradation using hybrid AOP of heterogeneous Fenton/persulfate system coupled with hydrodynamic cavitation. Chem Eng J 386:121294. https://doi.org/10.1016/j.cej.2019.03.170

Salem DB, Ouakouak A, Touahra F, et al (2023) Easy separable, floatable, and recyclable magnetic-biochar/alginate bead as super-adsorbent for adsorbing copper ions in water media. Bioresour Technol 383:129225. https://doi.org/10.1016/j.biortech.2023.129225

Santana Cadaval TR, Camara AS, Dotto GL, Pinto LADA (2013) Adsorption of Cr (VI) by chitosan with different deacetylation degrees. Desalination Water Treat 51:7690–7699. https://doi.org/10.1080/19443994.2013.778797

Shen S, Fu JJ, Wang HB (2021) Unravelling the favorable photocatalytic effect of hydrogenation process on the novel g-C_3N_4-TiO_2 catalysts for water purification. Diam Relat Mater 114:108292. https://doi.org/10.1016/j.diamond.2021.108292

Shi L, Xu F, Gao J, et al (2020) Nanostructured boron-doped diamond electrode for degradation of the simulation wastewater of phenol. Diam Relat Mater 109:108098. https://doi.org/10.1016/j.diamond.2020.108098

Sivasankar T, Moholkar VS (2009) Mechanistic approach to intensification of sonochemical degradation of phenol. Chem Eng J 149:57–69. https://doi.org/10.1016/j.cej.2008.10.004

Taghiloo B, Shahnazi A, Nabid MR (2024) Construction of nanocomposite hydrogel by TiO_2-carbon quantum dots encapsulated in alginate with a highly efficient adsorption and photodegradation of dye pollutants. J Alloys Compd 1005:175859. https://doi.org/10.1016/j.jallcom.2024.175859

Verma K, Moholkar VS (2023) Mineralization of Industrial Wastewater by a Hybrid Technique of Adsorption (Fe_3O_4@AC Nanocomposite) + Heterogeneous Fenton + Sonication and Discernment of Synergistic Effects. Ind Eng Chem Res acs.iecr.3c00427. https://doi.org/10.1021/acs.iecr.3c00427

Voinov MA, Sosa Pagán JO, Morrison E, et al (2011) Surface-mediated production of hydroxyl radicals as a mechanism of iron oxide nanoparticle biotoxicity. J Am Chem Soc 133:35–41. https://doi.org/10.1021/ja104683w

Wanchai K, Pichon R (2020) Synthesis of Fe_3O_4@chitosan beads for degradation of sulfanilamide using photo-fenton process. Pattaya, Thailand, p 130002

Wang Y, Li B, Zhou Y, Jia D (2008) Chitosan-induced synthesis of magnetite nanoparticles via iron ions assembly. Polym Adv Technol 19:1256–1261. https://doi.org/10.1002/pat.1121

Appendix A4

Table A4.1. Degradation/mineralization of recalcitrant pollutants using different hybrid AOPs

Target pollutant	Methodology used	Experimental attributes	Results	Reference
Congo Red (CR)	HC + UV + PS	Inlet pressure = 2-6 bar, PS = 50 mg/L, UV = 32 W	92.01% decolorization and 63.4% degradation were achieved	(Dehghani et al. 2024)
CIP	ZFO + TiO_2	CIP = 20 ppm, t = 60 min	98% CIP removal was achieved	(John et al. 2023)
Indigo Carmine	US +Fe^{2+} + H_2O_2 + UV	pH = 3, H_2O_2 = 200 mg/L, t = 70 min	100% degradation was achieved	(Hadjltaief et al. 2021)
SDZ	α-Fe2O3 catalyst + HC (Orifice)	SDZ initial conc. = 20 ppm, pH = 4, Inlet pressure = 10 atm, Na2S2O8 = 348.5 mg/L, H2O2 = 0.95 mL/L and α-Fe2O3 catalyst =181.8 mg/L	81.24 % degradation	(Roy and Moholkar 2020)
Methylparaben	Co-Fe carbon xerogel + US	CX/CoFe = 25 ppm, [MP] = 1 mg/L, t = 60 min	100 % degradation was achieved	(Zanias et al. 2020)
Sulfamethoxazole (SMX)	Fe_3O_4/Co_3O_4 + ozonation	SMX = 20 mg/L, O_3 = 6 mg/l, pH = 5.1, T = 25 ^oC, Catalyst = 0.1 g/L	60% TOC↓	(Chen and Wang 2019)
Brilliant Green dye	NiO supported over CeO_2 + US	Catalyst = 0.2 g/L, t = 4h	81.9% decolourization	(Sancheti et al. 2018)

Bisphenol A	MnO_2 + Stirred tank	Calcined at 400 ^oC, t = 4 hr	90% degradation	(Dietrich et al. 2017)
Diethyl phthalate	$Ce/SiO_2@Fe_2O_4$ +Ozonation	Calcined at 600 ^oC, t= 2 hr	97.6% degradation	(Wang et al. 2016)

Table A4.2. Summary of the previous literature on the removal of organic pollutants using chitosan-encapsulated hydrogel nanocomposite/beads

Specific Pollutants	Method/ catalyst	Process parameters	Results	References
Cr (VI)	Adsorption/ (Fe/CSCC) beads	[Cr (VI)] = 25 mg/L, m/v = 1 g/L, pH = 3, T = 25 ^{o}C and t = 2880 min	97.25 % removal was achieved and adsorption capacity was found to be 64.49 mg/g	(Liu et al. 2023)
Caffeine	Chitosan/ activated carbon beads	[CAF] = 20 mL, catalyst dose = 20 mg, stirring = 120 rpm and T = 25 ^{o}C	The maximum adsorption capacity was found to be 83.88 mg/g	(Quesada et al. 2022)
CIP	Sonocatalytic degradation/ TBCB	TBCB dose = 30 mg, [CIP] = 30 mL, pH = 6 and t = 25 min	85.23 % degradation efficiency was achieved	(Afzal et al. 2022)
Eriochrome black T (EBT) dye	Adsorption/ (chitosan/Fe_3O_4/GO) beads	Catalyst dose = 50 mg, [dye] = 100 ppm, stirring = 130 rpm, T = 26 ^{o}C and t = 300 min	292 mg/g maximum adsorption was achieved	(Jamali and Akbari 2021)
Methylene blue (MB) dye	Adsorption/ (chitosan/Fe_3O_4/GO) beads	Catalyst dose = 50 mg, [dye] = 100 ppm, stirring = 130 rpm, T = 26 ^{o}C and t = 300 min	289 mg/g maximum adsorption was achieved	
Ni (II)	Adsorption/ MACCS beads	Beads dose = 1 g/L, pH = 6, T = 25 ^{o}C and t = 6h	86.25 % removal efficiency was achieved along with 108.70 mg/g adsorption capacity	(Le et al. 2020)
Sulfanilamide	Photo- Fenton/ Fe_3O_4@chitosan beads	Beads dose = 100 g/ L, H_2O_2 loading = 0.32 mmol, pH = 3, [sulfanilamide] = 50 mg/L and t = 120 min	84.2 % degradation was obtained	(Wanchai and Pichon 2020)

Hg (II)	Adsorption/ magnetic chitosan beads	Beads dose = 0.1 g, [Hg(II)] = 25 ppm, stirring = 150 rpm and t = 40 min	0.4 mg/g adsorption capacity was obtained which was higher than pure chitosan	(Rahmi et al. 2019)
Cd (II)	Adsorption/ magnetic chitosan beads	Beads dose = 0.1 g, [Cd(II)] = 25 ppm, stirring = 150 rpm and t = 40 min	3.04 mg/g adsorption capacity was obtained which was higher than pure chitosan	
CIP	Adsorption/ CBHB	[CIP] = 200 mL, pH = 3, stirring = 250rpm and t = 48 h	32.69 mg/g adsorption capacity was achieved	(Afzal et al. 2018)
Pb^{2+}	Adsorption/ PMCH beads	$[Pb^{2+}]$ = 200 mg/L, beads dose = 2 g, stirring = 160 rpm and t = 24 h	84.02 mg/g adsorption capacity was achieved	(Pu et al. 2017)
MB	Adsorption/ (CTN/AC-Fe_3O_4) composite	Catalyst dose = 50 mg, [dye] = 100 ppm, stirring = 120 rpm, pH = 7.73 and t = 24 h	500 mg/g adsorption capacity was achieved	(Karaer and Kaya 2016)
RB4	Adsorption/ (CTN/AC-Fe_3O_4) composite	Catalyst dose = 50 mg, [dye] = 100 ppm, stirring = 120 rpm, pH = 6.64 and t = 24 h	250 mg/g adsorption capacity was achieved	
Industrial effluent	**Sono-Eenton/ Fe_3O_4@AC@CH hydrogel beads**	**Fe_3O_4@AC@CH beads dose = 1 g/L, pH = 5.12, H_2O_2 loading = 0.75 M, T = 25 ºC and t= 60 min**	**96.12% COD removal obtained along with 279.68 mg/g maximum adsorption capacity and 70% reduction in toxicity**	**This study**

Section A4.1. LC-MS/MS protocol

LC-ESI-MS/MS analysis was conducted with a ZORBAX Eclipse C_{18} (4.6× 100 mm, 3.5 µm) from Agilent Technologies (Santa Clara, US). The details of the instrumentation and mobile phase composition are given in Table A4.3. In the mass spectrophotometer, the spray and cone voltages applied were ±4500 V and ±1000 V, respectively. The drying gas flow rate was 12 L/min (593 K), and the nebulizer pressure was 3.4 bar (50 psi).

Table A4.3. The details of the instrumentation and mobile phase composition

Instrument	1290 Infinity HPLC system with 6545 Quadrupole-Time of Flight
Column temperature	45°C
Mobile Phase	Positive Mode A Milli-Q water with 0.1%FA B Methanol with 0.1% FA Negative Mode A Milli-Q water with 1% MeOH B Methanol with 10% H_2O
Flow rate	0.4 ml/min- Positive Mode 0.5 ml/min- Negative Mode
Mode	Gradient

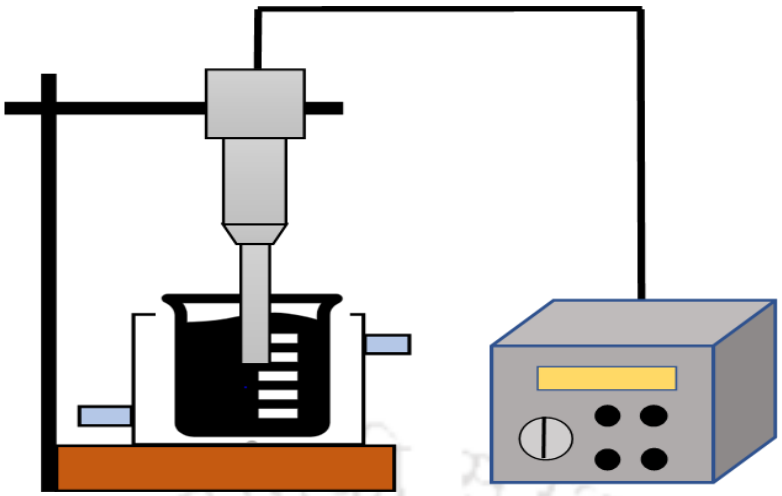

Figure A4.1. Schematic diagram of experimental setup

Table A4.4. Analysis of variance (ANOVA) for the response surface quadratic model

Source	Sum of Squares	df	Mean Square	*F*-value	*p*-value	
Model	2851.81	9	316.87	47.54	< 0.0001	significant
X_1	543.91	1	543.91	81.60	< 0.0001	
X_2	302.06	1	302.06	45.32	< 0.0001	
X_3	121.31	1	121.31	18.20	0.0016	
X_1X_2	0.1485	1	0.1485	0.0223	0.8843	
X_1X_3	0.0003	1	0.0003	0.0000	0.9947	
X_2X_3	0.9591	1	0.9591	0.1439	0.7124	
X_1X_1	311.59	1	311.59	46.75	< 0.0001	
X_2X_2	215.36	1	215.36	32.31	0.0002	
X_3X_3	20.87	1	20.87	3.13	0.1073	
Residual	66.65	10	6.67			
Lack of Fit	30.85	5	6.17	0.8615	0.5630	not significant
Pure Error	35.81	5	7.16			
Total	2918.46	19				
Quality of quadratic model						
R^2				0.9872		
Adjusted R^2				0.9566		
Predicted R^2				0.9081		
Adeq Precision				21.284		

Table A4.5. List of identified contaminants using LC-MS/QTOF

Compound name	Chemical formula	Retention time (min)	Mass (g/moL)	% Reduction
1,2,3,4,7,8,9-Heptachlorodibenzofuran (HPCDF)	C_{12} H Cl_7 O	11.45	409.3	100
1,2-Dichloropropane	C_3 H_6 Cl_2	1.25	113	99.99
1-Aminonaphthalene	C_{10} H_9 N	14.42	143.19	61.57
1-Hydroxypyrene	C_{16} H_{10} O	12.34	218	99.99
2-(N-Methyl-perfluorooctane sulfonamido) acetic acid (Me-PFOSA-AcOH or Me-FOSA-A)	C_{11} H_6 F_{17} N O_4 S	12.88	571.06	99.99
2,2' 5',2-Terthiophene	C_{12} H_8 S_3	7.46	248	56.04
2,2',3,3',4,4',5,5',6,6'-Decachlorobiphenyl (PCB 209)	C_{12} Cl_{10}	12.33	499	100
2,2',3,4,4',5',6-Heptabromodiphenyl ether (BDE 183)	C_{12} H_3 Br_7 O	12.45	722.48	100
2,2,4,4',5,6'-Hexabromodipheny ether (BDE 154)	C_{12} H_4 Br_6 O	12.75	643.6	99.99
2,3,4,5-Tetrabromobenzoic acid (TBBA)	C_{19} H_2 Br_4 O_2	12.14	577.8	99.07
2,3,4,5-Tetrachlroanisole	C_6 H_4 Cl_3 N	1.24	196.46	99.99
2,6-Dichlorobenzonitrile	C_7 H_3 Cl_2 N	6.48	172.01	99.99
2.2'.4.4'.6-Pentabromodiphenyl ether (BDE 100)	C_{12} H_5 Br_5 O	12.89	564.69	99.99
2-Amino-6-methyldipyrido[1,2-a:3',2'-d]imidazole (Glu-P1)	C_{11} H_{10} N_4	13.96	255.68	99.99
2-Isopropoxyphenol	C_9 H_{12} O_2	11.85	152.19	99.99
3-Amino-1,4-dimethyl-5H-pyrido[4,3-b]indole (Trp-P-1)	C_{13} H_{13} N_3	8.60	271.31	74.65
4,4'-Diaminodiphenylmethane (4MDA)	C_{13} H_{14} N_2	8.21	198.26	80.87
4-Aminobiphenyl	C_{12} H_{11} N	8.37	169.22	99.99
5-Nitro-o-toluidine	C_7 H_8 N_2 O_2	8.69	152.16	50.74
9-Chlorohexadecafluoro-3-oxanonane-1-sulfonic acid (9Cl-PF3ONS)	C_8 Cl F_{16} O_4 S	13.15	570.68	64.13
Aldrin	C_{12} H_8 Cl_6	10.52	364.91	82.30
Allidochlor	C_8 H_{12} Cl N O	11.80	173.64	75.11

Bensulfuron-methyl	$C16_6 H_{18} N_4 O_7 S$	0.90	410.44	99.99
Benzene	$C_6 H_6$	8.75	78.11	99.99
Benzonitrile	$C_7 H_5 N$	1.07	103.12	53.79
Benzyl butyl phthalate	$C_{19} H_{20} O_4$	10.65	312.36	100
bis(2-ethylhexyl) adipate	$C_{22} H_{42} O_4$	16.44	370.57	57.18
Bisphenol AF	$C_{15} H_{10} F_6 O_2$	13.56	336.23	54.03
Bisphenol S	$C_{12} H_{10} O_4 S$	1.06	250.28	99.99
Bromoxynil octanoic acid ester	$C_{15} H_{17} Br_2 N O_2$	12.04	403.11	99.99
Carbosulfan	$C_{20} H_{32} N_2 O_3 S$	11.51	380.55	99.99
Chlordene	$C_{10} H_6 Cl_6$	1.98	338.87	99.99
Cloquintocet-mexyl	$C_{18} H_{22} Cl N O_3$	8.31	335.8	99.99
Cresidine, p- 4-Dimethylaminophenol.	$C_8 H_{11} N O$	8.44	137.17	56.37
Cycloate	$C_{11} H_{21} N O S$	14.75	215.36	60.10
Cyenopyrafen	$C_{24} H_{31} N_3 O_2$	11.29	393.52	100
Cyfluthrin I	$C_{22} H_{18} Cl_2 F N O_3$	12.14	434.29	92.19
Diacetoxyscirpenol	$C_{19} H_{26} O_7$	10.37	366.41	99.99
Dibenzofuran	$C_{12} H_8 O$	1.10	168.19	83.08
Dibenzothiophene	$C_{12} H_8 S$	6.48	184.26	99.99
Diethyldithiophosphate (DEDTP)	$C_4 H_{11} O_2 P S_2$	6.48	186.23	99.99
Diethylphosphate (DEP)	$C_4 H_{11} O_4 P$	10.67	153.09	61.58
Dimethylphenol, 2,4- (2,4-xylenol)	$C_8 H_{10} O$	11.47	122.16	99.07
Dinitrotoluene, 2,4- nitro-benzoic acid	$C_7 H_6 N_2 O_4$	1.10	182.13	99.99
Diphenamid	$C_{16} H_{17} N O$	1.18	239.31	99.99
Endrin	$C_{12} H_8 Cl_6 O$	10.76	380.91	100
Fluvalinate I	$C_{26} H_{22} Cl F_3 N_2 O_3$	12.50	502.92	99.99
Fonofos	$C_{10} H_{15} O P S_2$	11.80	246.32	83.24
Genistein	$C_{15} H_{10} O_5$	12.57	270.24	99.99
Isobenzan	$C_9 H_4 Cl_8 O$	12.07	411.75	99.99
Isocarbamid	$C_8 H_{15} N_3 O_2$	7.43	231.25	99.99
Isofenphos oxon	$C_{15} H_{24} N O_5 P$	15.99	329.33	86.24
Isomethiozin	$C_{12} H_{20} N_4 O S$	14.47	268.38	43.89
Isophorone	$C_9 H_{14} O$	10.66	138.21	83.08
Isopropalin	$C_{15} H_{23} N_3 O_4$	8.48	309.36	79.77
Janthitrem C	$C_{37} H_{47} N O_4$	12.75	569.8	99.99
Kadethrin	$C_{23} H_{24} O_4 S$	12.53	396.50	88.28
Kinoprene	$C_{18} H_{28} O_2$	10.99	276.41	99.99
MCPA-butoxyethyl	$C_{15} H_{21} Cl O_4$	7.54	300.78	71.83

Mefluidide	C_{11} H_{13} F_3 N_2 O_3 S	6.17	310.29	99.99
Methfuroxam	C_{14} H_{15} N O_2	12.95	229.28	96.15
Methylcholanthrene, 3-	C_{21} H_{16}	16.08	268.35	68.89
Mirex	C_{10} Cl_{12}	12.17	545.55	98.02
Molinate	C_9 H_{17} N O S	10.69	187.30	100
Moskene	C_{14} H_{18} N_2 O_4	7.10	278.30	99.99
N-(2,4-dimethylphenyl)formamide	C_9 H_{11} N O	12.16	149.19	92.30
N,N-Diethyl-meta-toluamide (DEET)	C_{12} H_{17} N O	14.07	191.27	93.66
Nitrosodiphenylamine, N-	C_{12} H_{10} N_2 O	10.99	198.22	67.61
N-Nitrosomorpholine (NMOR)	C_4 H_8 N_2 O_2	6.48	116.12	100
p-Cresol	C_7 H_8 O	11.04	108.14	94.87
Pentachloroaniline	C_6 H_2 Cl_5 N	12.62	265.35	99.99
Perfluorobutanoic acid (PFBA)	C_4 H F_7 O_2	6.48	214.04	99.99
Perfluorodecanoic acid (PFDA)	C_{10} H F_{19} O_2	12.55	514.09	100

References

Afzal MZ, Sun X-F, Liu J, et al (2018) Enhancement of ciprofloxacin sorption on chitosan/biochar hydrogel beads. Sci Total Environ 639:560–569. https://doi.org/10.1016/j.scitotenv.2018.05.129

Afzal MZ, Zu P, Zhang C-M, et al (2022) Sonocatalytic degradation of ciprofloxacin using hydrogel beads of TiO_2 incorporated biochar and chitosan. J Hazard Mater 434:128879. https://doi.org/10.1016/j.jhazmat.2022.128879

Chen H, Wang J (2019) Catalytic ozonation of sulfamethoxazole over Fe_3O_4/Co_3O_4 composites. Chemosphere 234:14–24. https://doi.org/10.1016/j.chemosphere.2019.06.014

Dehghani A, Baradaran S, Movahedirad S (2024) Synergistic degradation of Congo Red by hybrid advanced oxidation via ultraviolet light, persulfate, and hydrodynamic cavitation. Ecotoxicol Environ Saf 272:116042. https://doi.org/10.1016/j.ecoenv.2024.116042

Dietrich M, Franke M, Stelter M, Braeutigam P (2017) Degradation of endocrine disruptor bisphenol A by ultrasound-assisted electrochemical oxidation in water. Ultrason Sonochem 39:741–749. https://doi.org/10.1016/j.ultsonch.2017.05.038

Hadjltaief HB, Bairq ZAS, Shi C, Benzina M (2021) Evaluation of sono-assisted solar/Fenton process for indigo carmine degradation over magnetic $ZnO\text{-}Fe_3O_4$ supported Tunisian kaolinite clay. Surf Interfaces 26:101395. https://doi.org/10.1016/j.surfin.2021.101395

Jamali M, Akbari A (2021) Facile fabrication of magnetic chitosan hydrogel beads and modified by interfacial polymerization method and study of adsorption of cationic/anionic dyes from aqueous solution. J Environ Chem Eng 9:105175. https://doi.org/10.1016/j.jece.2021.105175

John S, Rathinavelu S, Mary SMS, et al (2023) Solar-driven hybrid photo-Fenton degradation of persistent antibiotic ciprofloxacin by zinc ferrite-titania heterostructures: degradation pathway, intermediates, and toxicity analysis. Environ Sci Pollut Res 30:39605–39617. https://doi.org/10.1007/s11356-022-24926-1

Karaer H, Kaya İ (2016) Synthesis, characterization of magnetic chitosan/active charcoal composite and using at the adsorption of methylene blue and reactive blue4. Microporous Mesoporous Mater 232:26–38. https://doi.org/10.1016/j.micromeso.2016.06.006

Le VT, Dao MU, Le HS, et al (2020) Adsorption of Ni(II) ions by magnetic activated carbon/chitosan beads prepared from spent coffee grounds, shrimp shells and green tea extract. Environ Technol 41:2817–2832. https://doi.org/10.1080/09593330.2019.1584250

Liu Y, Shan H, Pang Y, et al (2023) Iron modified chitosan/coconut shell activated carbon composite beads for Cr(VI) removal from aqueous solution. Int J Biol Macromol 224:156–169. https://doi.org/10.1016/j.ijbiomac.2022.10.112

Pu S, Ma H, Zinchenko A, Chu W (2017) Novel highly porous magnetic hydrogel beads composed of chitosan and sodium citrate: an effective adsorbent for the removal of heavy metals from aqueous solutions. Environ Sci Pollut Res 24:16520–16530. https://doi.org/10.1007/s11356-017-9213-0

Quesada HB, De Araújo TP, Cusioli LF, et al (2022) Caffeine removal by chitosan/activated carbon composite beads: Adsorption in tap water and synthetic hospital wastewater. Chem Eng Res Des 184:1–12. https://doi.org/10.1016/j.cherd.2022.05.044

Rahmi, Fathurrahmi, Lelifajri, et al (2019) Preparation of Magnetic Chitosan Beads for Heavy Metal Ions Removal from Water. IOP Conf Ser Earth Environ Sci 276:012004. https://doi.org/10.1088/1755-1315/276/1/012004

Roy K, Moholkar VS (2020) Sulfadiazine degradation using hybrid AOP of heterogeneous Fenton/persulfate system coupled with hydrodynamic cavitation. Chem Eng J 386:121294. https://doi.org/10.1016/j.cej.2019.03.170

Sancheti SV, Saini C, Ambati R, Gogate PR (2018) Synthesis of ultrasound assisted nanostuctured photocatalyst (NiO supported over CeO_2) and its application for photocatalytic as well as sonocatalytic dye degradation. Catal Today 300:50–57. https://doi.org/10.1016/j.cattod.2017.02.047

Wanchai K, Pichon R (2020) Synthesis of Fe_3O_4@chitosan beads for degradation of sulfanilamide using photo-fenton process. Pattaya, Thailand, p 130002

Wang Y, Yang W, Yin X, Liu Y (2016) The role of Mn-doping for catalytic ozonation of phenol using Mn/γ-Al_2O_3 nanocatalyst: Performance and mechanism. J Environ Chem Eng 4:3415–3425. https://doi.org/10.1016/j.jece.2016.07.016

Zanias A, Frontistis Z, Vakros J, et al (2020) Degradation of methylparaben by sonocatalysis using a Co–Fe magnetic carbon xerogel. Ultrason Sonochem 64:105045. https://doi.org/10.1016/j.ultsonch.2020.105045

CHAPTER 5

Intensification of treatment of industrial wastewater using hydrodynamic-based hybrid ternary advanced oxidation processes

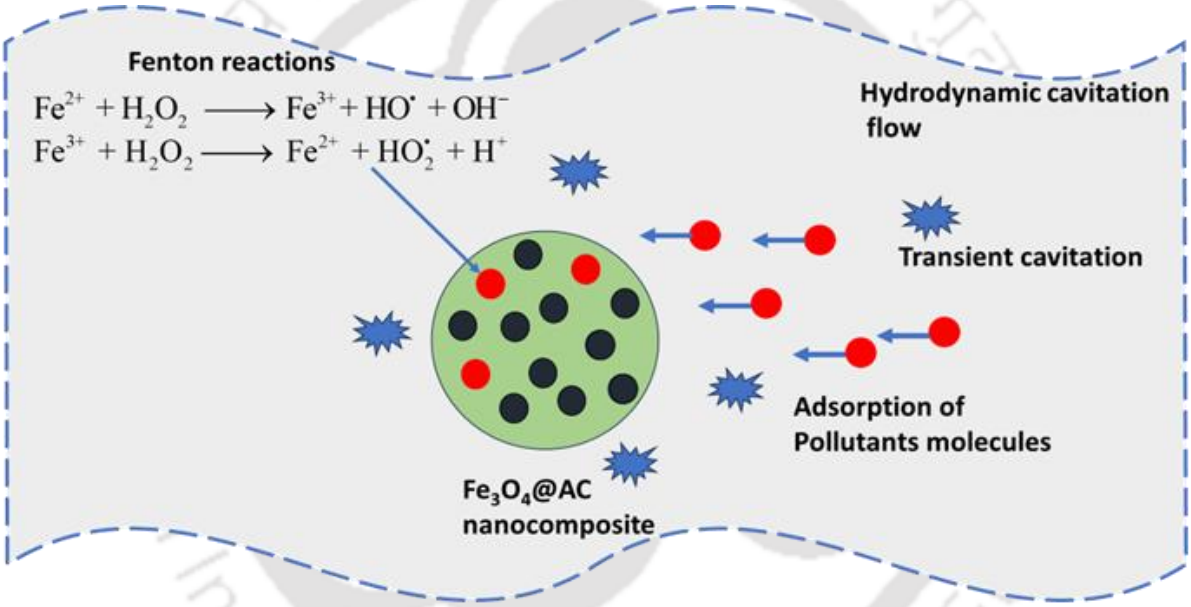

Online: Verma, K., Moholkar, V. S. Intensification of industrial wastewater treatment using hydrodynamic cavitation-based hybrid ternary advanced oxidation processes. *Chemical Engineering Research and Design*. https://doi.org/10.1016/j.cherd.2025.05.054.

CHAPTER 5

INTENSIFICATION OF TREATMENT OF INDUSTRIAL WASTEWATER USING HYDRODYNAMIC-BASED HYBRID TERNARY ADVANCED OXIDATION PROCESSES

5.1 Introduction

Wastewater discharges from chemical and process industries contain numerous recalcitrant pollutants that are not easily degraded using conventional aerobic treatments (Darandale et al. 2023; Patil et al. 2023). To meet increasingly stringent wastewater discharge standards, there is a pressing need for innovative techniques tailored to effectively reduce parameters such as Chemical Oxygen Demand (COD) and Total Organic Carbon (TOC) in wastewater. Among the modern technologies of wastewater treatment, advanced oxidation processes (AOPs), which use oxidizing radicals for degradation and mineralization of the pollutants, have proven effective for the textiles, dyes, pesticides, herbicides, organic intermediates, and pharmaceutical industries. Among oxidizing radicals, the hydroxyl radicals have the largest oxidative potential, ranging from 1.95 to 2.81 eV, depending on the pH, which makes them highly effective for wastewater treatment. Cavitation is a relatively new AOP that relies on the production of hydroxyl radicals as the primary oxidizing agents and has recently gained attention as a promising technology in wastewater treatment. Cavitation can be produced either using ultrasound (acoustic cavitation) or a throttling flow (hydrodynamic cavitation). Acoustic cavitation has limitations for large-scale applications due to operational issues of producing

high-power sonication for treating large volumes of wastewater. On the other hand, hydrodynamic cavitation is a relatively much simpler technology and can effectively handle large volumes of wastewater (Wang et al. 2022; Lakshmi et al. 2022; Korpe et al. 2023; Patil et al. 2023; Kanthale et al. 2023; Kakama et al. 2024). Wastewater treatment using hydrodynamic cavitation (HC) alone may require large processing times or fail to achieve targeted pollutant removal, particularly in complex effluents with high salt or inorganic content (Burzio et al. 2020; Darandale et al. 2023). Combining HC with other advanced oxidation processes (AOPs) offers an attractive solution for enhanced treatment, due to the synergistic interactions among HC and other AOPs. This approach can effectively degrade both organic and inorganic pollutants in the effluent, achieving higher treatment efficiency in a shorter period as compared to HC alone. Few previous authors have reported enhanced wastewater treatment using hydrodynamic cavitation-based hybrid AOPs. Kore et al. (2023) studied the treatment of textile dye wastewater utilizing the hybrid approach (HC + UV + H_2O_2). This study obtained an 87.7% COD reduction with a 1.92 synergistic index. Deng et al. (2024) reported that 33.2% COD removal was obtained using the HC + Fenton oxidative hybrid system for the treatment of coking wastewater. Gawande et al. (2024) have reported that the HC + Fenton process was a promising AOP for dairy wastewater treatment. The authors reported 92.60% degradation by HC + Fenton-based AOP.

In an earlier work, Verma and Moholkar (2023), we used a ternary hybrid system (Ultrasound + Fenton + Adsorption) for mineralization of industrial wastewater. In this study, we have attempted to use the same ternary hybrid system, replacing ultrasound with hydrodynamic cavitation. This ternary AOP combines the two phenomena of adsorption and radical-induced oxidative degradation. Few previous authors have reported combinations of adsorption and hydrodynamic cavitation for wastewater treatment. Medina-Collana et al. (2023) reported the process of adsorption combined with hydrodynamic cavitation for the removal of Pb, Cu, and

Sb. Bethi et al. (2018) have shown that the combined process of HC and adsorption intensified the adsorption of rhodamine-B dye onto the hydrogel. In a similar study, Raj et al. (2018) found that the hybrid system intensifies the removal of dye compared to its individual operation. In these studies, however, the process of adsorption (using a column) followed the treatment using hydrodynamic cavitation. This work, however, aims to explore the enhancement in degradation and mineralization of industrial wastewater with the simultaneous application of hydrodynamic cavitation, adsorption and Fenton reactions with the addition of Fe3O4@AC nanocomposite. Here, the nanocomposite serves both as an adsorbent and a catalyst for in-situ Fenton reactions. The strong convection and turbulence produced by the cavitating flow intensified the mass transfer across the Fe3O4@AC nanocomposite (adsorption of pollutants and desorption of the products). This study's key innovation and novelty is the treatment of high-COD effluent in a bench-scale 10 L capacity HC reactor using a ternary hybrid advanced oxidation process of HC + Fenton process + Adsorption. To the best of our knowledge, industrial wastewater treatment using this combination has not been previously reported in the literature. This study has four specific objectives or components: (1) statistical optimization of the process parameters (inlet pressure, nanocomposite dosage, pH, and H_2O_2 loading) of the ternary hybrid advanced oxidation process for maximum removal of COD and TOC from the wastewater; (2) kinetic analysis of the COD reduction profiles of wastewater using different binary and ternary AOPs, (3) LC-MS analysis of the wastewater to identify the specific pollutants that undergo maximum degradation during treatment, and (4) determination of the energy consumption and cavitational yield for different binary and ternary hybrid AOPs for assessment of their efficiencies.

5.2. Materials and methods

5.2.1 Reagents

$FeCl_3 \cdot 6H_2O$, $FeSO_4 \cdot 7H_2O$, H_2O_2, activated charcoal powder, $KMnO_4$, and hydrochloric acid were purchased from Himedia Ltd (India). Hydrazine hydrate and sodium carbonate anhydrous were obtained from Sigma-Aldrich. The chemicals were utilized in their analytical purity without any preprocessing. The wastewater (WW) originated from the collective effluents discharged by nearby industries and academic institutions, including ours, into a local water body. After filtration, the WW was stored in sealed bottles in a dark refrigerator at 4°C. Before analysis, the WW samples were diluted with deionized water to achieve the desired initial COD values.

5.2.2 Synthesis of Fe_3O_4@AC nanocomposite

Fe_3O_4@AC nanocomposite was synthesized via the co-precipitation method, as previously described (Verma and Moholkar 2023). Please refer to the Appendix A5 methods for detailed synthesis and analysis procedures (see Appendix A5, section A5.1).

5.2.3 Experimental

5.2.3.1 Setup of the hydrodynamic cavitation system

The pilot-scale HC setup was constructed in the laboratory. A schematic diagram of the HC system is presented in Figure 5.1(a). The actual photograph of the hydrodynamic cavitation reactor is given in Appendix A5 (Fig. A5.1). The setup consisted of a stainless steel structure mounted on a square iron frame. The wastewater sample tank had a maximum capacity of 30 liters. The HC reactor was structured as a closed loop circuit, incorporating a feed tank, a main line, a bypass line, and a reciprocating pump with a power rating of 1.1 kW. Three control

valves (V1, V2, V3) were strategically placed within the reactor: V1 controlled the bypass line connecting the pump outlet to the tank inlet, V2 regulated the flow rate of the process liquid in the main line, and V3 facilitated sample collection at the reactor drain. The pump motor was managed by a Variable Frequency Drive (VFD) that adjusted the motor speed by varying the frequency and voltage of the supplied power. The motor speed dictated the pump's piston strokes per unit time, thereby regulating the flow rate. The bypass line, serving as a pump discharge short circuit into the tank, offered a contingency to control the flow rate through the main line in case of VFD malfunction. Pressure gauges were installed to measure the inlet pressure (P1) in the main line and the fully recovered downstream pressure (P2), which equaled 1 atm. The main line featured a cavitation device in the form of an orifice plate for generating transient cavitation bubbles. A water-cooling jacket surrounded the feed tank to maintain the flow temperature. The design of the orifice plate, aimed at cavitation generation, was informed by previous computational and experimental studies (Roy and Moholkar 2020). Fabricated from stainless steel SS-316, the orifice plate had a diameter of 98 mm, a thickness of 2 mm, and included two 4 mm diameter holes. Figure 5.1(b) depicts the schematic of the orifice plate. The setup was cleaned by circulating water for 5 min before each experiment. During the cleaning process, the orifice was removed and thoroughly cleaned with detergent. All water was drained from the system beforehand to avoid sample contamination and dilution.

5.2.3.2 Experimental procedure

During initial trials with untreated WW in a hydrodynamic cavitation system, the orifice became blocked due to suspended solids. Hence, to ensure uninterrupted flow and enable cavitation phenomena, experiments were conducted using effluent followed by sedimentation. In this investigation, all experiments involved treating a consistent volume of industrial wastewater set at 10 L. The temperature of the solution (30 ± 2 ˚C) remained stable through the use of circulating cooling water in a jacket. Each experiment had a fixed treatment duration of

60 min, during which samples were regularly collected for analysis. The solution pH was adjusted using 1 M HCl or 1 M NaOH. A known amount of H_2O_2 and Fe_3O_4@AC nanocomposites were added, and the solution underwent pump circulation. Samples of 5 mL were taken at 10-min intervals and centrifuged at 5000 rpm for 10 min. The supernatant was then analyzed to determine the percentage of COD removal.

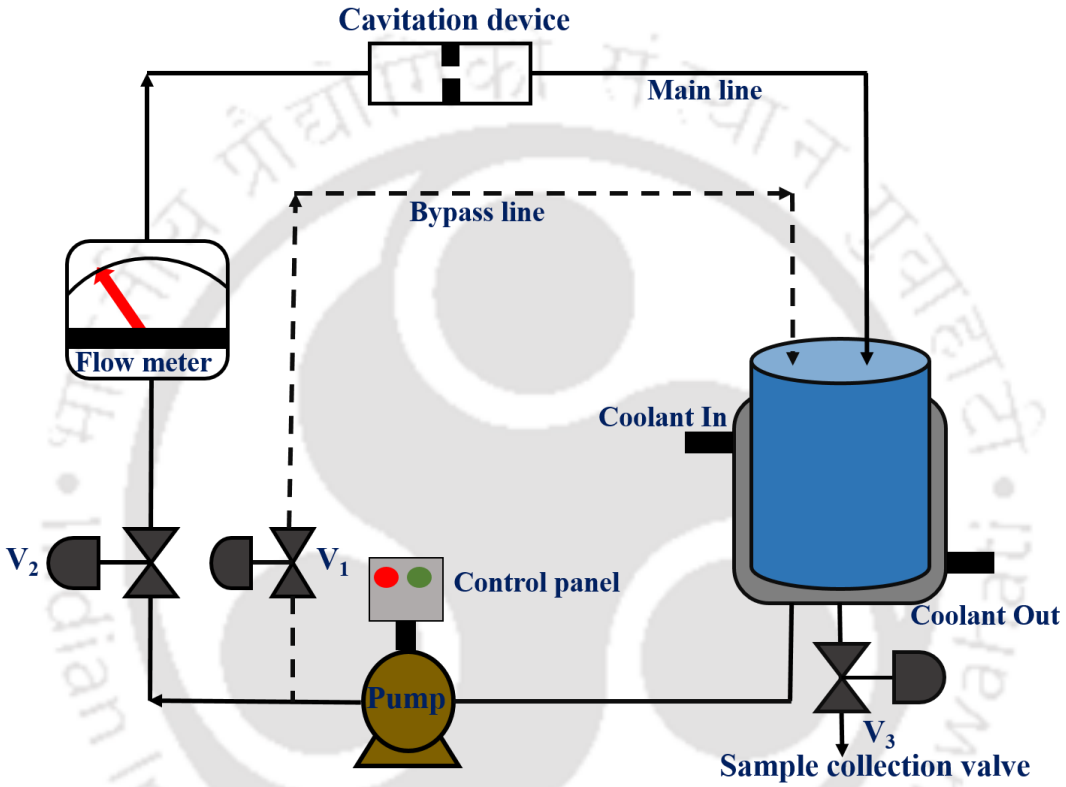

(a)

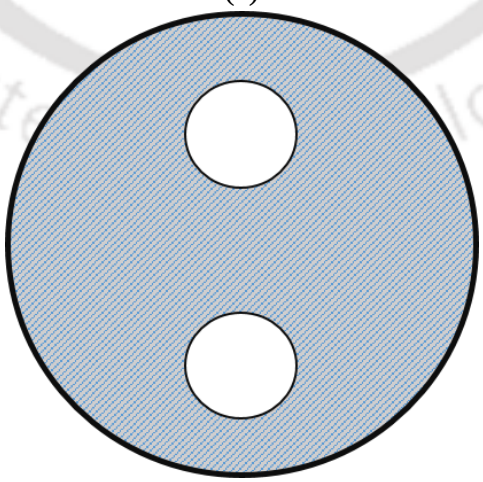

(b)

Figure 5.1. Schematic representation of (a) orifice-embedded HC setup, (b) orifice cavitating device with two holes (diameter of each hole: 4 mm, flow area: 25.12 mm^2 and perimeter of holes: 25.12 mm)

After the treatment process, the Fe_3O_4@AC nanocomposites were separated magnetically and thoroughly washed with deionized water to remove any adsorbed pollutants that hadn't degraded. The wash water was combined with the wastewater, and the resulting solution was analyzed for COD and TOC levels. Due to the complexity of pollutants in actual wastewater, all results are reported as the percentage reduction in COD of the samples at regular intervals. All experiments were performed in triplicate to ensure the reproducibility of the results. The percentage of COD removal was analyzed by following method 5220 D. It was determined using the closed reflux acidic digestion method, with potassium dichromate as the oxidizing agent, at 150 °C for two hours (Merck, ECO25 Thermoreactor VELP SCIENTIFICA). The total organic carbon (TOC) in the treated wastewater was measured using a TOC analyzer (Shimadzu, Model: TOC-LCPN+SSM). For further analysis, the wastewater was examined using LC-MS/MS at the advanced analytical instrumentation facility at NIPER Guwahati. LC-ESI-MS/MS analysis was carried out with a ZORBAX Eclipse C18 column (4.6×100 mm, 3.5 µm) from Agilent Technologies (Santa Clara, US).

5.2.4 Experimental design

Response surface methodologies are widely applied to investigate the impact of key parameters on treatment outcomes. This study used the Stat-Ease Design Expert software version 11.1.2.0 to identify the significant factors. A 3-level Box-Behnken design was employed to devise the experimental matrix and statistically analyze the results. Based on the preliminary experiments, the parameters and their ranges for optimization were decided as: inlet pressure (*A*): 4-10 atm;

nanocomposite dosage (*B*): 0.1-0.8 g/L; pH (*C*): 2-7; and H_2O_2 loading (*D*): 0.21-0.64 M. Tables 5.1 and 5 2 represent the details of the statistical design of experiments.

Table 5.1. Optimization parameters and their levels for the design of experiments

Parameters	Unit	Level		
		Low (-1)	Middle (0)	High (+1)
Inlet pressure (*A*)	atm	4	7	10
Nanocomposite dosage (*B*)	g/L	0.1	0.45	0.8
pH (*C*)	-	2	4.5	7
H_2O_2 loading (*D*)	M	0.21	0.43	0.64

5.2.5 Analysis and processing of experimental data

In addition to the experiments in Box-Behnken statistical design, additional control experiments were also conducted using individual treatment techniques and their combinations as follows: (1) HC treatment alone, (2) HC with H_2O_2 addition, (3) HC + Fe_3O_4 nanoparticles, (4) HC + H_2O_2 + Fe_3O_4, and (5) HC + Fe_3O_4@AC. A kinetic analysis of the COD reduction profiles in these experiments was also done using a pseudo-first-order model described by Eq. (5.1), (Flores Alarcón et al. 2022; Askarniya et al. 2022; Azizollahi et al. 2023). Notations: k = the 1st order kinetic rate constant (min^{-1}), COD_o and COD_t = initial and final COD values of the wastewater, respectively.

$$\ln\left(\frac{COD_t}{COD_o}\right) = -kt \qquad (5.1)$$

Table 5.2. Design of experiments using Box – Behnken method and obtained results

Run	**A**: inlet pressure (atm)	**B**: nanocomposite dosage (g/L)	**C**: pH (-)	**D**: H_2O_2 loading (M)	%COD removal (Pred.)	% COD removal (Exp.)
1	7	0.8	2	0.43	67.42	68.87
2	4	0.45	4.5	0.64	71.23	70.87
3	4	0.45	2	0.43	53.89	52.87
4	7	0.1	4.5	0.64	71.48	72.87
5	4	0.1	4.5	0.43	52.79	55.87
6	7	0.1	7	0.43	70.45	71.87
7	4	0.45	7	0.43	70.98	69.87
8	7	0.45	4.5	0.43	99.12	97.87
9	7	0.45	2	0.31	70.45	71.87
10	7	0.45	4.5	0.43	99.56	97.87
11	4	0.45	4.5	0.21	60.23	61.87
12	10	0.45	7	0.43	81.31	80.87
13	7	0.8	7	0.43	89.01	90.87
14	10	0.1	4.5	0.43	69.25	68.87
15	7	0.45	7	0.21	80.11	79.87
16	7	0.1	2	0.43	63.23	60.87
17	7	0.45	4.5	0.43	99.45	97.87
18	7	0.8	4.5	0.21	80.45	82.87
19	10	0.45	4.5	0.64	81.25	80.87
20	7	0.1	4.5	0.21	64.28	66.87
21	10	0.8	4.5	0.43	80.78	81.87
22	10	0.45	2	0.43	69.25	68.87
23	7	0.45	4.5	0.43	99.12	97.87
24	7	0.45	2	0.64	68.01	67.87
25	7	0.8	4.5	0.64	87.14	87.87
26	7	0.45	7	0.64	89.14	90.87
27	7	0.45	4.5	0.64	99.02	97.87
28	4	0.8	4.5	0.64	68.78	67.87
29	10	0.45	4.5	0.21	75.69	76.87

Consequently, the energy consumption of HC-based AOPs was analyzed in terms of electrical energy per order (E_{EO}) and cavitational yield (Bolton et al. 2001; Lai et al. 2022). The E_{EO} is expressed as:

$$E_{EO} = \frac{P \times t \times 1000}{V \times 60 \times \log\left(\frac{COD_o}{COD_t}\right)} \quad (5.2)$$

Notation: P = the rated power (kW) of the pump in the HC setup, t = treatment time (h), V = volume of the treated wastewater (L). Assuming the reaction follows a 1st order kinetic model, the equation can be expressed as follows, where $k_{indi.p}$ represents the 1st-order kinetic rate constant of COD reduction for individual processes.

$$E_{EO} = \frac{38.4P}{V \cdot k_{indi.p}} \quad (5.3)$$

5.3 Results and Discussion

5.3.1 Flow characteristic of the cavitation device

The intensity of transient cavitation phenomena occurring in the flow in a hydrodynamic cavitation reactor can be determined using the cavitation number (C_v). This is a dimensionless parameter that links the inlet pressure to the fluid velocity at the throat of the cavitation device (Pinjari and Pandit 2010; Wang et al. 2021a). The cavitation number (C_v) was determined using Eq. (5.4):

$$C_v = \frac{P_2 - P_v}{(1/2)\rho v_o^2} \quad (5.4)$$

Notation: P_2 = fully recovered downstream pressure, P_v = vapor pressure of the liquid, and v_o = velocity at the throat of the orifice. Preliminary experiments were conducted to examine the effect of inlet pressure variation (2 to 10 atm) before the design of experiments. The inlet pressure of the cavitation device (an orifice plate in the present study) plays a crucial role in the performance of a hydrodynamic cavitation (HC) reactor, especially in the context of the degradation of organic pollutants in wastewater. A 4 mm throat diameter orifice plate was used as the cavitation device in the HC reactor. The fresh WW was treated using hydrodynamic cavitation for 60 min at an inlet pressure of 2 atm, and samples were collected every 10 min for %COD analysis. The same procedure was repeated using inlet pressures of 4, 6, 8, and 10 atm. Table 5.3 outlines the flow characteristics of the cavitation device. The general criterion for the inception of transient cavitation in hydrodynamic flow in a cavitation reactor is $C_v \leq 1$. As noted earlier, the intensity of the cavitation phenomenon in the hydrodynamic flow increases as C_v falls below 1. This is attributed to the formation of an increasing number of cavitation bubbles at the orifice that results in the generation of a larger number of radicals at their transient collapse with the recovery of pressure in the flow. Furthermore, higher flow velocity at lower C_v values results in more passes through the cavitation device, extending the exposure time of pollutants in the cavitation zone (Joshi and Gogate 2019; Patil et al. 2023). These factors contribute to a greater extent to pollutant degradation at lower C_v values. A similar trend in C_v values was observed in this study, as shown in Figure 5.2(a). However, increasing the pressure beyond a certain threshold led to a reduction in overall COD removal efficiency. Figure 5.2(b) illustrates the % COD removal at various inlet pressures in hydrodynamic cavitation. It was observed that the %COD removal increased with rising pressure, peaking at 8 atm, but decreased beyond that point. As pressure increased, the flow rate through the orifice also rose, leading to more passes through the cavitation zone, which in turn enhanced %COD removal.

Table 5.3. Hydrodynamic cavitation parameters

Inlet Pressure (atm)	Volumetric flow rate (L/s)	Velocity (m/s)	Cavitation number (C_v)	Number of passes
2	0.325	12.9	1.16	117
4	0.45	17.9	0.61	162
6	0.54	21.5	0.42	194
8	0.64	25.5	0.31	230
10	0.7	27.9	0.25	252

This effect can be attributed to the greater exposure time of the pollutants in the cavitation zone. However, at pressures exceeding 8 atm, the %COD removal decreased, likely due to the onset of choked cavitation. Under choked cavitation conditions, cavitation bubbles are generated in excessively large numbers, leading to their coalescence into larger bubbles (Bethi et al. 2018). These larger bubbles drift away in the liquid flow and do not undergo volume oscillations and transient collapse. This leads to a reduction in the generation of •OH radicals and subsequent degradation of the pollutants.

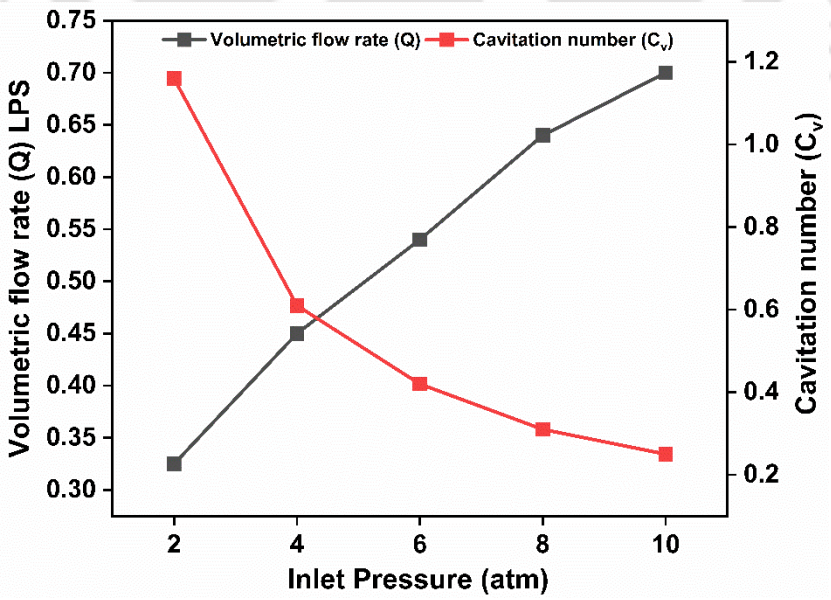

(a)

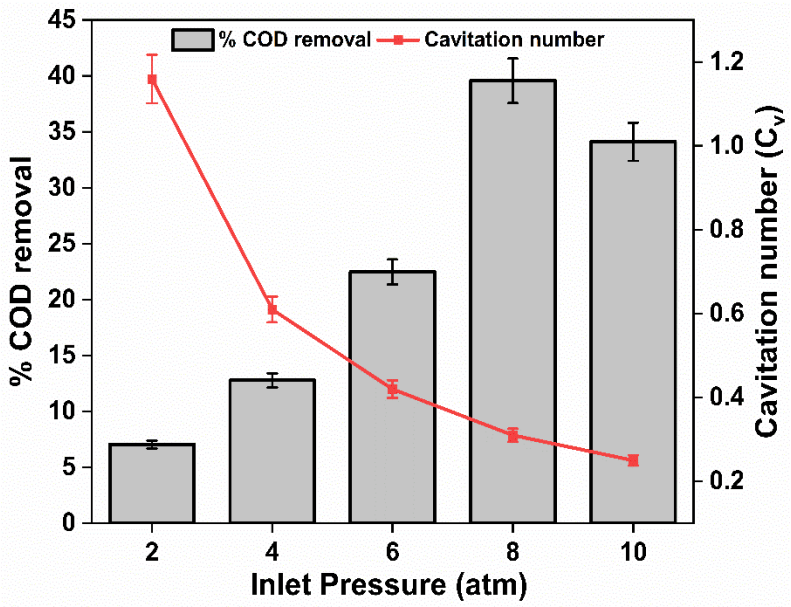

(b)

Figure 5.2. (a) Effect of Inlet pressure on flow rate and cavitation number, (b) Effect of inlet pressure on %COD removal.

5.3.2 Statistical analysis

The Box-Benken design (BBD) results in Table 5.2 indicate that the optimization parameters (pH, H_2O_2 loading, inlet pressure, and Fe_3O_4@AC nanocomposite dose) significantly influence COD removal. In the 29 individual experiments of the Box-Behnken design shown in Table 5.2, the COD removal varied from 52% to 97%. A 2^{nd}-order polynomial model (refer to Eq. 5.5) was fitted to the experimental data, which correlates the response variable (COD removal) to the optimization variables. Additionally, statistical analysis of variance (ANOVA) was conducted to evaluate the model's compatibility with the experimental data, with the results presented in Table A5.1 (provided in Appendix A5).

$$\%\ COD\ removal = 97.87 + 6.58A + 6.92B + 7.75C + 2.58D + 0.25A \cdot B - 1.25A \cdot C - 1.25A \cdot D + 2.75B \cdot C - 0.25B \cdot D + 3.75C \cdot D - 17.21\,A^2 - 12.21\,B^2 - 12.46\,C^2 - 7.96\,D^2 \quad (5.5)$$

The statistical design of experiments predicted the following set of parameters for maximum COD removal of 98.94%: inlet pressure = 8 atm, nanocomposite dosage = 0.55 g/L, pH = 4.5, and H_2O_2 loading = 0.43 M.

The ANOVA results show that the overall *F*-value of the model, which is the ratio of the source's mean square to the residual mean square, is 397.82. This high *F*-value confirms the statistical significance of the quadratic model, demonstrating its accuracy in predicting the observed data (Jafarikojour et al. 2017). Based on ANOVA, model terms (or optimization parameters) with *p*-values < 0.05 are regarded as significant, while *p*-values > 0.1 indicate that the corresponding parameter doesn't have a significant influence on the response variable. The overall *p*-value for the model is < 0.0001, which also indicates the significance of the model. The coefficient of determination (R^2) and the adjusted R^2, which reflect the model's accuracy in fitting the data, were 0.9975 and 0.9950, respectively. These values confirm the model's effectiveness in aligning with the experimental data and its strong predictive capabilities. The value of Lack-of-fit for the model was 1.23, indicating its insignificance. Additionally, the *F*-values for the optimization parameters were as follows: inlet pressure = 590.36, Fe_3O_4@AC nanocomposite dosage = 651.66, pH = 818.15, and H_2O_2 loading = 90.91. These values indicate that pH is the most influential parameter, followed by nanocomposite dosage and inlet pressure.

A plausible physical explanation for this concept is that the nature and state of pollutants, whether ionic or molecular, significantly impact their degradation under cavitating conditions. Pollutants are broken down by hydroxyl radicals produced during the degradation process (Chakinala et al. 2008). Therefore, understanding the molecular structure and the types of functional groups present in the pollutants is crucial. Acidic conditions enhance the production of hydroxyl radicals with higher oxidation potential. It has also been noted that the

rate of radical recombination is lower in acidic environments (Dhanke and Wagh 2020). As the pH increases, the degradation efficiency declines. This is due to the instability of H_2O_2 at alkaline pH, where it decomposes into oxygen and water (Wei et al. 2015). Additionally, the HO_2^- ions formed rapidly react with hydroxyl radicals, producing superoxide anions, which have a lower oxidizing potential than hydroxyl radicals (Azizollahi et al. 2023). Patil et al. (2014) demonstrated that imidacloprid breaks down more quickly in acidic conditions, with the highest degradation of 23.85% observed at a pH of 3.0. Similarly, Barik and Gogate (2018) studied the degradation of 2, 4, and 6-trichlorophenol across a pH range of 3 to 11 and found that at an optimal pH of 5, the maximum degradation achieved was 32.13%. %. As per the ANOVA results shown in the supplementary material, the interactions between two factors, viz. inlet pressure & nanocomposite loading, and nanocomposite loading & H_2O_2 loading, are insignificant. The probable reasons for the above-mentioned interactions being insignificant are as follows:

1. The nanocomposite loading varied in the 0.1 to 0.8 g/L range. This is too small a solid concentration in the liquid to significantly influence the flow characteristics. Therefore, the solid concentration has no effect on the inlet pressure. In terms of the chemistry of the system, the inlet pressure affects the intensity of the transient cavitation in the system, which in turn results in in-situ generation of H_2O_2, whereas the nanocomposites added to the system generate oxidizing radicals through Fenton reactions. The Fenton reactions are induced by both externally added and in-situ generated H_2O_2. Since the total H_2O_2 in the system is contributed mainly by the externally added H_2O_2, the Fenton reactions are independent of the inlet pressure.

2. The reason underlying the relative independence of nanocomposite loading and H_2O_2 loading could be that the latter is in large excess. The nanocomposite loading was relatively small – in the range of 0.1 to 0.9 g/L, whereas the H_2O_2 concentration varied in the range of 0.21 to 0.64 M. Thus, the COD reduction of wastewater – which was due to the

degradation by the oxidizing radicals generated by Fenton reactions was not influenced by the interactions between the parameters of H_2O_2 and nanocomposite loading.

5.3.3. Optimization and result validation

A validation experiment was conducted using RSM-BBD at the optimum conditions. The results indicated COD and TOC removal efficiencies of 99.37% and 88.80%, respectively, at the conditions: inlet pressure = 8 atm, nanocomposite dosage = 0.55 g/L, pH = 4.5, and H_2O_2 loading = 0.43 M. The experimental COD removal (99.37%) is very close to the model-predicted removal of 98.94%. The time profile of COD reduction in the validation experiment is shown in Fig. 5.3. Close agreement between the experimental and model-predicted response variable (COD removal) at the optimum conditions underscores the validity of the model. The interaction between the optimization variables is illustrated through RSM-BBD 3D plots in section A5.2 (provided in Appendix A5). The *p*-value of the interaction coefficient between inlet pressure and the nanocomposite dose is insignificant. Similarly, the interaction between nanocomposite dosage and H_2O_2 loading is also insignificant. Physically, these results can be interpreted as follows: (1) the relation between inlet pressure and nanocomposite dose is in terms of leaching of Fe^{2+}/Fe^{3+} ions from the surface of Fe_3O_4 particle present in the Fe_3O_4@AC nanocomposite. An insignificant *p*-value of the interaction for these parameters means that surface leaching of Fe_3O_4 particles in Fe_3O_4@AC composite does not change with inlet pressure. The interaction between nanocomposite dosage and H_2O_2 loading is in terms of the Fenton reactions induced between Fe-ions leached from Fe_3O_4 particles and H_2O_2 added to the wastewater solution. An insignificant *p*-value of this interaction indicates that H_2O_2 is present in large excess in the medium.

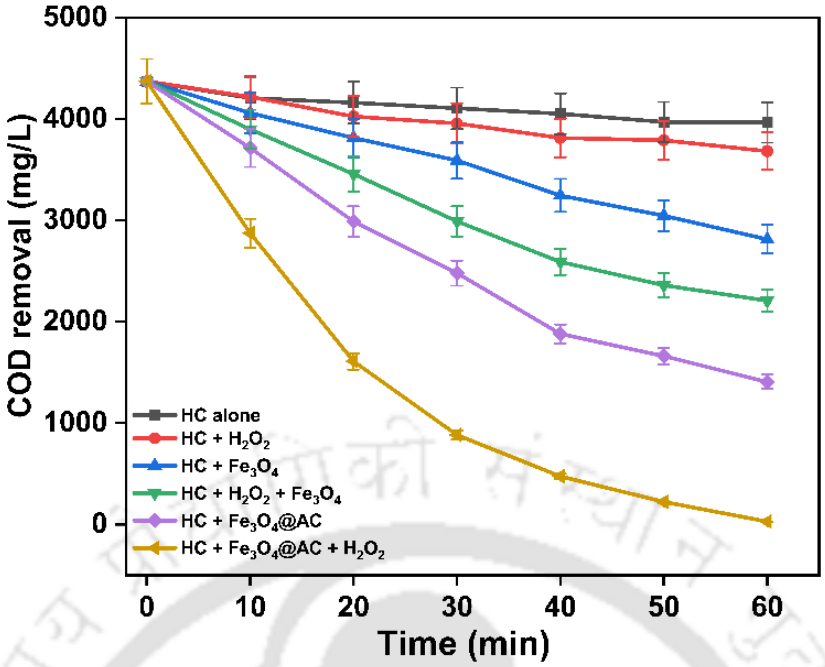

Figure5.3. COD removal at different processes (operating condition: pressure = 8 atm, pH = 4.5, H_2O_2 loading = 0.43 M, nanocomposite dosage = 0.55 g/L, and Fe_3O_4 dose = 0.044 g/L)

5.3.4 Kinetic study of COD reduction

As noted in section 5.2.5, in addition to the experiments with ternary hybrid AOP of HC + Fe_3O_4@AC + H_2O_2, several control experiments were also conducted using individual treatment techniques and their combinations. The time profiles of COD reduction of the wastewater in these experiments are shown in Fig. 5.3. All time profiles of COD reduction (including the profile of the validation experiment mentioned in the previous section) were fitted with a pseudo-1st-order kinetic model. The kinetic rate constants for all treatments are listed in Table 5.4, along with the total COD removal achieved in each treatment of 60 min. As shown in Figure 5.4, wastewater treatment with only hydrodynamic cavitation (without the addition of any other chemical to the wastewater) exhibited the lowest efficiency, achieving a %COD removal of 9.34% and a first-order rate constant of 1.6×10^{-3} min^{-1}. In the binary systems, the COD removal increased with the addition of external components, viz. H_2O_2,

Fe_3O_4 native particles, and Fe_3O_4@AC nanocomposite. Among other binary processes, HC+H_2O_2, HC+Fe_3O_4, and HC+Fe_3O_4@AC achieved degradation rates of 15.78% (k = 2.8 × 10^{-3} min^{-1}), 35.67% (k = 7.4 × 10^{-3} min^{-1}) and 67.85% (k = 19.6 × 10^{-3} min^{-1}), respectively. The two ternary systems, viz. HC+H_2O_2+Fe_3O_4 and HC+H_2O_2+Fe_3O_4@AC achieved COD reductions of 49.54 and 99.37% each. Before comparing the extent of COD reductions in different systems, we must note the mechanism of oxidizing radical production and pollutant degradation in these systems.

In the system of hydrodynamic cavitation alone, the radicals are produced through transient cavitation (transient collapse of the bubbles) in the flow. Some of these radicals ($^{\cdot}OH$) can recombine to generate H_2O_2 in the system. With the external addition of H_2O_2 to the system, the extent of radical production increases due to the evaporation and dissociation of H_2O_2 in the cavitation bubble. In the system of HC+Fe_3O_4 and HC+Fe_3O_4@AC, the radicals are generated through two sources, viz., the transient cavitation and the Fenton reactions occurring between the in-situ generated H_2O_2 and Fe-ions leached from the Fe_3O_4 particles. Finally, in the ternary system, the generation of OH and other radicals occurs through two sources: transient cavitation (with H_2O_2 dissociation) and Fenton reactions between Fe-ions leached from the Fe_3O_4 particles and the H_2O_2, both externally added and in-situ generated. Nonetheless, we see a large difference in the COD reduction achieved in the two binary systems, viz. HC+Fe_3O_4 and HC+Fe_3O_4@AC. Similarly, the COD reduction achieved in the ternary system of HC+H_2O_2+Fe_3O_4@AC is almost double that of the system of HC+H_2O_2+Fe_3O_4. An explanation for these results can be given on the basis of the adsorption of the organic pollutants in wastewater on the surface of the Fe_3O_4@AC nanocomposite. Before discussing this point in greater detail, we present the adsorption characteristics of the Fe_3O_4@AC nanocomposite in the next section.

Table 5.4. Degradation performances of HC-based hybrid advanced oxidation processes

Process type	% COD removal	Kinetic rate constant ($k \times 10^{-3}$ min^{-1})	R^2
HC alone	9.34	1.6	0.95
HC + H_2O_2	15.78	2.8	0.97
HC + Fe_3O_4	35.67	7.4	0.99
HC + H_2O_2 + Fe_3O_4	49.54	11.9	0.99
HC + Fe_3O_4@AC	67.85	19.6	0.99
HC + H_2O_2 + Fe_3O_4@AC	99.37	47.2	0.99

5.3.5 Adsorption behavior of nanocomposite

Adsorption, a surface phenomenon, is often analyzed using various adsorption isotherm models to understand its behavior. This study employed widely used adsorption isotherm, such as the Langmuir model, to describe the equilibrium removal of organic pollutants. The Langmuir isotherm operates on the premise that adsorption occurs as a monolayer, where the adsorbent surface is uniformly covered by the adsorbate molecules at maximum adsorption capacity. The Langmuir isotherm assumes that adsorption occurs in a uniform layer without any interactions between the adsorbed molecules. The mathematical expression for the Langmuir isotherm is as follows:

$$\frac{C_e}{q_e} = \frac{1}{q_{max} b} + \frac{C_e}{q_{max}} \qquad (5.6)$$

Where q_{max} (mg/g) represents the maximum adsorption capacity of the Fe_3O_4@AC nanocomposite during the treatment process. Figure 5.5(a-b) depicted that the experimental

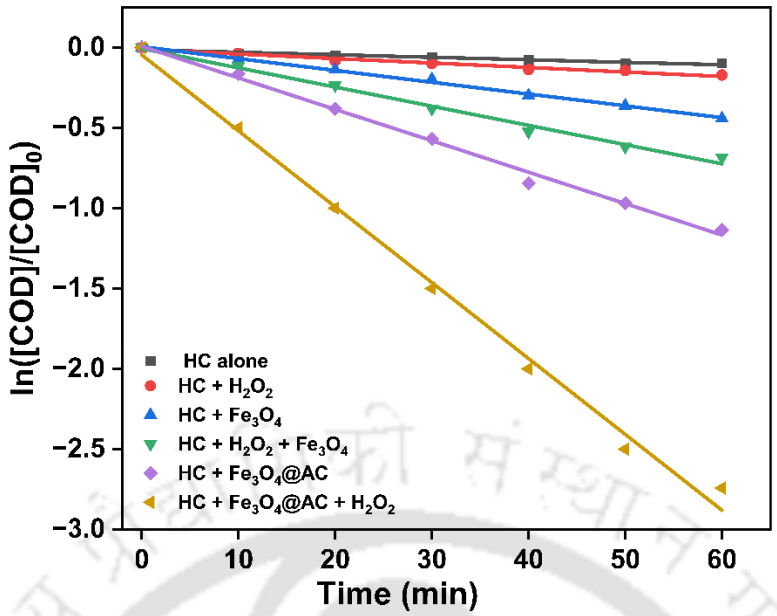

(a)

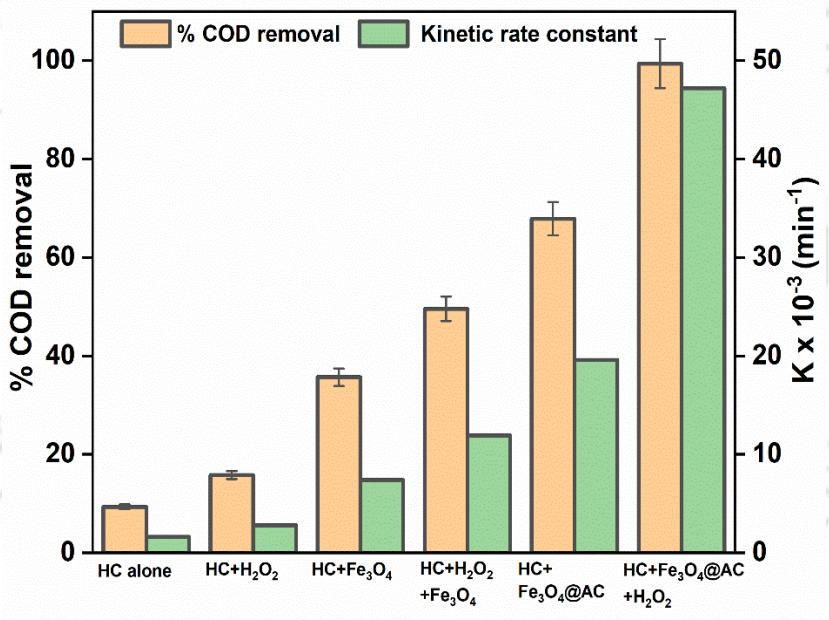

(b)

Figure 5.4. (a) Pseudo-first-kinetic plot, (b) %COD removal and kinetic rate constant at each process (operating condition: pressure = 8 atm, pH = 4.5, H_2O_2 loading = 0.43 M, nanocomposite dosage = 0.55 g/L, and Fe_3O_4 dose = 0.044 g/L)

data fit the Langmuir adsorption isotherm model well (R^2 = 0.9997). From the graph, the value of Langmuir constant *b* is found to be 2 (L/mg), and the maximum adsorption capacity q_m is

270.27 mg/g. The separation factor R_L for the Fe_3O_4@AC nanocomposite is found to be 0.0015, which indicates that the nature of the adsorption process is favorable. This essentially means that a significant fraction of the organic pollutants present in the wastewater gets adsorbed onto the surface of the charcoal, leading to their local concentration in the solution.

Synergistic interactions in the hybrid processes: As noted in the previous section, the COD reduction achieved in the binary and ternary hybrid processes using Fe_3O_4@AC nanocomposite is much higher than the native Fe_3O_4 particles. This is attributed to the synergistic interactions among the surface adsorption of pollutants and radical generation through Fenton reactions. These radicals are extremely and do not diffuse into the medium from the point of generation. Therefore, the utility of these radicals towards the degradation of the pollutant depends on the probability of interaction between the pollutant molecules and the radicals. In the case of Fe_3O_4@AC nanocomposite, the radicals generated on the surface of the composite can easily interact with the adsorbed pollutant molecules, leading to their decomposition. On the other hand, the extent of pollutant adsorption on the native Fe_3O_4 particles is low (due to small surface area and also agglomeration), and thus, the radicals generated through the Fenton reactions are not effectively utilized, leading to relatively smaller degradation.

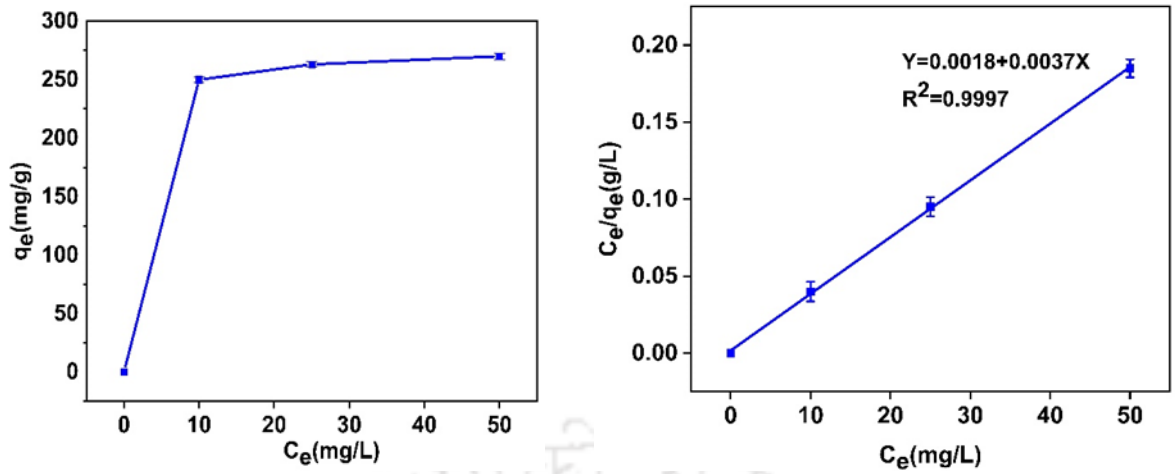

(a) (b)

Figure 5.5. (a) Plot of q_e vs. C_e and (b) Langmuir adsorption isotherm plot

5.3.6 Comparative analysis of cavitational yield and energy consumption

The efficiency of cavitation-based oxidation processes can be assessed by cavitational yield (mg/J), which is the ratio of the COD removal in 1 h of treatment to the energy dissipated per unit volume.

Sample calculation of cavitational yield and E_{EO}:

Optimum inlet pressure = 8 atm (810600 N/m^2)

Downstream pressure = 1 atm (101325 N/m^2)

Volumetric flow rate = 6.4×10^{-4} m^3/s

Volume of wastewater = 10 L

Power dissipation = optimum inlet pressure × volumetric flow rate

= ($810600 \times 6.4 \times 10^{-4}$) = 518.78 W

The power dissipated per unit volume = (518.78/10) = 51.88 W/L

Energy dissipated per unit volume = power dissipated × time = (51.88×3600) = 1.87×10^5 J/L

Cavitational yield = (COD removal/Energy dissipated)

COD removal (HC alone) = 408.34 mg/L

Cavitational yield = (408.34 mg/L/1.87 × 10^5 J/L) = 2.19 × 10^{-3} mg/J

Electrical energy E_{EO} (HC alone) = (38.4 × P)/(V × $k_{indi,p}$)

= (38.4 × 1.1)/ (10 × 1.6 × 10^{-3}) = 2640 kWh m^{-3} $order^{-1}$

The primary energy input for generating cavitation in an HC reactor comes from the pump's energy consumption, with power dissipation recorded at 1.87 × 10^5 J/L. Among various HC combined advanced oxidation processes, the ternary hybrid AOP (HC + H_2O_2 + Fe_3O_4@AC) achieved the highest cavitational yield of 2.33 × 10^{-2} mg/J and the highest %COD removal of 99.37%, as listed in Table 5.5.

Table 5.5. Comparison of energy consumption for HC-based advanced oxidation processes

Process	**E_{EO} (kWh m^{-3} $order^{-1}$)**	**Cavitational yield in 60 min treatment (mg/J)**
HC alone	2640	2.19 x 10^{-3}
HC + H_2O_2	1508.57	3.69 x 10^{-3}
HC + Fe_3O_4	570.81	8.35 x 10^{-3}
HC + H_2O_2 + Fe_3O_4	354.95	1.16 x 10^{-2}
HC + Fe_3O_4@AC	215.51	1.59 x 10^{-2}
HC + H_2O_2 + Fe_3O_4@AC	89.49	2.33 x 10^{-2}

This outcome is primarily due to the synergistic interactions between pollutant adsorption on activated charcoal and surface Fenton reactions, as noted in the previous section. Moreover, the intense turbulence and shear generated in the orifice flow in the hydrodynamic cavitation reactor facilitated faster mass transport of pollutants between the Fe_3O_4@AC nanocomposite and the solution, enhancing adsorption and desorption processes. This enhanced mass transfer further boosted the interactions and reactions between radicals and pollutants, resulting in

efficient wastewater mineralization. Furthermore, energy efficiency was evaluated through the electrical energy per order (E_{EO}) values, where HC alone had the highest E_{EO} = 2640 kWh m^{-3} $order^{-1}$ with only 9.34% COD removal, while HC + Fe_3O_4@AC had the lowest E_{EO} = 215.51 kWh m^{-3} $order^{-1}$ among binary advanced oxidation processes (AOPs). The ternary hybrid AOP had the lowest overall E_{EO} = 89.49 kWh m^{-3} $order^{-1}$, indicating almost complete COD removal and has the least cost of treatment. This makes the ternary hybrid AOP (HC + H_2O_2 + Fe_3O_4@AC) the most potential process for scale-up and commercialization.

5.3.7 LC-MS/MS analysis of wastewater

LC-MS analysis of the original WW and treated WW allowed the identification of organic compounds and their intermediates by matching their MS spectra with standard data. Table A5.2 (provided in Appendix A5) presents the compounds and their corresponding percentage degradation found in WW both before and after treatment. The table depicted that more than 15 contaminants were found to be 100% degraded, which are DEF, Desmetryn, Diethatyl-ethyl, Dimethipin, Di-n-propyl phthalate, Fenamiphos, Hydroxycotinine, Iprobenfos, Isomethiozin, Lenacil, Metsulfuron-methyl. Figures 5.6(a) and (b) illustrate chromatograms at various retention times for both original and treated WW. The spectrum showed a reduction of the major peaks present in the original WW by approximately 60%−80% using the ternary hybrid AOPs HC + H_2O_2 + Fe_3O_4@AC combination. The decrease in peak intensities, along with the appearance of new peaks and the disappearance of others, indicated that the combined system effectively degraded larger carbon chain compounds into smaller molecular chain compounds.

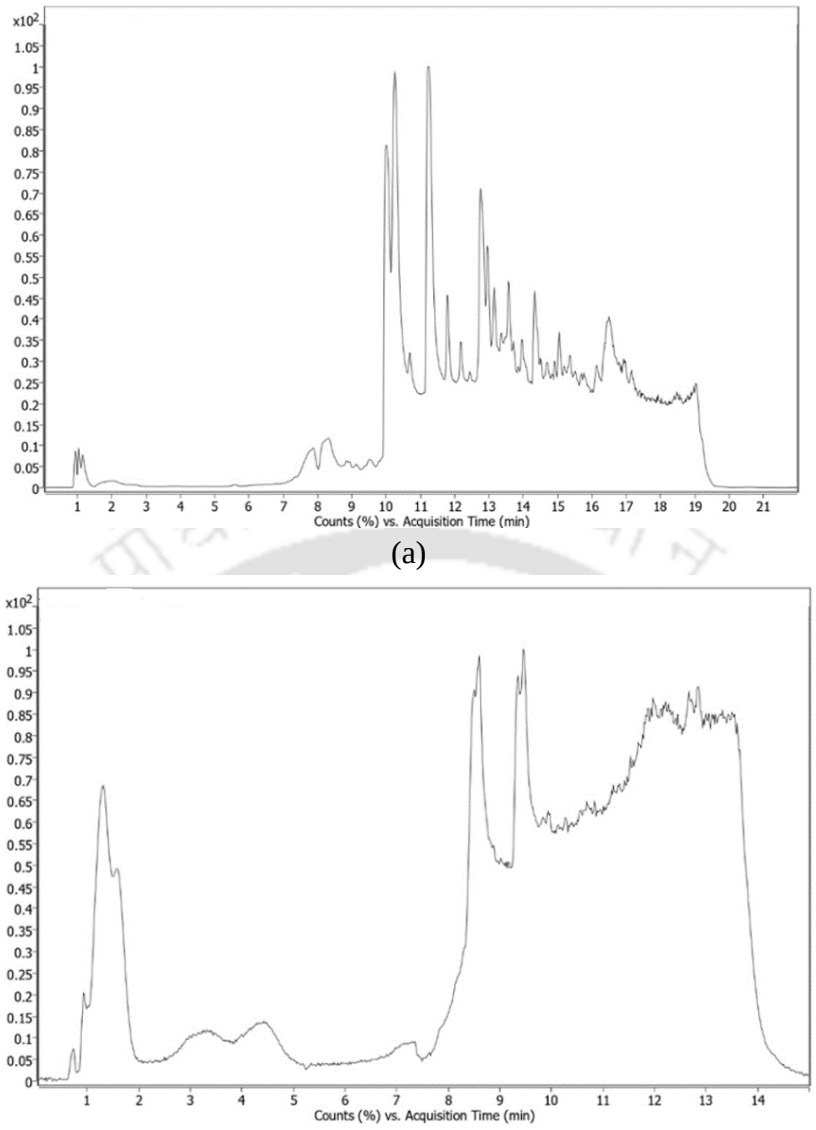

Figure 5.6. LC-MS chromatogram (a) original WW and (b) treated WW

5.3.8 Recovery and recycle stability of nanocomposite

The stability and reusability of Fe_3O_4@AC nanocomposites were evaluated in consecutive 6 experiments under optimal conditions. Due to their magnetic properties, the Fe_3O_4@AC nanocomposites were effectively separated from the reaction mixture using an external magnet. The particles were washed multiple times with water and then three times with ethanol, after which they were dried overnight in a vacuum oven at 80°C. This process was repeated for 6

cycles, yielding %COD removal efficiencies of 99.37%, 98.78%, 98%, 97.59%, 96.89, and 96%. The figure 5.7 illustrates the removal efficiency and catalyst recovery over 6 consecutive cycles.

The Fe_3O_4@AC nanocomposite demonstrated excellent recovery efficiency, with more than 96 wt% being recovered in successive treatment cycles. This indicates that the nanocomposite can be easily and effectively recycled, maintaining its catalytic performance. Even after six cycles of recovery and reuse, the Fe_3O_4@AC nanocomposite retained its catalytic effectiveness, showcasing its stability and reusability in wastewater treatment applications.

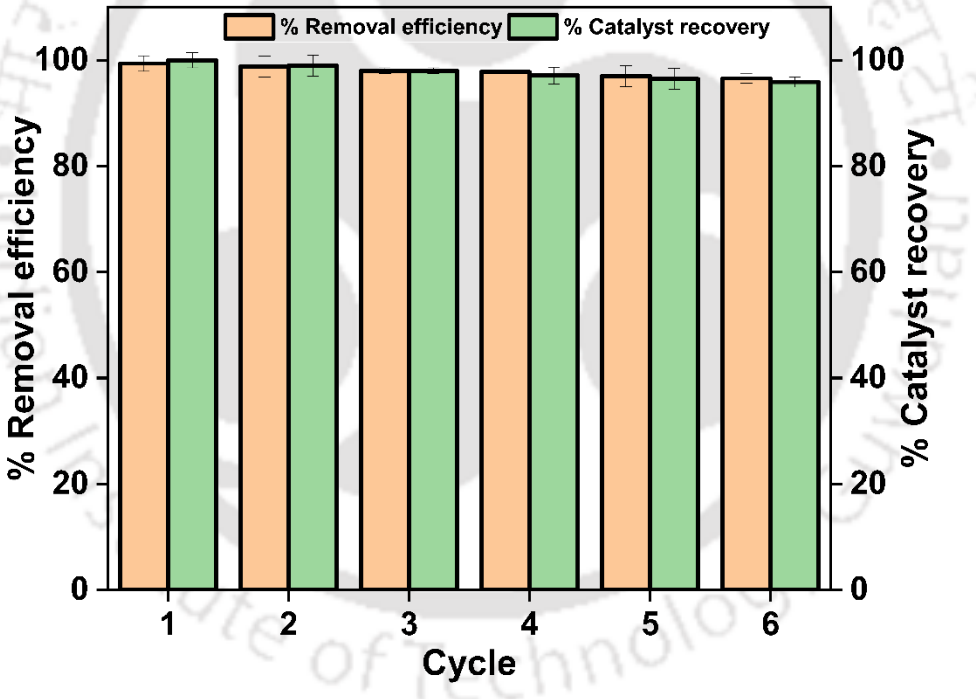

Figure 5.7. Reusability and recovery of Fe_3O_4@AC nanocomposite in the ternary process (hydrodynamic cavitation + Fenton + adsorption) under at optimized condition (inlet pressure = 8 atm, pH = 4.5, H_2O_2 loading = 0.43 M, nanocomposite dosage = 0.55 g/L)

5.4 Conclusion

In this study, a novel ternary hybrid advanced oxidation process (AOP), combining hydrodynamic cavitation (HC), adsorption, and the Fenton reaction, was employed to degrade and mineralize industrial wastewater. This method integrates the adsorption of organic pollutants onto a surface and the subsequent Fenton reaction at that surface. Various operating parameters such as inlet pressure, dosage of Fe_3O_4@AC nanocomposite, pH, and H_2O_2 loading were systematically examined for their impact on wastewater degradation and mineralization. Additionally, the combined processes' synergistic effects and reaction kinetics were evaluated. Key findings can be summarized as follows:

(1) The impact of inlet pressure, Fe_3O_4@AC nanocomposite dosage, pH, and H_2O_2 loading was explored using the Box-Behnken Design (BBD). A polynomial model was applied to the experimental data, and the model's adequacy was assessed using Analysis of Variance (ANOVA).

(2) Through parameter optimization, the highest degradation/mineralization was achieved at an inlet pressure of 8 atm, Fe_3O_4@AC dosage of 0.55 g/L, pH of 4.5, and H_2O_2 loading of 0.43 M. Under these optimized conditions, COD and TOC removal efficiencies reached 99.37% and 88.80%, respectively.

(3) Comparatively, under the same optimized conditions, the binary processes of HC + H_2O_2, HC + Fe_3O_4, and HC + Fe_3O_4@AC achieved removal efficiencies of 15.78%, 35.67%, and 67.85%, respectively.

(4) Energy consumption analysis revealed that the HC + Fe_3O_4@AC + H_2O_2 process was the most efficient, with the least E_{EO} value of 89.49 kWh m^3 $order^{-1}$.

(5) LC-MS analysis identified the primary compounds in the wastewater before and after treatment, further supporting the process's effectiveness. The HC + Fe_3O_4@AC + H_2O_2

combination demonstrated the highest levels of degradation and mineralization, with the best synergy coefficient and the lowest energy consumption.

In conclusion, this ternary hybrid advanced oxidation process shows great promise as an effective, sustainable technology for industrial wastewater treatment, offering high removal efficiency and low energy requirements. With continued research into ternary hybrid HC-based AOPs, this approach could potentially be scaled up for broader applications in wastewater treatment.

References

Askarniya Z, Baradaran S, Sonawane SH, Boczkaj G (2022) A comparative study on the decolorization of Tartrazine, Ponceau 4R, and Coomassie Brilliant Blue using persulfate and hydrogen peroxide based Advanced Oxidation Processes combined with Hydrodynamic Cavitation. Chem Eng Process - Process Intensif 181:109160. https://doi.org/10.1016/j.cep.2022.109160

Azizollahi N, Taheri E, Mehdi Amin M, et al (2023) Hydrodynamic cavitation coupled with zero-valent iron produces radical sulfate radicals by sulfite activation to degrade direct red 83. Ultrason Sonochem 95:106350. https://doi.org/10.1016/j.ultsonch.2023.106350

Barik AJ, Gogate PR (2018) Hybrid treatment strategies for 2,4,6-trichlorophenol degradation based on combination of hydrodynamic cavitation and AOPs. Ultrason Sonochem 40:383–394. https://doi.org/10.1016/j.ultsonch.2017.07.029

Bethi B, Manasa V, Srinija K, Sonawane SH (2018) Intensification of Rhodamine-B dye removal using hydrodynamic cavitation coupled with hydrogel adsorption. Chem Eng Process - Process Intensif 134:51–57. https://doi.org/10.1016/j.cep.2018.10.017

Bolton JR, Bircher KG, Tumas W, Tolman CA (2001) Figures-of-merit for the technical development and application of advanced oxidation technologies for both electric- and solar-driven systems (IUPAC Technical Report). Pure Appl Chem 73:627–637. https://doi.org/10.1351/pac200173040627

Burzio E, Bersani F, Caridi GCA, et al (2020) Water disinfection by orifice-induced hydrodynamic cavitation. Ultrason Sonochem 60:104740. https://doi.org/10.1016/j.ultsonch.2019.104740

Chakinala AG, Gogate PR, Burgess AE, Bremner DH (2008) Treatment of industrial wastewater effluents using hydrodynamic cavitation and the advanced Fenton process. Ultrason Sonochem 15:49–54. https://doi.org/10.1016/j.ultsonch.2007.01.003

Darandale GR, Jadhav MV, Warade AR, Hakke VS (2023) Hydrodynamic cavitation a novel approach in wastewater treatment: A review. Mater Today Proc 77:960–968. https://doi.org/10.1016/j.matpr.2022.12.075

Dehghani A, Baradaran S, Movahedirad S (2024) Synergistic degradation of Congo Red by hybrid advanced oxidation via ultraviolet light, persulfate, and hydrodynamic cavitation. Ecotoxicol Environ Saf 272:116042. https://doi.org/10.1016/j.ecoenv.2024.116042

Deng D, Huang T, Li Q, et al (2024) Treatment of Coking Wastewater Using Hydrodynamic Cavitation Coupled with Fenton Oxidation Process. Molecules 29:1057. https://doi.org/10.3390/molecules29051057

Dhanke P, Wagh S (2020) Intensification of the degradation of Acid RED-18 using hydrodynamic cavitation. Emerg Contam 6:20–32. https://doi.org/10.1016/j.emcon.2019.12.001

Flores Alarcón MAD, Arenas Jarro RY, Ahmed MA, et al (2022) Intensification of Red-G dye degradation used in the dyeing of alpaca wool by advanced oxidation processes assisted by hydrodynamic cavitation. Ultrason Sonochem 89:106144. https://doi.org/10.1016/j.ultsonch.2022.106144

Gawande G, Chougule S, Bangar S, et al (2024) Hydrodynamic cavitation and its hybridization with Fenton process as a promising AOP for dairy wastewater treatment. Mater Today Proc S2214785324000324. https://doi.org/10.1016/j.matpr.2024.01.032

Jafarikojour M, Dabir B, Sohrabi M, Royaee SJ (2017) Evaluation and optimization of a new design photocatalytic reactor using impinging jet stream on a TiO2 coated disc. Chem Eng Process Process Intensif 121:215–223. https://doi.org/10.1016/j.cep.2017.08.011

Joshi SM, Gogate PR (2019) Intensification of industrial wastewater treatment using hydrodynamic cavitation combined with advanced oxidation at operating capacity of 70 L. Ultrason Sonochem 52:375–381. https://doi.org/10.1016/j.ultsonch.2018.12.016

Kakama NK, Petrik LF, Ojumu TV (2024) The Optimization of Hydrodynamic Cavitation as an Advanced Oxidation Option for the Removal of Persistent Contaminants in Wastewater. Water Air Soil Pollut 235:193. https://doi.org/10.1007/s11270-024-06924-w

Kanthale P, Pandey R, Thakur D, et al (2023) Application of combined hydrodynamic cavitation and Fenton reagent for COD reduction of cellulosic fiber industry effluents. J Water Process Eng 56:104500. https://doi.org/10.1016/j.jwpe.2023.104500

Kore VS, Manjare SD, Patil AD, Dhanke PB (2023) A parametric study on intensified degradation of textile dye water using hydrodynamic cavitation based hybrid technique. Chem Eng Process - Process Intensif 193:109550. https://doi.org/10.1016/j.cep.2023.109550

Korpe S, Rao PV, Sonawane SH (2023) Performance evaluation of hydrodynamic cavitation in combination with AOPs for degradation of tannery wastewater. J Environ Chem Eng 11:109731. https://doi.org/10.1016/j.jece.2023.109731

Lai F, Tian F-X, Xu B, et al (2022) A comparative study on the degradation of phenylurea herbicides by UV/persulfate process: Kinetics, mechanisms, energy demand and toxicity evaluation associated with DBPs. Chem Eng J 428:132088. https://doi.org/10.1016/j.cej.2021.132088

Lakshmi NJ, Agarkoti C, Gogate PR, Pandit AB (2022) Acoustic and hydrodynamic cavitation-based combined treatment techniques for the treatment of industrial real effluent containing mainly pharmaceutical compounds. J Environ Chem Eng 10:108349. https://doi.org/10.1016/j.jece.2022.108349

Medina-Collana JT, Sejje Suárez WD, Anyosa Cáceres N, et al (2023) Intensification of Lead, Copper and Antimony Removal Using Brown Algae Adsorption Coupled to Hydrodynamic Cavitation. Sustainability 15:3453. https://doi.org/10.3390/su15043453

Patil AL, Patil PN, Gogate PR (2014) Degradation of imidacloprid containing wastewaters using ultrasound based treatment strategies. Ultrason Sonochem 21:1778–1786. https://doi.org/10.1016/j.ultsonch.2014.02.029

Patil Y, Sonawane SH, Shyam P, et al (2023) Hybrid hydrodynamic cavitation (HC) technique for the treatment and disinfection of lake water. Ultrason Sonochem 97:106454. https://doi.org/10.1016/j.ultsonch.2023.106454

Pinjari DV, Pandit AB (2010) Cavitation milling of natural cellulose to nanofibrils. Ultrason Sonochem 17:845–852. https://doi.org/10.1016/j.ultsonch.2010.03.005

Raj A, Bethi B, Sonawane SH (2018) Investigation of removal of crystal violet dye using novel hybrid technique involving hydrodynamic cavitation and hydrogel. J Environ Chem Eng 6:5311–5319. https://doi.org/10.1016/j.jece.2018.08.016

Roy K, Moholkar VS (2020) Sulfadiazine degradation using hybrid AOP of heterogeneous Fenton/persulfate system coupled with hydrodynamic cavitation. Chem Eng J 386:121294. https://doi.org/10.1016/j.cej.2019.03.170

Verma K, Moholkar VS (2023) Mineralization of Industrial Wastewater by a Hybrid Technique of Adsorption (Fe_3O_4@AC Nanocomposite) + Heterogeneous Fenton + Sonication and Discernment of Synergistic Effects. Ind Eng Chem Res acs.iecr.3c00427. https://doi.org/10.1021/acs.iecr.3c00427

Wang B, Su H, Zhang B (2021) Hydrodynamic cavitation as a promising route for wastewater treatment – A review. Chem Eng J 412:128685. https://doi.org/10.1016/j.cej.2021.128685

Wang B, Wang T, Su H (2022) A dye-methylene blue (MB)-degraded by hydrodynamic cavitation (HC) and combined with other oxidants. J Environ Chem Eng 10:107877. https://doi.org/10.1016/j.jece.2022.107877

Wei H, Hu D, Su J, Li K (2015) Intensification of levofloxacin sono-degradation in a US/H_2O_2 system with Fe_3O_4 magnetic nanoparticles. Chin J Chem Eng 23:296–302. https://doi.org/10.1016/j.cjche.2014.11.011https://doi.org/10.1016/j.ijpharm.2007.09.004

Appendix A5

Section A5.1: Synthesis of Fe_3O_4@AC nanocomposite

Fe_3O_4 nanoparticles were prepared using the co-precipitation method, as reported in Choudhury et al. (2021), with minor modifications. In a typical process to fabricate magnetite (Fe_3O_4) nanoparticles, a sonication bath was used to dissolve $FeCl_3 \cdot 6H_2O$ (2.2 g) completely and $FeSO_4 \cdot 7H_2O$ (1.2 g) in 100 mL of DI water. After gradually adding sodium carbonate (10.6 g, 100 mL) to the solution, as mentioned above, hydrazine hydrate (5 mL) was added dropwise in the presence of sonication. The solution was transferred to an oil bath and continuously stirred at 80 °C, followed by another 15 min sonication. After one hour, the solution was removed from the oil bath and cooled to room temperature. A permanent magnet was employed to gather the Fe_3O_4 nanoparticles that precipitated as an agglomerated black mass. This black mass was washed many times with deionized water, and the resulting Fe_3O_4 nanoparticles were dried for 12 h at 70 °C under a vacuum. Next, activated carbon (3 g) was dispersed into 100 mL of DI water using a sonication bath for 30 min. The synthesized Fe_3O_4 nanoparticles (500 mg) were added to this suspension (which makes the Fe_3O_4:AC ratio = 5:30), and the mixture was stirred for one hour at 600 rpm in an oil bath at 80°C. The solution was cooled to room temperature, and the Fe_3O_4@AC nanocomposite particles were separated using a magnet. These particles were washed 3× with DI water to bring the pH of the wash water to a neutral level, followed by vacuum-drying for 12 h at 70°C.

Figure A5.1. Photograph of the hydrodynamic cavitation reactor used in this study

Table A5.1. ANOVA analysis for the design of experiments

Source	Sum of Squares	df	Mean Square	F-value	p-value	
Model	4906.49	14	350.46	397.82	< 0.0001	significant
A-A	520.08	1	520.08	590.36	< 0.0001	
B-B	574.08	1	574.08	651.66	< 0.0001	
C-C	720.75	1	720.75	818.15	< 0.0001	
D-D	80.08	1	80.08	90.91	< 0.0001	
AB	0.2500	1	0.2500	0.2838	0.6026	
AC	6.25	1	6.25	7.09	0.0185	
AD	6.25	1	6.25	7.09	0.0185	
BC	30.25	1	30.25	34.34	< 0.0001	
BD	0.2500	1	0.2500	0.2838	0.6026	
CD	56.25	1	56.25	63.85	< 0.0001	
A^2	1920.82	1	1920.82	2180.39	< 0.0001	
B^2	966.77	1	966.77	1097.41	< 0.0001	
C^2	1006.77	1	1006.77	1142.82	< 0.0001	
D^2	410.82	1	410.82	466.34	< 0.0001	
Residual	12.33	14	0.8810			
Lack of Fit	12.33	10	1.23			
Pure Error	0.0000	4	0.0000			
Cor Total	4918.83	28				

Std. Dev.	0.9386	**R^2**	0.9975
Mean	77.25	**Adjusted R^2**	0.9950
C.V. %	1.22	**Predicted R^2**	0.9856
		Adeq Precision	67.0341

Section A5.2. RSM-BBD 3D plots of process variables

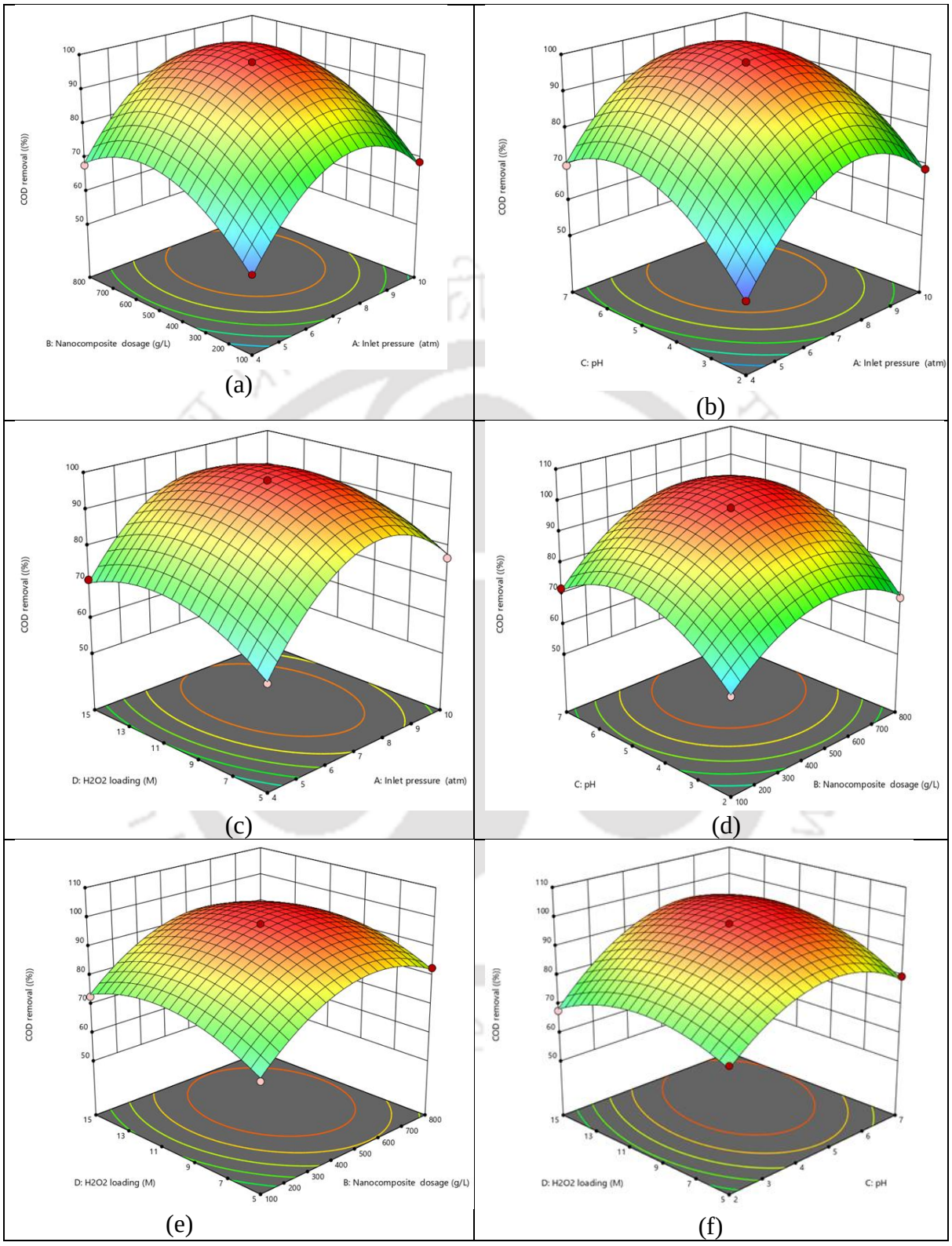

Table A5.2. List of contaminants identified using LC-MS analysis

Compound name	Formula	Retention time (min)	Mass (g/mol)	% degradation
1,2,3,4,7,8,9-Heptachlorodibenzofuran (HPCDF)	C_{12} H Cl_7 O	11.454	409.3	69.2
1-Aminonaphthalene	$C1_0$ H_9 N	14.415	143.19	81.1
2,2' 5',2-Terthiophene	C_{12} H_8 S_3	7.46	248	56.8
2,3,4,5-Tetrabromobenzoic acid (TBBA)	C_{19} H_2 Br_4 O_2	12.14	577.8	55.5
4,4'-Diaminodiphenylmethane (4MDA)	C_{13} H_{14} N_2	8.215	198.26	100
4-Aminobiphenyl	C_{12} H_{11} N	8.374	169.22	82.9
4-benzoylbiphenyl	C_{19} H_{14} O	14.636	306.3	55.4
5-Nitro-o-toluidine	C_7 H_8 N_2 O_2	8.69	152.16	71
9-Chlorohexadecafluoro-3-oxanonane-1-sulfonic acid (9Cl-PF3ONS)	C_8 Cl F_{16} O_4 S	13.154	570.68	100
Aldrin	C_{12} H_8 Cl_6	10.52	364.91	54.9
Benthiavalicarb-isopropyl	C_{18} H_{24} F N_3 O_3 S	13.813	381.46	59.9
Benzene	C_6 H_6	8.751	78.11	66.3
Benzonitrile	C_7 H_5 N	1.073	103.12	51.9
Benzyl butyl phthalate	C_{19} H_{20} O_4	10.652	312.36	71.1
Bisphenol AF	C_{15} H_{10} F_6 O_2	13.565	336.23	75.4
Butamifos	C_{13} H_{21} N_2 O_4 P S	15.231	332.35	100
Carbosulfan	C_{20} H_{32} N_2 O_3 S	11.518	380.55	62.5
Cycloate	C_{11} H_{21} N O S	14.753	215.36	62.4
Cyenopyrafen	C_{24} H_{31} N_3 O_2	11.291	393.52	73.9
DEF	C_{12} H_{27} O P S_3	14.381	314.51	100
Desmetryn	C_8 H_{15} N_5 S	14.623	213.30	100

Diacetoxyscirpenol	$C_{19}H_{26}O_7$	10.378	366.41	63.4
Diethatyl-ethyl	$C_{16}H_{22}ClNO_3$	14.427	311.80	100
Diethylphosphate (DEP)	$C_4H_{11}O_4P$	10.677	153.09	63.7
Dimethipin	$C_6H_{10}O_4S_2$	6.721	146.14	100
Dimethylphenol, 2,4- (2,4-xylenol)	$C_8H_{10}O$	11.475	122.16	95.5
Di-n-propyl phthalate	$C_{14}H_{18}O_4$	14.445	250.29	100
Endrin	$C_{12}H_8Cl_6O$	10.764	380.91	71.5
Fenamiphos	$C_{13}H_{22}NO_3PS$	14.521	303.4	100
Hydroxycotinine	$C_{10}H_{12}N_2O_2$	11.073	192.21	100
Iprobenfos	$C_{13}H_{21}O_3PS$	14.552	288.34	100
Isocarbamid	$C_8H_{15}N_3O_2$	7.431	231.25	60.5
Isofenphos oxon	$C_{15}H_{24}NO_5P$	15.99	329.33	80.7
Isomethiozin	$C_{12}H_{20}N_4OS$	14.476	268.38	100
Isopropalin	$C_{15}H_{23}N_3O_4$	8.481	309.36	65.4
isoxadifen-ethyl	$C_{18}H_{17}NO_3$	12.25	295.33	53.7
Kadethrin	$C_{23}H_{24}O_4S$	12.532	396.50	77.3
Lenacil	$C_{13}H_{18}N_2O_2$	11.599	234.29	100
Mephosfolan	$C_8H_{16}NO_3PS_2$	14.418	269.32	98
Metsulfuron-methyl	$C_{14}H_{15}N_5O_6S$	19.419	381.36	100
MGK-264	$C_{17}H_{25}NO_2$	14.516	275.39	74
Molinate	$C_9H_{17}NOS$	10.695	187.30	69.6
Mono-methyl phthalate (MMP)	$C_9H_8O_4$	1.122	180.16	100
N,N-Diethyl-3-(hydroxymethyl) benzamide (DHMB)	$C_{12}H_{17}NO_2$	12.687	207.26	98.6
N-Acetyl-S-(3-hydroxypropyl)-L-cysteine	$C_8H_{15}NO_4S$	14.159	189.21	100
n-Heptane	C_7H_{16}	7.777	100.2	100
Nitroaniline, 2-	$C_6H_6N_2O_2$	14.524	138.13	70.6
p-Cresol	C_7H_8O	11.04	108.13	94.8
Phorate sulfoxide oxon	$C_7H_{17}O_4PS_2$	1.686	260.31	70.4

Piperophos	C_{14} H_{28} N O_3 P S_2	14.925	353.48	100
P-Phenylenediamine (PPDA)	C_6 H_8 N_2	8.358	108.1	86.6
Prosulfocarb	C_{14} H_{21} N O S	1.157	251.32	100
Pyributicarb	C_{18} H_{22} N_2 O_2 S	11.296	330.44	100
Pyrimitate	C_{11} H_{20} N_3 O_3 P S	8.018	305.33	82.8
Pyroquilon	C_{11} H_{11} N O	11.477	173.21	71.2
Thionazin	C_8 H_{13} N_2 O_3 P S	11.063	248.24	94.9
Toluene	C_7 H_8	12.857	92.14	97.7
Triapenthenol	C_{15} H_{25} N_3 O	12.061	263.2	74.2
Trimethylnaphthalene, 2,3,5-	C_{13} H_{14}	8.725	170.25	65.5
Benzophenone-2	C_{13} H_{10} O_5	8.041	246.21	100
Butyraldehyde	C_4 H_8 O	7.046	72.11	77.1

References

Choudhury BJ, Roy K, Moholkar VS (2021) Improvement of Supercapacitor Performance through Enhanced Interfacial Interactions Induced by Sonication. Ind Eng Chem Res 60:7611–7623. https://doi.org/10.1021/acs.iecr.1c00279

CHAPTER 6

OVERVIEW AND SUGGESTIONS FOR FUTURE WORK

6.1 Overview

This dissertation has clearly demonstrated the efficacy of cavitation-based hybrid AOPs for treating and mineralizing industrial wastewater. All hybrid AOPs attempted in different studies have demonstrated more than 90% COD removal with equal TOC removal rates in relatively very short treatment periods. Thus, the cavitation-based hybrid AOPs have a high potential for application in industry. The present study has been carried out on a laboratory scale and is mainly aimed at deducing the physical mechanism and synergism in the hybrid AOPs. For translational research, these studies must be carried out on the pilot scale. Nonetheless, the results of this thesis provide a foundation for transforming the concepts and knowledge gained here into a practical, large-scale industrial process.

In this chapter, we present a summary or overview of all individual studies reported in the previous chapters, which have dealt with different cavitation-based hybrid AOPs for the treatment and mineralization of actual wastewater from industrial and domestic sectors. Some specific recommendations for future research directions follow this.

Chapter 2 has presented investigations in the mineralization of industrial wastewater (COD = 3246 mg/L, TOC = 2500 mg/L) using a ternary (ultrasound + Fenton + adsorption) hybrid advanced oxidation process. Fe_3O_4 decorated activated charcoal (Fe_3O_4@AC) nanocomposites (surface area = 538.88 m2/g; adsorption capacity = 294.31 mg/g) were synthesized using coprecipitation. The wastewater treatment process was optimized using central composite statistical design. At optimum conditions, viz. pH = 4.2, H_2O_2 loading = 0.71 M, adsorbent dose = 0.34 g/L, reduction in COD and TOC of wastewater were 94.75% and 89%, respectively. These results are attributed to synergistic interactions between the adsorption of pollutants on Fe_3O_4@AC, surface Fenton reactions, and enhanced mass transfer due to sonication. This synergism boosted the interactions among •OH radicals and pollutant molecules, leading to effective degradation and mineralization. The Fe_3O_4@AC showed excellent recovery (>90 wt %) and reusability (>90% COD removal) in 5 successive cycles of treatment

Chapter 3 has reported studies in the treatment of industrial wastewater (WW) (for chemical oxygen demand (COD), total organic carbon, and toxicity reduction) using a Fe_3O_4@Laccase nanocomposite in the presence of sonication. The nanocomposite was synthesized by immobilization of laccase on the surface of amino-functionalized magnetic Fe_3O_4 nanoparticles. Statistical optimization of physical parameters of WW treatment was done using mechanical agitation of 300 rpm. The optimization resulted in 61.7% COD removal at pH = 4.5, temperature = 66.5 °C, and Fe_3O_4@Laccase loading of 1.46 g/L. The COD removal was enhanced by ∼46% with the application of 35 kHz sonication (at 10% duty cycle) in addition to mechanical agitation. Analysis of the deconvolution of FTIR spectra of the Fe_3O_4@Laccase nanocomposite revealed a reduction in α-helix and β-turn content and a rise in random coil content of the immobilized laccase after sonication. These changes in the secondary structure of laccase enhanced the activity of the enzyme, which resulted in faster kinetics of COD

removal. The toxicity of treated WW was reduced by ~70%. LC-MS analysis of the original and treated WW helped in the identification of more than 15 contaminants that underwent >75% degradation. The Fe_3O_4@Laccase biocatalyst also showed excellent recoverability and 72% retention of enzymatic activity (with just a 15% reduction in COD removal) for six consecutive treatment cycles.

Chapter 4 has dealt with the treatment of industrial wastewater (WW) with a hybrid advanced oxidation process (AOP) that uses sonication in the presence of floatable chitosan-based hydrogel beads. These hydrogel beads were synthesized with Fe_3O_4 decorated activated charcoal nanoparticles (Fe_3O_4@AC nanocomposites) as filler material. The hydrogel beads (Fe_3O_4@AC@CH) served dual purpose as adsorbents and heterogeneous Fenton reagents. Statistical experimental design was used to optimize the hybrid AOP. At optimal conditions (0.75 M H_2O_2, 1 g/L Fe_3O_4@AC@CH beads, pH 5.12), a COD removal of 96.12 % and TOC removal of 78.14 % was achieved in 1 h treatment. Several control experiments were performed concurrently to identify synergistic interactions in the hybrid AOP. The surface and porous structure of the hydrogels absorbed substantial amounts of pollutants. Fenton reactions occurring on the hydrogel beads' surface produced radicals $^{\bullet}OH$ and $HO_2^{\bullet}$ that successfully degraded and mineralized the pollutants. Sonication induced intense micro-mixing in the medium, enhancing mass transfer between bulk medium and surface/pores of hydrogel beads. The toxicity of WW was reduced by ~ 70 % after treatment. Major contaminants in the WW degraded during treatment were identified using LC-MS analysis. Fe_3O_4@AC@CH hydrogel beads had excellent recyclability till six consecutive treatment cycles

Chapter 5 has examined a novel industrial wastewater treatment process that synergistically combined hydrodynamic cavitation (HC, orifice configuration) and Fe_3O_4@AC nanocomposites. The investigation includes assessment and optimization of the effects of various operating conditions, such as inlet pressure, initial pH, Fe_3O_4@AC dosage, and H_2O_2

loading, on the reduction in chemical oxygen demand (COD) of the wastewater. Liquid chromatography-mass spectrometry (LC-MS) was utilized to identify specific organic contaminants in wastewater before and after treatment. Optimization of the process parameters was done using techniques of response surface methodology (RSM) with a Box-Behnken design (BBD). A maximum COD removal of 99.37% with 88.80% total organic carbon (TOC) removal was achieved for the optimal conditions: inlet pressure = 8 atm, pH = 4.5, Fe_3O_4@AC dosage = 0.55 g/L, and H_2O_2 loading = 0.43 M. The reaction rate constant notably improved from 1.6×10^{-3} to 47.2×10^{-3} min^{-1} when HC was paired with the adsorption and the Fenton process. The effectiveness of cavitation-based oxidation was evaluated in terms of cavitational yield (mg/J), with the highest yield (2.33×10^{-2} mg/J) achieved for the ternary hybrid AOP (HC + adsorption + Fenton). The Fe_3O_4@AC nanocomposite retained its catalytic efficiency even after six cycles of recovery and reuse, demonstrating its stability for wastewater treatment applications. These findings underscore the potential of HC-based ternary hybrid AOPs for efficient treatment and mineralization of industrial wastewater.

The results of the above studies show that although the ultrasonic or hydrodynamic cavitation technique is capable of degradation and mineralization of the wastewater, it needs to be coupled with other techniques to achieve maximum efficiency. Mere high production of the oxidizing radicals during the treatment is not sufficient, but their interaction with the pollutants is equally crucial to have effective utilization of these radicals. Thus, local concentration of the pollutants in the wastewater is essential in the close vicinity of the location of the production of the radicals. In this thesis, we have tried to achieve the same using the composite of iron oxide and activated charcoal. This composite is very simple and easy to synthesize, almost fully recoverable and recyclable with retention of efficiency and also highly economical for large-scale operations. For eco-friendlier operations, we have also attempted the enzyme-based composite of Fe_3O_4-Laccase. Although the enzyme component, in this case,

is expensive, it is immobilized to the magnetic Fe_3O_4 nanoparticles and thus almost completely recoverable and recyclable. Thus, effective immobilization of the enzyme (which will avoid loss during operation) is key to the success of the enzyme-based processes. In summary, the cavitation-based hybrid processes reported in this thesis have a high potential for implementation in the industry to mitigate the pollutants in wastewater discharges. Of course, significant translational research is also necessary, but we hope that our methodologies and results will provide crucial and valuable input for translational research.

6.2 Suggestions for Future Work

1. Scaling Up: For ultrasonic cavitation-based hybrid AOPs, the main challenge is to design and operate a high-power ultrasound-generating device. The optimization of the sonic reactors for the proper distribution of ultrasound power in a large volume is crucial. This will require the design and fabrication of an effective transducer and high-power and high-frequency electrical power that will drive these transducers. The hydrodynamic cavitation technique is relatively much easier to design and operate. The use of a power pump along with a properly designed orifice or venture-based cavitation device would be sufficient. Nonetheless, optimization of such a reactor for effective and consistent operation for wastewater inputs from different sources (with varying COD, BOD, and other parameters) is also a major challenge. Future research can address these two issues that could pave the way for industrial implementation of cavitation-based wastewater treatment.

2. Operational and Economic Assessment: Implementing this process in real-world applications would help identify practical challenges that arise during operation, along with insights into its economic viability. A thorough economic study of cavitation-based wastewater treatment needs to be conducted.

3. **Component-Specific Impact on BOD**: Given the complexity of real wastewater, which contains thousands of compounds, further work is needed to determine which specific components contribute most to biochemical oxygen demand (BOD).

4. **Biological Techniques Coupled with Ultrasonic or Hydrodynamic Cavitation:** While this study focused on different cavitation-based hybrid advanced oxidation processes (AOP), there is significant potential to explore the coupling of conventional biological techniques with either ultrasonic or hydrodynamic cavitation to enhance wastewater treatment efficiency. These techniques are expected to be eco-friendlier than the hybrid AOPs.

RESEARCH OUTPUTS

PUBLISHED IN PEER-REVIEWED INTERNATIONAL JOURNALS

Research outputs from the Thesis

1. **Verma, K,** Moholkar, V.S. Intensification of Industrial wastewater treatment using hydrodynamic cavitation-based ternary hybrid advanced oxidation processes. *Chemical Engineering Research and Design*, doi.org/10.1016/j.cherd.2025.05.054. **(2025)**
2. **Verma, K.**, Moholkar, V. S. Investigations in Sonoenzymatic Treatment of Industrial Wastewater Using Fe_3O_4@Laccase Nanocomposites. *ACS ES&T Water*, doi.org/10.1021/acsestwater.3c00697. **(2024)**
3. **Verma, K,** Moholkar, V. S. COD and toxicity reduction of wastewater using a hybrid advanced oxidation process of sonication with chitosan-based hydrogel beads. *Process Safety and Environmental Protection*, https://doi.org/10.1016/j.psep.2024.11.024. **(2024)**
4. **Verma, K.,** Moholkar, V. S. Mineralization of Industrial Wastewater by a Hybrid Technique of Adsorption (Fe_3O_4@AC Nanocomposite) + Heterogeneous Fenton + Sonication and Discernment of Synergistic Effects. *Industrial and Engineering Chemistry Research*, doi.org/10.1021/acs.iecr.3c00427. **(2023**)

Book chapters

1. **Verma, K.,** Moholkar, V. S. Emerging Technologies in Wastewater Treatment. Innovative Approaches in Industrial Wastewater Treatment for Environmental Sustainability. (under review)
2. **Verma, K.,** Moholkar, V. S. Advanced Oxidation Processes (AOPs). Innovative Approaches in Industrial Wastewater Treatment for Environmental Sustainability. (under review)

Conferences Presented

1. Verma, K., Moholkar, V. S. Enhancing industrial wastewater treatment through Fe_3O_4 nanoparticles-loaded activated charcoal: Design and optimization for sustainable development. *International Conference on Technologies and Innovations for Sustainable Development 2023* at MNNIT Allahabad. **(oral)**
2. Verma, K., Moholkar, V. S. Treatment of industrial wastewater by a hybrid technique of AOPs using Fe_3O_4@AC nanocomposite. *SCIENTIFIQUE at RIC 2023* IIT Guwahati. **(oral)**
3. Verma, K., Moholkar, V. S. Unlocking Environmental Solutions: Catalysis in Hybrid Advanced Oxidation Processes for Wastewater Treatment. *Lucknow University (UP).* **(guest lecture)**
4. Verma, K., Moholkar, V. S. Enhancing Industrial Wastewater Treatment: Efficacy and Optimization of Ultrasound assisted Laccase Immobilized on Magnetic Fe_3O_4 Nanoparticles. *Global Congress of Catalysis 2024, Paris, France*. **(Keynote lecture online)**
5. Verma, K., Moholkar, V. S. Innovative Synthesis of Fe_3O_4 Nanoparticles-Loaded Activated Charcoal for Advanced Industrial Wastewater Treatment. *International Workshop on Recent Advancements in Magnetism and Magnetic Materials 2024 (i-ReAd MAGMA 24).* **(Best Oral)**
6. Verma, K., Moholkar, V. S. Revolutionizing Industrial Wastewater Treatment: Harnessing Ultrasound Enhanced Laccase Immobilization on Magnetic Fe3O4 Nanoparticles for Superior Efficiency and Optimization. *International Conference on Environmental Challenges, Opportunities and Sustainable Solutions 2024 at IIT Guwahati*. **(oral)**
7. Verma, K., Moholkar, V. S. Enhancing Sustainability: Remediation through Heterogeneous Catalysts in Hybrid Advanced Oxidation Processes for Wastewater Treatment. International conference on Sustainable Energy and Green Technology SEGT 2024 at Bangkok Thailand. **(oral)**
8. Verma, K., Moholkar, V. S. Optimizing Sustainability: Heterogeneous Catalyst-Driven Remediation using Fe_3O_4@AC nanocomposite in Hybrid Advanced Oxidation Processes for wastewater treatment. *Leadership Summit 2024 at IIT Guwahati.* **(poster)**